

Contact methods integrating plasticity models with application to soil mechanics

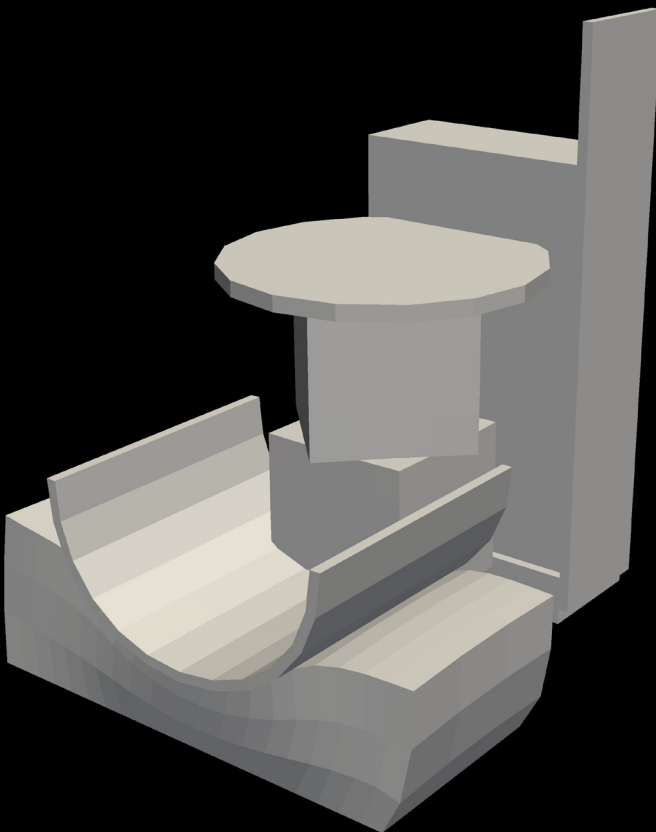
B13/1

Christian Weißenfels

Leibniz
Universität
Hannover



Institut für
Kontinuumsmechanik



Contact methods integrating plasticity models with application to soil mechanics

Von der Fakultät für Maschinenbau
der Gottfried Wilhelm Leibniz Universität Hannover

zur Erlangung des akademischen Grades
Doktor-Ingenieur

genehmigte Dissertation
von

Dipl.-Ing. Christian Weißenfels

geboren am 30.01.1979 in Rosenheim

2013

Herausgeber:

Prof. Dr.-Ing. Peter Wriggers

Verwaltung:

Institut für Kontinuumsmechanik
Gottfried Wilhelm Leibniz Universität Hannover
Appelstraße 11
30167 Hannover

Tel: +49 511 762 3220
Fax: +49 511 762 5496
Web: www.ikm.uni-hannover.de

© Dipl.-Ing. Christian Weißenfels
Institut für Kontinuumsmechanik
Gottfried Wilhelm Leibniz Universität Hannover
Appelstraße 11
30167 Hannover

Alle Rechte, insbesondere das der Übersetzung in fremde Sprachen, vorbehalten. Ohne Genehmigung des Autors ist es nicht gestattet, dieses Heft ganz oder teilweise auf photomechanischem, elektronischem oder sonstigem Wege zu vervielfältigen.

ISBN 978-3-941302-06-8

1. Referent: Prof. Dr.-Ing. Peter Wriggers
2. Referent: Prof. Dr.-Ing. Karl Schweizerhof
Tag der Promotion: 13.12.2012

Zusammenfassung

Der Schwerpunkt der vorliegenden Arbeit liegt in der Entwicklung von neuartigen Konzepten zur direkten Integration von drei-dimensionalen Plastizitätsmodellen in eine Kontaktformulierung. Die allgemeinen Konzepte wurden speziell auf Boden Bauwerk Interaktionen angewandt und im Rahmen der Mortar-Methode numerisch umgesetzt.

Zwei unterschiedliche Strategien wurden dabei verfolgt. Die Erste integriert die Bodenmodelle in eine Standard-Kontaktdiskretisierung, wobei die zweite Variante die Kontaktformulierung in Richtung eines drei-dimensionalen Kontaktelements erweitert.

Innerhalb der ersten Variante wurden zwei unterschiedliche Konzepte ausgearbeitet, wobei das erste Konzept das Bodenmodell mit dem Reibbeiwert koppelt. Dabei muss die Höhe der Lokalisierungszone entlang der Kontaktfläche bestimmt werden. Das zweite Konzept basiert auf einer Umformulierung der Fließbedingung und der Einführung einer zusätzlichen Kraft, mit deren Hilfe Dilatanzeffekte in der Kontaktschicht wiedergegeben werden können. Ein Vergleich zwischen den numerischen Ergebnissen eines direkten Scher- und eines Triaxialversuchs zeigt, dass Bodenmodelle erfolgreich auf die Kontaktfläche projiziert werden können.

Ebenfalls konnte in dieser Arbeit gezeigt werden, dass ein Zusammenhang zwischen der Kontinuums- und der Kontaktkinematik besteht. Dieser Zusammenhang basiert dabei auf dem 'Solid-shell'-Konzept zusammen mit einer Integration der Kinematik über die Höhe sowie einem anschließenden Grenzübergang der Höhe gegen Null. Unter Vernachlässigung des Grenzübergangs wurde ein neuartiges drei-dimensionales Kontaktelement entwickelt, mit dem Materialgesetze des Kontinuums direkt in die Kontaktformulierung integriert werden können.

All diese Methoden können auch auf multiphysikalische Problemstellungen erweitert werden, was anhand der Theorie poröser Medien aufgezeigt wurde.

Da eine numerische Simulation von Boden-Bauwerk-Interaktionen mit der Finite-Element-Methode eine große Herausforderung darstellt, wurden im Rahmen der Mortar-Methode vier verschiedene Lösungsmethoden und zwei verschiedene Varianten der Kontaktkinematik miteinander verglichen und hinsichtlich ihrer Robustheit überprüft. Dabei wurde zum ersten Mal eine reine Lagrange Multiplikator Methode und eine gemischte Variante, bestehend aus der 'augmented Lagrangian'-Methode für den Normal- und der Penaltyregularisierung für den Tangentialkontakt, im Rahmen der Mortar-Methode implementiert.

Abschließend wird noch ein Konzept vorgestellt, mit dem die Kontaktgleichungen in die eXtended-Finite-Element-Methode integriert werden können. Dieses Konzept zeigt dabei einen glatten Übergang zwischen beiden Kontaktkörpern wobei keine Stabilisierungstechniken benötigt werden.

Schlagworte: Kontaktmechanik, Finite-Element-Methode, Bodenmechanik, Reibgesetze, Mortar-Methode, eXtended-Finite-Element-Methode

Abstract

This work is focused on the development of novel concepts for a direct integration of three-dimensional plasticity models into a contact formulation which can be applied to different kinds of contact discretization. These generic concepts are applied to the investigation of soil structure interactions where the new friction laws are implemented into the Mortar method.

Thereby two different strategies were elaborated. The first one integrates the soil model into standard contact discretization and the latter one extends the contact formulation towards a three-dimensional contact element.

Within the first strategy, one version couples the soil model directly to the coefficient of friction where an intrinsic height of the localization zone at the contact surface has to be determined. In the second version, the plasticity model is reformulated and an additional force is introduced which represents the influence of dilatancy effects at the contact surface. For both variants, the soil model is successfully projected since the evaluation of the direct shear and the triaxial test shows the same behavior.

In this work it is also shown that there exists a link between the three-dimensional continuum kinematics and the contact constraints. This connection follows directly from the application of the solid-shell concept and a subsequent integration of the kinematics over the height. In the limit, if the height goes to zero, the contact kinematics evolve. Neglecting the limit, a three-dimensional contact element is obtained where the three-dimensional material description can be embedded directly into the contact formulation.

All these methods can be extended to multiphysics which is shown theoretically by the theory of porous media.

Since the numerical simulation of soil structure interactions is very challenging with finite elements, four different solution methods and two different treatments of the contact kinematics within the Mortar framework are valued at robustness to choose the best discretization scheme for the new friction laws. Within the Mortar framework for the first time a pure Lagrange multiplier method and a mixed version consisting of the augmented Lagrangian method for the normal contact and of the penalty regularization for the tangential part are presented in this work.

At the end a concept to integrate the contact formulations into the eXtended-Finite-Element-Method is presented which is based on the Hu Washizu principle and shows a smooth transition between the contacting bodies without any stabilization schemes.

Keywords: Contact mechanics, Finite-Element-Method, Soil mechanics, Friction laws, Mortar method, eXtended-Finite-Element-Method

Acknowledgements

This work is the result of my research work during my time at the Institute of Mechanics and Computational Mechanics (IBMN) and at the Institute of Continuum Mechanics (IKM) both at the University of Hannover and was founded by the German Research Foundation (DFG) within the research group 1136 GeoTech.

First of all, my special thanks go to my doctoral adviser Prof. Dr.-Ing. Peter Wriggers. Especially his unrestricted trust, his beneficial support and his encouragement gave me the opportunity to learn a lot within and beyond the field of numerical mechanics and enabled me to pursue and actualize my own ideas.

Furthermore, I would like to thank my second referee Prof. Dr.-Ing. Karl Schweizerhof for his earnest interest in my work, the fruitful discussions we had and his helpful comments which influenced this work positively.

At the end, I want also to thank my office mate Dr. İlker Temizer who helped my especially at the beginning of my research work with a lot of good advices. My special thanks go also to Vera Halfar for her help in the jungle of bureaucracy, to the administrator team for keeping my computer alive and especially to all my former colleagues at the IBNM and IKM for a delightful atmosphere.

Hannover, January 2013

Christian Weißenfels

Contents

1	Introduction	1
1.1	State of the art	3
1.2	Structure of this work	4
2	Continuum mechanics	7
2.1	Kinematics	8
2.1.1	Motion	8
2.1.2	Deformation measures	9
2.2	Balance principles	10
2.2.1	Continuity equation	10
2.2.2	Momentum, mechanical energy and angular momentum	10
2.2.3	Energy and entropy	11
2.3	Constitutive models	13
2.3.1	Elasticity	14
2.3.2	Plasticity	15
2.4	Variational form	18
2.4.1	Reduction to surface description	18
2.4.2	Reduction to contact description	21
3	Finite elements	27
3.1	Concept of finite elements	28
3.2	Space discretization	31
3.3	Newton iteration for nonlinear equations	33
3.4	Assembling and solver	35
4	Contact discretization	37
4.1	Contact solution methods	38
4.1.1	Lagrange multiplier method	40
4.1.2	Penalty method	40
4.1.3	Augmented method	41
4.2	Node to surface	44
4.2.1	Global search of contact elements	44
4.2.2	Projection point and base vectors	46
4.2.3	Contact kinematical relations	47
4.2.4	Integration domain	48

4.2.5	Linearized quantities	49
4.2.6	Residual vector and tangent matrix	50
4.3	Mortar method	53
4.3.1	Setup of contact element	53
4.3.2	Integration point and base vectors	56
4.3.3	Integration	57
4.3.4	Kinematical contact relations	57
4.3.5	Linearized quantities	60
4.3.5.1	Contact element quantities	61
4.3.5.2	Kinematical quantities	65
4.3.6	Residual vector and tangent matrix	69
4.3.6.1	Lagrange multiplier method	70
4.3.6.2	Penalty method	73
4.3.6.3	Augmented Lagrange multiplier method	75
4.3.6.4	Mixed method	77
4.4	Numerical solutions	80
4.4.1	Hertzian contact	80
4.4.2	Rotating blocks	81
4.4.3	Ironing	83
5	Soil mechanics	87
5.1	Classification of the soil	87
5.2	Behavior under loading	89
5.2.1	Plastic behavior	89
5.2.2	Change of volume	89
5.2.3	Dependency on pressure and porosity	90
5.2.4	Localization	91
5.2.5	Shakedown and runaway ratcheting	91
5.2.6	Liquefaction and consolidation	92
5.3	Modeling strategies	92
5.4	Ehlers soil models	94
5.4.1	Stress strain relation	94
5.4.2	Yield criterion and evolution equation	95
5.4.3	Hardening concept	97
5.4.4	Derivatives	97
5.4.5	Algorithmic implementation	98
5.4.6	Substepping scheme	101
5.4.7	Viscoplastic regularization	102
5.4.8	Numerical triaxial and footing test	102
6	Theory of porous media	107
6.1	Concept of volume fractions	107
6.2	Kinematics of the mixture	108
6.3	Balance of mass and momentum of the mixture	108
6.4	Incompressible biphasic model	109

6.5	Weak form of porous media	111
6.6	Discretization of porous media	112
6.7	Consolidation test	113
7	Projection strategies	115
7.1	Projection over the coefficient of friction	115
7.1.1	Link between contact and continuum	116
7.1.2	Linearization	118
7.2	Direct link between yield and slip criterion	119
7.2.1	Projection of Ehlers yield criterion	121
7.2.2	Linearization	124
7.3	Connection to the theory of porous media	125
7.4	Numerical tests	125
7.4.1	Direct shear test	125
7.4.2	Pull out of a wall	128
8	3D contact element	133
8.1	3D contact kinematical relations	133
8.2	Linearized quantities	136
8.3	Residual vector and tangent matrix	140
8.4	Connection to the theory of porous media	142
8.5	Numerical direct shear test	143
9	XFEM contact element	145
9.1	Description of elements with interfaces	145
9.2	Linear embedded element	147
9.2.1	Weak form	148
9.2.2	Discretization	149
9.2.3	Solution algorithm	152
9.3	Linear embedded contact element	152
9.3.1	Weak form	153
9.3.2	Segmentation	153
9.3.3	Discretization	154
9.3.4	Solution algorithm	156
9.4	Numerical examples	157
10	Conclusion and Outlook	161
A	Principle stresses	165
B	Voigt notation	167
B.1	B matrices	167
B.2	Elastic strain tensor	168
B.3	Invariants and its derivations	168
B.4	Shell transformation tensor	169

C	Contact vectors and storage arrays	171
C.1	Node to surface vectors	171
C.2	Mortar tensors	172
C.3	Mortar storage arrays	173
D	Derivation of the Reynolds equation	175

Index

In the following, all symbols, operators and quantities are listed subdivided into continuum, shell, theory of porous media, finite element and contact parts. The equation number states where this quantity is specified.

Symbols and Operators

$\delta(\bullet)$	Symbol of a virtual quantity
$\Delta(\bullet)$	Symbol of linearized quantity
$\dot{\bullet}$	Material time derivative
$\dot{\bullet}$	Lie time derivative
Δ_t	Time step increment
div	Divergence current configuration
Div	Divergence initial configuration
grad	Gradient current configuration
Grad	Gradient initial configuration
h	Discretized quantity
$I(\bullet), II(\bullet), III(\bullet)$	First, second and third invariant of a quantity
$\varphi(\bullet)$	Mapping of a quantity into current config.
$n+1$	Actual time step
n	Old time step
tr	Trial quantity
ξ^1, ξ^2, ξ^3	curved convective coordinates
$\bar{\bullet}$	Enriched quantity (XFEM)
$\tilde{\bullet}$	Standard and enriched quantity (XFEM)

Continuum quantities

\mathbf{a}	Acceleration vector (6.18)
α_i	Internal variables (2.54)
B	Material domain of a body (2.1)
∂B_u	Displacement boundary (3.5)
∂B_σ	Traction boundary (2.18, 3.5)
\mathbf{b}	Right Cauchy Green tensor (2.11)
$\bar{\mathbf{b}}$	Inner acceleration term (2.18)
c	Heat capacity (2.41)
c^v	Porosity factor (5.9)
\mathbf{C}	Left Cauchy Green tensor (2.11)
\mathbf{c}	Fourth order material tensor current config. (3.31)
D_{int}	Internal dissipation (2.36)
\mathbf{d}	Deformation velocity tensor (2.12)
δ	local deformation measure (2.7)
\mathbf{E}	Green Lagrange strain tensor (2.10)
\mathbf{e}	Euler Almansi strain tensor (2.10)

ε	Linear strain tensor (2.50)
$\varepsilon^e, \varepsilon^p$	Elastic and plastic linear strain tensor (2.50)
f	Yield criterion (2.52)
f_{rt}	Root part of yield criterion (5.26)
\mathbf{F}	Deformation gradient tensor continuum (2.9)
G	Weak form (2.55)
g	Plastic potential (2.51)
g_{rt}	Root part of plastic potential (5.18)
$\mathbf{g}, \mathbf{g}^{-1}$	Co- and contravariant metric tensor current configuration (2.45)
$\mathbf{g}_i, \mathbf{g}^i$	Co- and contravariant base vector continuum current configuration (2.5)
$\mathbf{G}_i, \mathbf{G}^i$	Co- and contravariant base vector continuum initial configuration (2.5)
h_i	Hardening functions (2.54)
\mathbf{h}	Hardening variables vector (5.23)
J	Determinant of the deformation gradient (2.40)
K	Kinetic energy (2.20)
\mathbf{l}	Velocity gradient tensor current configuration (2.12)
λ	Plastic flow (2.51)
n, e	Volume ratio, void ratio (5.10)
n^{vp}, \mathbf{n}^{ep}	Volumetric and deviatoric part of plastic flow direction (5.36)
η	Entropy (2.31)
$\boldsymbol{\eta}$	Weighting function (2.55)
P_{int}, P_{ext}	Internal and external power (2.20)
\mathbf{P}	1 st Piola Kirchhoff stress tensor (2.20)
φ	Friction angle (5.2)
Ψ	Helmholtz free energy function, strain energy function (2.32)
Π	Potential, functional (3.13)
Q	Production of heat (2.28)
\mathbf{q}	Heat flux current configuration (2.33)
\mathbf{Q}	Heat flux initial configuration (2.28)
\mathbf{q}_i	Hardening stresses (2.54)
r	Inner heat production current configuration (2.33)
R	Inner heat production initial configuration (2.28)
ρ	Density current configuration (2.16)
ρ_0	Density initial configuration (2.15)
$\sigma_1, \sigma_2, \sigma_3$	Principal stresses (5.4, A.6)
$\boldsymbol{\sigma}$	Cauchy stress tensor (2.23)
\mathbf{s}	Deviator of the Cauchy stress tensor (2.48)
\mathbf{S}	2 nd Piola Kirchhoff stress tensor initial configuration (2.57)
\mathbf{t}	Surface load current configuration (2.56)
\mathbf{T}	Surface load initial configuration (2.18)
Θ	Absolute temperature (2.31), Lode angle (5.6)
$\boldsymbol{\tau}$	Kirchhoff stress tensor (2.46)
U	Inner energy (2.28)
\mathbf{u}	Displacement vector (2.6)

\mathbf{v}	Velocity vector (2.4)
ν^p	Dilatancy angle (5.19)
w_i	Irreversible inner power (2.29)
\mathbf{x}	Position vector current configuration (2.1)
\mathbf{X}	Position vector initial configuration (2.2)

Shell quantities

$\mathbf{a}_\alpha, \mathbf{a}^\alpha$	Co - and contravariant base vector shell middle surface current config. (2.62)
$\mathbf{A}_\alpha, \mathbf{A}^\alpha$	Co - and contravariant base vector shell middle surface initial config. (2.62)
\mathbf{d}	Director current configuration (2.59)
\mathbf{E}^m	Membrane part of the Green Lagrange strain tensor (2.58)
\mathbf{E}^b	Bending part of the Green Lagrange strain tensor (2.58)
\mathbf{E}^s	Shear part of the Green Lagrange strain tensor (2.58)
\mathbf{N}	Normal force tensor (2.58)
\mathbf{N}	Normal vector (2.59)
\mathbf{M}	Couple tensor (2.58)
\mathbf{Q}	Shear force tensor (2.58)
\mathbf{u}_s	Surface displacement vector (2.63)
\mathbf{w}	Difference vector (2.63)
\mathbf{x}_s	Surface position vector current configuration (2.59)
\mathbf{X}_s	Surface position vector initial configuration (2.59)
\mathbf{z}	Shifter tensor current configuration (2.62)
\mathbf{Z}	Shifter tensor initial configuration (2.62)

Theory of porous media operators and quantities

$(\bullet)'_\alpha$	Material derivative of a constituent (6.7)
n^α	Volume fraction (6.2)
p	Fluid pressure (6.19)
$\hat{\mathbf{p}}^\alpha$	Production of momentum (6.9)
$\rho_0^\alpha, \rho^\alpha$	Material and partial density (6.3)
$\hat{\rho}^\alpha$	Production of mass (6.9)
\mathbf{w}_f	Seepage velocity (6.14)

Finite element quantities

\mathbf{D}	Material matrix (3.30)
\mathbf{j}	Jacobian current configuration (3.12)
N_I	Shape function of node I (3.10)
\mathbf{K}	Stiffness matrix, tangent (3.30)
\mathbf{P}	Loading vector (3.20)
\mathbf{R}	Residual vector (3.20)
W	Weighting of the integration point (3.21)

Contact symbols and operators

1	Slave surface
2	Master surface
s	Slave node (NTS formulation)
A	Slave node (Mortar formulation)
\bullet	Quantity projected master surface (NTS formulation)
$\tilde{\bullet}$	Quantity projected master surface old time step (NTS formulation)
$\bar{\bullet}$	Nodal averaged quantity (Mortar formulation)
$\tilde{\bullet}$	Quantities Cartesian coordinate system (3D contact element)
$\Omega(\bullet)$	Cross product matrix

Contact quantities

a	Nodal contact area NTS - (4.45) and Mortar formulation (4.80)
$\mathbf{a}_\alpha^i, \mathbf{a}^{i\alpha}$	Co- and contravariant base vectors of surface i current config. (2.74, 4.5)
$\mathbf{A}_\alpha^i, \mathbf{A}^{i\alpha}$	Co- and contravariant base vector of surface i initial config. (2.74)
$a_{\alpha\beta}, a^{\alpha\beta}$	Co- and contravariant contact metric coefficients (4.39)
$b_{\alpha\beta}, b^{\alpha\beta}$	Co- and contravariant curvature coefficients (4.39)
∂B_c	Contact boundary (4.1)
c_N, c_T, c_C	Penalty parameter for normal, tangential and slip part (4.11)
\mathbf{c}_s	Solution vector slip (4.132)
\mathbf{d}_s	Solution vector displacements (4.103)
$D_{\alpha\beta}$	Contact material matrix components (4.169)
\mathbf{e}_T	Normalized slip base vector (4.41)
$\det \mathbf{j}$	Determinant of Jacobian Mortar formulation (4.81)
$\dot{\gamma}$	Slip rate (4.2)
$\bar{\mathbf{e}}$	Over the height integrated Euler Almansi stain tensor (2.78, ff)
f^c	Friction law (4.2)
G_u^c	Weak form of virtual contact work (4.6)
G_l^c	Weak form of enforcement contact constraints (4.6)
$\bar{\mathbf{g}}$	Averaged gap vector (4.85)
g_N	Normal penetration (2.89)
\mathbf{g}_T	Over the height integrated metric tensor current config. (2.89)
h_A	Nodal contact height (8.32)
$H_{\alpha\beta}, H^{\alpha\beta}$	Co- and contravariant auxiliary variable coefficients (4.39)
L_α	Contact coupled material Lagrange multiplier vector (4.169)
\mathbf{l}_s	Solution vector Lagrange multiplier (4.132, 4.142)
$\boldsymbol{\lambda}$	Unknown contact stress vector (2.87)
λ_N	Unknown normal contact pressure (2.87)
$\boldsymbol{\lambda}_T$	Unknown tangential contact stress vector (2.87)
$\hat{\lambda}_N$	Augmented normal contact pressure (4.17)
$\hat{\boldsymbol{\lambda}}_T$	Augmented tangential contact stress vector (4.17)
μ	Coefficient of friction (4.4)
n_{AB}	Nodal mass matrix (4.86)

N_A^d	Nodal dual shape function (4.93)
\mathbf{n}^i	Normal vector of surface i (2.83, 4.5)
\mathbf{n}_0	Normal vector center of element (4.71)
M_A	Optional nodal shape function (4.95)
\mathbf{s}_T	Slip vector (4.41)
$\mathbf{t}_\alpha^1, \mathbf{t}_\alpha^2$	Normalized base vectors of surface i (4.5)
t_N	Normal contact pressure (4.12)
\mathbf{t}_T	Tangential contact stress vector (4.12)
t_D	Dilatancy contact stress (7.23)
$\bar{\xi}^\alpha$	Local projection point NTS formulation (4.30)
$\bar{\xi}^\alpha$	Integration point Mortar formulation (4.76)
$\bar{\mathbf{x}}_I^i$	Nodal position vector of surface i on plane surface (4.72, 4.73)
$\bar{\mathbf{x}}_{int}$	Intersection point on plane surface (4.74)
$\bar{\mathbf{x}}_c$	Centroid point on plane surface (4.75)
$\bar{\mathbf{x}}_p$	Pallet point on plane surface (4.75)

Chapter 1

Introduction

Each structure can only be founded on soils which are able to carry the load of that structure without large deformations. Therefore in the planning process many investigations have to be undertaken to determine how the soil behaves under loading. However during the construction due to the multitude of supporting works like excavations, installing of anchors, sheet walls and especially piles, the existing state of the soil can change significantly. For example, figure 1.1 shows the horizontal displacement of a slotted wall during the whole excavation process at the Postdamer Platz in Berlin (see Triantafyllidis [1998]). Therein the main part of the displacements results from the installation of the piles which are hammered into the soil with high frequency. Figure

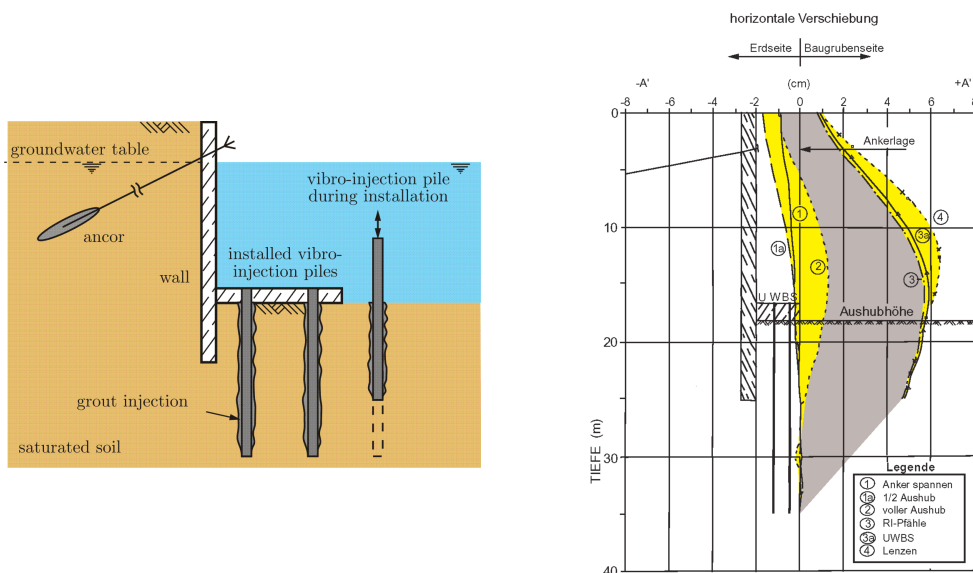


Figure 1.1: Schematic representation of the excavation pit at the Postdamer Platz in Berlin (left) and horizontal displacement of the slotted wall during the supporting works measured in Triantafyllidis [1998] (right)

1.1 shows also that the installation of the piles and the concreting of the foundation are performed completely under water where the vibrators are located on pontoons swim-

ming on the groundwater (see also figure 1.2¹). To capture all the influences of the



Figure 1.2: Picture of the Postdamer Platz during the construction showing pontoons on the groundwater table

supporting works on the soil behavior, a numerical simulation tool can help to predict the modification of the load capacity during the complete construction work. Therefore in addition to soil models and robust numerical algorithms, especially high precision contact models for the soil structure interaction are necessary, since the use of standard slip criteria, like the Coulomb law (Haraldsson [2003]), lead to unsatisfactoring results.

On the other hand, measurements of a direct shear test between concrete and sand (Reul [2000], Potyondy [1961], Uesugi et al. [1990]) show that for rough structures the friction angle is equal to the same test procedure where two sand specimens are sheared. This result leads to the assumption that for rough surfaces the real contact zone lies completely within the soil (figure 1.3) and a projection of the soil model onto

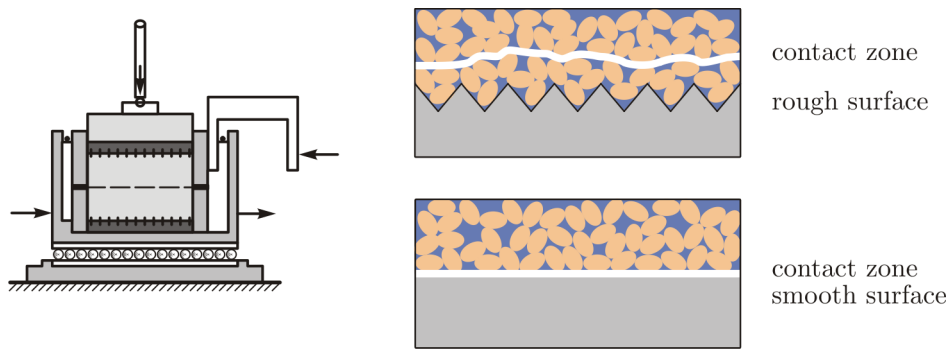


Figure 1.3: Zoom into the contact zone of a rough and a smooth surface within a direct shear test between soil and concrete

the contact surface could yield to an improvement of the frictional description which is the point of departure and the motivation of this work.

Two novel strategies for modeling frictional behavior in the context of soil structure interactions with rough surfaces are developed in this work. The first one embeds the soil model into the contact formulation either by a projection of the yield criterion and the potential onto the contact surface or by an integration of the soil characteristics into the coefficient of friction. The second strategy extends the contact methods towards a

¹©www.zellerprojektsteuerung.de

three-dimensional contact formulation where the soil or other plasticity models can be implemented directly into the contact discretization.

Since the numerical simulation of geotechnical processes is very challenging within the finite element framework, a stable and robust contact scheme is also necessary for the application of the developed contact models. Therefore the Mortar method (Bernardi et al. [1990], Bernardi et al. [1992], Belgacem et al. [1998], Puso and Laursen [2004b], Hübner and Wohlmuth [2005], Popp et al. [2010b]) is used for the discretization of the contact constraints. To choose a proper solution method within the Mortar framework, besides the well known penalty and augmented Lagrangian method, a new pure Lagrange multiplier and a new mixed version are developed which are compared to the standard cases.

1.1 State of the art

Within the numerical modeling of soil structure interactions with finite elements, different concepts have been applied during recent years. To start with, so called interface elements were developed. They either can be based on the same soil model as for the material but only with different parameters (Desai [1974]) or a completely different type of soil model is used (Zaman et al. [1984]). Alternatively, special kinematical assumptions are made for these interface elements which can be based for instance on a relative displacement between the two bodies (Ghaboussi et al. [1973]). In other mechanical fields, the concept of an interface element was also applied successfully. For the simulation of adhesion effects (Edlund [1994]) or for the post critical behavior of shear bands (Larsson and Runesson [1992], Miehe and Schröder [1994]), special strain measures were introduced for these elements. The kinematics of the interface element for shear bands is also closely related to the contact formulation as shown in Leppin [1999]. The drawback of these interface elements are their limiting relative sliding distance between the soil and the structure, since the mesh gets distorted for large displacements.

Another option to model soil structure interactions is to neglect the contact part and replace the interaction with proper boundary conditions. In Tejchmann and Wu [2010], micro-polar boundary conditions were applied to capture the rotational effects of the grains at rough surfaces.

The influence of rotational effects can also be qualitatively modeled by use of the Discrete-Element-Method (DEM). In Tillemans and Herrmann [1995] it is shown that dilatancy effects and shear hardening are the natural outcome of this kind of simulations. The influence of a roughness on the soil behavior close to the interface zone during a shearing process can also be estimated with the DEM (see Jensen et al. [1999]). The drawback of the DEM is the large number of particles needed for a realistic simulation which is not feasible with modern computer systems. To reduce the number of particles the whole domain under consideration can be split into a near field which is modeled with the DEM and a far field where the FEM is applied. At the interface, both methods can be coupled using the Arlequin method (Wellmann and Wriggers [2012]).

In soil engineering mostly the standard Coulomb law is applied if soil structure

interactions are investigated (Casciati and Borja [2004], Anastasopoulos and Gazetas [2007]), but in Haraldsson [2003] it is shown that the application of this model leads to a strong discrepancy of the computed numerical results compared to experimental measurements. Hence in Haraldsson [2003], two different concepts are developed leading to a small improvement of the soil structure interaction. In the first concept, a numerical testing strategy on a smaller scale is performed to determine the friction law, see also Haraldsson and Wriggers [2000]. In the second concept, the coefficient of friction is a function of the normal pressure and the sliding distance where the frictional parameters inside this model have to be fitted to experimental data.

Due to the lack of robustness of contact methods especially within a frictional contact regime under extreme loadings, in soil engineering soil structure interactions are mostly investigated only for supporting works such as piles (Maharaj and Gandhi [2004] or Zhao et al. [2008]) which are already installed. But in Sheng et al. [2005] it is shown that pushed-in pile installations can be simulated even with a node to segment strategy and some improvements on this kind of simulation are provided in Sheng et al. [2006], Fischer et al. [2007] and Sheng et al. [2009] or alternatively in Savidis et al. [2008].

1.2 Structure of this work

In chapter 2 all the kinematical descriptions, balance principles and constitutive relations needed in the subsequent chapters are summarized briefly. At the end, it is shown that contact relations can be derived from the continuum by integrating the strain over the height. The connection between the virtual work of the continuum and the shell is also listed to highlight the difference to the contact derivation.

Chapter 3 briefly describes the idea, the advantages and the limits of the Finite-Element-Method (FEM) which is the most common tool for the solution of differential equations. The treatment of geometrical and material nonlinearities is also presented which is applied within the contact algorithms and within the solution strategies of the soil models.

The discretization of the contact constraints in the framework of the Finite-Element-Method is focused on in chapter 4, with special reference to the implementation of the Mortar method which is presented in detail and opposed to the node to surface formulation. Besides the well known penalty and augmented Lagrangian method, for the first time a pure Lagrange multiplier method and a mixed version, composed of the augmented Lagrangian method for the normal contact and the penalty regularization for the tangential part, are implemented into the Mortar code and compared to other solution methods.

In chapter 5, after a short introduction into soil mechanics, the Ehlers soil model and its numerical implementation is presented in detail together with two regularization schemes improving its numerical behavior. To include the influence of liquids and gas inside the pores of the soil, the Theory of Porous Media (TPM) is described in chapter 6 and its behavior is tested at a simple numerical consolidation example.

Two concepts to project three-dimensional plasticity models onto the contact surface are introduced in chapter 7. Within the first version, the complete soil behavior is

coupled to the coefficient of friction in terms of the friction angle whilst the second concept links the yield criterion to the slip rule introducing a new dilatancy force into the contact formulation. In chapter 8, the Mortar method is extended towards the third direction which enables the direct implementation of the desired soil model.

For the simulation of a hammered pile installation into a non predrilled soil, special simulation tools have to be applied to cover the material separation. Therefore the eXtended-Finite-Element-Method (XFEM) can be used, but first a stable contact element has to be developed guaranteeing a smooth transition between the two bodies which is presented in chapter 9.

Chapter 2

Continuum mechanics

The theory of continuum mechanics characterizes the material behavior of a three-dimensional body in terms of mathematical equations. The setting up of the resulting differential equations for these continuous materials can be divided into four steps, namely, specifying the kinematical relations, choosing a proper deformation measure, describing the stress behavior in terms of generic balance equations and linking the stress with the deformation measure for the material under investigation. This topic has been widely covered in a number of manuscripts each of them with different focus points. In Truesdell and Toupin [1960], a comprehensive overview of mechanical relations extended to thermal and electrical fields is given. A generic treatise on constitutive relations can be found in Truesdell and Noll [2004] or Haupt [2002]. Additionally, textbooks with a specialized focus on nonlinear elastic behavior (Ogden [1984]) or on viscoelastic modeling and thermal effects (Holzapfel [2000]) should also be emphasized.

In engineering practice, thin structures are more advantageous and therefore a special mathematical treatment of this kind of structures is necessary which is summarized in the shell theory (Naghdi [1972], Y.Basar and Krätzig [2000] or Simo and Fox [1989]). The interaction between different bodies is also an important field in engineering science. Theoretical formulations can be found in Fischer-Cripps [2007] or Johnson [1985] and a computational implementation of the contact equations with finite elements are given in Wriggers [2006] or Laursen [2006] where in the former one a comprehensive description of different concepts for the solution of contact problems is listed and in the latter one a detailed explanation of a single contact formulation is highlighted.

The focus of this work lies on an engineering representation of the equations necessary for the understanding of the physical processes. A deeper insight into the mathematical representation of continuum mechanics based on differential geometry can be found in Marsden and Hughes [1983] or in a more succinct form in Aubram [2009]. A good introduction for engineers into the underlying mathematics is given in the manuscripts of Bowen and Wang [1976] and Bishop and Goldberg [1980]. The first sections highlight the most important equations needed in the subsequent chapters and the last two sections show the derivation of the shell and of the contact equations from the three-dimensional virtual work.

2.1 Kinematics

2.1.1 Motion

A body B is defined as a set of material points $X \in B$ and a configuration is a one-to-one mapping $\chi : B \rightarrow \mathbb{E}^3$ which locates the material points in the three-dimensional Euclidian space \mathbb{E}^3 . A motion is a one parameter function of configurations $\mathbf{x} := \chi(X, t)$ where \mathbf{x} is the current position vector of the considered material point. Normally, an initial configuration is established where a time t_0 is chosen as the origin and the position vector is defined as $\mathbf{X} := \chi(X, t_0)$. Eliminating the mapping χ (see Holzapfel [2000]), a connection between the initial and the current position vector can be formulated. The material or Lagrangian description maps points of the initial configuration onto its current state

$$\mathbf{x} = \boldsymbol{\varphi}(\mathbf{X}, t), \quad \mathbf{x} \in \mathbb{E}^3 \quad (2.1)$$

where $\boldsymbol{\varphi}$ is also one-to-one. Assuming that the inverse exist, the spacial or Eulerian description represents all values in terms of the current configuration including the initial position vector

$$\mathbf{X} = \boldsymbol{\varphi}^{-1}(\mathbf{x}, t), \quad \mathbf{X} \in \mathbb{E}^3. \quad (2.2)$$

The Lagrangian description is mostly used in solid mechanics where it is of utmost interest to analyze the displacements of the material point until failure. In fluid dynamics it is easier to capture the behavior at a special position than of a single material point and the Eulerian description is preferred. The material derivative describes the

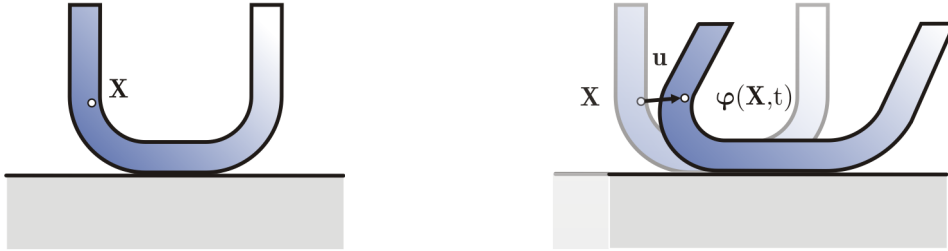


Figure 2.1: Initial (left) and current (right) configuration of an U-profile

change of a variable \bullet in dependency of the material point

$$\dot{\bullet}(\mathbf{X}, t) = \frac{d\bullet(\mathbf{X}, t)}{dt} = \left. \frac{\partial \mathbf{x}(\mathbf{X}, t)}{\partial t} \right|_{\mathbf{x}}. \quad (2.3)$$

For quantities given in the current configuration, the material derivative consists of the spatial derivative where the current position vector is hold fixed and of an additional convective term

$$\frac{d\bullet(\mathbf{x}, t)}{dt} = \left. \frac{\partial \bullet(\mathbf{x}, t)}{\partial t} \right|_{\mathbf{x}} + \text{grad } \bullet(\mathbf{x}, t) \mathbf{v}(\mathbf{x}, t). \quad (2.4)$$

Defining an intrinsic coordinate system $\xi^i \in \mathbb{R}^3$ which is valid here in both configurations, the base vectors $\mathbf{g}_i, \mathbf{G}_i$ for the current and the initial configuration, respectively,

are defined as

$$\mathbf{g}_i = \frac{\partial \mathbf{x}(\xi^i)}{\partial \xi^i}, \quad \mathbf{G}_i = \frac{\partial \mathbf{X}(\xi^i)}{\partial \xi^i}. \quad (2.5)$$

This enables every quantity in the Euclidian space \mathbb{E}^3 to be represented in terms of a triple of real numbers \mathbb{R}^3 which will be used in the following statements. The variable of utmost importance in solid mechanics is the displacement field

$$\mathbf{u} = \mathbf{x} - \mathbf{X} \in \mathbb{R}^3 \quad (2.6)$$

which measure the difference of a point in the current configurations to its position in the initial configuration (figure 2.1).

2.1.2 Deformation measures

The local deformation measure used more often in continuum mechanics is defined as the half of the difference between the square of the spatial and the material line element

$$\delta := \frac{1}{2} (\mathrm{d}\mathbf{x}^2 - \mathrm{d}\mathbf{X}^2). \quad (2.7)$$

The connection between both line elements can be established using a Taylor series expansion for points close to the current position vector (Spencer [1980])

$$\mathbf{x} + \delta \mathbf{x} = \mathbf{x}(\mathbf{X} + \delta \mathbf{X}) = \mathbf{x}(\mathbf{X}) + \frac{\partial \mathbf{x}(\mathbf{X})}{\partial \mathbf{X}} \delta \mathbf{X} + \frac{1}{2} \frac{\partial^2 \mathbf{x}(\mathbf{X})}{\partial \mathbf{X} \partial \mathbf{X}} \delta \mathbf{X} \otimes \delta \mathbf{X} + \mathcal{O}\{\delta \mathbf{X}^3\}. \quad (2.8)$$

In the limit $\delta \mathbf{X} \rightarrow 0$, both line elements are linked through a linear mapping where \mathbf{F} is denoted as the deformation gradient

$$\mathrm{d}\mathbf{x} = \mathbf{F} \, \mathrm{d}\mathbf{X} \quad \text{where} \quad \mathbf{F} = \frac{\partial \mathbf{x}}{\partial \mathbf{X}}. \quad (2.9)$$

Alternatively, higher order gradients can also be taken into account where a second order theory can be found for instance in Mindlin [1965]. Normally, in classical continuum mechanics each material point is considered as rigid. But within the micro-polar or Cosserat theory for each particle a rotational degree of freedom is assigned and in the micromorphic theory each particle is viewed as deformable. An introduction to these kind of theories can be found in Eringen and Kafadar [1976]. Considering only a first order theory based on rigid particles and exploiting (2.7) and (2.9), the Green Lagrange strain tensor \mathbf{E} of the initial configuration and the Euler Almansi strain tensor \mathbf{e} of the current configuration are obtained

$$\mathbf{E} = \frac{1}{2} (\mathbf{C} - \mathbf{G}), \quad \text{and} \quad \mathbf{e} = \frac{1}{2} (\mathbf{g} - \mathbf{b}^{-1}) \quad (2.10)$$

where \mathbf{C} denotes the right and \mathbf{b} the left Cauchy Green tensor, respectively

$$\mathbf{C} = \mathbf{F}^T \mathbf{F} \quad \text{with} \quad \mathbf{b} = \mathbf{F} \mathbf{F}^T. \quad (2.11)$$

The material derivatives of the strain tensors are specified as

$$\dot{\mathbf{E}} = \text{sym} \left(\mathbf{F}^T \dot{\mathbf{F}} \right), \quad \dot{\mathbf{e}} = \mathbf{d} = \text{sym} (\mathbf{l}), \quad \mathbf{l} = \dot{\mathbf{F}} \mathbf{F}^{-1}, \quad \dot{\mathbf{F}} = \text{Grad } \dot{\mathbf{x}}. \quad (2.12)$$

The deformation gradient (2.9) can also be written in dependency of the base vectors

$$\mathbf{F} = \mathbf{g}_i \otimes \mathbf{G}^i, \quad i = 1, 3 \quad (2.13)$$

and hence the strain measures can be specified in component form

$$\begin{aligned} \mathbf{E} &= E_{ij} \mathbf{G}^i \otimes \mathbf{G}^j, & E_{ij} &= \frac{1}{2} (\mathbf{g}_i \cdot \mathbf{g}_j - \mathbf{G}_i \cdot \mathbf{G}_j) = \frac{1}{2} (g_{ij} - G_{ij}) \\ \mathbf{e} &= e_{ij} \mathbf{g}^i \otimes \mathbf{g}^j, & e_{ij} &= \frac{1}{2} (\mathbf{g}_i \cdot \mathbf{g}_j - \mathbf{G}_i \cdot \mathbf{G}_j) = \frac{1}{2} (g_{ij} - G_{ij}) \end{aligned} \quad (2.14)$$

where the components of the Green Lagrange and the Euler Almansi strain tensor are equal. Alternative strain tensors based on a generic formula can be found in Ogden [1984].

2.2 Balance principles

In this section only the most important balance equations will be listed in integral form for the initial configuration and in local form written in the current configuration. Additionally, only closed systems will be taken into account. Extension to open systems where the exchange of mass with the surrounding is allowed can be found in Truesdell and Toupin [1960] or in Haupt [2002].

2.2.1 Continuity equation

The continuity equation states that the mass of a body is always constant, i.e. the material derivative of the mass is equal to zero

$$\dot{M} = 0, \quad M = \int_B dM = \int_B \rho_0 dV. \quad (2.15)$$

The local form of the continuity equation shows that the density ρ at each point does not have to be constant

$$\dot{\rho} + \rho \text{div } \dot{\mathbf{x}} = 0. \quad (2.16)$$

Only for an incompressible material, the restriction $\dot{\rho} = 0$ is fulfilled.

2.2.2 Momentum, mechanical energy and angular momentum

The balance of momentum states that the change of the momentum of a body is equal to the resulting force applied

$$\dot{\mathbf{L}} = \mathbf{F} \quad (2.17)$$

where the force can be subdivided into a surface load \mathbf{T} and an inner acceleration term $\bar{\mathbf{b}}$

$$\mathbf{L} = \int_B \dot{\mathbf{x}} dM, \quad \mathbf{F} = \int_{\partial B_\sigma} \mathbf{T} dA + \int_B \bar{\mathbf{b}} dM. \quad (2.18)$$

Alternatively, the balance of mechanical energy can be formulated instead of the balance of momentum which postulates that any change of the kinetic energy is motivated by the difference between the external and the internal power

$$\dot{K} = P_{ext} - P_{int}. \quad (2.19)$$

The components are given as

$$K = \int_B \frac{1}{2} \dot{\mathbf{x}} \cdot \dot{\mathbf{x}} dM \quad P_{ext} = \int_{\partial B_\sigma} \mathbf{T} \cdot \dot{\mathbf{x}} dA + \int_B \bar{\mathbf{b}} \cdot \dot{\mathbf{x}} dM \quad P_{int} = \int_B \mathbf{P} \cdot \dot{\mathbf{F}} dV \quad (2.20)$$

where the first Piola Kirchhoff stress tensor \mathbf{P} is work conjugate to the time derivative of the deformation gradient. The balance of angular momentum states that the change of the angular momentum is equal to the resulting moment applied

$$\dot{\mathbf{J}} = \mathbf{M}. \quad (2.21)$$

The contributions in (2.21) can be obtained from (2.18) multiplying the momentum and the force with the lever arm $\mathbf{r} = \mathbf{x} - \mathbf{x}_0$ consisting of the current \mathbf{x} and of a fixed reference position vector \mathbf{x}_0 , respectively,

$$\mathbf{J} = \int_B \mathbf{r} \times \dot{\mathbf{x}} dM \quad \mathbf{M} = \int_{\partial B_\sigma} \mathbf{r} \times \mathbf{T} dA + \int_B \mathbf{r} \times \bar{\mathbf{b}} dM. \quad (2.22)$$

If the body is C^1 - continuous and using the Gaussian integral theorem (Holzapfel [2000]), the local form of the balance of momentum can be written in dependency of the Cauchy stress tensor $\boldsymbol{\sigma}$ as

$$\rho \ddot{\mathbf{x}} = \operatorname{div} \boldsymbol{\sigma} + \rho \bar{\mathbf{b}}. \quad (2.23)$$

The balance of angular momentum in local form

$$\mathbf{r} \times \rho \ddot{\mathbf{x}} = \operatorname{grad} \mathbf{r} \times \boldsymbol{\sigma} + \mathbf{r} \times \operatorname{div} \boldsymbol{\sigma} + \mathbf{r} \times \rho \bar{\mathbf{b}} \quad (2.24)$$

yields to a restriction of the symmetric Cauchy stress tensor

$$\boldsymbol{\sigma} = \boldsymbol{\sigma}^T. \quad (2.25)$$

2.2.3 Energy and entropy

This work is restricted to mechanical processes, but in the constitutive theory the second law of thermodynamics is a very important restriction and hence the equations for energy and entropy will be presented as well. A brief but precise overview regarding thermal processes can be found in Miehe [1988]. If other fields, like chemical or electrical

ones, have to be taken into account, the thermodynamical laws have to be adjusted. For an extension to electrical and magnetical fields see Hutter and van de Ven [1978] or Kovetz [2000]. The balance of energy in thermodynamics states that the change of the inner and of the kinetic energy equals the external power and the production of heat Q

$$\dot{U} + \dot{K} = P_{ext} + Q. \quad (2.26)$$

By means of (2.19), the balance of energy can be rewritten only in terms of the inner energy also known as the first law of thermodynamics

$$\dot{U} = P_{int} + Q \quad (2.27)$$

where Q consists of an inner heat production and a heat flux part R and \mathbf{Q} , respectively, where the latter one determines the rate at which heat enters the body

$$U = \int_B u \, dM, \quad P_{int} = \int_B \mathbf{P} \cdot \dot{\mathbf{F}} \, dV, \quad Q = \int_B R \, dM + \int_{\partial B_\sigma} \mathbf{Q} \cdot \mathbf{N} \, dA. \quad (2.28)$$

The internal power can be subdivided into a reversible and a generic irreversible contribution \dot{w}_i (Miehe [1988])

$$P_{int} = \int_B \left(\mathbf{P} \cdot \dot{\mathbf{F}}_r + \dot{w}_i \right) dV. \quad (2.29)$$

The entropy inequality states that the production of entropy \dot{S} has to be larger or equal to the production of the reversible entropy \dot{S}^r

$$\Gamma = \dot{S} - \dot{S}^r \geq 0 \quad (2.30)$$

which is also known as the Clausius Duhem inequality. In cases where the energy is conserved, like elasticity, no additional entropy can be produced and $\Gamma = 0$. In the reference configuration each contribution can be specified as

$$\Gamma = \int_B \gamma \, dM, \quad S = \int_B \eta \, dM, \quad \dot{S}^r = - \int_{\partial B_\sigma} \frac{\mathbf{Q}}{\Theta} \cdot \mathbf{N} \, dA + \int_B \frac{R}{\Theta} \, dM \quad (2.31)$$

where Θ is the absolute temperature. In the constitutive theory, the material behavior is characterized in terms of the strain energy function Ψ . In the thermodynamical regime Ψ is also known as the Helmholtz free energy function and is linked to the inner energy and the entropy over the Legendre transformation

$$\Psi = u - \Theta \eta. \quad (2.32)$$

Using the strain energy function, the local form of the first law of thermodynamics formulated in the current configuration reads

$$\rho \dot{\Psi} + \rho \dot{\Theta} \eta + \rho \Theta \dot{\eta} = \boldsymbol{\sigma} \cdot \mathbf{d}_r + \dot{w}_i - \operatorname{div} \mathbf{q} + \rho r \quad (2.33)$$

and correspondingly, the second law of thermodynamics is written as

$$\rho\Theta\gamma = \boldsymbol{\sigma} \cdot \mathbf{d}_r + \dot{w}_i - \rho\dot{\Psi} - \rho\dot{\Theta}\eta - \frac{1}{\Theta}\mathbf{q} \cdot \text{grad } \Theta \geq 0. \quad (2.34)$$

Since heat flows always from the warmer to the colder region, the inequality

$$-\frac{1}{\Theta}\mathbf{q} \cdot \text{grad } \Theta \geq 0 \quad (2.35)$$

has to hold of its own which is known as the Duhamel law of heat conduction. The remaining part of the second law of thermodynamics leads to a stronger requirement and specifies the internal dissipation

$$D_{int} := \boldsymbol{\sigma} \cdot \mathbf{d}_r + \dot{w}_i - \rho\dot{\Psi} - \rho\dot{\Theta}\eta \geq 0 \quad (2.36)$$

which is known as the Clausius Planck inequality. With the definition of the internal dissipation, the first law of thermodynamics (2.33) can be rewritten in its final form

$$\rho\Theta\dot{\eta} = D_{int} - \text{div } \mathbf{q} + \rho r \quad (2.37)$$

2.3 Constitutive models

Macroscopic constitutive models are mainly developed on the basis of experimental observations, but some physical principles act as natural bounds in the derivation of material equations. Walter Noll formulated three principles which have to be considered in the case of a simple material

- **Determinism:** The material depends only on the actual and/or the former action of the input variables and not on future or stochastic quantities
- **Local action:** Only the closest vicinity influences the behavior of the material point, which is defined over the deformation gradient
- **Frame indifference:** The mathematical description of the model shall not depend on the viewpoint of the observer (objectivity).

More principles and a detailed description of their meaning can be found for instance in Truesdell and Noll [2004]. In the main, the behavior of a material in the macroscopic constitutive theory is characterized using rheological elements (cf. Krawietz [1986]), for example, and most importantly, springs describe the behavior of elasticity, dampers the viscosity and slip elements the plasticity, but also some mathematical requirements, like the growth condition, have to be taken into account. For large positive strains, the stress has to go to infinity and for cases with a large compression, the stress has to go to minus infinity. Very important is also the uniqueness of the solution of the material model. For hyperelastic materials, the strain energy function has to be polyconvex to ensure that the solution exists. For more detailed explanations about the concept of polyconvexity, it should be referred to the literature (Ball [1977], Marsden and Hughes [1983], Ciarlet [1988] or Silhavy [1997]).

2.3.1 Elasticity

Using the concept of hyperelasticity, the material behavior is formulated in terms of the strain energy function which can depend on the temperature and in the case of the current configuration on the left Cauchy Green tensor. For isotropic materials the strain energy function can also be written in form of the strain invariants

$$\Psi(\mathbf{b}, \Theta) = \Psi(I_{\mathbf{b}}, II_{\mathbf{b}}, III_{\mathbf{b}}, \Theta). \quad (2.38)$$

For elastic materials, the internal dissipation (2.36) has to vanish. By means of (2.38)

$$D_{int} = \left(\boldsymbol{\sigma} - \frac{2}{J} \rho \mathbf{b} \frac{\partial \Psi}{\partial \mathbf{b}} \right) \cdot \mathbf{d} + \left(-\eta - \frac{\partial \Psi}{\partial \Theta} \dot{\Theta} \right) \rho \dot{\Theta} = 0 \quad (2.39)$$

where $j = \det \mathbf{F}$, the constitutive relations for the stress tensor and the entropy can be stated as

$$\boldsymbol{\sigma} = \frac{1}{J} \rho \frac{\partial \Psi}{\partial \mathbf{b}} \dot{\mathbf{b}} = \frac{1}{J} \rho \frac{\partial \Psi}{\partial \mathbf{b}} (\mathbf{l}\mathbf{b} + \mathbf{b}\mathbf{l}^T) = \frac{2}{J} \rho \mathbf{b} \frac{\partial \Psi}{\partial \mathbf{b}} \mathbf{d}, \quad \eta = -\frac{\partial \Psi}{\partial \Theta} \dot{\Theta} \quad (2.40)$$

where the symmetry of stress tensor is used and the material time derivative is applied instead of the objective Lie derivative normally preferred in continuum mechanics. For a detailed description of finite elastic behavior conducted in the current configuration, see Miehe [1994]. The first law of thermodynamics (2.37) can also be rewritten in the case of an elastic material

$$-\rho \Theta \rho 2 \mathbf{b} \frac{\partial^2 \Psi}{\partial \Theta \partial \mathbf{b}} \mathbf{d} + \rho c \dot{\Theta} = -\operatorname{div} \mathbf{q} + \rho r \quad \text{where} \quad c = -\Theta \frac{\partial^2 \Psi}{\partial \Theta^2}. \quad (2.41)$$

The first term characterizes the Gough Joule effect which is non zero only at large strains and can normally be neglected (see Boley and Weiner [1960]) and c is the heat capacity. A lot of strain energy functions for elastic materials can be deduced from the generic formulation developed by Ogden (see for instance Ogden [1984])

$$\rho \Psi(\mathbf{b}) = \sum_{i=1}^r \frac{\mu_i}{\alpha_i} (\lambda_{\mathbf{b}1}^{\alpha_i} + \lambda_{\mathbf{b}2}^{\alpha_i} + \lambda_{\mathbf{b}3}^{\alpha_i}) + g(J) \quad (2.42)$$

which fits well to experimental observations. The first term characterizes the incompressible contribution and the second term $g(J)$ indicates the extension to compressible materials. Different functions for the compressible part have been formulated in the literature

$$g(J) = \frac{\lambda}{4} (J^2 - 1) - \frac{\lambda}{2} \ln J - \mu \ln J, \quad g(J) = \frac{\lambda}{2} (\ln J)^2 - \mu \ln J. \quad (2.43)$$

where the first version refers to Ciarlet [1988] and the second one can be found in Simo and Pister [1984]. Using $r = 1$, $\mu_1 = \mu$ and $\alpha_1 = 2$, the Neo Hookian model evolves from the Ogden model

$$\rho \Psi(\mathbf{b}) = \frac{\mu}{2} (I_{\mathbf{b}} - 3) + g(J) \quad (2.44)$$

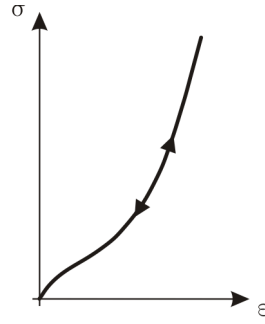


Figure 2.2: Qualitative stress strain curve of a rubber like material

and the Neo Hookian stress tensor based on the compressible term of Ciarlet [1988] can be obtained from (2.40) together with the derivative of the invariants with respect to the stress (cf. Holzapfel [2000])

$$\boldsymbol{\sigma} = \frac{\lambda}{2J} (J^2 - 1) \mathbf{g}^{-1} + \frac{\mu}{J} (\mathbf{b} - \mathbf{g}^{-1}). \quad (2.45)$$

where \mathbf{g}^{-1} defines the contravariant metric tensor in the current configuration. The linear elastic stress tensor evolves by a linearization of the Kirchhoff stress tensor $\boldsymbol{\tau} = J \boldsymbol{\sigma}$ where the linearized quantities can be identified as

$$\Delta J \rightarrow J \operatorname{div} \mathbf{u}, \quad \Delta \mathbf{b} \rightarrow \mathbf{0}, \quad \Delta \mathbf{g}^{-1} \rightarrow -2 \operatorname{sym}(\operatorname{grad} \mathbf{u}). \quad (2.46)$$

For an overview of linearized kinematical quantities, see Miehe [1988]. With $J = 1$ and $\mathbf{g}^{-1} = \mathbf{1}$ in the linear case, the elastic stress tensor can be written in its usual form

$$\boldsymbol{\sigma} = \lambda (\operatorname{div} \mathbf{u}) \mathbf{1} + 2\mu \operatorname{sym}(\operatorname{grad} \mathbf{u}) = \lambda \operatorname{tr} \boldsymbol{\epsilon} \mathbf{1} + 2\mu \boldsymbol{\epsilon} \quad (2.47)$$

2.3.2 Plasticity

Plastic behavior is characterized by a permanent deformation, if the load is removed. Perfect plasticity is also rate independent, since the deformation depends only on the load level and not on time. Figure 2.3 sketches a typical stress strain curve in the case of plasticity and an uniaxial strain loading. It can be seen that up to a specific tensile strain the material behaves elastic (σ_t) and beyond that limit plastic deformations occur and the material hardens leading to a higher maximal stress. Afterwards, the material is loaded into the opposite direction (compression) and a smaller elastic limit as for the original loading (tension) is often observed which is known as the Bauschinger effect. The same behavior is also observed, if the sequence of loading is switched. Isotropic hardening (figure 2.4) is characterized by an increase of the elastic stress, if the load goes beyond the initial elastic stress limit σ_c or σ_t . In comparison, kinematic hardening (figure 2.5) is characterized by a shift of the elastic domain in the Haigh-Westergaard stress space (figure 2.3). In the textbook of Lemaitre and Chaboche [1990], physical observations and mathematical models describing the material behavior are given in more detail. Experimental tests often show a different behavior of the material, if a

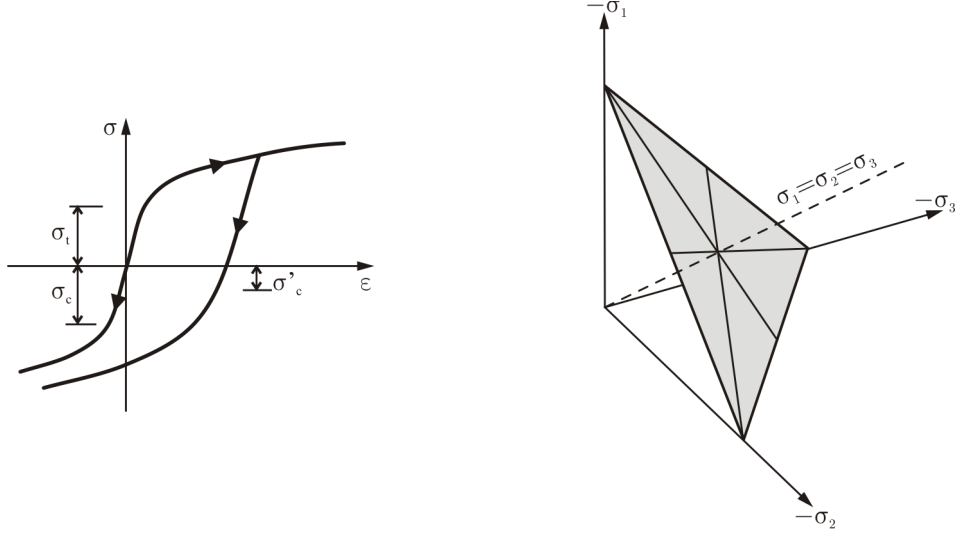


Figure 2.3: Qualitative stress strain curve of metals (left) and Haigh-Westergard stress space (right)

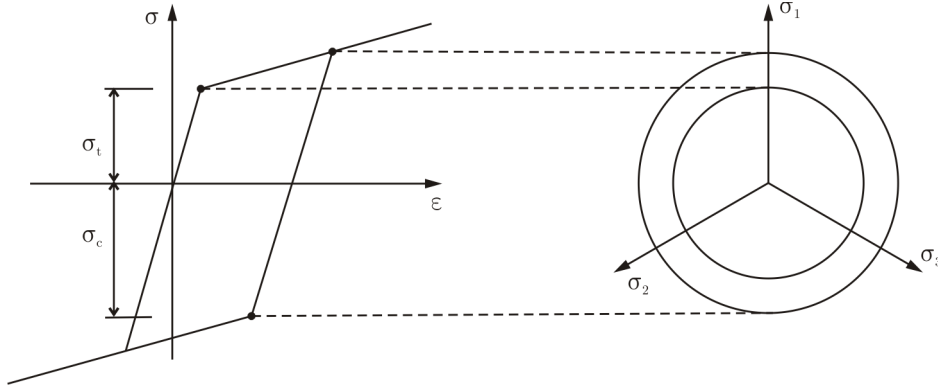


Figure 2.4: Plasticity model displaying isotropic hardening

pure hydrostatic or a pure shear loading is applied to the specimen, hence a split of the stress into a volumetric and deviatoric part is more convenient

$$\boldsymbol{\sigma} = \frac{1}{3} \text{tr } \boldsymbol{\sigma} \mathbf{1} + \mathbf{s}, \quad \text{or} \quad \mathbf{s} = \boldsymbol{\sigma} - \frac{1}{3} \text{tr } \boldsymbol{\sigma} \mathbf{1}. \quad (2.48)$$

In the Haigh-Westergard stress space (figure 2.3), the space diagonal indicates the volumetric or hydrostatic stress contribution and the distance normal to the diagonal displays the deviatoric part of the stress. The plane normal to the space diagonal is also called octahedral or π -plane. The distance d on the hydrostatic axis and the radius r on the π -plane

$$d = \sqrt{3} \frac{1}{3} \text{tr } \boldsymbol{\sigma}, \quad r = \sqrt{2} \sqrt{\Pi_s}, \quad \Pi_s = \frac{1}{2} \mathbf{s} \cdot \mathbf{s} \quad (2.49)$$

can be computed in terms of the applied stress (see for instance Desai and Siriwardane [1984]). In the linear theory the linear strain tensor can be split into an elastic and a

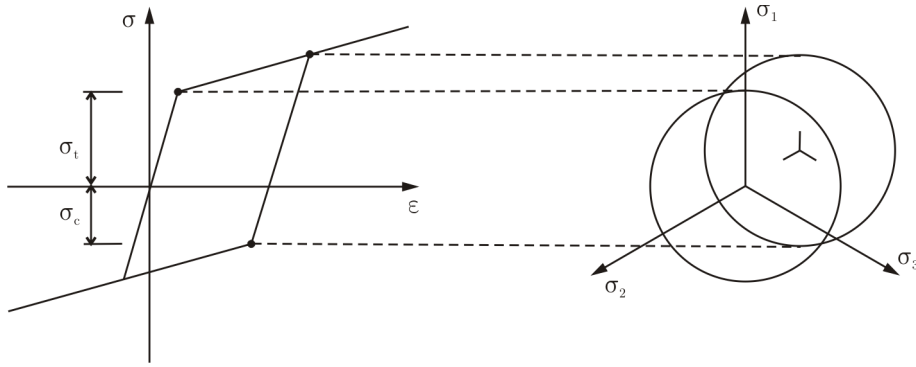


Figure 2.5: Plasticity model displaying kinematic hardening

plastic part

$$\boldsymbol{\varepsilon} = \boldsymbol{\varepsilon}^e + \boldsymbol{\varepsilon}^p. \quad (2.50)$$

Prandl and Reuss stated that for metals the principle axis of the plastic strain coincide with the principle axis of the deviatoric stress leading to the relationship $d\boldsymbol{\varepsilon}^p = d\lambda \mathbf{s}$ (cf. Hill [1950]) where $d\lambda$ is the incremental plastic flow. Based on this observation, a generic formulation for the evolution of the plastic strain

$$\dot{\boldsymbol{\varepsilon}}^p = \dot{\lambda} \frac{\partial g}{\partial \boldsymbol{\sigma}} \quad (2.51)$$

has been developed where the flow direction is formulated as the derivative of the potential g in the direction of the actual stress $\boldsymbol{\sigma}$. To model the limit of the elastic stress, a yield criterion is applied which has to be determined based on experimental observations. If the yield criterion is lower than zero ($f < 0$), the material point behaves elastic and for plastic deformations $f = 0$ has to hold. The yield criterion can also be combined with the rate of the plastic flow $\dot{\lambda}$ leading to the Karush-Kuhn-Tucker condition

$$\dot{\lambda} f = 0, \quad \dot{\lambda} \geq 0, \quad f \leq 0 \quad (2.52)$$

where for an elastic or plastic material behavior either $\dot{\lambda}$ or f is equal to zero. Hardening effects can be included using internal variables α_i and the strain energy function has to be extended by means of these variables (see Lubliner [1990]). For isothermal processes $\dot{\Theta} = 0$ and the dissipation equation (2.37) can be specified for the linear elasto-plastic case as

$$D_{int} = \boldsymbol{\sigma} \cdot \dot{\boldsymbol{\varepsilon}}^p - \rho \sum_{i=1}^N \frac{\partial \Psi}{\partial \alpha_i} \dot{\alpha}_i \geq 0 \quad (2.53)$$

where for the internal power $\dot{w}_i = \boldsymbol{\sigma} \cdot \dot{\boldsymbol{\varepsilon}}^p$ is used. Each hardening stress \mathbf{q}_i follows directly from the strain energy function and additional functions h_i have to be formulated for the evolution equation of the internal variables α_i

$$\mathbf{q}_i = \frac{\partial \Psi}{\partial \alpha_i}, \quad \dot{\alpha}_i = \frac{\partial h_i}{\partial q_i}. \quad (2.54)$$

In the case of associated plasticity, the yield criterion, the potential and the hardening function are all equal $f = g = h$. The plastic behavior can also be extended to the case of finite deformations as can be found for example in Miehe [1993].

2.4 Variational form

Some methods for solving PDEs need the differential equations in a weak form. For the mechanical part, the balance of momentum in the current configuration (2.23) is therefore multiplied with a test function, integrated over the whole domain and set to zero

$$G(\mathbf{u}, \boldsymbol{\eta}) = \int_{\varphi(B)} \boldsymbol{\eta} \cdot (\operatorname{div} \boldsymbol{\sigma} + \rho \bar{\mathbf{b}} - \rho \ddot{\mathbf{u}}) \, dv = 0. \quad (2.55)$$

The derivation of the weak form is explained in more detail in chapter 3. Applying the product rule and the divergence theorem (for instance Holzapfel [2000]), (2.55) can be reformulated in terms of the virtual Almansi strain $\delta \boldsymbol{\varepsilon}$

$$G(\mathbf{u}, \boldsymbol{\eta}) = \int_{\varphi(B)} (\delta \boldsymbol{\varepsilon} \cdot \boldsymbol{\sigma} - \boldsymbol{\eta} \cdot \rho \bar{\mathbf{b}} + \boldsymbol{\eta} \cdot \rho \ddot{\mathbf{u}}) \, dv - \int_{\varphi(\partial B^\sigma)} \boldsymbol{\eta} \cdot \bar{\mathbf{t}} \, da = 0 \quad (2.56)$$

where the maximal order of the derivation of the primal variable \mathbf{u} is reduced to 1. The weak form (2.56) can also be transformed to the initial configuration

$$G(\mathbf{u}, \boldsymbol{\eta}) = \int_B (\delta \mathbf{E} \cdot \mathbf{S} - \boldsymbol{\eta} \cdot \rho_0 \bar{\mathbf{b}} + \boldsymbol{\eta} \cdot \rho_0 \ddot{\mathbf{u}}) \, dV - \int_{\partial B^\sigma} \boldsymbol{\eta} \cdot \bar{\mathbf{T}} \, dA = 0. \quad (2.57)$$

written in terms of the second Piola Kirchhoff stress tensor \mathbf{S} defined completely in the initial configuration.

2.4.1 Reduction to surface description

For thin structures, normally the shell theory is used to describe the material behavior under loading. The formulations of the shell theory are the results of some simplifications of the three-dimensional continua. The reduction to the surface description is performed on the virtual inner work part of (2.57), normally split into work conjugate shearing, normal and bending pairs

$$\int_B \delta \mathbf{E} \cdot \mathbf{S} \, dV = \int_A (\delta \mathbf{E}^m \cdot \mathbf{N} + \delta \mathbf{E}^b \cdot \mathbf{M} + \delta \mathbf{E}^s \cdot \mathbf{Q}) \, dA. \quad (2.58)$$

The normal force \mathbf{N} , the shear force \mathbf{Q} and the couple \mathbf{M} result from an integration of the corresponding stress components over the height which will be specified in the following statements.

Due to the assumption that the cross section of the shell remains straight the position vectors can be represented in terms of a surface position vector $\mathbf{x}_s, \mathbf{X}_s$ and a linear extension along the director \mathbf{d} in the current or along the normal vector \mathbf{N} in the initial configuration, respectively,

$$\mathbf{x}(\xi^\alpha, \xi) = \mathbf{x}_s(\xi^\alpha) + \xi \mathbf{d}(\xi^\alpha), \quad \mathbf{X}(\xi^\alpha \xi) = \mathbf{X}_s(\xi^\alpha) + \xi \mathbf{N}(\xi^\alpha). \quad (2.59)$$

Normally, the director is not perpendicular to the shell surface $\mathbf{d} \neq \mathbf{n}$ and three additional unknowns have to be introduced into the system (6 parameter model). In case

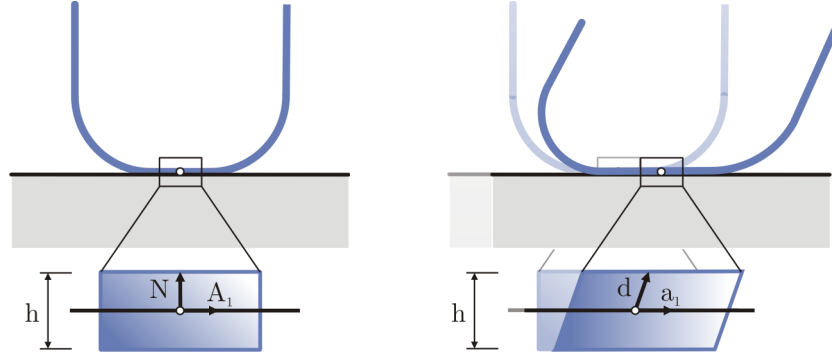


Figure 2.6: Initial shell configuration (left) and current shell configuration (right)

of an inextensible director where the thickness of the shell remains constant, the determination of the director can be realized through a rotation of the initial normal vector. Then only the two angles of the rotation are the additional unknowns (5 parameter model). For the Kirchhoff-Love shell theory $\mathbf{d} = \mathbf{n}$, i.e. no transverse shear strain effects, no additional unknowns are needed (3 parameter model). The base vectors of the shell follows directly from (2.5) exploiting (2.59)

$$\mathbf{g}_\alpha = \frac{\partial \mathbf{x}}{\partial \xi^\alpha} = \mathbf{a}_\alpha + \xi \mathbf{d}_{,\alpha}, \quad \mathbf{g}_3 = \frac{\partial \mathbf{x}}{\partial \xi} = \mathbf{d} \quad (2.60)$$

for the current as well as for the initial configuration, respectively,

$$\mathbf{G}_\alpha = \frac{\partial \mathbf{X}}{\partial \xi^\alpha} = \mathbf{A}_\alpha + \xi \mathbf{N}_{,\alpha}, \quad \mathbf{G}_3 = \frac{\partial \mathbf{X}}{\partial \xi} = \mathbf{N}, \quad \mathbf{N} = \frac{\mathbf{A}_1 \times \mathbf{A}_2}{\|\mathbf{A}_1 \times \mathbf{A}_2\|} \quad (2.61)$$

where \mathbf{a}_α , \mathbf{A}_α are the base vectors of the middle surface in the corresponding configuration and linked to the base vectors of the continuum by means of the shifter tensors

$$\mathbf{z} = \mathbf{g}_i \otimes \mathbf{a}^i, \quad \text{and} \quad \mathbf{Z} = \mathbf{G}_i \otimes \mathbf{A}^i. \quad (2.62)$$

As with the position vectors (2.59), the displacement field can also be formulated in terms of a surface part \mathbf{u}_s and a linear deviation around the middle surface in form of the difference vector \mathbf{w}

$$\mathbf{u} = \mathbf{u}_s + \xi \mathbf{w} \quad \text{where} \quad \mathbf{w} = \mathbf{d} - \mathbf{N}. \quad (2.63)$$

The deformation gradient follows directly according to (2.13) together with (2.60) and (2.61) to

$$\mathbf{F} = (\mathbf{a}_\alpha + \xi \mathbf{d}_{,\alpha}) \otimes \mathbf{G}^\alpha + \mathbf{d} \otimes \mathbf{N}. \quad (2.64)$$

Depending on ξ , the components of the Green Lagrange strain tensor can be assigned as constant, linear or quadratic. Depending on the base vectors of the strain, the

components can also be classified into membrane, shear or normal components. The constant membrane part characterizes the normal strain

$$E_{\alpha\beta}^m = \frac{1}{2} (\mathbf{a}_\alpha \cdot \mathbf{a}_\beta - \mathbf{A}_\alpha \cdot \mathbf{A}_\beta) \quad (2.65)$$

and the linear term specifies the bending strain of the shell structure

$$E_{\alpha\beta}^b = (\mathbf{a}_\alpha \cdot \mathbf{d}_{,\beta} - \mathbf{A}_\alpha \cdot \mathbf{N}_{,\beta}). \quad (2.66)$$

For the shearing part only the constant term is considered and indicates the transverse shear strain

$$2 E_{\alpha 3}^q = \mathbf{a}_\alpha \cdot \mathbf{d} \quad (2.67)$$

and the normal part describes the extension in the thickness direction

$$E_{33}^n = \frac{1}{2} (\mathbf{d} \cdot \mathbf{d} - \mathbf{N} \cdot \mathbf{N}). \quad (2.68)$$

For a detailed explanation of each component, see Bischoff [2000]. All contributions not mentioned above are normally neglected in shell computations (see for instance Wagner [1985]). Using the shifter tensor, the Green Lagrange strain can also be written depending on the base vectors of the middle surface

$$\mathbf{E}_s = \mathbf{Z}^{-T} \mathbf{E} \mathbf{Z}^{-1} = E_{ij} \mathbf{A}^i \otimes \mathbf{A}^j. \quad (2.69)$$

Based on all the derivations made, the integration of the stress components over the height in (2.58) can now be specified in detail

$$\begin{aligned} \mathbf{N} &= \int_{-h/2}^{+h/2} S^{\alpha\beta} \mathbf{A}_\alpha \otimes \mathbf{A}_\beta \det \mathbf{z} d\xi, \quad \mathbf{Q} = \int_{-h/2}^{+h/2} S^{\alpha 3} \mathbf{A}_\alpha \otimes \mathbf{N} \det \mathbf{z} d\xi \\ \mathbf{M} &= \int_{-h/2}^{+h/2} \xi S^{\alpha\beta} \mathbf{A}_\alpha \otimes \mathbf{A}_\beta \det \mathbf{z} d\xi. \end{aligned} \quad (2.70)$$

The contribution of the normal part perpendicular to the middle surface to the virtual inner work is normally neglected, since $S^{33} = 0$ is assumed (e.g. in Wagner [1985]). A detailed derivation of the virtual work in (2.58) can be found in Berg [1983].

For the integration over the height, the determinant of the shifter tensor has to be taken into account which can be assumed as 1, if the normal base vector \mathbf{g}_3 is normalized

$$\det \mathbf{z} = \frac{j}{\bar{j}} = \frac{(\mathbf{g}_1 \times \mathbf{g}_2) \cdot \mathbf{g}_3}{\|\mathbf{a}_1 \times \mathbf{a}_2\|} \approx \|\mathbf{g}_3\| = 1. \quad (2.71)$$

Alternatively, instead of the normal base vector, the integration domain can be normalized, see for instance Bischoff [2000]. In standard textbooks (Naghdi [1972], Y.Basar and Krätzig [2000]) normally Christoffel tensors have to be used in conjunction with the shell theory, but through the introduction of an additional reference configuration, the mathematical derivation of the shell formulas can be simplified (Simo and Fox [1989]) which fits very well with the concept of the Finite Element Method. Nowadays, a numerical integration over the height is performed directly in the continuum form (2.58) avoiding the usage of the shifter and of the stress or couple resultants (see for instance Eberlein [1997]).

2.4.2 Reduction to contact description

In this section it will be shown that the contact kinematics can also be developed through a reduction of the strain in continuum form. This means that contact can be viewed as an infinitesimal thin layer between the contacting bodies. The starting point is also the virtual work (2.56) where now the strain is integrated over the height. Afterwards, the limit of the height towards zero is performed on the strain

$$\int_{\varphi(B^c)} \delta \mathbf{e} \cdot \boldsymbol{\sigma} \, dv = \lim_{h \rightarrow 0} \int_{\gamma^c} \int_0^h \delta \mathbf{e} d\xi \cdot \boldsymbol{\sigma} \, da. \quad (2.72)$$

To abbreviate the notation, the integration domain along the contact surface is indicated as $\varphi(\partial B^c) = \gamma^c$. Analogous to the solid-shell concept, the position vector and the weighting function are written in terms of the two surfaces also denoted as slave (1) and master (2) (Hallquist [1979])

$$\begin{aligned} \mathbf{x}(\xi^\alpha, \xi) &= \mathbf{x}^1(\xi^{1\alpha}) + \frac{\xi}{h} [\mathbf{x}^2(\xi^{2\alpha}) - \mathbf{x}^1(\xi^{1\alpha})] \\ \boldsymbol{\eta}(\xi^\alpha, \xi) &= \boldsymbol{\eta}^1(\xi^{1\alpha}) + \frac{\xi}{h} [\boldsymbol{\eta}^2(\xi^{2\alpha}) - \boldsymbol{\eta}^1(\xi^{1\alpha})]. \end{aligned} \quad (2.73)$$

Within the formulation of the solid-shell concept no director has to be introduced. This idea goes back to Schoop [1986] and is further developed and accommodated to the finite element method in Parisch [1995], Hauptmann and Schweizerhof [1998] or Klinkel et al. [1999]. In the following statements, the dependency of the position vector and

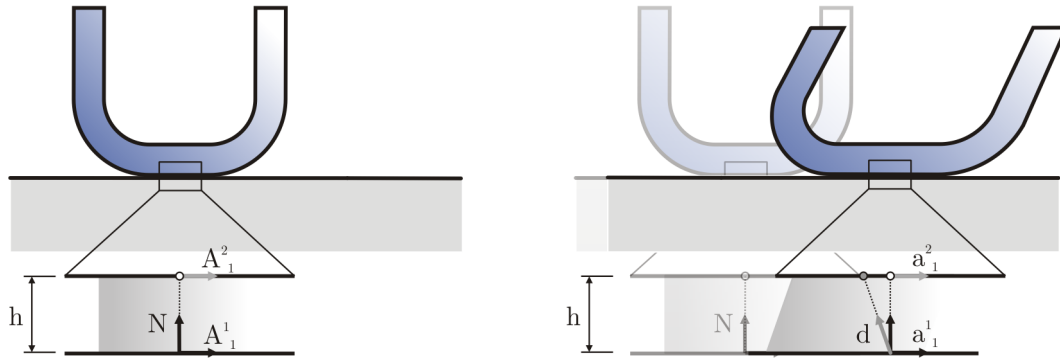


Figure 2.7: Initial contact configuration (left) and current contact configuration (right)

the weighting function on the intrinsic coordinate system $\xi^{1\alpha}, \xi^{2\alpha}$ will be neglected to ease the notation. Exploiting (2.73), the base vectors (2.5) of both configurations

$$\begin{aligned} \mathbf{g}_\alpha &= \frac{\partial \mathbf{x}}{\partial \xi^\alpha} = \left(1 - \frac{\xi}{h}\right) \mathbf{a}_\alpha^1 + \frac{\xi}{h} \mathbf{a}_\alpha^2, & \mathbf{g}_3 &= \frac{\partial \mathbf{x}}{\partial \xi} = \frac{1}{h} [\mathbf{x}^2 - \mathbf{x}^1] \\ \mathbf{G}_\alpha &= \frac{\partial \mathbf{X}}{\partial \xi^\alpha} = \left(1 - \frac{\xi}{h}\right) \mathbf{A}_{,\alpha}^1 + \frac{\xi}{h} \mathbf{A}_\alpha^2, & \mathbf{G}_3 &= \frac{\partial \mathbf{X}}{\partial \xi} = \frac{1}{h} [\mathbf{X}^2 - \mathbf{X}^1], \end{aligned} \quad (2.74)$$

the virtual base vectors

$$\begin{aligned}\delta \mathbf{g}_\alpha &= \frac{\partial \boldsymbol{\eta}}{\partial \xi^\alpha} = \left(1 - \frac{\xi}{h}\right) \boldsymbol{\eta}_{,\alpha}^1 + \frac{1}{h} \boldsymbol{\eta}_{,\alpha}^2 = \left(1 - \frac{\xi}{h}\right) \delta \mathbf{a}_\alpha^1 + \frac{\xi}{h} \delta \mathbf{a}_\alpha^2 \\ \delta \mathbf{g}_3 &= \frac{\partial \boldsymbol{\eta}}{\partial \xi} = \frac{1}{h} [\boldsymbol{\eta}^2 - \boldsymbol{\eta}^1]\end{aligned}\tag{2.75}$$

and also the deformation gradient according to (2.13)

$$\mathbf{F} = \left[\left(1 - \frac{\xi}{h}\right) \mathbf{a}_\alpha^1 + \frac{\xi}{h} \mathbf{a}_\alpha^2 \right] \otimes \mathbf{G}^\alpha + \frac{1}{h} [\mathbf{x}^2 - \mathbf{x}^1] \otimes \mathbf{N}\tag{2.76}$$

can be specified for the solid-shell case. For the components of the Almansi strain tensor, first the metric components and their virtual counterparts are integrated over the height and afterwards, the limit is performed directly on the strain contribution. Starting with the membrane part

$$\begin{aligned}\bar{g}_{\alpha\beta} &= \int_0^h g_{\alpha\beta} \det \mathbf{z} d\xi = \frac{h}{3} [\mathbf{a}_\alpha^1 \cdot \mathbf{a}_\beta^1 + \mathbf{a}_\alpha^2 \cdot \mathbf{a}_\beta^2] + \frac{h}{6} [\mathbf{a}_\alpha^1 \cdot \mathbf{a}_\beta^2 + \mathbf{a}_\alpha^2 \cdot \mathbf{a}_\beta^1] \\ \bar{G}_{\alpha\beta} &= \int_0^h G_{\alpha\beta} \det \mathbf{z} d\xi = \frac{h}{3} [\mathbf{A}_\alpha^1 \cdot \mathbf{A}_\beta^1 + \mathbf{A}_\alpha^2 \cdot \mathbf{A}_\beta^2] + \frac{h}{6} [\mathbf{A}_\alpha^1 \cdot \mathbf{A}_\beta^2 + \mathbf{A}_\alpha^2 \cdot \mathbf{A}_\beta^1] \\ \delta \bar{g}_{\alpha\beta} &= \int_0^h \delta g_{\alpha\beta} \det \mathbf{z} d\xi = \frac{h}{3} [\boldsymbol{\eta}_{,\alpha}^1 \cdot \mathbf{a}_\beta^1 + \boldsymbol{\eta}_{,\alpha}^2 \cdot \mathbf{a}_\beta^2] + \frac{h}{6} [\boldsymbol{\eta}_{,\alpha}^1 \cdot \mathbf{a}_\beta^2 + \boldsymbol{\eta}_{,\alpha}^2 \cdot \mathbf{a}_\beta^1] \\ &\quad + \frac{h}{3} [\mathbf{a}_\alpha^1 \cdot \boldsymbol{\eta}_{,\beta}^1 + \mathbf{a}_\alpha^2 \cdot \boldsymbol{\eta}_{,\beta}^2] + \frac{h}{6} [\mathbf{a}_\alpha^1 \cdot \boldsymbol{\eta}_{,\beta}^2 + \mathbf{a}_\alpha^2 \cdot \boldsymbol{\eta}_{,\beta}^1],\end{aligned}\tag{2.77}$$

the metric depends on the height and in the limit no contribution to the virtual contact work has to be considered

$$\begin{aligned}\bar{e}_{\alpha\beta} &= \lim_{h \rightarrow 0} \frac{1}{2} (\bar{g}_{\alpha\beta} - \bar{G}_{\alpha\beta}) = 0_{\alpha\beta} \\ \delta \bar{e}_{\alpha\beta} &= \lim_{h \rightarrow 0} \frac{1}{2} \delta \bar{g}_{\alpha\beta} = 0_{\alpha\beta}.\end{aligned}\tag{2.78}$$

The bar over the geometrical quantity indicates an integrated value. Strictly speaking, the contact quantities are hence not strain measures anymore, since the values are now given in a length unit, but to show the connection between the continuum strain components and the contact quantities the term strain will be used as well for the integrated contact values.

In contrast to the membrane part the shearing part has to be regarded in the virtual contact work and it denotes the influence of the relative motion between the two

contacting bodies

$$\begin{aligned}
\bar{g}_{\alpha 3} &= \int_0^h g_{\alpha 3} \det \mathbf{z} d\xi = [\mathbf{x}^2 - \mathbf{x}^1] \cdot \frac{1}{2} [\mathbf{a}_\beta^1 + \mathbf{a}_\beta^2] \\
\bar{G}_{\alpha 3} &= \int_0^h G_{\alpha 3} \det \mathbf{z} d\xi = [\mathbf{X}^2 - \mathbf{X}^1] \cdot \frac{1}{2} [\mathbf{A}_\beta^1 + \mathbf{A}_\beta^2] \\
\delta \bar{g}_{\alpha 3} &= \int_0^h \delta g_{\alpha 3} \det \mathbf{z} d\xi = [\boldsymbol{\eta}^2 - \boldsymbol{\eta}^1] \cdot \frac{1}{2} [\mathbf{a}_\beta^1 + \mathbf{a}_\beta^2] + [\mathbf{x}^2 - \mathbf{x}^1] \cdot \frac{1}{2} [\boldsymbol{\eta}_{,\beta}^1 + \boldsymbol{\eta}_{,\beta}^2].
\end{aligned} \tag{2.79}$$

In the case of contact (figure 2.7), the base vectors of the two surfaces are pointing towards the same direction and for simplicity, it can be assumed that both base vectors are equal in length and direction

$$\mathbf{a}_\alpha^1 = \mathbf{a}_\alpha^2 = \mathbf{a}_\alpha. \tag{2.80}$$

The resulting shear components of the strain measure can then be written as

$$\begin{aligned}
2\bar{e}_{\alpha 3} &= \lim_{h \rightarrow 0} (\bar{g}_{\alpha 3} - \bar{G}_{\alpha 3}) = [\mathbf{x}^2 - \mathbf{x}^1] \cdot \mathbf{a}_\alpha - [\mathbf{X}^2 - \mathbf{X}^1] \cdot \mathbf{A}_\alpha \\
2\delta \bar{e}_{\alpha 3} &= \lim_{h \rightarrow 0} \delta \bar{g}_{\alpha 3} = [\boldsymbol{\eta}^2 - \boldsymbol{\eta}^1] \cdot \mathbf{a}_\alpha + [\mathbf{x}^2 - \mathbf{x}^1] \cdot \boldsymbol{\eta}_{,\alpha}.
\end{aligned} \tag{2.81}$$

Integrating the normal part

$$\begin{aligned}
\bar{g}_{33} &= \int_0^h g_{33} \det \mathbf{z} d\xi = \frac{1}{h} [\mathbf{x}^2 - \mathbf{x}^1] \cdot [\mathbf{x}^2 - \mathbf{x}^1] \\
\bar{G}_{33} &= \int_0^h G_{33} \det \mathbf{z} d\xi = \frac{1}{h} [\mathbf{X}^2 - \mathbf{X}^1] \cdot [\mathbf{X}^2 - \mathbf{X}^1] \\
\delta \bar{g}_{33} &= \int_0^h \delta g_{33} \det \mathbf{z} d\xi = \frac{2}{h} [\boldsymbol{\eta}^2 - \boldsymbol{\eta}^1] \cdot [\mathbf{x}^2 - \mathbf{x}^1],
\end{aligned} \tag{2.82}$$

all the formulations are multiplied with the difference vector $\mathbf{x}^2 - \mathbf{x}^1$ divided by the height. Following the computation of the normal vector in standard contact textbooks, like Wriggers [2006],

$$\mathbf{n} = \frac{\mathbf{x}^2 - \mathbf{x}^1}{\|\mathbf{x}^2 - \mathbf{x}^1\|} = \frac{1}{h} [\mathbf{x}^2 - \mathbf{x}^1] \tag{2.83}$$

the difference vector corresponds exactly to the normal at the contact surface. It is also assumed that at the initial state of contact the normal gap is equal to zero, hence $\bar{G}_{33} = 0$. With these modifications, all the components of the strain tensor are now specified for the contact case

$$\begin{aligned}
\bar{e}_{33} &= \lim_{h \rightarrow 0} \frac{1}{2} (\bar{g}_{33} - \bar{G}_{33}) = \frac{1}{2} \|\mathbf{x}^2 - \mathbf{x}^1\| = \frac{1}{2} [\mathbf{x}^2 - \mathbf{x}^1] \cdot \mathbf{n} \\
\delta \bar{e}_{33} &= \lim_{h \rightarrow 0} \frac{1}{2} \delta \bar{g}_{33} = [\boldsymbol{\eta}^2 - \boldsymbol{\eta}^1] \cdot \mathbf{n}
\end{aligned} \tag{2.84}$$

and the virtual contact work (2.72) simplifies to

$$G_u^c = \int_{\gamma^c} (2 \delta \bar{e}_{\alpha 3} \sigma^{\alpha 3} + \delta \bar{e}_{33} \sigma^{33}) \, da. \quad (2.85)$$

Comparing the resulting strain components of the virtual contact work with the literature (Wriggers [2006])

$$\begin{aligned} 2 \delta \bar{e}_{\alpha 3} &= \lim_{h \rightarrow 0} \delta \bar{g}_{\alpha 3} = [\boldsymbol{\eta}^2 - \boldsymbol{\eta}^1] \cdot \mathbf{a}_\alpha \\ \delta \bar{e}_{33} &= \lim_{h \rightarrow 0} \frac{1}{2} \delta \bar{g}_{33} = [\boldsymbol{\eta}^2 - \boldsymbol{\eta}^1] \cdot \mathbf{n}, \end{aligned} \quad (2.86)$$

the second term of the virtual shear strain is missing due to the different derivation of the virtual contact work. Normally, at the contact surface, the Neumann boundaries are coupled using the principle of sections $\boldsymbol{\lambda} = \mathbf{t}^1 = -\mathbf{t}^2$

$$\begin{aligned} G_u^c &= - \int_{\gamma^c} (\mathbf{t}^1 \cdot \boldsymbol{\eta}^1 + \mathbf{t}^2 \cdot \boldsymbol{\eta}^2) \, da = \int_{\gamma^c} \boldsymbol{\lambda} \cdot (\boldsymbol{\eta}^2 - \boldsymbol{\eta}^1) \, da \\ &= \int_{\gamma^c} \lambda_N (\boldsymbol{\eta}^2 - \boldsymbol{\eta}^1) \cdot \mathbf{n} + \int_{\gamma^c} \lambda^{\text{T}\alpha} (\boldsymbol{\eta}^2 - \boldsymbol{\eta}^1) \cdot \mathbf{a}_\alpha \end{aligned} \quad (2.87)$$

where the domain of the contact surface γ^c and the contact stress vector $\boldsymbol{\lambda}$ are the unknowns. Afterwards, the contact stress vector can be split into a normal and a tangential part leading to the formulations given in (2.86). Alternatively, for the shearing part $2 e_{\alpha 3}$ a tangential movement \mathbf{g}_T based on the parameterization of the master surface $\xi^{2\alpha}$ can be defined (for the 2D case in Wriggers and Miehe [1992] and generalized to the 3D case in Wriggers and Miehe [1994]). The objective Lie derivative and the variation of \mathbf{g}_T fits very well to the node to surface formulation in conjunction with the Finite-Element-Method

$$\dot{\mathbf{g}}_T = \dot{\xi}^\alpha \mathbf{a}_\alpha, \quad \delta \mathbf{g}_T = \delta \xi^\alpha \mathbf{a}_\alpha. \quad (2.88)$$

The virtual contact work now becomes

$$G_u^c = \int_{\gamma^c} (\lambda_N \delta g_N + \boldsymbol{\lambda}_T \cdot \delta \mathbf{g}_T) \, da \quad (2.89)$$

where the first term is written in form of the virtual normal penetration

$$\delta g_N = (\boldsymbol{\eta}^2 - \boldsymbol{\eta}^1) \cdot \mathbf{n}. \quad (2.90)$$

A third way of formulating contact constraints is based on an interface zone with an assumed virtual strain tensor of the form (Larsson and Runesson [1992], Miehe and Schröder [1994])

$$\delta \mathbf{e} = \frac{1}{h} [\boldsymbol{\eta}^2 - \boldsymbol{\eta}^1] \cdot \mathbf{n} \quad (2.91)$$

used for the description of localization phenomena. With (2.91) and $\boldsymbol{\sigma}\mathbf{n} = \boldsymbol{\lambda}$, a straightforward translation from the continuum interface to the contact surface is possible, see also Leppin [1999]

$$\int_{\varphi(B^c)} \boldsymbol{\sigma} \cdot \delta \mathbf{e} \, dv = \int_{\gamma^c} \boldsymbol{\sigma} \cdot \frac{1}{h} [\boldsymbol{\eta}^2 - \boldsymbol{\eta}^1] \otimes \mathbf{n} \, h \, da = \int_{\gamma^c} \boldsymbol{\lambda} \cdot [\boldsymbol{\eta}^2 - \boldsymbol{\eta}^1] \, da \quad (2.92)$$

Alternatively, the contact surface can be viewed as a singular surface (Kosinski [1986]) at which the balance of equations can be stated. For more details see Scherf [1997] or Strömberg et al. [1996]. A contact formulation based on the Riemann geometry and Christoffel tensors is also given in Konyukhov and Schweizerhof [2005].

In conclusion it has to be mentioned that comparing figure 2.7 with figure 2.6, the director in the case of contact points towards the opposite direction as in the classical shell theory. This reasons the minus sign $\mathbf{t}_T = -c_T \mathbf{g}_T$ in the penalty regularization.

Chapter 3

Finite elements

Analytical solutions of the differential equations of chapter 2 are only available for some geometrical specimens with a specific load applied. Numerical solution schemes are more powerful in solving different classes (elliptic, parabolic or hyperbolic) of partial differential equations (PDEs). An early numerical solution scheme is the Finite-Difference-Method (FDM) which solves the differential equation by using numerical differentiation rules. Complex geometries of the underlying continuum and difficulties with the solution, if Neumann boundaries are applied, lead to improved solution schemes. Currently, the Finite-Element-Method (FEM) is mostly applied in engineering practice which is based on the idea that the most accurate solution under all possible trial functions is the one minimizing the error. The first instances on using finite elements for the solution of differential equations can be found in Courant [1943]. Later on, further improvements and new techniques based on finite elements were developed. A comprehensive and detailed explanation of this method can be found for example in the work of Zienkiewicz and Taylor, especially the 4th edition (Zienkiewicz and Taylor [1989], Zienkiewicz and Taylor [1991]) includes a detailed description of coding a finite element program on the basis of FEAP. After the engineering success, also mathematicians became interested in this method giving the theory a mathematical basis. Mathematical textbooks suitable for engineers are for example Strang and Fix [1973], or Braess [2007].

In the following statements only the continuum part will be considered and the extension to the contact case is given in the next chapter. Summarizing the results of chapter 2, the differential equation describing the mechanical behavior under loading is the balance of momentum

$$\operatorname{div} \boldsymbol{\sigma}(\mathbf{u}) - \rho(\bar{\mathbf{b}} - \ddot{\mathbf{u}}) = 0 \quad \text{in } \varphi(B) \quad (3.1)$$

which has to be fulfilled at each local point inside of the domain $\varphi(B)$. The elastic stress is defined in terms of a constitutive relation

$$\boldsymbol{\sigma} = \frac{2}{J} \mathbf{b} \rho \frac{\partial \Psi}{\partial \mathbf{b}} \quad \text{in } \varphi(B) \quad (3.2)$$

depending on the left Cauchy strain tensor \mathbf{b} which is linked to the solution vector \mathbf{u}

via the deformation gradient \mathbf{F}

$$\mathbf{b} = \mathbf{F}\mathbf{F}^T, \quad \mathbf{F} = \mathbf{G} + \text{Grad } \mathbf{u} \quad \text{in } \varphi(B) \quad (3.3)$$

where $\mathbf{G} = \mathbf{G}_i \otimes \mathbf{G}^i$ indicates the covariant unity tensor in the initial configuration. Together with the Neumann and the Dirichlet boundary conditions, respectively

$$\boldsymbol{\sigma}\mathbf{n} = \bar{\mathbf{t}} \quad \text{on } \varphi(\partial_\sigma B) \quad \text{and} \quad \mathbf{u} = \bar{\mathbf{u}} \quad \text{on } \varphi(\partial B_u) \quad (3.4)$$

the whole set of equations are formulated. It is worth noting that the whole boundary is split either into a Neumann or a Dirichlet part

$$\varphi(\partial B) = \varphi(\partial B_u) \cup \varphi(\partial B_\sigma), \quad \text{and} \quad \varphi(\partial B_u) \cap \varphi(\partial B_\sigma) = \emptyset. \quad (3.5)$$

3.1 Concept of finite elements

The Finite Element Method is a combination of three different schemes, namely, the Rayleigh Ritz approximation, the Galerkin method of a minimized residual and the subdivision of the desired domain into elements of finite dimensions. Using the Rayleigh Ritz method, the solution vector (or primary variable) is approximated through the product of linear independent functions C_i with some coefficients \mathbf{q}_i

$$\mathbf{u} = \mathbf{q}_0 + \sum_{i=1}^n C_i \mathbf{q}_i \quad (3.6)$$

where \mathbf{q}_0 fulfills the inhomogeneous boundary conditions. This kind of approximation renders the solution of the differential equation to a solution of algebraic equations for the unknown coefficients \mathbf{q}_i which is convenient for the calculation with computers. The Galerkin method does not try to find the coefficients fulfilling the differential equation exactly, but seeks for the set of trial functions (3.6) which minimizes the error inside of the domain. Therefore the differential equation in terms of the primary variable $\mathbf{R}(\mathbf{u})$ multiplied with some weighting function $\boldsymbol{\eta}$ and integrated over the desired domain has to be equal to zero

$$G(\mathbf{u}, \boldsymbol{\eta}) = \int_{\partial(B)} \boldsymbol{\eta} \cdot \mathbf{R}(\mathbf{u}) \, dv = 0 \quad (3.7)$$

which is often called the weak form of the differential equation. Also the weighting or test function is approximated over some linear independent functions with proper coefficients

$$\boldsymbol{\eta} = \sum_{i=1}^n D_i \mathbf{p}_i \quad (3.8)$$

where the coefficients for the inhomogeneous boundary conditions \mathbf{p}_0 are equal to zero. If the same functions $C_i = D_i$ are used for the approximation of \mathbf{u} and $\boldsymbol{\eta}$, the method is outlined as Bubnov Galerkin method otherwise as Petrov Galerkin method, the latter

being applied for instance in fluid dynamic simulations. To simplify the integration of (3.7), the domain is subdivided into conforming elements (figure 3.1).

$$\varphi(B) = \bigcup_{e=1}^{n_e} \varphi(\Omega_e). \quad (3.9)$$

The vertices of the elements are called nodes and for each node one function is addressed which is 1 at that node and zero at all other nodes. This ensures the linear independency of the functions and leads to a compact structure of the matrix to be solved. The coefficients are also the exact solutions of the differential equation at that node. For a detailed explanation on a simple example see Hughes [1987]. In the finite element context the C_i are called shape functions N_I and the coefficients \mathbf{q}_i corresponds to the approximated variable \mathbf{u}_I . The discretization is often performed element wise and the mechanical solution vector is approximated by

$$\mathbf{u}^e = \sum_{I=1}^n N_I(\boldsymbol{\xi}) \mathbf{u}_I \quad (3.10)$$

where n corresponds to the number of nodes per element. Different types of shape functions N_I can be used for the partitioning of the domain. Mostly triangles or rectangles for the 2D case, or tetrahedral or hexahedral elements for the 3D case are preferred, but other types are also possible, see Dhett and Touzot [1984]. To ensure that rigid body movements and homogeneous deformations are rendered correctly, the requirements

$$\sum_{I=1}^n N_I(\boldsymbol{\xi}) = 1, \quad \sum_{I=1}^n N_I(\boldsymbol{\xi})_{,\mathbf{x}} = 0 \quad (3.11)$$

have to be fulfilled. The order of the polynom of the shape function has also to be larger or equal to the order of the differential equation. For a deeper insight into the mathematical formulation and the requirements on the shape functions, see Braess [2007] or Strang and Fix [1973]. Nowadays, the concept of isoparametric elements is preferred where the geometry and the unknowns are discretized with the same shape functions and the integration as well as the derivatives of the desired quantities are performed on a reference element (figure 3.1). The Jacobian

$$\mathbf{j}^e = \frac{\partial \mathbf{x}}{\partial \boldsymbol{\xi}} = \sum_{I=1}^n \mathbf{x}_I \otimes N_{I,\xi}(\boldsymbol{\xi}) \mathbf{E}_\xi = \sum_{I=1}^n \mathbf{x}_I \otimes \text{Grad}_\xi N_I \quad (3.12)$$

maps coordinates from the current configuration to the unity mesh (reference configuration). The advantage of the isoparametric concept is its simple numerical integration. All derivatives can be computed directly on the reference configuration with fixed orthonormal base vectors and hence Christoffel tensors have not to be specified explicitly. A more detailed introduction to the concept of the Finite-Element-Method can be found for instance in Schwarz [1991].

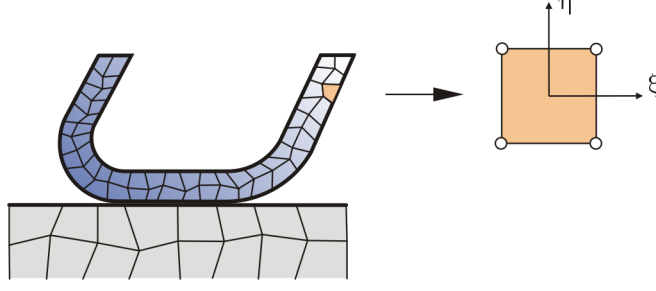


Figure 3.1: Discretized U-profile (left) and reference element for the 2D case (right)

If no dissipational effects have to be considered, the differential equation can be written in form of a potential. The solution field is then exactly the trial function which minimizes the energy

$$\Pi(\mathbf{u}) \rightarrow \min. \quad (3.13)$$

Three different energy methods are shown in the following being formulated in the initial configuration. The first one is the principle of virtual work

$$\Pi = \int_B [W(\mathbf{F}) - \rho_0 \bar{\mathbf{b}} \cdot \mathbf{x}] \, dv - \int_{\partial B_\sigma} \bar{\mathbf{t}} \cdot \mathbf{x} \, da. \quad (3.14)$$

The variation of the potential in the direction of the primary variable has to be equal to zero and corresponds to the weighted balance of momentum (3.7)

$$D\Pi(\mathbf{u}) \cdot \boldsymbol{\eta} = \int_B \left[\frac{\partial W(\mathbf{F})}{\partial \mathbf{F}} \cdot \text{Grad } \boldsymbol{\eta} - \rho_0 \bar{\mathbf{b}} \cdot \boldsymbol{\eta} \right] \, dv - \int_{\partial B_\sigma} \bar{\mathbf{t}} \cdot \boldsymbol{\eta} \, da = 0 \quad (3.15)$$

where only the constitutive equation (2.40) is embedded in the formulation and the geometrical equations

$$\mathbf{F} = \text{Grad } \mathbf{x} \quad \text{in } B, \quad \mathbf{u} = \bar{\mathbf{u}} \quad \text{on } B_u \quad (3.16)$$

have to be considered. The variation corresponds also to the directional or Gateaux differential of the unknown variable in the direction of its variation

$$D\Pi(\mathbf{u}) \cdot \delta \mathbf{u} = \left. \frac{d}{d\epsilon} \Pi(\mathbf{u} + \epsilon \delta \mathbf{u}) \right|_{\epsilon=0}. \quad (3.17)$$

For cases where the differential equation cannot be written in form of a potential, like in plasticity or friction, the starting equation is the variational form (3.15) where the dissipational effects are included as additional work terms. As a result, the weighted and the virtual work are equal and in the following examples the notion virtual will be applied in the context of weak formulations. The Hu-Washizu principle (Washizu [1975]) is often used for the construction of more advanced finite elements and an overview of some of these can be found in Wriggers [2001]. To describe a standard

element, the Hu-Washizu principle is formulated as a three field functional

$$\begin{aligned} \Pi(\mathbf{u}, \mathbf{F}, \mathbf{P}) = & \int_B [\mathbf{W}(\mathbf{F}) + \mathbf{P} \cdot (\text{Grad } \mathbf{x} - \mathbf{F}) - \rho_0 \bar{\mathbf{b}} \cdot \mathbf{x}] \, dv \\ & - \int_{\partial B_\sigma} \bar{\mathbf{t}} \cdot \mathbf{x} \, da + \int_{\partial B_u} \mathbf{P} \mathbf{N} \cdot (\mathbf{u} - \bar{\mathbf{u}}) \, da \rightarrow \text{stat} \end{aligned} \quad (3.18)$$

where the constitutive relation and the geometrical constraints are enforced in a weak sense. Other options are energy methods which are based on the complementary potential, like the Hellinger-Reissner principle (Hellinger [1914], Reissner [1950])

$$\begin{aligned} \Pi(\mathbf{P}, \mathbf{u}) = & \int_B [\mathbf{W}(\mathbf{P}) + \mathbf{u} \cdot (\text{Div } \mathbf{P} + \rho_0 \bar{\mathbf{b}})] \, dv \\ & + \int_{\partial B_\sigma} (\bar{\mathbf{t}} - \mathbf{t}) \cdot \mathbf{u} \, da - \int_{\partial B_u} \mathbf{P} \mathbf{N} \cdot \bar{\mathbf{u}} \, da \rightarrow \text{stat}. \end{aligned} \quad (3.19)$$

The advantage of this approach compared to the Hu-Washizu principle is the reduced number of unknowns (stress and displacement), but for a lot of materials the complementary potential is hard to define.

At the end of this introduction, it has to be noted that finite element approximations have some natural limitations, especially the Lagrangian description where the mesh deforms during the loading process. At large deformations, the mesh gets distorted and the results deteriorate or the complete solution procedure fails. Crack propagation, contact computation or fluid structure interactions need a special treatment of the mesh which might get complicated and inherits some uncertainties for the solution process. As a result, for some purposes different methods can be more profitable leading to simpler and more robust solution schemes, like meshless methods (Li and Liu [2007]) for instance.

3.2 Space discretization

Using (3.9), the weak form (2.55) or (3.7) can also be viewed as an assembly over all elements n_e

$$G^h(\mathbf{u}, \boldsymbol{\eta}) = \bigcup_{e=1}^{n_e} [\boldsymbol{\eta} \cdot \mathbf{R}^e(\mathbf{u}) + \boldsymbol{\eta} \cdot \mathbf{P}^e(\mathbf{u})] \quad (3.20)$$

consisting of a volume \mathbf{R}^e and a loading part \mathbf{P}^e where the superscript h indicates the discretized form of the desired quantity. In the discretized volume contribution

$$\boldsymbol{\eta} \cdot \mathbf{R}^e = \sum_{I=1}^n \boldsymbol{\eta}_I \sum_{g=1}^{n_{gp}} [\mathbf{B}_{Ig} \boldsymbol{\sigma}_g(\mathbf{u}) + \rho N_{Ig} \ddot{\mathbf{u}}_g] \det \mathbf{j}_g^e W_g, \quad (3.21)$$

the symmetry of the stress and strain tensor is exploited leading to a description in vector form for the stress and the strain and in a matrix form for the material tensor

(Voigt notation). The derivative of the weighted function at the integration point is then represented in terms of a B matrix (see appendix B.1).

$$\text{grad } \boldsymbol{\eta}_g = \sum_{I=1}^n \boldsymbol{\eta}_I \otimes \mathbf{j}_g^{e-T} N_{I,\xi g} = \sum_{I=1}^n \mathbf{B}_{Ig} \boldsymbol{\eta}_I. \quad (3.22)$$

The discretization of the loading part can also be further subdivided into a body and a boundary loading part

$$\boldsymbol{\eta} \cdot \mathbf{P}^e = \sum_{I=1}^n \boldsymbol{\eta}_I \sum_{g=1}^{n_{gp}} \rho N_{Ig} \bar{\mathbf{b}} \det \mathbf{j}_g^e W_g + \sum_{B=1}^{n_s} \boldsymbol{\eta}_B \sum_{p=1}^{n_{gp}^s} N_{Ip}^s \bar{\mathbf{t}}_p(\mathbf{u}) \det \mathbf{j}_p^s W_p^s \quad (3.23)$$

where the second part is only nonzero at elements which shares a nonzero boundary of a Neumann type. The determinant of the Jacobian tensor for the surface can be specified as

$$\det \mathbf{j}_p^s = \|\mathbf{x}_{,1g} \times \mathbf{x}_{,2g}\|. \quad (3.24)$$

More details regarding a displacement dependent loading can be found in Schweizerhof and Ramm [1984] or Simo et al. [1991] and a detailed description of the space discretization in standard FEM textbooks (Wriggers [2001], Hughes [1987], Zienkiewicz and Taylor [1989], Zienkiewicz and Taylor [1991]).

The unknown acceleration $\ddot{\mathbf{u}}_g$ in (3.21) can be linked to the displacement field using a time integration scheme. Introductory textbooks on time integration include Hairer et al. [2008] and with a focus on differential algebraic system (DAE) Hairer and Wanner [2002]. Differential algebraic equations can occur, if the set of differential equations is supplemented by additional algebraic equations, as for the dynamic formulation of the theory of porous media (see section 6). An introduction to DAEs from a viewpoint of an engineer and explained using simple examples is given in Lutzenberger [2002]. Different types of time integration algorithms are possible like the Generalized- α method (Chung and Hulbert [1993]) which dissipates energy to guarantee a numerical stability and is based on the Newmark time integration scheme. Other types conserve the energy and the momentum leading also to a stable time integration scheme. Prominent schemes are the energy momentum method (EMM) based on Simo and Tarnow [1991] and extended to a generalized form (GEMM) in Kuhl and Crisfield [1999]. Additionally, schemes based on the Galerkin methods have been developed (Betsch and Steinmann [2001]) which fit better to the finite element procedure and share the same benefits as the EMM or the GEMM. The drawback of the energy conserving methods compared to the Newmark type is the large effort to implement them. Applying one of these time integration schemes, the volume term (3.21)

$$\boldsymbol{\eta} \cdot \mathbf{R}^e = \sum_{I=1}^n \boldsymbol{\eta}_I \sum_{g=1}^{n_{gp}} [\mathbf{B}_{Ig} \boldsymbol{\sigma}_g(\mathbf{u}_{n+1}) + \rho N_{Ig} \ddot{\mathbf{u}}_{gn+1}] \det \mathbf{j}_g^e W_g \quad (3.25)$$

can be written only in dependency of the actual solution field \mathbf{u}_{n+1} and of the values at the old time step which are already known.

3.3 Newton iteration for nonlinear equations

If the geometrical description, the material behavior or the physical process is not linear, a direct solution of (3.20) is not possible and special solution techniques for the nonlinear equations have to be applied. Under the variety of solution schemes for nonlinear problems (Schwetlick and Kretzschmar [1991] or Wriggers [2001]), the Newton Raphson iteration or shortly the Netwon iteration is the procedure mostly preferred. The advantage of this method is its quadratic convergence rate and the disadvantage is the computation of the tangent at each iteration step and its dependency on the starting value. For some mechanical applications, like nonlinear yield criteria in plasticity, an incorrect starting value can lead to the wrong solution or to no convergence. Remedies for such cases include for instance a line search technique (Crisfield [1991]) or based on such a procedures a substepping scheme (Sloan [1987]) which is especially developed for nonlinear yield functions and is applied in section 5.4. Instead of (3.7), the linearized equation

$$G(\mathbf{u}) + DG(\mathbf{u}) \cdot \Delta \mathbf{u} = 0 \quad (3.26)$$

has to be solved within a loop until (3.7) is obtained where the Gateaux differential similar to (3.17) is used

$$D \bullet (\mathbf{u}) \cdot \Delta \mathbf{u} = \left. \frac{d}{d\epsilon} \bullet (\mathbf{u} + \epsilon \Delta \mathbf{u}) \right|_{\epsilon=0}. \quad (3.27)$$

In most textbooks and also in the following examples of this work, only the differential (3.27) is denoted as the linearization instead of the whole equation (3.26).

After the discretization of (3.26) the correct solution of (3.7) within the Newton iteration is obtained, if the residuum $\|\mathbf{R}\|$ is less than a given tolerance δ multiplied with the norm of the initial residuum $\|\mathbf{R}_0\|$

$$\|\mathbf{R}\| \leq \delta \|\mathbf{R}_0\|. \quad (3.28)$$

Alternatively, the energy norm $\mathbf{R} \cdot \Delta \mathbf{u}$ can be used as a convergence criterion. If the convergence rate of the Newton iteration is quadratic (Schwetlick and Kretzschmar [1991]), then all the essential derivatives of the residual are implemented correctly.

For the assembled algebraic equation the condition number κ of the stiffness matrix \mathbf{K}

$$\kappa(\mathbf{K}) = \|\mathbf{K}\| \|\mathbf{K}^{-1}\| \quad (3.29)$$

ensures that a small residual implies also a small deviation of the exact solution of the algebraic equation where the norm of the matrix can be the Euclidian norm, the maximum norm or other norms (Demmel [1997]). Since the inverse of the matrix is very expensive to compute, other types of condition numbers are preferred. For direct solvers the quotient of the smallest and the largest entry on the diagonal of the decomposed (L-U) matrix is an acceptable estimate for the error of the solution.

For values given in the current configuration, first a pull-back of the values to the initial configuration has to be performed. After the directional derivative (3.27), the

values are pushed-forward to the current configuration (Marsden and Hughes [1983]). In the case of geometric nonlinearities, the linearization of (3.21)

$$\begin{aligned} \boldsymbol{\eta} \cdot \mathbf{K}^e [\Delta \mathbf{u}] = & \sum_{g=1}^{n_{gp}} \sum_{I=1}^n \sum_{J=1}^n \boldsymbol{\eta}_I \left\{ (\mathbf{B}_{Ig} \boldsymbol{\sigma}_g \mathbf{B}_{vJg} \mathbf{1} + \mathbf{B}_{Ig} \mathbf{D}_g \mathbf{B}_{Jg}) \Delta \mathbf{u}_J \right. \\ & \left. + \rho N_{Ig} N_{Jg} \Delta \ddot{\mathbf{u}}_J \right\} \det \mathbf{j}_g^e \mathbf{W}_g \end{aligned} \quad (3.30)$$

leads to the element tangent \mathbf{K}^e . The first term stems from the gradient of the weighting function formulated in the current configuration (3.22) and the second term indicates the current stiffness of the material. For the Neo Hookian stress (2.45), the fourth order material tensor \mathbf{c} corresponds to the second derivative of the strain energy function with respect to the left Cauchy Green tensor (Miehe [1994])

$$\mathbf{c} = \frac{4}{J} \mathbf{b} \rho \frac{\partial \Psi}{\partial \mathbf{b} \partial \mathbf{b}} \mathbf{b} = \lambda J^2 \mathbf{g}^{-1} \otimes \mathbf{g}^{-1} + [2\mu - \lambda (J^2 - 1)] \mathbf{1}_{\mathbf{g}^{-1}} \quad (3.31)$$

where the derivatives

$$\frac{\partial I_{\mathbf{b}}}{\partial \mathbf{b}} = \mathbf{g}^{-1}, \quad \frac{\partial J}{\partial \mathbf{b}} = \frac{J}{2} \mathbf{b}^{-1} \frac{\partial \mathbf{b}^{-1}}{\partial \mathbf{b}} = \mathbf{b}^{-1} \mathbf{1}_{\mathbf{g}^{-1}} \mathbf{b}^{-1} \quad (3.32)$$

are used. The forth order tensor $\mathbf{1}_{\mathbf{g}^{-1}}$ can be found for instance in (Miehe [1988]). The reduction of the forth order material tensor \mathbf{c} to the matrix \mathbf{D} can be found in the appendix B.

For material nonlinearities sometimes an additional Newton iteration has to be applied on a local level (at each integration point). In the case of a material which can undergo permanent deformations, the stress is limited due to the yield criterion. Most of the algorithms on computational plasticity are nowadays based on the work of Simo and Taylor [1985] who presented an algorithm leading to a consistent tangent in the context of an implicit return mapping algorithm. A detailed description of that method can be found in Simo [1998]. Here the method will be illustrated for a plasticity model without hardening formulated in the linear regime. The first step is to integrate the plastic evolution equation (2.51) with the implicit backward Euler scheme

$$\boldsymbol{\varepsilon}_{n+1}^p = \boldsymbol{\varepsilon}_n^p + \gamma_{n+1} \frac{\partial g}{\partial \boldsymbol{\sigma}} \Big|_{n+1} \quad (3.33)$$

where $\gamma_{n+1} = \Delta t \lambda_{n+1}$. Based on the actual elastic stress

$$\boldsymbol{\sigma}_{n+1} = \mathbf{D}^e [\boldsymbol{\varepsilon}_{n+1} - \boldsymbol{\varepsilon}_{n+1}^p] = \mathbf{D}^e \left[\boldsymbol{\varepsilon}_{n+1} - \boldsymbol{\varepsilon}_n^p - \gamma_{n+1} \frac{\partial g}{\partial \boldsymbol{\sigma}} \Big|_{n+1} \right], \quad (3.34)$$

the trial stress can be obtained by freezing the update of the plastic part

$$\boldsymbol{\sigma}_{n+1}^{tr} = \mathbf{D}^e [\boldsymbol{\varepsilon}_{n+1} - \boldsymbol{\varepsilon}_n^p] \quad (3.35)$$

where \mathbf{D}^e is the linear elastic material tensor (see appendix B.3). The trial stress determines the actual state of the integration point. If (3.35) lies within the elastic

domain ($f(\boldsymbol{\sigma}_{n+1}^{tr}) \leq 0$), the current stress is equal to its trial version and the tangent corresponds to the elastic material tensor

$$\begin{aligned}\boldsymbol{\sigma}_{n+1} &= \boldsymbol{\sigma}_{n+1}^{tr} \\ \mathbf{D}_{gn+1} &= \mathbf{D}^e.\end{aligned}\tag{3.36}$$

If the yield criterion is violated ($f(\boldsymbol{\sigma}_{n+1}^{tr}) > 0$), the material point undergoes plastic deformations. The stress can then be computed in terms of the set of equations

$$\begin{aligned}\mathbf{R}_{\sigma n+1} &= \mathbf{D}^{e-1} \boldsymbol{\sigma}_{n+1} - \boldsymbol{\varepsilon}_{n+1} + \boldsymbol{\varepsilon}_n^p + \gamma_{n+1} \frac{\partial g}{\partial \boldsymbol{\sigma}} \Big|_{n+1} = 0 \\ \mathbf{R}_{\gamma n+1} &= f(\boldsymbol{\sigma}_{n+1}) = 0.\end{aligned}\tag{3.37}$$

Using the Newton method at each iteration step, the algebraic equation

$$\begin{bmatrix} \mathbf{D}^{e-1} + \gamma_{n+1} \frac{\partial^2 g}{\partial \boldsymbol{\sigma} \partial \boldsymbol{\sigma}} \Big|_{n+1}^{(k)} & \frac{\partial g}{\partial \boldsymbol{\sigma}} \Big|_{n+1}^{(k)} \\ \frac{\partial f}{\partial \boldsymbol{\sigma}} \Big|_{n+1}^{(k)} & 0 \end{bmatrix} \begin{bmatrix} \Delta \boldsymbol{\sigma}_{n+1}^{(k+1)} \\ \Delta \gamma_{n+1}^{(k+1)} \end{bmatrix} = - \begin{bmatrix} \mathbf{R}_{\sigma n+1}^{(k)} \\ \mathbf{R}_{\gamma n+1}^{(k)} \end{bmatrix}\tag{3.38}$$

has to be solved until $\mathbf{R}_{\gamma n+1}^{(k)} < \delta$ is smaller than a given tolerance δ . During the iteration, the stress $\boldsymbol{\sigma}_{n+1}^{(k+1)} = \boldsymbol{\sigma}_{n+1}^{(k)} + \Delta \boldsymbol{\sigma}_{n+1}^{(k+1)}$ and the plastic increment $\gamma_{n+1}^{(k+1)} = \gamma_{n+1}^{(k)} + \Delta \gamma_{n+1}^{(k+1)}$ have to be updated at each step (k+1). The computation of the material tangent is based on the converged and inverted tangent matrix in (3.38)

$$\begin{bmatrix} \mathbf{A}_{\sigma\sigma n+1} & \mathbf{A}_{\sigma\gamma n+1} \\ \mathbf{A}_{\gamma\sigma n+1} & \mathbf{A}_{\gamma\gamma n+1} \end{bmatrix} = \begin{bmatrix} \mathbf{D}^{e-1} + \gamma_{n+1} \frac{\partial^2 g}{\partial \boldsymbol{\sigma} \partial \boldsymbol{\sigma}} \Big|_{n+1} & \frac{\partial g}{\partial \boldsymbol{\sigma}} \Big|_{n+1} \\ \frac{\partial f}{\partial \boldsymbol{\sigma}} \Big|_{n+1} & 0 \end{bmatrix}^{-1}\tag{3.39}$$

and the material tensor follows then to (see also Wriggers [2001])

$$\mathbf{D}_{gn+1} = \mathbf{A}_{\sigma\sigma n+1}.\tag{3.40}$$

An alternative way of computing the tangent can be found in Simo [1998] and examples of standard plasticity models used for metals and soils are given in de Souza Neto et al. [2008].

3.4 Assembling and solver

After the local residual vectors and the local tangent matrices are determined for each element, they have to be assembled leading to the global residual vector and the global tangent matrix. At the end of this chapter, only a brief explanation of the assembling and the solution of the global algebraic equation is highlighted. The management of local and global equations numbers within a finite element program can be found in Zienkiewicz and Taylor [1989] where a detailed manual of the finite element program

FEAP is also listed and for an introductory work on the solution of algebraic equations, see Demmel [1997]. Beside the local residual vector and the local tangent matrix, an array is also needed where the assignments of the local equation numbers of each element to their global counterparts are stored. Depending on the type of the solver (direct or iterative), different assembling techniques are used. Two formats for the storage of matrices with a small bandwidth are the so called skyline or the CRS format. In the skyline format for each global equation number (GEN), the lowest global equation number where this GEN is connected to indicates the bandwidth of each column and is stored in an array. In this assembling strategy, zero entries are also stored whereas in the CRS format only non zero entries are regarded. Thereby besides the array of all non zero entries, one array stores the column number of all non zero entries and in a second array the number of entries of each row are listed. Modern solvers are based on the CRS format, like PARDISO which is a parallel sparse direct solver with an iterative preconditioner (Schenk et al. [2001]).

Chapter 4

Contact discretization

Within the last 40 years starting with the work of Wilson and Parson [1970], a lot of different strategies to incorporate contact constraints into the Finite-Element-Method have been developed which can be classified with regards to the deformation regime, the coupling strategy, the type of the contact element and the solution methods to incorporate the contact constraints (table 4.1). In the small deformation regime where

deformation	coupling	contact element	solution methods
small	strong	node to node	Lagrange multiplier
large	weak	node to segment	penalty
		segment to segment	augmented Lagrangian

Table 4.1: Classification of contact methods

the linear theory can be applied, the implementation of the contact constraints simplifies, since no contact search has to be performed, but on the other hand no large slip is allowed. The more general case of contact includes large deformations where an arbitrary long sliding distance between the contacting bodies is possible. Early implementations of the contact constraints within the small deformation regime can be found in Chan and Tuba [1971] and focused on large deformations in Hallquist [1979]. At the beginning the strong coupling of the slave nodes with the master surface was the standard discretization technique within contact algorithms (see Wriggers and Miehe [1994] or Laursen and Simo [1993]), but recently, the Mortar method (Bernardi et al. [1990], Bernardi et al. [1992] extended to contact by Belgacem et al. [1998]) based on a weak coupling of the contacting bodies leads to a more robust algorithm and is therefore preferred in modern contact codes. Different contact elements have also been developed over the years. For matching grids the node to node element formulation (Francavilla and Zienkiewicz [1975]) can be used where each slave node is linked to a master node. Otherwise, for the case of non matching grids, a node to segment formulation (Chan and Tuba [1971]) or a segment to segment concept (Simo et al. [1985] and extended to the large deformation regime in Papadopoulos and Taylor [1992]) are applied. In the former one, for each slave node the projected master element is determined and in the latter one, the overlap between each slave and master element is computed. The segment to segment concept is preferred for contact formulations based

on the Mortar method, since the integration over the contact surface can be performed much more accurately. The Lagrange multiplier method (Hughes et al. [1976]) and the penalty formulation (Oden [1981]) were the first solution methods for the contact constraints, but since the Lagrange multiplier method can lead to oscillations and in the penalty formulation the constraints are enforced only approximated, the augmented Lagrangian method was introduced to overcome these drawbacks. One version of the augmented method (Simo and Laursen [1992]) uses an intrinsic loop to update the Lagrange multiplier in order to avoid additional unknowns (Uzawa algorithm). Alart and Curnier [1991] developed another version where the augmented Lagrange multiplier is directly implemented into the contact constraints leading to additional unknowns in the system, but no additional loop occurs. Alternative formulations within the Mortar framework are also available. In Fischer and Wriggers [2005] and Fischer and Wriggers [2006], the active set is checked at each integration point for the penalty regularization and at each segment in case of the Lagrange multiplier method. In Tur et al. [2009], a 2D version is proposed based on the averaged normal penetration and the averaged tangential movement and in Temizer [2012], the Mortar method is formulated based on the mixed concept of Papadopoulos and Taylor [1992]. The node to segment contact element is also coupled to the Mortar method in Hübner and Wohlmuth [2005] and Hübner et al. [2008] by means of dual shape functions (Wohlmuth [2000]). For a comprehensive overview of methods used within the small and the large deformation regimes, see Wriggers [2006], or for a detailed description of a node to segment formulation based on a strong coupling and formulated within the large deformation regime, see Laursen [2006]. A more mathematical approach of contact formulations can be found in Kikuchi and Oden [1988] or Wohlmuth [2011].

This chapter is focused on the implementation of the standard node to segment approach together with a penalty regularization and on the implementation of the Mortar method based on four different solution methods to incorporate the contact constraints (Lagrange multiplier, penalty regularization, augmented Lagrangian method and a mixed version consisting of the augmented and the penalty method) and two different versions to formulate contact kinematics into a finite element code. All methods are formulated for the three-dimensional case including large deformations. If contact takes place, additional tangent matrices and residual vectors have to be added to the continuum contributions. Based on the local/global equation number array of each contact element, the bandwidth of the global matrix changes and as a result the skyline profile or the CRS format (section 3.4) has to be adjusted before each iteration step. If Lagrange multipliers have to be taken into account, additional DOFs have also to be assigned to the system. In that case, every slave node, if active or not, gets additional equations numbers to simplify the profiling. Hence for inactive nodes the additional constraint of no contact stress has also to be considered.

4.1 Contact solution methods

In the case of contact, additional boundary conditions have to be added to the continuum form (3.1)-(3.4). In contrast to (3.5), the whole surface ($i = 1, 2$) of the two

bodies is now subdivided into three different parts, the Neumann, the Dirichlet and the contact boundary, respectively

$$\begin{aligned}\varphi(\partial B^i) &= \varphi(\partial B_u^i) \cup \varphi(\partial B_\sigma^i) + \varphi(\partial B_c), \\ \varphi(\partial B_u^i) \cap \varphi(\partial B_\sigma^i) \cap \varphi(\partial B_c) &= \emptyset.\end{aligned}\tag{4.1}$$

Going back to Hallquist [1979], the contacting surfaces are denoted as slave (i=1) and master (i=2) surface, respectively, where on the slave side the integration is performed. The additional contact boundary conditions can be written shortly in Karush-Kuhn-Tucker form

$$g_N \lambda_N = 0 \quad \text{and} \quad \dot{\gamma} f_c = 0 \quad \text{on} \quad \varphi(\partial B_c).\tag{4.2}$$

Explaining in detail, if the normal penetration (2.90) is larger than zero ($g_N > 0$), the normal stress component has to vanish ($\lambda_N = 0$). On the other hand, if contact takes place ($g_N = 0$), a pressure is induced between both bodies ($\lambda_N < 0$). The formulation for the normal contact in (4.2) is also known as the Hertz-Signorini-Moreau condition. For the tangential part, a slip criterion indicates whether the bodies sticks on each other ($f_c < 0$) or slips ($f_c = 0$). In the case of stick, the slip rate has to be equal to zero ($\dot{\gamma} = 0$) and if one body slips on the other surface ($\dot{\gamma} > 0$), the evolution equation for the tangential movement in the direction of the tangential contact stress vector

$$\dot{\mathbf{g}}_T = \dot{\gamma} \frac{\boldsymbol{\lambda}_T}{\|\boldsymbol{\lambda}_T\|}\tag{4.3}$$

has to be taken into account with $\boldsymbol{\lambda}_T$ as the tangential stress. The slip criterion mostly implemented in standard contact algorithms is the Coulomb law

$$f^c = \|\boldsymbol{\lambda}_T\| - \mu |\lambda_N| \leq 0\tag{4.4}$$

which will be also used within this chapter and where μ denotes the coefficient of friction. Applying a parameterization ($\xi^{\alpha i}$) for each of the contacting bodies, the base vectors can be defined

$$\mathbf{a}_\alpha^i = \frac{\partial \mathbf{x}^i}{\partial \xi^\alpha} = \mathbf{x}_{,\alpha}^i, \quad \mathbf{t}_\alpha^i = \frac{\mathbf{a}_\alpha^i}{\|\mathbf{a}_\alpha^i\|}, \quad \mathbf{n}^i = \frac{\mathbf{a}_1^i \times \mathbf{a}_2^i}{\|\mathbf{a}_1^i \times \mathbf{a}_2^i\|}.\tag{4.5}$$

Further on, the contact weak form of each solution method described in the next sections

$$G^c(\mathbf{u}, \boldsymbol{\lambda}, \boldsymbol{\eta}, \delta \boldsymbol{\lambda}) = G_u^c + G_l^c\tag{4.6}$$

can be subdivided into a virtual contact work part G_u^c and a weak enforcement of the contact constraints G_l^c . Additionally, the active set strategy which is explained in detail in Luenberger [1984] is applied to formulate the inequalities in (4.2) as contact equalities. Hence for each point at the contact surface, a unique status (active or inactive, stick or slip) can be assigned.

4.1.1 Lagrange multiplier method

The advantage of the Lagrange multiplier method is the exact enforcement of the contact constraints, but the different weak forms depending on the status can lead to oscillations, if the desired point at the surface lies closely to the active/inactive or stick/slip transition zone. The constraint for points at the contact surface to switch its status are listed in (4.7)

$$\begin{aligned} \text{inactive to active} &\rightarrow g_{Nn+1} \leq 0 & \text{active to inactive} &\rightarrow \lambda_{Nn+1} > 0 \\ \text{stick to slip} &\rightarrow f_{n+1}^c > 0 & \text{slip to stick} &\rightarrow \Delta_t \gamma_{n+1} \leq 0 \end{aligned} \quad (4.7)$$

where $\Delta_t \gamma_{n+1} = \gamma_{n+1} - \gamma_n$ corresponds to the incremental slip rate. The virtual contact work indicates the contribution of the Lagrange multipliers to the virtual work of the two bodies

$$G_u^c = \int_{\gamma_c} (\delta g_{Nn+1} \lambda_{Nn+1} + \delta \mathbf{g}_{Tn+1} \cdot \boldsymbol{\lambda}_{Tn+1}) da. \quad (4.8)$$

The weak form for the stick case

$$G_l^c = \int_{\gamma_c} \left(\delta \lambda_{Nn+1} g_{Nn+1} + \delta \boldsymbol{\lambda}_{Tn+1} \cdot (\mathbf{g}_{Tn+1} - \mathbf{g}_{Tn}) + \delta \gamma_{n+1} \frac{1}{c_C} \Delta_t \gamma_{n+1} \right) da = 0 \quad (4.9)$$

includes that no penetration, no tangential movement and no incremental slip are allowed. Conversely, for the slip case

$$\begin{aligned} G_l^c = \int_{\gamma_c} \left(\delta \lambda_{Nn+1} g_{Nn+1} + \delta \boldsymbol{\lambda}_{Tn+1} \cdot \left[\mathbf{g}_{Tn+1} - \mathbf{g}_{Tn} - \Delta_t \gamma_{n+1} \frac{\boldsymbol{\lambda}_{Tn+1}}{\|\boldsymbol{\lambda}_{Tn+1}\|} \right] \right. \\ \left. + \delta \gamma_{n+1} f_{n+1}^c \right) da = 0, \end{aligned} \quad (4.10)$$

the non penetration condition, the evolution equation for the tangential movement in integrated form and the slip criterion have to be fulfilled. The normal and the tangential stress as well as the slip increment have to be zero for points which are not in contact

$$G_l^c = \int_{\gamma_c} \left(\delta \lambda_{Nn+1} \frac{1}{c_N} \lambda_{Nn+1} + \delta \boldsymbol{\lambda}_{Tn+1} \frac{1}{c_T} \boldsymbol{\lambda}_{Tn+1} + \delta \gamma_{n+1} \frac{1}{c_C} \Delta_t \gamma_{n+1} \right) da = 0 \quad (4.11)$$

where the additional parameter c_N, c_T, c_C are used only for unity reasons, but its values can be oriented on the material parameters to guarantee a good condition of the stiffness matrix.

4.1.2 Penalty method

The disadvantage of the penalty method is that for small penalty parameters the contact constraints are approximated only imprecisely, and for larger parameters the solution would improve, but the tangent matrix gets also more and more ill-conditioned.

On the other hand, the penalty method can be used to develop new phenomenological models for the normal and the tangential contact. Especially, based on the analogy between friction and plasticity (Curnier [1984], Michalowski and Mroz [1978] and for a summary Wriggers [2006]) new slip criteria can be formulated. No additional unknowns have to be introduced to the system avoiding zeros on the diagonal of the global tangent matrix. The normal stress component and the tangential stress vector

$$\mathbf{t}_{Nn+1} = c_N g_{Nn+1}, \quad \mathbf{t}_{Tn+1} = -c_T \mathbf{g}_{Tn+1}^e \quad (4.12)$$

are regularized via the penalty parameters c_N, c_T where the tangential movement is split into an elastic and a plastic part

$$\mathbf{g}_{Tn+1} = \mathbf{g}_{Tn+1}^e + \mathbf{g}_{Tn+1}^p, \quad \mathbf{g}_{Tn+1}^p - \mathbf{g}_{Tn}^p = \Delta t \gamma_{n+1} \frac{\boldsymbol{\lambda}_{Tn+1}}{\|\boldsymbol{\lambda}_{Tn+1}\|} \quad (4.13)$$

and the evolution equation for the plastic tangential movement is integrated using the implicit backward Euler scheme. Based on the trial stress and the trial slip criterion

$$\mathbf{t}_{Tn+1}^{tr} = -c_T (\mathbf{g}_{Tn+1} - \mathbf{g}_{Tn}^p), \quad f_{n+1}^{ctr} = f^c(\mathbf{t}_{Tn+1}^{tr}), \quad (4.14)$$

the status of a point at the contact surface can be determined

$$\begin{aligned} \text{active} & : g_{Nn+1} \leq 0 & \text{inactive} & : g_{Nn+1} > 0 \\ \text{slip} & : f_{n+1}^{ctr} > 0 & \text{stick} & : f_{n+1}^{ctr} \leq 0. \end{aligned} \quad (4.15)$$

In the case of the penalty method, the virtual contact work

$$G_u^c = \int_{\gamma_c} (\delta g_{Nn+1} \mathbf{t}_{Nn+1} - \delta \mathbf{g}_{Tn+1} \cdot \mathbf{t}_{Tn+1}) da \quad (4.16)$$

is the only contribution to the weak form of the continuum. The minus sign compared to (2.89) is due to the minus sign in the determination of the tangential stress vector in (4.12).

4.1.3 Augmented method

Due to the disadvantages of the Lagrange multiplier method (section 4.1.1) and the penalty regularization (section 4.1.2) the idea of an augmented method, sometimes called primal dual method, evolves which combines the advantages of both methods leading to a smoother transition between active/inactive and stick/slip although the contact constraints are enforced exactly. The idea is to introduce an augmented normal stress component and an augmented tangential stress vector

$$\begin{aligned} \hat{\lambda}_{Nn+1} &= \lambda_{Nn+1} + c_N g_{Nn+1} \\ \hat{\boldsymbol{\lambda}}_{Tn+1} &= \boldsymbol{\lambda}_{Tn+1} - c_T (\mathbf{g}_{Tn+1} - \mathbf{g}_{Tn}^p) \end{aligned} \quad (4.17)$$

where to the unknown Lagrange multipliers the corresponding penalty formulations are added. For the augmented method, two different strategies exist. The first one is based on an update of the Lagrange multiplier within an extra loop (Simo and Laursen [1992]) which is also known as the Uzawa algorithm. The advantage is that no additional unknowns have to be computed within the Newton iteration, but the additional loop slows down the solution process. Another way is to formulate an augmented Lagrangian functional (for small deformations Alart and Curnier [1991] and extended to large deformations in Pietrzak and Curnier [1999]) where the virtual contact work evolves from the derivative of the functional with respect to the normal penetration and to the tangential movement. The weak enforcement of the contact constraints results from the derivative with respect to the normal and to the tangential Lagrange multipliers. Within the Mortar method an additional loop in the virtual contact work has to be implemented due to the augmented Lagrange multiplier which slows down the solution process as well. Descriptions where the augmented Lagrange multipliers (4.17) are only applied in the weak enforcement of the contact constraints are based on a minimization operator (Christensen et al. [1998]) or on a nonlinear complementarity function (Hüeber and Wohlmuth [2005] for the normal and Hüeber et al. [2008] for the frictional treatment of contact problems in the linear theory). For a mathematical background on the nonlinear complementarity function (NCF), see Stadler [2004]. Minimization operator and NCF means from an engineering point the same and since the CPU time is decreased compared to the other types, this algorithm is preferred in this work. If dual shape functions (Wohlmuth [2000]) are used, the Lagrange multipliers can be condensed from the global matrix in order to avoid zero entries on the diagonal. An extension of the NCF concept together with dual shape functions to the nonlinear theory can be found in Popp et al. [2009] for the 2D and in Popp et al. [2010a] for the 3D frictionless case, respectively. In Popp et al. [2010b], a 2D version including friction is presented.

Following Hüeber and Wohlmuth [2005] and Hüeber et al. [2008], the transitions between active/inactive and stick/slip are formulated in terms of the nonlinear complementarity function and the augmented Lagrange multipliers (4.17)

$$\begin{aligned} \frac{1}{c_N} \left(\lambda_{Nn+1} - \min\{\hat{\lambda}_{Nn+1}, 0\} \right) &= 0 \\ \frac{1}{c_T} \left(\lambda_{Tn+1} - \mu |\hat{\lambda}_{Nn+1}| \frac{\hat{\lambda}_{Tn+1}}{\max\{\mu |\hat{\lambda}_{Nn+1}|, \|\hat{\lambda}_{Tn+1}\|\}} \right) &= 0 \end{aligned} \quad (4.18)$$

where the different use of the min or max functions compared to the literature depends on the sign of the augmented Lagrange multipliers. Additionally, different to the literature here the nonlinear complementarity functions are divided by the penalty parameters due to unity reasons. The contact contribution to the virtual contact work is thereby identical to the Lagrange multiplier case (4.8)

$$G_u^c = \int_{\gamma_c} (\delta g_{Nn+1} \lambda_{Nn+1} + \delta \mathbf{g}_{Tn+1} \cdot \lambda_{Tn+1}) \, da. \quad (4.19)$$

Depending on the min or max function in (4.18), points at the contact surface are active if

$$\hat{\lambda}_{Nn+1} = \lambda_{Nn+1} + c_N g_{Nn+1} \leq 0 \quad (4.20)$$

and stick on the other surface if

$$f^c = \|\hat{\boldsymbol{\lambda}}_{Tn+1}\| - \mu|\hat{\lambda}_{Nn+1}| \leq 0. \quad (4.21)$$

The weak form of the stick contribution follows then directly from the fulfillment of (4.18) exploiting (4.17), (4.20) and (4.21) which is almost identical to the case of a pure Lagrange multiplier formulation (4.9) where only the incremental slip part is neglected

$$G_l^c = \int_{\gamma_c} (\delta\lambda_{Nn+1} g_{Nn+1} + \delta\boldsymbol{\lambda}_{Tn+1} \cdot (\mathbf{g}_{Tn+1} - \mathbf{g}_{Tn})) da = 0. \quad (4.22)$$

If

$$f^c = \|\hat{\boldsymbol{\lambda}}_{Tn+1}\| - \mu|\hat{\lambda}_{Nn+1}| \leq 0, \quad (4.23)$$

the weak form of the slip constraint can be formulated based on the fulfillment of (4.18) together with (4.17) as

$$G_l^c = \int_{\gamma_c} \left(\delta\lambda_{Nn+1} g_{Nn+1} + \delta\boldsymbol{\lambda}_{Tn+1} \cdot \frac{1}{c_T} \left(\boldsymbol{\lambda}_{Tn+1} - \mu|\lambda_{Nn+1} + c_N g_{Nn+1}| \frac{\boldsymbol{\lambda}_{Tn+1} - c_T (\mathbf{g}_{Tn+1} - \mathbf{g}_{Tn})}{\|\boldsymbol{\lambda}_{Tn+1} - c_T (\mathbf{g}_{Tn+1} - \mathbf{g}_{Tn})\|} \right) \right) da = 0. \quad (4.24)$$

For points at the contact surface which are not active

$$\hat{\lambda}_{Nn+1} > 0 \quad (4.25)$$

and fulfilling (4.18), the normal and the tangential stress contributions have to be equal to zero leading to the weak form

$$G_l^c = \int_{\gamma_c} \left(\delta\lambda_{Nn+1} \frac{1}{c_N} \lambda_{Nn+1} + \delta\boldsymbol{\lambda}_{Tn+1} \cdot \frac{1}{c_T} \boldsymbol{\lambda}_{Tn+1} \right) da = 0. \quad (4.26)$$

In the next section, two classical discretization techniques will be presented. The node to surface formulation is based on a strong coupling of the contact constraints and regularized with the penalty method. In the Mortar method, the two bodies are coupled in a weak sense and all three solution methods and also a mixed version are presented where the focus lies on the implementation of these methods into a finite element code.

4.2 Node to surface

The steps within the node to surface formulation are to determine for each slave node its status and to set up the residual vector and the tangent matrix for that node. The coupling between both surfaces is performed over a projection of the slave node onto the parametrized master surface

$$\mathbf{x}_{n+1}^2(\xi_{n+1}^\alpha) = \sum_{I=1}^{n^2} N_I(\xi_{n+1}^\alpha) \mathbf{x}_{n+1}^2 \quad (4.27)$$

where usually linear shape functions are used. For each slave node a contact element is derived consisting of one slave and four master nodes (see figure 4.1). The contact

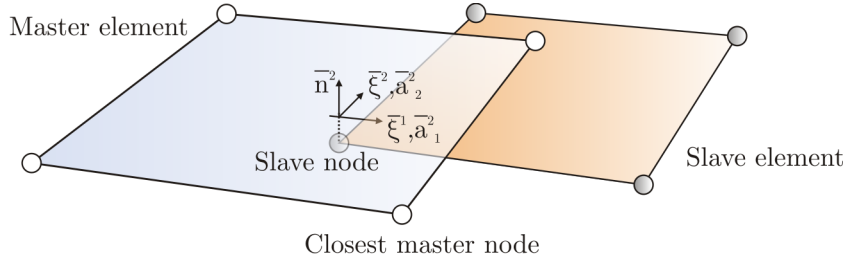


Figure 4.1: Node to segment contact element

vectors formulating the residual is then a subset of \mathbb{R}^{15} and the tangent matrix is a subset of $\mathbb{R}^{15 \times 15}$. The search algorithm assigns to each contact element the five global node numbers. Here it is assumed that the two contacting bodies are already known. An overview of search algorithms for the case of contact between more than two bodies, see Wriggers [2006].

4.2.1 Global search of contact elements

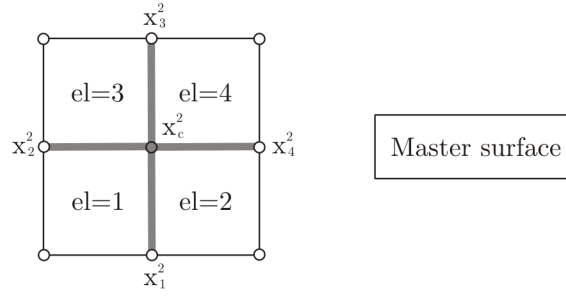
The first step is to find for each slave node s the closest master node computing the distance between the slave and all master nodes n_m . The minimal distance yields then the closest master node \mathbf{x}_c^2

$$\mathbf{x}_{cn+1}^2 : \quad \|\mathbf{x}_{sn+1}^1 - \mathbf{x}_{jn+1}^2\| = \min, \quad j = 1, \dots, n^m. \quad (4.28)$$

Afterwards, the corresponding master element of the slave node s can be determined using the scalar product of the four edges adjacent to the closest master node ($a = 1, \dots, 4$)

$$d_a = (\mathbf{x}_{an+1}^2 - \mathbf{x}_{cn+1}^2) \cdot (\mathbf{x}_{sn+1}^1 - \mathbf{x}_{cn+1}^2), \quad (4.29)$$

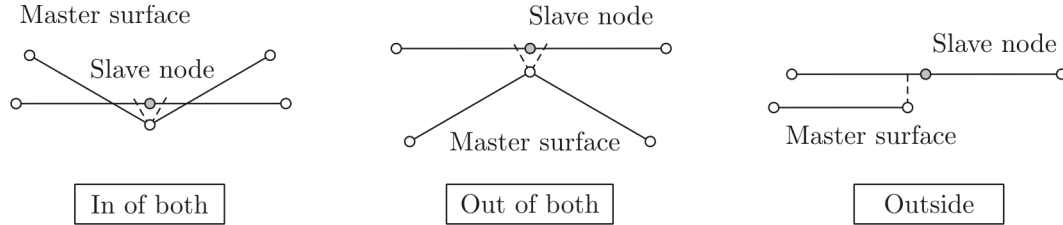
see also figure 4.2. Depending on the sign of each scalar product d_a , the corresponding master element can be assigned to each slave node (table 4.2). Since the finite element mesh is generally not smooth, cases evolve where a unique master element can not be found. For mathematical investigations regarding the uniqueness of the projection algorithm, see Curnier et al. [1995]. Three different so called pathological cases have

**Figure 4.2:** Node to segment master patch

el = 1	$d_1 \geq 0 \cap d_2 \geq 0 \cap d_3 < 0 \cap d_4 < 0$
el = 2	$d_1 \geq 0 \cap d_2 < 0 \cap d_3 < 0 \cap d_4 \geq 0$
el = 3	$d_1 < 0 \cap d_2 \geq 0 \cap d_3 \geq 0 \cap d_4 < 0$
el = 4	$d_1 < 0 \cap d_2 < 0 \cap d_3 \geq 0 \cap d_4 \geq 0$

Table 4.2: Assignment of master element: istgt = 1

to be taken into account namely: (i) inside (type = i) if more than one master element can be addressed to the slave node or (ii) outside (type = o) if no master element can be assigned to the slave node or (iii) if the slave node lies completely outside of the master surface (type = -1). Figure 4.3 shows the three types of pathological cases for

**Figure 4.3:** Pathological cases for the node to segment formulation: Graphical illustration for the 2 D case

the 2D case which can be extended straightforward to the 3D case where it has also to be distinguished between inside/outside of two elements or inside/outside of all four elements. In the first case, the slave node is placed onto the corresponding master edge (table 4.3) and the master element can be chosen as one of the two elements. In the second case, the slave node is placed directly onto the closest master node (table 4.4) and the master element is one of the four possible elements. Close to the boundary of the master element, sometimes it is not possible to specify all four distances d_a . Within such cases the missing distance is set to 1 and if the assigned master element does not exist the projection point lies outside of the domain. The slave node is then per definition inactive and labeled with the status type = -1.

ed = 1/2	$d_1 \geq 0 \cap d_2 < 0 \cap d_3 < 0 \cap d_4 < 0$	type = o
ed = 1/2	$d_1 \geq 0 \cap d_2 \geq 0 \cap d_3 < 0 \cap d_4 \geq 0$	type = i
el = 2/3	$d_1 < 0 \cap d_2 \geq 0 \cap d_3 < 0 \cap d_4 < 0$	type = o
el = 2/3	$d_1 \geq 0 \cap d_2 \geq 0 \cap d_3 \geq 0 \cap d_4 < 0$	type = i
ed = 3/4	$d_1 < 0 \cap d_2 < 0 \cap d_3 \geq 0 \cap d_4 < 0$	type = o
ed = 3/4	$d_1 < 0 \cap d_2 \geq 0 \cap d_3 \geq 0 \cap d_4 \geq 0$	type = i
el = 4/1	$d_1 < 0 \cap d_2 < 0 \cap d_3 < 0 \cap d_4 \geq 0$	type = o
el = 4/1	$d_1 \geq 0 \cap d_2 < 0 \cap d_3 \geq 0 \cap d_4 \geq 0$	type = i

Table 4.3: Assignment of master edge: istgt = 2

el = 1	$d_1 < 0 \cap d_2 < 0 \cap d_3 < 0 \cap d_4 < 0$	type = o
el = 2	$d_1 \geq 0 \cap d_2 \geq 0 \cap d_3 \geq 0 \cap d_4 \geq 0$	type = i

Table 4.4: Assignment of master node: istgt = 3

Another possibility is to use a tolerance δ within the assignment of the master element (table 4.2). Then no pathological cases, like inside or outside, exist and projection points with local coordinates larger than 1 are allowed within the computation. The tolerance depends then on the smoothness of the surface and for a very uneven mesh a large tolerance is needed.

4.2.2 Projection point and base vectors

After the contact element is specified, the slave node has to be projected onto the master element. The algorithm is thereby based on computing the minimal distance of the slave node $\mathbf{x}_{s n+1}^1$ onto the master element. The projected master point $\bar{\mathbf{x}}_{n+1}^2$ has to fulfill

$$[\mathbf{x}_{s n+1}^1 - \bar{\mathbf{x}}_{n+1}^2] \cdot \bar{\mathbf{a}}_{\alpha n+1}^2 = \left[\mathbf{x}_{s n+1}^1 - \sum_{I=1}^n N_I \left(\bar{\xi}_{n+1}^\beta \right) \mathbf{x}_{I n+1}^2 \right] \cdot \sum_{I=1}^n N_{, \alpha} \left(\bar{\xi}_{n+1}^\beta \right) \mathbf{x}_{I n+1}^2 = 0. \quad (4.30)$$

Quantities of the master surface with a bar indicate the desired value at the projection point. For the solution of the nonlinear equation, the Newton iteration is applied. With

the start value $\bar{\xi}_0^\beta = 0$, the equation

$$\left[\bar{\mathbf{a}}_{\alpha n+1}^{2(i)} \cdot \bar{\mathbf{a}}_{\beta n+1}^{2(i)} - \left(\mathbf{x}_{s n+1}^{1(i)} - \bar{\mathbf{x}}_{n+1}^{2(i)} \right) \cdot \bar{\mathbf{a}}_{\alpha, \beta n+1}^{2(i)} \right] \Delta \bar{\xi}_{i+1}^\beta = - \left[\mathbf{x}_{s n+1}^{1(i)} - \bar{\mathbf{x}}_{n+1}^{2(i)} \right] \cdot \bar{\mathbf{a}}_{\alpha n+1}^{2(i)} \quad (4.31)$$

is solved at each step i and the projected local coordinate is updated $\bar{\xi}_{i+1}^\beta = \bar{\xi}_i^\beta + \Delta \bar{\xi}_{i+1}^\beta$. The Newton loop ends, if the incremental local coordinate is lower than a given tolerance δ . For the incremental tangential movement defined in the next section, the projection point of the slave node at the old time step $\mathbf{x}_{s n}^1$ onto the actual master element has also to be determined in the same way as in (4.30) and (4.31)

$$\left[\tilde{\mathbf{a}}_{\alpha n+1}^{2(i)} \cdot \tilde{\mathbf{a}}_{\beta n+1}^{2(i)} - \left(\mathbf{x}_{s n}^{1(i)} - \tilde{\mathbf{x}}_{n+1}^{2(i)} \right) \cdot \tilde{\mathbf{a}}_{\alpha, \beta n+1}^{2(i)} \right] \Delta \bar{\xi}_{i+1}^\beta = - \left[\mathbf{x}_{s n}^{1(i)} - \tilde{\mathbf{x}}_{n+1}^{2(i)} \right] \cdot \tilde{\mathbf{a}}_{\alpha n+1}^{2(i)}. \quad (4.32)$$

The tilde over the quantities indicates the corresponding quantity at the old local projection point. The actual base vectors at the projection point are obtained directly via the algorithm described in (4.30) and (4.31). The normalized normal vector $\bar{\mathbf{n}}_{n+1}^2$ is determined using the cross product of the two base vectors

$$\bar{\mathbf{n}}_{n+1}^2 = \frac{\bar{\mathbf{a}}_{1 n+1}^2 \times \bar{\mathbf{a}}_{2 n+1}^2}{\|\bar{\mathbf{a}}_{1 n+1}^2 \times \bar{\mathbf{a}}_{2 n+1}^2\|}. \quad (4.33)$$

An alternative algorithm is based on the cross product of the distance and the normal at the projected point

$$\left[\mathbf{x}_{s n+1}^1 - \sum_{I=1}^n N_I \left(\bar{\xi}_{n+1}^\beta \right) \mathbf{x}_{I n+1}^2 \right] \times \sum_{I=1}^n N_I \left(\bar{\xi}_{n+1}^\beta \right) \mathbf{n}_{I n+1}^2 = 0 \quad (4.34)$$

which has to be zero. This algorithm is more advantageous in the case of averaged base vectors (as used in the Mortar method 4.3), since averaged tangential base vectors are hard to determine at corners of the body. Alternative ways of smoothing the master surface in the node to surface framework can be found in Wriggers [2006] or Laursen [2006].

4.2.3 Contact kinematical relations

The normal penetration for the node to surface formulation corresponds to

$$\bar{g}_{N n+1} = \left(\mathbf{x}_{s n+1}^1 - \bar{\mathbf{x}}_{n+1}^2 \right) \cdot \bar{\mathbf{n}}_{n+1}^2. \quad (4.35)$$

Following Wriggers and Miehe [1992] and Wriggers and Miehe [1994], the tangential movement can be specified as the rate of the local projection point in the direction of the tangential base vectors at that point

$$\dot{\bar{\mathbf{g}}}_{T n+1} = \dot{\bar{\xi}}_{n+1}^\alpha \bar{\mathbf{a}}_{\alpha n+1}^2. \quad (4.36)$$

This description has the advantage of being an objective measure of the sliding distance, see Laursen [2006]. For instance in Rieger [2002] and Wriggers [2006] (remark 4.3), it is shown that (4.36) is equal to the Lie derivative of the tangential gap

$$\dot{\bar{\mathbf{g}}}_{T n+1} = \mathbf{F}_{T n+1} \overline{\mathbf{F}_{T n+1}^{-1} \dot{\bar{\xi}}_{n+1}^\alpha \bar{\mathbf{a}}_{\alpha n+1}^2} = \dot{\bar{\xi}}_{n+1}^\alpha \bar{\mathbf{a}}_{\alpha n+1}^2, \quad \mathbf{F}_{T n+1} = \bar{\mathbf{a}}_{\alpha n+1}^2 \otimes \bar{\mathbf{A}}_{n+1}^{2\alpha} \quad (4.37)$$

which is a priori objective. The rate of the local projection point in (4.36) follows by the time derivative of (4.30)

$$\dot{\bar{\xi}}_{n+1}^{\alpha} = \bar{H}_{n+1}^{\alpha\beta} [(\mathbf{v}_{s n+1}^1 - \bar{\mathbf{v}}_{n+1}^2) \cdot \bar{\mathbf{a}}_{\alpha n+1}^2 + \bar{g}_{N n+1} \mathbf{v}_{,\beta n+1}^2 \cdot \mathbf{n}_{n+1}^2]. \quad (4.38)$$

The contact metric, the curvature components and also the auxiliary variable $\bar{H}_{\alpha\beta}$ used in (4.38) are defined as

$$\begin{aligned} \bar{H}_{\alpha\beta n+1} &= \bar{a}_{\alpha\beta n+1} - \bar{g}_{N n+1} \bar{b}_{\alpha\beta n+1} \\ \bar{a}_{\alpha\beta n+1} &= \bar{\mathbf{a}}_{\alpha n+1}^2 \cdot \bar{\mathbf{a}}_{\beta n+1}^2, \quad \bar{b}_{\alpha\beta n+1} = \bar{\mathbf{a}}_{\alpha,\beta n+1}^2 \cdot \bar{\mathbf{n}}_{n+1}^2. \end{aligned} \quad (4.39)$$

Integrating (4.36) with the implicit backward Euler scheme, the tangential movement of the slave node on the master surface can be specified in its incremental form

$$\Delta_t \bar{\mathbf{g}}_{T n+1} = \bar{\mathbf{g}}_{T n+1} - \bar{\mathbf{g}}_{T n} = (\bar{\xi}_{n+1}^{\alpha} - \bar{\xi}_n^{\alpha}) \bar{\mathbf{a}}_{\alpha n+1}^2 = \Delta_t \bar{\xi}_{n+1}^{\alpha} \bar{\mathbf{a}}_{\alpha n+1}^2. \quad (4.40)$$

In the literature different explanations and different definitions of the tangential movement are used for the description of the stick-slip behavior. One alternative is based on the total amount of the slip $\bar{\mathbf{g}}_{T n+1}$ together with the normalized slip direction $\bar{\mathbf{e}}_{T n+1}$

$$\bar{\mathbf{s}}_{T n+1} = \bar{\mathbf{g}}_{T n+1} \bar{\mathbf{e}}_{T n+1}. \quad (4.41)$$

The total amount can be computed by an integration along the slip path

$$\bar{\mathbf{g}}_{T n+1} = \int_{t_0}^t \|\dot{\bar{\xi}}_{n+1}^{\alpha} \bar{\mathbf{a}}_{\alpha n+1}^2\| dt = \int_{t_0}^t \sqrt{\dot{\bar{\xi}}_{n+1}^{\alpha} \dot{\bar{\xi}}_{n+1}^{\beta} \bar{a}_{\alpha\beta n+1}} dt \quad (4.42)$$

which is used for instance in de Saracibar [1997] where the slip amount is computed independently of the underlying mesh. For the 2D case, the integration can be computed directly in (4.42)

$$\begin{aligned} \bar{\mathbf{g}}_{T n+1} &= \int_{\xi_0}^{\xi} \sqrt{\bar{A}_{\xi\xi n+1}} d\xi = (\bar{\xi}_{n+1} - \bar{\xi}_n) \bar{L}_n \quad \text{or} \\ \bar{\mathbf{g}}_{T n+1} &= \int_{\xi_0}^{\xi} \sqrt{\bar{a}_{\xi\xi n+1}} d\xi = (\bar{\xi}_{n+1} - \bar{\xi}_n) \bar{L}_{n+1} \end{aligned} \quad (4.43)$$

where the former term is based on the reference configuration, see Wriggers et al. [1990], and the latter term is based on the current configuration, see Zavarise and Taylor [1996]. For the 2D case, the expressions (4.40) and (4.43 b) are equal. Additionally, in Tur et al. [2009] the incremental movement is expressed in terms of the incremental position vector multiplied with the normalized base vector.

4.2.4 Integration domain

The integration domain of one slave node is assembled by the surface contributions of the four adjacent slave elements (cf. figure 4.4). The computation of the area of one

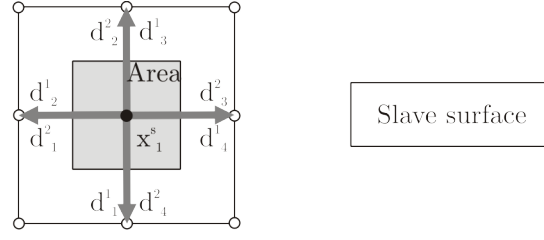


Figure 4.4: Integration domain of one slave node

slave element is based on the distance vectors of the slave node to the adjacent nodes of each element e

$$\mathbf{d}_{en+1}^1 = \mathbf{x}_{1en+1}^1 - \mathbf{x}_{sn+1}^1, \quad \mathbf{d}_{en+1}^2 = \mathbf{x}_{2en+1}^1 - \mathbf{x}_{sn+1}^1. \quad (4.44)$$

The whole area is the sum of the four contributions of each element determined by the cross product of the distance vectors

$$a_{sn+1} = \sum_{e=1}^4 \frac{1}{4} \sqrt{\mathbf{d}_{en+1}^1 \times \mathbf{d}_{en+1}^2}. \quad (4.45)$$

Alternatively, the computation of the integration domain can be related to the initial configuration

$$\mathbf{d}_{en+1}^1 = \mathbf{X}_{1e}^1 - \mathbf{X}_s^1, \quad \mathbf{d}_{en+1}^2 = \mathbf{X}_{2e}^1 - \mathbf{X}_s^1 \quad (4.46)$$

which simplifies the linearization and the assembling process and hence will be used in the following examples.

4.2.5 Linearized quantities

Most of the quantities depend on the actual time step and hence in the next sections the subscripts $n + 1$ will be neglected. Exceptions will be declared if necessary. The linearization of the projection point follows analogue to its time derivative (4.38)

$$\Delta \bar{\xi}^\beta = \bar{H}^{\alpha\beta} [(\Delta \mathbf{u}_s^1 - \Delta \bar{\mathbf{u}}^2) \cdot \bar{\mathbf{a}}_\alpha^2 + \bar{g}_N \bar{\mathbf{n}}^2 \cdot \Delta \bar{\mathbf{u}}_{,\alpha}^2]. \quad (4.47)$$

The projection point $\bar{\xi}_n^\beta$ has also to be linearized since the only fixed value is the slave node position vector at the old time step

$$\Delta \bar{\xi}_n^\beta = \tilde{H}^{\alpha\beta} [(-\Delta \bar{\mathbf{u}}^2) \cdot \tilde{\mathbf{a}}_\alpha^2 + \tilde{g}_N \tilde{\mathbf{n}}^2 \cdot \Delta \tilde{\mathbf{u}}_{,\alpha}^2]. \quad (4.48)$$

At the projection point, the gap between the slave node and the master surface is parallel to the normal vector and the linearization of the normal gap simplifies to

$$\Delta \bar{g}_N = (\Delta \mathbf{u}_s^1 - \Delta \bar{\mathbf{u}}^2) \cdot \bar{\mathbf{n}}^2. \quad (4.49)$$

Since the Gateaux differential is used for the linearization, the time derivative and the variation, all variations corresponds to its linearized quantities

$$\begin{aligned} \delta \bar{g}_N &= (\boldsymbol{\eta}_s^1 - \bar{\boldsymbol{\eta}}^2) \cdot \bar{\mathbf{n}}^2 \\ \delta \bar{\xi}^\beta &= \bar{H}^{\alpha\beta} [(\boldsymbol{\eta}_s^1 - \bar{\boldsymbol{\eta}}^2) \cdot \bar{\mathbf{a}}_\alpha^2 + \bar{g}_N \bar{\mathbf{n}}^1 \cdot \bar{\boldsymbol{\eta}}_{,\alpha}^2] \end{aligned} \quad (4.50)$$

and the linearization of the former variation leads to

$$\begin{aligned} \Delta \delta \bar{g}_N = & -\bar{\eta}_{,\alpha}^2 \cdot \bar{\mathbf{n}}^1 \Delta \bar{\xi}^\alpha - \delta \bar{\xi}^\alpha \Delta \bar{\mathbf{u}}_{,\alpha}^2 \cdot \bar{\mathbf{n}}^1 - \bar{b}_{\alpha\beta} \delta \bar{\xi}^\alpha \Delta \bar{\xi}^\beta + \bar{g}_N \bar{a}^{\alpha\beta} \bar{\eta}_{,\alpha}^2 \cdot \bar{\mathbf{n}}^2 \bar{\eta}_{,\beta}^2 \cdot \bar{\mathbf{n}}^2 \\ & + \bar{g}_N \bar{a}^{\alpha\gamma} \bar{b}_{\alpha\beta} \delta \bar{\xi}^\beta \Delta \bar{\mathbf{u}}_{,\gamma}^2 \cdot \bar{\mathbf{n}}^2 + \bar{g}_N \bar{a}^{\alpha\gamma} \bar{b}_{\gamma\beta} \bar{\eta}_{,\alpha}^2 \cdot \bar{\mathbf{n}}^2 \Delta \bar{\xi}^\beta + \bar{g}_N \bar{a}^{\alpha\gamma} \bar{b}_{\alpha\beta} \bar{b}_{\gamma\delta} \delta \bar{\xi}^\beta \Delta \bar{\xi}^\delta \end{aligned} \quad (4.51)$$

and of the latter one reads

$$\begin{aligned} \Delta \delta \bar{\xi}^\alpha = & \bar{H}^{\alpha\beta} \left[-\bar{\eta}_{,\gamma}^2 \cdot \bar{\mathbf{a}}_\beta^2 \Delta \bar{\xi}^\gamma - \Delta \bar{\mathbf{u}}_{,\gamma}^2 \cdot \bar{\mathbf{a}}_\beta^2 \delta \bar{\xi}^\gamma - (\bar{\mathbf{a}}_{\gamma,\delta}^2 \cdot \bar{\mathbf{a}}_\beta^2 - \bar{g}_N \bar{\mathbf{n}}^2 \cdot \bar{\mathbf{a}}_{\beta,\gamma\delta}^2) \delta \bar{\xi}^\gamma \Delta \bar{\xi}^\delta \right. \\ & - \delta \bar{\xi}^\gamma \bar{\mathbf{a}}_\gamma^2 \cdot (\Delta \bar{\mathbf{u}}_{,\beta}^2 + \bar{\mathbf{a}}_{\beta,\delta}^2 \Delta \bar{\xi}^\delta) - \Delta \bar{\xi}^\gamma \bar{\mathbf{a}}_\gamma^2 \cdot (\bar{\eta}_{,\beta}^2 + \bar{\mathbf{a}}_{\beta,\delta}^2 \delta \bar{\xi}^\delta) \\ & - \bar{g}_N \bar{\mathbf{n}}^2 \cdot (\delta \bar{\xi}^\gamma \Delta \bar{\mathbf{u}}_{,\beta\gamma}^2 + \bar{\eta}_{,\beta\gamma}^2 \Delta \bar{\xi}^\gamma) + (\bar{\eta}^1 - \bar{\eta}^2) \cdot (\Delta \bar{\mathbf{u}}_{,\beta}^2 + \bar{\mathbf{a}}_{\beta,\gamma}^2 \Delta \bar{\xi}^\gamma) \\ & \left. + (\Delta \bar{\mathbf{u}}_s^1 - \Delta \bar{\mathbf{u}}^2) \cdot (\bar{\eta}_{,\beta}^2 + \bar{\mathbf{a}}_{\beta,\gamma}^2 \delta \bar{\xi}^\gamma) \right]. \end{aligned} \quad (4.52)$$

Using the covariant unity tensor of the master surface localized at the projection point $\mathbf{g} = \bar{\mathbf{n}}^2 \otimes \bar{\mathbf{n}}^2 + \bar{a}^{\alpha\beta} \bar{\mathbf{a}}_\alpha^2 \otimes \bar{\mathbf{a}}_\beta^2$, the linearization changes to

$$\begin{aligned} \Delta \delta \bar{\xi}^\alpha = & \bar{H}^{\alpha\beta} \left[-\bar{\eta}_{,\gamma}^2 \cdot \bar{\mathbf{a}}_\beta^2 \Delta \bar{\xi}^\gamma - \Delta \bar{\mathbf{u}}_{,\gamma}^2 \cdot \bar{\mathbf{a}}_\beta^2 \delta \bar{\xi}^\gamma - (\bar{\mathbf{a}}_{\gamma,\delta}^2 \cdot \bar{\mathbf{a}}_\beta^2 - \bar{g}_N \bar{\mathbf{n}}^2 \cdot \bar{\mathbf{a}}_{\beta,\gamma\delta}^2) \delta \bar{\xi}^\gamma \Delta \bar{\xi}^\delta \right. \\ & - \delta \bar{\xi}^\gamma \bar{\mathbf{a}}_\gamma^2 \cdot (\Delta \bar{\mathbf{u}}_{,\beta}^2 + \bar{\mathbf{a}}_{\beta,\delta}^2 \Delta \bar{\xi}^\delta) - \Delta \bar{\xi}^\gamma \bar{\mathbf{a}}_\gamma^2 \cdot (\bar{\eta}_{,\beta}^2 + \bar{\mathbf{a}}_{\beta,\delta}^2 \delta \bar{\xi}^\delta) \\ & - \bar{g}_N \bar{\mathbf{n}}^2 \cdot (\delta \bar{\xi}^\gamma \Delta \bar{\mathbf{u}}_{,\beta\gamma}^2 + \bar{\eta}_{,\beta\gamma}^2 \Delta \bar{\xi}^\gamma) + (\bar{\eta}_s^1 - \bar{\eta}^2) \cdot \bar{\mathbf{n}}^2 (\Delta \bar{\mathbf{u}}_{,\beta}^2 + \bar{\mathbf{a}}_{\beta,\gamma}^2 \Delta \bar{\xi}^\gamma) \cdot \bar{\mathbf{n}}^2 \\ & + (\Delta \bar{\mathbf{u}}_s^1 - \Delta \bar{\mathbf{u}}^2) \cdot \bar{\mathbf{n}}^2 (\bar{\eta}_{,\beta}^2 + \bar{\mathbf{a}}_{\beta,\gamma}^2 \delta \bar{\xi}^\gamma) \cdot \bar{\mathbf{n}}^2 + \bar{a}^{\delta\epsilon} (\bar{\eta}_s^1 - \bar{\eta}^2) \cdot \bar{\mathbf{a}}_\delta^2 (\Delta \bar{\mathbf{u}}_{,\beta}^2 + \bar{\mathbf{a}}_{\beta,\gamma}^2 \Delta \bar{\xi}^\gamma) \cdot \bar{\mathbf{a}}_\epsilon^2 \\ & \left. + \bar{a}^{\delta\epsilon} (\Delta \bar{\mathbf{u}}_s^1 - \Delta \bar{\mathbf{u}}^2) \cdot \bar{\mathbf{a}}_\delta^2 (\bar{\eta}_{,\beta}^2 + \bar{\mathbf{a}}_{\beta,\gamma}^2 \delta \bar{\xi}^\gamma) \cdot \bar{\mathbf{a}}_\epsilon^2 \right]. \end{aligned} \quad (4.53)$$

A detailed conduction of the linearization of all contact quantities can be found for instance in Rieger [2002] or Wriggers [2006].

4.2.6 Residual vector and tangent matrix

Only for active nodes the nodal contact residual vector and the tangent matrix will be computed and assembled to the global stiffness matrix. For the penalty method, (4.15) is replaced by an active set search for each slave node

$$\begin{aligned} \bar{g}_N \leq \delta \cap \text{type} & \neq -1 \quad \rightarrow \text{node active} \\ \bar{g}_N > \delta \cup \text{type} & = -1 \quad \rightarrow \text{node inactive} \end{aligned} \quad (4.54)$$

where the tolerance δ is used to avoid that nodes which are slightly positive are not taken into account. The weak form can be derived from (4.16) by using instead of the tangential movement (4.36) its variation

$$G_c^h = \delta \bar{g}_N \bar{\mathbf{t}}_N \bar{a}_s - \delta \bar{\xi}^\alpha \bar{\mathbf{t}}_{T\alpha} \bar{a}_s. \quad (4.55)$$

Rieger [2002] and Laursen and Simo [1993] show that the weak form can be obtained directly from the reduced continuum form (2.87) by using the variation (instead of the time derivative) of the local projection point (4.38) on the real contact plane ($\bar{g}_N = 0$). For the normal stress component

$$\bar{t}_N = c_N \bar{g}_N, \quad (4.56)$$

the standard penalty regularization is used. The determination of the tangential stress components

$$\bar{t}_{T\alpha} = -c_T \left[\bar{a}_{\alpha\beta} \Delta_t \bar{\xi}^\alpha + \Delta_t \gamma \frac{\bar{t}_{T\alpha}}{\|\bar{\mathbf{t}}_T\|} \right] + \bar{t}_{T\alpha n}, \quad \|\bar{\mathbf{t}}_T\| = \sqrt{\bar{t}_{T\alpha} \bar{t}_{T\beta} \bar{a}^{\alpha\beta}} \quad (4.57)$$

follows by an implicit return mapping algorithm developed in Simo and Taylor [1985] and adapted for contact computations in Wriggers [1987] and Giannakopoulos [1989] where $\bar{t}_{t\alpha n}$ corresponds to the stress component at the old time step. Defining the trial tangential stress components

$$\bar{t}_{T\alpha}^{tr} = -c_T \bar{a}_{\alpha\beta} \Delta_t \bar{\xi}^\beta + \bar{t}_{T\alpha n}, \quad (4.58)$$

the real stress can be computed depending on the trial state of the slip criterion

$$\begin{aligned} \text{stick : } \bar{t}_{T\alpha} &= -c_T \bar{a}_{\alpha\beta} \Delta_t \bar{\xi}_{n+1}^\beta + \bar{t}_{T\alpha n} & \text{if } \frac{f(\bar{\mathbf{t}}_T^{tr})}{c_T} \leq \delta \\ \text{slip : } \bar{t}_{T\alpha} &= \mu |\bar{t}_N| \frac{\bar{t}_{T\alpha}^{tr}}{\|\bar{\mathbf{t}}_T^{tr}\|} & \text{if } \frac{f(\bar{\mathbf{t}}_T^{tr})}{c_T} > \delta \end{aligned} \quad (4.59)$$

where a tolerance δ is also used to guarantee a stick state at the beginning of each time step. The Coulomb slip criterion is used for the computations within this chapter written in terms of the trial stress as

$$f(\bar{\mathbf{t}}_T^{tr}) = \|\bar{\mathbf{t}}_T^{tr}\| - \mu |\bar{t}_N|. \quad (4.60)$$

Using friction laws which are nonlinear with respect to $\|\bar{\mathbf{t}}_T\|$, a Newton iteration has to be applied to determine the stress components (see for instance Haraldsson [2003] for soil structure interactions or Weißenfels and Wriggers [2010] for mechanical and electrical wear investigations). The residual vector can be split into a normal and a tangential part

$$\mathbf{R}_N^s = -\bar{t}_N \bar{a}_s \mathbf{N}_s, \quad \mathbf{R}_T^s = \bar{t}_{T\alpha} \bar{a}_s \mathbf{D}_s^\alpha \quad (4.61)$$

where all the contact stiffness vectors like $\mathbf{N}_s, \mathbf{D}_s$ are specified explicitly in the appendix C.1. The linearized weak form can be subdivided into four terms

$$\Delta G_c^h = c_N \Delta \bar{g}_N \delta \bar{g}_N \bar{a}_s + \bar{t}_N \Delta \delta \bar{g}_N \bar{a}_s - \Delta \bar{t}_{T\alpha} \delta \bar{\xi}^\alpha \bar{a}_s - \bar{t}_{T\alpha} \Delta \delta \bar{\xi}^\alpha \bar{a}_s. \quad (4.62)$$

The first one indicates the material or linear part of the normal penetration

$$\mathbf{K}_{Nm}^s = c_N \bar{a}_s \mathbf{N}_s \mathbf{N}_s^T \quad (4.63)$$

and the second one the nonlinear or geometrical normal term

$$\begin{aligned} \mathbf{K}_{Ng}^s = & -c_N \bar{g}_N \bar{a}_s \left\{ \mathbf{N}_\alpha \mathbf{D}^{\alpha T} + \mathbf{D}^\alpha \mathbf{N}_\alpha^T + \bar{b}_{\alpha\beta} \mathbf{D}^\alpha \mathbf{D}^{\beta T} \right. \\ & \left. - \bar{g}_N \bar{a}^{\alpha\gamma} \left[\mathbf{N}_\alpha \mathbf{N}_\gamma^T + \bar{b}_{\alpha\beta} \mathbf{D}^\beta \mathbf{N}_\gamma^T + \bar{b}_{\gamma\delta} \mathbf{N}_\alpha \mathbf{D}^{\delta T} + \bar{b}_{\alpha\beta} \bar{b}_{\gamma\delta} \mathbf{D}^\beta \mathbf{D}^{\delta T} \right] \right\}. \end{aligned} \quad (4.64)$$

For the material part of the tangential contact formulation, the tangent stress components have to be linearized. For the case of stick

$$\begin{aligned} \Delta \bar{t}_{T\alpha} = \Delta \bar{t}_{T\alpha}^{tr} = & -c_T \bar{a}_{\alpha\beta} \left(\Delta \bar{\xi}^\beta - \Delta \bar{\xi}_n^\beta \right) - c_T \bar{a}_{\alpha\beta} \Delta_t \bar{\xi}^\beta \left[\Delta \bar{\mathbf{u}}_{,\alpha}^2 \cdot \bar{\mathbf{a}}_\beta^2 \right. \\ & \left. + \bar{\mathbf{a}}_{\alpha,\gamma}^1 \cdot \bar{\mathbf{a}}_\beta^2 \Delta \bar{\xi}^\gamma + \Delta \bar{\mathbf{u}}_{,\beta}^2 \cdot \bar{\mathbf{a}}_\alpha^2 + \bar{\mathbf{a}}_{\beta,\gamma}^2 \cdot \bar{\mathbf{a}}_\alpha^2 \Delta \bar{\xi}^\gamma \right], \end{aligned} \quad (4.65)$$

the discretized linearization leads to the desired tangent in vector form

$$\begin{aligned} \mathbf{K}_{Tm}^s = & c_T \bar{a}_{\alpha\beta} \bar{a}_s \mathbf{D}^\alpha \mathbf{D}^{\beta T} - c_T \bar{a}_{\alpha\beta} \bar{a}_s \mathbf{D}^\alpha \tilde{\mathbf{D}}^{\beta T} + c_T \Delta_t \bar{\xi}^\beta \bar{a}_s \left[\mathbf{D}^\alpha \mathbf{T}_{\beta\alpha}^T \right. \\ & \left. + \mathbf{D}^\alpha \mathbf{T}_{\alpha\beta}^T + (\bar{\mathbf{a}}_{\alpha,\gamma}^2 \cdot \bar{\mathbf{a}}_\beta^2 + \bar{\mathbf{a}}_{\beta,\gamma}^2 \cdot \bar{\mathbf{a}}_\alpha^2) \mathbf{D}^\alpha \mathbf{D}^{\gamma T} \right] \end{aligned} \quad (4.66)$$

where the vector $\tilde{\mathbf{D}}^\alpha$ is due to (4.48) and is based on the modified vector \mathbf{D}^α in (C.2). If the slave node slips along the master surface, the linearization of the tangential stress components reads

$$\begin{aligned} \Delta \bar{t}_{T\alpha} = & \mu \text{sign}(\bar{t}_N) c_N (\Delta \bar{\mathbf{u}}_s^1 - \Delta \bar{\mathbf{u}}_s^2) \cdot \bar{\mathbf{n}}^2 \frac{\bar{t}_{T\alpha}^{tr}}{\|\bar{\mathbf{t}}_T^{tr}\|} + \mu |\bar{t}_N| \frac{\Delta \bar{t}_{T\alpha}^{tr}}{\|\bar{\mathbf{t}}_T^{tr}\|} \\ & - \mu |\bar{t}_N| \frac{\bar{t}_{T\alpha}^{tr}}{\|\bar{\mathbf{t}}_T^{tr}\|^3} (\Delta \bar{t}_{T\beta}^{tr} \bar{t}_{T\gamma}^{tr} \bar{a}^{\beta\gamma} - \bar{t}_{T\beta}^{tr} \bar{t}_{T\gamma}^{tr} \bar{a}^{\beta\delta} \bar{a}^{\epsilon\gamma} \Delta \bar{\mathbf{a}}_\delta^2 \cdot \bar{\mathbf{a}}_\epsilon) \end{aligned} \quad (4.67)$$

and additionally, the contribution to the tangent has to be adjusted

$$\begin{aligned} \mathbf{K}_{Tm}^S = & -\mu \text{sign}(\bar{t}_N) c_N \bar{a}_s \frac{\bar{t}_{T\alpha}^{tr}}{\|\bar{\mathbf{t}}_T^{tr}\|} \mathbf{D}^\alpha \mathbf{N}^T \\ & + \mu |\bar{t}_N| \bar{a}_s \frac{c_T}{\|\bar{\mathbf{t}}_T^{tr}\|} \left(\delta_\alpha^\beta - \frac{\bar{t}_{T\alpha}^{tr} \bar{t}_{T\gamma}^{tr} \bar{a}^{\beta\gamma}}{\|\bar{\mathbf{t}}_T^{tr}\|^3} \right) \left\{ \bar{a}_{\beta\delta} \mathbf{D}^\alpha \mathbf{D}^{\delta T} - \bar{a}_{\beta\delta} \mathbf{D}^\alpha \tilde{\mathbf{D}}^{\delta T} \right. \\ & \left. + \Delta_t \bar{\xi}^\delta \left[\mathbf{D}^\alpha \mathbf{T}_{\delta\beta}^T + \mathbf{D}^\alpha \mathbf{T}_{\beta\delta}^T + (\bar{\mathbf{a}}_{\beta,\epsilon}^2 \cdot \bar{\mathbf{a}}_\delta^2 + \bar{\mathbf{a}}_{\delta,\epsilon}^2 \cdot \bar{\mathbf{a}}_\beta^2) \mathbf{D}^\alpha \mathbf{D}^{\epsilon T} \right] \right\} \\ & - \mu |\bar{t}_N| \bar{a}_s \frac{\bar{t}_{T\alpha}^{tr}}{\|\bar{\mathbf{t}}_T^{tr}\|^3} \bar{t}_{T\beta}^{tr} \bar{t}_{T\gamma}^{tr} \bar{a}^{\beta\delta} \bar{a}^{\epsilon\gamma} \mathbf{D}^\alpha \mathbf{T}_{\epsilon\delta}^T. \end{aligned} \quad (4.68)$$

The last part of the tangent matrix includes the contribution of $\Delta \delta \bar{\xi}^\alpha$

$$\begin{aligned} \mathbf{K}_{Tg}^s = & -\bar{t}_{T\alpha} \bar{a}_s \bar{H}^{\alpha\beta} \left[\mathbf{T}_{\beta\gamma} \mathbf{D}^{\gamma T} + \mathbf{D}^\gamma \mathbf{T}_{\beta\gamma}^T + \bar{\mathbf{a}}_{\gamma,\delta}^2 \cdot \bar{\mathbf{a}}_\beta^2 \mathbf{D}^\gamma \mathbf{D}^{\delta T} \right. \\ & + (\mathbf{T}_{\gamma\beta} + \bar{\mathbf{a}}_{\beta,\delta}^2 \cdot \bar{\mathbf{a}}_\gamma^2 \mathbf{D}^\delta) \mathbf{D}^{\gamma T} + \mathbf{D}^\gamma (\mathbf{T}_{\gamma\beta}^T + \bar{\mathbf{a}}_{\beta,\delta}^2 \cdot \bar{\mathbf{a}}_\gamma^2 \mathbf{D}^{\delta T}) \\ & + g_N (\mathbf{N}_{\beta\gamma} \mathbf{D}^{\gamma T} + \mathbf{D}^\gamma \mathbf{N}_{\beta\gamma}^T) - \mathbf{N} (\mathbf{N}_\beta^T + \bar{b}_{\beta\gamma} \mathbf{D}^{\gamma T}) \\ & - (\mathbf{N}_\beta + \bar{b}_{\beta\gamma} \mathbf{D}^\gamma) \mathbf{N}^T - \bar{a}^{\delta\epsilon} \mathbf{T}_\delta (\mathbf{T}_{\epsilon\beta}^T + \bar{\mathbf{a}}_{\beta,\gamma}^2 \cdot \bar{\mathbf{a}}_\epsilon^2 \mathbf{D}^{\gamma T}) \\ & \left. + \bar{a}^{\delta\epsilon} (\mathbf{T}_{\epsilon\beta} + \bar{\mathbf{a}}_{\beta,\gamma}^2 \cdot \bar{\mathbf{a}}_\epsilon^2 \mathbf{D}^\gamma) \mathbf{T}_\delta^T \right]. \end{aligned} \quad (4.69)$$

4.3 Mortar method

As for the node to surface formulation, the status and the assembling of the residual vector and the tangent matrix are also specified nodal wise, but now the kinematical contact quantities are averaged over the adjacent slave elements of the desired node. Therefore a segment to segment strategy is advantageous. To locate the quantities at the integration points, standard shape functions are used for the position vectors of each surface for example. Additionally, special shape functions M_B can be used for the Lagrange multipliers

$$\begin{aligned} \mathbf{x}_{n+1}^1 &= \sum_{B=1}^{n_s} N_B(\boldsymbol{\xi}_{n+1}^1) \mathbf{x}_{Bn+1}^1, & \mathbf{x}_{n+1}^2 &= \sum_{C=1}^{n_m} N_C(\boldsymbol{\xi}_{n+1}^2) \mathbf{x}_{Cn+1}^2 \\ \boldsymbol{\lambda}_{n+1} &= \sum_{B=1}^{n_s} M_B(\boldsymbol{\xi}^1) \boldsymbol{\lambda}_{Bn+1}. \end{aligned} \quad (4.70)$$

The elements adjacent to the slave node and all the master elements which overlap with these slave elements represent the whole contact element of this slave node. To simplify the assembling of the contact element, the tangent matrix and the residual vector of each pair consisting of one slave and one master element (see figure 4.5) is sent to the global assembler. Each residual vector is then a subset of \mathbb{R}^{24} and each tangent matrix of $\mathbb{R}^{24 \times 24}$, if no Lagrange multipliers are applied. The algorithm to determine

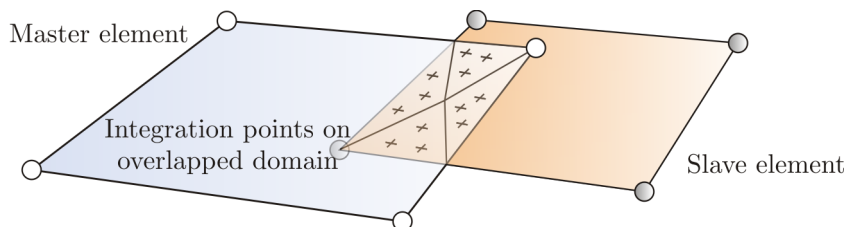


Figure 4.5: Mortar contact element

the overlap of the slave with each master element will be explained in the next sections. Each slave node is labeled with an A instead of a s which is common in Mortar works and hence will be continued in this work. In the literature, the slave and the master surface is also called non-Mortar and Mortar surface, respectively, which will not be used in the following statements.

4.3.1 Setup of contact element

The idea to use a segment to segment approach instead of a node to segment treatment was pursued the first time in the work of Simo et al. [1985]. El-Abbasi and Bathe [2001] shows that a segment to segment strategy where the integration points are located inside the overlap of one slave and one master element passes the patch test, since the integration is evaluated more accurately. An algorithm computing the overlapped domain is proposed in Puso [2004]. Within the loop over all slave elements, the nodes

of one slave element are used to form a plane surface which is defined through the normal vector at the center of the local coordinate system of that element

$$\mathbf{x}_{0n+1}^1 = \sum_{I=1}^{n_e} N_I(\mathbf{0}) \mathbf{x}_{In+1}^1, \quad \mathbf{n}_{0n+1}^1 = \frac{\mathbf{x}_{0,1n+1}^1 \times \mathbf{x}_{0,2n+1}^1}{\|\mathbf{x}_{0,1n+1}^1 \times \mathbf{x}_{0,2n+1}^1\|}. \quad (4.71)$$

The projection of each slave node onto this surface is conducted via

$$\bar{\mathbf{x}}_{In+1}^1 = \mathbf{x}_{In+1}^1 - [(\mathbf{x}_{In+1}^i - \mathbf{x}_{0n+1}^1) \cdot \mathbf{n}_{0n+1}^1] \mathbf{n}_{0n+1}^1 \quad (4.72)$$

where the bar over the quantity indicates points on the projected plane. For each slave element an additional loop over all master elements is performed where each master node is also projected onto this plane surface

$$\bar{\mathbf{x}}_{In+1}^2 = \mathbf{x}_{In+1}^2 - [(\mathbf{x}_{In+1}^2 - \mathbf{x}_{0n+1}^1) \cdot \mathbf{n}_{0n+1}^1] \mathbf{n}_{0n+1}^1. \quad (4.73)$$

For each edge of the slave element the intersection with each master edge has to be computed. Here the Cyrus-Beck algorithm (Cyrus and Beck [1978]) well known in computer graphics (Foley et al. [1996] for instance) is used to determine the intersection point of two lines on an even plane

$$\begin{aligned} \bar{\mathbf{x}}_{intn+1} &= \bar{\mathbf{x}}_{1n+1}^1 - \xi_{n+1} (\bar{\mathbf{x}}_{2n+1}^1 - \bar{\mathbf{x}}_{1n+1}^1), \\ \xi_{n+1} &= \frac{[(\bar{\mathbf{x}}_{1n+1}^1 - \bar{\mathbf{x}}_{1n+1}^2) \times (\bar{\mathbf{x}}_{2n+1}^2 - \bar{\mathbf{x}}_{1n+1}^2)] \cdot \mathbf{n}_{0n+1}}{[(\bar{\mathbf{x}}_{2n+1}^1 - \bar{\mathbf{x}}_{1n+1}^1) \times (\bar{\mathbf{x}}_{2n+1}^2 - \bar{\mathbf{x}}_{1n+1}^2)] \cdot \mathbf{n}_{0n+1}}, \\ \bar{\mathbf{x}}_{intn+1} &= \bar{\mathbf{x}}_{1n+1}^2 - \eta_{n+1} (\bar{\mathbf{x}}_{2n+1}^2 - \bar{\mathbf{x}}_{1n+1}^2), \\ \eta_{n+1} &= \frac{[(\bar{\mathbf{x}}_{1n+1}^1 - \bar{\mathbf{x}}_{1n+1}^2) \times (\bar{\mathbf{x}}_{2n+1}^1 - \bar{\mathbf{x}}_{1n+1}^1)] \cdot \mathbf{n}_{0n+1}}{[(\bar{\mathbf{x}}_{2n+1}^1 - \bar{\mathbf{x}}_{1n+1}^1) \times (\bar{\mathbf{x}}_{2n+1}^2 - \bar{\mathbf{x}}_{1n+1}^2)] \cdot \mathbf{n}_{0n+1}} \end{aligned} \quad (4.74)$$

where $\xi_{n+1} \in [-1, 1]$ corresponds to the relative distance on the slave edge and $\eta_{n+1} \in [-1, 1]$ to the relative distance on the master edge (figure 4.6). Depending on the values

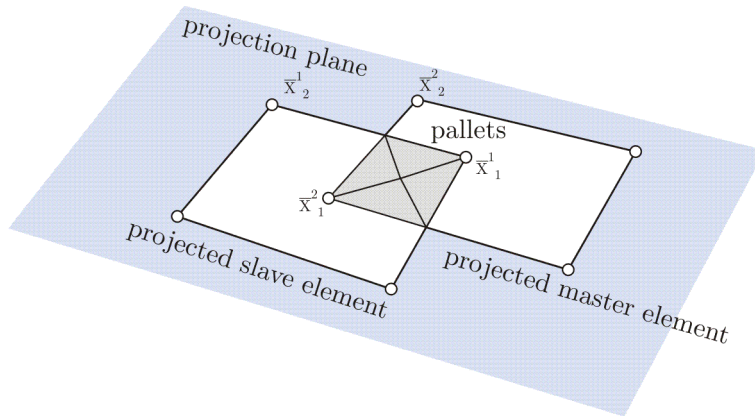


Figure 4.6: Clipping of one slave and one master element

for ξ_{n+1} and η_{n+1} , 11 different cases (see table 4.5) can occur where a tolerance δ is

-1	$\{\xi > -\delta \cup \xi + 1 < \delta\} \cup \{\eta > -\delta \cup \eta + 1 < \delta\}$	outside
0	ξ not defined	parallel sides
1	$\{\xi < -\delta \cap \xi + 1 > \delta\} \cap \{\eta < -\delta \cap \eta + 1 > \delta\}$	intersection point
2	$ \xi \leq \delta \cap \{\eta < -\delta \cap \eta + 1 > \delta\}$	1 st slave node on master edge
3	$ \xi + 1 \leq \delta \cap \{\eta < -\delta \cap \eta + 1 > \delta\}$	2 nd slave node on master edge
4	$\{\xi < -\delta \cap \xi + 1 > \delta\} \cap \eta \leq \delta$	1 st master node on slave edge
5	$\{\xi < -\delta \cap \xi + 1 > \delta\} \cap \eta + 1 \leq \delta$	2 nd master node on slave edge
6	$ \xi \leq \delta \cap \eta \leq \delta$	1 st slave node on 1 st master node
7	$ \xi + 1 \leq \delta \cap \eta \leq \delta$	2 nd slave node on 1 st master node
8	$ \xi \leq \delta \cap \eta + 1 \leq \delta$	1 st slave node on 2 nd master node
9	$ \xi + 1 \leq \delta \cap \eta + 1 \leq \delta$	2 nd slave node on 2 nd master node

Table 4.5: List of different intersection cases

used to capture mainly standard intersection cases (type 1). Cases where a node lies within the element of the other surface can also be determined based on the Cyrus-Beck algorithm. If the two adjacent edges of the slave or master node have more than one intersection point, then this node lies within the master or slave element. The

**Figure 4.7:** Pathological cases within the clipping algorithm

advantage of that algorithm is that only normalized quantities (ξ, η) determine the intersection points and hence the tolerances have not been adapted to the length of the elements. All the intersection points of one slave and one master element define a polygon or segment. After all points are stored, a filter is used to delete intersection points which lie close to each other. If the area of the segment is smaller than a

defined value that polygon is not considered anymore. Using only one algorithm for the determination of the polygon points and applying a filter after the algorithm and not before rise the robustness of the contact code, since the computation of the polygon points is more unique. If the surfaces are relatively close, the intersection points define a convex domain and the convex hull algorithm (de Berg et al. [2010] or Sedgewick [1992]) together with a bubble sort algorithm (Sedgewick [1992]) are used to order the polygon points clockwise. Afterwards, the segment is further subdivided into pallets (triangles) composed of two neighboring intersection points and the centroid $\bar{\mathbf{x}}_c$ of all polygon points $\bar{\mathbf{x}}^p$

$$\bar{\mathbf{x}}_{cn+1} = \frac{1}{n_{pa}} \sum_{p=1}^{n_{pa}} \bar{\mathbf{x}}_{pn+1}^p \quad (4.75)$$

where n_{pa} is the number of the intersection points. In the appendix C.3 the arrays to be stored are listed in more detail.

4.3.2 Integration point and base vectors

The coordinates of the vertices of the pallets together with standard linear shape functions for the triangles define the coordinates of the integration points. The back projection of the integration point onto the slave or master surface is performed by setting the integration point of the pallet equal to the corresponding coordinate at the desired surface (Puso [2004])

$$\bar{\mathbf{x}}_{gn+1}^p = \sum_{I=1}^3 N_I(\xi_{gn+1}^p) \bar{\mathbf{x}}_{In+1}^p = \sum_{I=1}^{n_i} N_I(\xi_{gn+1}^i) \mathbf{x}_{In+1}^i = \mathbf{x}_{gn+1}^i. \quad (4.76)$$

For the solution of the nonlinear equation, the Newton iteration is used to compute the local coordinates of the slave (i=1) and the master (i=2) integration point

$$\sum_{I=1}^{n_i} N_{I,\alpha}(\xi_{gn+1}^i) \mathbf{x}_{In+1}^i \Delta \xi_{n+1}^{i\alpha} = \sum_{I=1}^3 N_I(\xi_{gn+1}^p) \bar{\mathbf{x}}_{In+1}^p - \sum_{I=1}^{n_i} N_I(\xi_{gn+1}^i) \mathbf{x}_{In+1}^i, \quad (4.77)$$

$$\Delta \xi_{n+1}^{i\alpha} = [\bar{\mathbf{x}}_{gn+1}^p - \mathbf{x}_{gn+1}^i] \cdot \mathbf{a}_{\beta gn+1}^i \mathbf{a}_{n+1}^{\alpha\beta i}.$$

An alternative algorithm is used in Popp et al. [2010a] where the back projection is performed along the normal vector at the center of the slave element

$$\mathbf{x}_{gn+1}^p + \alpha \mathbf{n}_{0n+1} = \sum_{I=1}^{n_i} N_I(\xi_{gn+1}^i) \mathbf{x}_{In+1}^i. \quad (4.78)$$

To smoothen the slave surface, the base vectors and the normalized normal vector of each node \bar{I} are averaged over the base and normal vectors at that node at each adjacent element a (see figure 4.8) where $\bar{\boldsymbol{\xi}}_{\bar{I}}$ corresponds to the local coordinate of the desired node

$$\mathbf{a}_{I\alpha n+1}^1 = \sum_{a=1}^{n_{ae}^1} N_{\bar{I},\alpha n+1}(\bar{\boldsymbol{\xi}}_{\bar{I}n+1}) \mathbf{x}_{In+1}^1, \quad \mathbf{n}_{\bar{I}n+1}^1 = \frac{\mathbf{a}_{\bar{I}1n+1}^1 \times \mathbf{a}_{\bar{I}2n+1}^1}{\|\mathbf{a}_{\bar{I}1n+1}^1 \times \mathbf{a}_{\bar{I}2n+1}^1\|}. \quad (4.79)$$

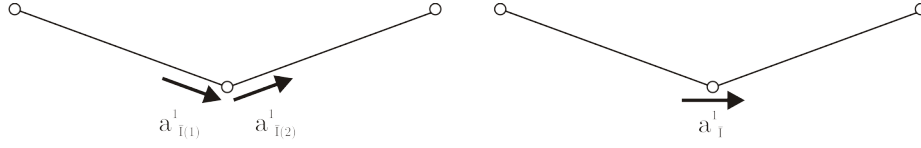


Figure 4.8: Averaged base vector schematically for the 2D case

4.3.3 Integration

The integration over the domain of one slave node is defined as the sum over each adjacent slave element n_{ad}^1 , over all segments n_{seg} , over all pallets n_{pa} and at last over all integration points of that pallet n_{gp}^{pa}

$$a_{n+1} = \sum_{a=1}^{n_{ad}^1} \sum_{s=1}^{n_{seg}} \sum_{p=1}^{n_{pa}} \sum_{g=1}^{n_{gp}^{pa}} \det \mathbf{j}_{n+1}^{(a s p)} W_g. \quad (4.80)$$

The Jacobian is defined as the area of the pallet on the even plane

$$\det \mathbf{j}_{n+1}^{(a s p)} = \frac{1}{2} \| (\bar{\mathbf{x}}_{2n+1}^p - \bar{\mathbf{x}}_{1n+1}^p) \times (\bar{\mathbf{x}}_{3n+1}^p - \bar{\mathbf{x}}_{1n+1}^p) \| \quad (4.81)$$

and W_g corresponds to the weighting of the triangle. To shorten the notation, all the summations are comprised to the summation over all integration points n_{gp}

$$a_{n+1} = \sum_{g=1}^{n_{gp}} \det \mathbf{j}_{n+1} W_g \quad (4.82)$$

and the labels $(a s p)$ of the determinant are neglected.

4.3.4 Kinematical contact relations

Similar to the node to surface description, the determination of the status and the assembling are performed nodal wise, but in contrast to the node to surface formulation both surfaces are coupled in a weak or averaged sense. Therefore averaged nodal kinematical contact quantities are used in the Mortar method. The connection of the weak form and the averaged contact quantities can be shown exemplary for an alternative form (see Wriggers [2006] section 6.5.3) of the discretized virtual enforcement of the stick constraint

$$\begin{aligned} G_l^{ch} = & \sum_A^{n_s} \sum_{g=1}^{n_{gp}} M_A (\boldsymbol{\xi}_{gn+1}^1) \delta \lambda_{An+1} \cdot \left(\sum_{C=1}^{n_m} N_C (\boldsymbol{\xi}_{gn+1}^2) \mathbf{x}_{Cn+1}^2 \right. \\ & \left. - \sum_{B=1}^{n_s} N_B (\boldsymbol{\xi}_{gn+1}^1) \mathbf{x}_{Bn+1}^1 \right) \det \mathbf{j}_{n+1} W_g. \end{aligned} \quad (4.83)$$

The equation above can now be reformulated as the product of the virtual Lagrange multiplier and the averaged gap of that node

$$G_l^{ch} = \sum_A^{n_s} \delta \lambda_{A n+1} \cdot \bar{\mathbf{g}}_A \quad (4.84)$$

where the averaged nodal gap is specified as

$$\begin{aligned} \bar{\mathbf{g}}_A &= \sum_{g=1}^{n_{gp}} M_A (\boldsymbol{\xi}_{g n+1}^1) \left(\sum_{C=1}^{n_m} N_C (\boldsymbol{\xi}_{g n+1}^2) \mathbf{x}_{C n+1}^2 - \sum_{B=1}^{n_s} N_B (\boldsymbol{\xi}_{g n+1}^1) \mathbf{x}_{B n+1}^1 \right) \det \mathbf{j}_{n+1} W_g \\ &= \sum_{g=1}^{n_{gp}} M_A (\boldsymbol{\xi}_{g n+1}) (\mathbf{x}_{n+1}^2 (\boldsymbol{\xi}_{g n+1}^2) - \mathbf{x}_{n+1}^1 (\boldsymbol{\xi}_{g n+1}^1)) \det \mathbf{j}_{n+1} W_g. \end{aligned} \quad (4.85)$$

The bar over the quantity indicates an averaged value and since the even plane is not involved in the descriptions of the averaging, no confusion with the projected position vectors of section 4.3.2 can occur. Additionally, the index $n + 1$ is neglected for the averaged quantities, since all of them are defined at the actual time step. Alternatively, so called mass matrices (Puso [2004]) can be defined for the contribution of the slave n_{AB} and of the master side n_{AC} in (4.85)

$$\begin{aligned} n_{AB n+1} &= \sum_{g=1}^{n_{gp}} M_A (\boldsymbol{\xi}_{g n+1}^1) \sum_{B=1}^{n_s} N_B (\boldsymbol{\xi}_{g n+1}^1) \det \mathbf{j}_{n+1} W_g \\ n_{AC n+1} &= \sum_{g=1}^{n_{gp}} M_A (\boldsymbol{\xi}_{g n+1}^1) \sum_{C=1}^{n_m} N_C (\boldsymbol{\xi}_{g n+1}^2) \det \mathbf{j}_{n+1} W_g. \end{aligned} \quad (4.86)$$

The nodal gap can then be rewritten as

$$\bar{\mathbf{g}}_A = n_{AC n+1} \mathbf{x}_{C n+1}^2 - n_{AB n+1} \mathbf{x}_{B n+1}^1 \quad (4.87)$$

For the frictional contact constraints, the evolution equation for the tangential movement has to be integrated

$$\dot{\bar{\mathbf{g}}}_{\text{T}\alpha A} = \dot{\bar{\mathbf{g}}}_A \cdot \mathbf{t}_{A\alpha} = \dot{\gamma}_A \frac{\bar{\boldsymbol{\lambda}}_A \cdot \mathbf{t}_{A\alpha}}{\|\bar{\boldsymbol{\lambda}}_{\text{T}A}\|} = \dot{\gamma}_A \frac{\bar{\lambda}_{\text{T}\alpha A}}{\|\bar{\boldsymbol{\lambda}}_{\text{T}A}\|}, \quad \|\bar{\boldsymbol{\lambda}}_{\text{T}A}\| = \sqrt{(\bar{\boldsymbol{\lambda}}_A \cdot \mathbf{t}_{A\alpha})^2}. \quad (4.88)$$

To define an objective derivative of the nodal gap, Yang et al. [2005] restricted the time derivative only to the mass matrices

$$\dot{\bar{\mathbf{g}}}_A \cdot \mathbf{t}_{A\alpha} = (\dot{n}_{AC n+1} \mathbf{x}_{C n+1}^2 - \dot{n}_{AB n+1} \mathbf{x}_{B n+1}^1) \cdot \mathbf{t}_{A\alpha n+1} \quad (4.89)$$

leading to the incremental tangential movement within the implicit backward Euler time integration scheme as the difference of the tangential gap at the actual and at the old integration points, respectively,

$$\Delta_t \bar{\mathbf{g}}_A \cdot \mathbf{t}_{A\alpha} = [\bar{\mathbf{g}}_{A n+1} (\boldsymbol{\xi}_{g n+1}) - \bar{\mathbf{g}}_{A n+1} (\boldsymbol{\xi}_{g n})] \cdot \mathbf{t}_{A\alpha n+1} = [\bar{\mathbf{g}}_A - \bar{\mathbf{g}}_A^o] \cdot \mathbf{t}_{A\alpha} \quad (4.90)$$

where the averaged gap at the old time step is given as

$$\bar{\mathbf{g}}_A^o = \sum_{g=1}^{n_{gp}} M_A(\boldsymbol{\xi}_{gn}^1) (\mathbf{x}_{n+1}^2(\boldsymbol{\xi}_{gn}^2) - \mathbf{x}_{n+1}^1(\boldsymbol{\xi}_{gn}^1)) \det \mathbf{j}_n W_g. \quad (4.91)$$

Using Lagrange multipliers (also called dual variables) within the Mortar method, special dual shape functions N_A^d can be applied which are defined in such a way that the mass matrix n_{AB} has a diagonal structure, i.e. the biorthogonality condition

$$\sum_{q=1}^{n_{gp}} \sum_{A=1}^{n_s} \sum_{B=1}^{n_s} N_A^d(\boldsymbol{\xi}_{qn+1}^1) N_B(\boldsymbol{\xi}_{qn+1}^1) \det \mathbf{j}_{n+1} W_q = \sum_{q=1}^{n_{gp}} \sum_{A=1}^{n_s} \sum_{B=1}^{n_s} \delta_{AB} N_B(\boldsymbol{\xi}_{qn+1}^1) \det \mathbf{j}_{n+1} W_q \quad (4.92)$$

has to be fulfilled (Wohlmuth [2000]). Thereby n_{gp}^1 indicates the sum over all integration points of the slave element, i.e. the sum over all segments plus the sum over the integration points of that segment. Formulating the dual shape functions in dependency of the standard shape functions

$$\sum_{A=1}^{n_s} N_A^d(\boldsymbol{\xi}_{gn+1}^1) = \sum_{A=1}^{n_s} \sum_{B=1}^{n_s} A_{AB} N_B(\boldsymbol{\xi}_{gn+1}^1), \quad (4.93)$$

the coefficient matrix $A_{AB} = D_{AC} M_{CB}^{-1}$ can then be determined where

$$\begin{aligned} D_{AC} &= \delta_{AC} \sum_{q=1}^{n_{gp}} \sum_{A=1}^{n_s} N_C(\boldsymbol{\xi}_{qn+1}^1) \det \mathbf{j}_{n+1} W_q, \\ M_{CB} &= \sum_{q=1}^{n_{gp}} \sum_{C=1}^{n_s} \sum_{B=1}^{n_s} N_C(\boldsymbol{\xi}_{qn+1}^1) N_B(\boldsymbol{\xi}_{qn+1}^1) \det \mathbf{j}_{n+1} W_q. \end{aligned} \quad (4.94)$$

Now for the discretization of the Lagrange multiplier standard or dual shape functions can be used

$$M_A(\boldsymbol{\xi}_{gn+1}^1) = N_A(\boldsymbol{\xi}_{gn+1}^1), \quad \text{or} \quad M_A(\boldsymbol{\xi}_{gn+1}^1) = N_A^d(\boldsymbol{\xi}_{gn+1}^1). \quad (4.95)$$

Due to the diagonal structure of n_{AB} in the case of dual shape functions, the Lagrange multipliers can be condensed from the global tangent matrix without large computational effort, see Hübner and Wohlmuth [2005]. On the other hand due to

$$n_{ABn+1} \mathbf{x}_{Bn+1}^1 = \mathbf{x}_{An+1}^1 \quad (4.96)$$

in the case of dual shape functions, the Mortar method can also be viewed as a node to surface formulation as mentioned at the beginning of that chapter. On the basis of the above mentioned averaging procedure, different nodal quantities needed for the subsequent developments can be defined, like the averaged virtual gap

$$\delta \bar{\mathbf{g}}_A = \sum_{g=1}^{n_{gp}} M_A(\boldsymbol{\xi}_{gn+1}^1) (\boldsymbol{\eta}_{n+1}^2(\boldsymbol{\xi}_{gn+1}^2) - \boldsymbol{\eta}_{n+1}^1(\boldsymbol{\xi}_{gn+1}^1)) \det \mathbf{j}_{n+1} W_g \quad (4.97)$$

and the averaged Lagrange multipliers

$$\bar{\lambda}_A = \sum_{g=1}^{n_{gp}} M_A(\boldsymbol{\xi}_{g,n+1}^1) \lambda_{n+1}(\boldsymbol{\xi}_{g,n+1}^1) \det \mathbf{j}_{n+1} W_g. \quad (4.98)$$

In the case of dual shape functions, the averaged Lagrange multiplier simplifies to

$$\bar{\lambda}_A = \lambda_A a_A, \quad \text{where} \quad a_A = \sum_{g=1}^{n_{gp}} M_A(\boldsymbol{\xi}_{g,n+1}^1) \det \mathbf{j}_{n+1} W_g \quad (4.99)$$

is the area around the slave node A . Another possibility is to compute directly the normal penetration and its virtual counterpart in an averaged sense

$$\begin{aligned} \bar{g}_{NA} &= \sum_{g=1}^{n_{gp}} M_A(\boldsymbol{\xi}_{g,n+1}^1) (\mathbf{x}_{n+1}^2(\boldsymbol{\xi}_{g,n+1}^2) - \mathbf{x}_{n+1}^1(\boldsymbol{\xi}_{g,n+1}^1)) \cdot \mathbf{n}_{n+1}^1(\boldsymbol{\xi}_{g,n+1}^1) \det \mathbf{j}_{n+1} W_g \\ \delta \bar{g}_{NA} &= \sum_{g=1}^{n_{gp}} M_A(\boldsymbol{\xi}_{g,n+1}^1) (\boldsymbol{\eta}_{n+1}^2(\boldsymbol{\eta}_{g,n+1}^2) - \boldsymbol{\eta}_{n+1}^1(\boldsymbol{\xi}_{g,n+1}^1)) \cdot \mathbf{n}_{n+1}^1(\boldsymbol{\xi}_{g,n+1}^1) \det \mathbf{j}_{n+1} W_g \end{aligned} \quad (4.100)$$

where the same procedure have to be applied to the tangential gap, its virtual counterpart at the actual time step and to the tangential gap at the old time step

$$\begin{aligned} \bar{g}_{T\alpha A} &= \sum_{g=1}^{n_{gp}} M_A(\boldsymbol{\xi}_{g,n+1}^1) (\mathbf{x}_{n+1}^2(\boldsymbol{\xi}_{g,n+1}^2) - \mathbf{x}_{n+1}^1(\boldsymbol{\xi}_{g,n+1}^1)) \cdot \mathbf{t}_{\alpha,n+1}^1(\boldsymbol{\xi}_{g,n+1}^1) \det \mathbf{j}_{n+1} W_g \\ \delta \bar{g}_{T\alpha A} &= \sum_{g=1}^{n_{gp}} M_A(\boldsymbol{\xi}_{g,n+1}^1) (\boldsymbol{\eta}_{n+1}^2(\boldsymbol{\eta}_{g,n+1}^2) - \boldsymbol{\eta}_{n+1}^1(\boldsymbol{\xi}_{g,n+1}^1)) \cdot \mathbf{t}_{\alpha,n+1}^1(\boldsymbol{\xi}_{g,n+1}^1) \det \mathbf{j}_{n+1} W_g \\ \bar{g}_{T\alpha A}^o &= \sum_{g=1}^{n_{gp}} M_A(\boldsymbol{\xi}_{g,n}^1) (\mathbf{x}_{n+1}^2(\boldsymbol{\xi}_{g,n}^2) - \mathbf{x}_{n+1}^1(\boldsymbol{\xi}_{g,n}^1)) \cdot \mathbf{t}_{\alpha,n+1}^1(\boldsymbol{\xi}_{g,n}^1) \det \mathbf{j}_n W_g. \end{aligned} \quad (4.101)$$

Additionally, the Lagrange multipliers being split into normal and tangential components have to be averaged

$$\begin{aligned} \lambda_{NA} &= \sum_{g=1}^{n_{gp}} M_A(\boldsymbol{\xi}_{g,n+1}) \lambda_{N,n+1}(\boldsymbol{\xi}_{g,n+1}^1) \det \mathbf{j}_{n+1} W_g \\ \lambda_{T\alpha A} &= \sum_{g=1}^{n_{gp}} M_A(\boldsymbol{\xi}_{g,n+1}) \lambda_{T\alpha,n+1}(\boldsymbol{\xi}_{g,n+1}^1) \det \mathbf{j}_{n+1} W_g. \end{aligned} \quad (4.102)$$

4.3.5 Linearized quantities

Since the assembly process is performed over each segment, the linearization of the contact element and of the kinematical quantities are also evaluated at each segment.

The linearized solution vector for the displacements

$$\begin{aligned} \mathbf{d}_s &= [\Delta \mathbf{u}_1^1, \dots, \Delta \mathbf{u}_4^1, \Delta \mathbf{u}_1^2, \dots, \Delta \mathbf{u}_4^2]^T \\ \delta \mathbf{d}_s &= [\delta \mathbf{u}_1^1, \dots, \delta \mathbf{u}_4^1, \delta \mathbf{u}_1^2, \dots, \delta \mathbf{u}_4^2]^T \end{aligned} \quad (4.103)$$

is then a subset of \mathbb{R}^{24} as well as the virtual solution vector $\delta \mathbf{d}_s$. The subscript $n + 1$ is neglected in the following equations, since the linearized quantities depend only on the actual time step.

4.3.5.1 Contact element quantities

Before the residual vector and the tangent matrix can be formulated in detail, all the individual steps for the derivation of the contact element have to be linearized.

Projection points

Starting with the linearization of the position vector at the center of the slave element (4.71)

$$\Delta \mathbf{x}_0 = \sum_{I=1}^{n_s} N_I(\mathbf{0}) \Delta \mathbf{u}_I^1 = \mathbf{P}_{N_I(\mathbf{0})}^1 \mathbf{d}_s, \quad (4.104)$$

the linearization of the normal at the center (4.71) can be obtained in terms of the matrix $\mathbf{E}_{n_0} \in \mathbb{R}^{3 \times 24}$ as

$$\Delta \mathbf{n}_0 = \frac{1}{\|\mathbf{a}_{01}^1 \times \mathbf{a}_{02}^1\|} [\mathbf{1} - \mathbf{n}_0 \otimes \mathbf{n}_0] \left[-\Omega(\mathbf{a}_{02}^1) \mathbf{P}_{N_{1,1}(\mathbf{0})}^1 + \Omega(\mathbf{a}_{01}^1) \mathbf{P}_{N_{0,2}(\mathbf{0})}^1 \right] \mathbf{d}_s = \mathbf{E}_{n_0} \mathbf{d}_s \quad (4.105)$$

where the matrix $\mathbf{P}_N^1 \in \mathbb{R}^{3 \times 24}$ is a projection matrix for the nodal shape functions of the slave side and can be found together with all other projection matrices in (C.5). The linearization of the projected slave (4.72) or master nodes (4.73)

$$\begin{aligned} \Delta \bar{\mathbf{x}}_I^i &= [\mathbf{1} - \mathbf{n}_0 \otimes \mathbf{n}_0] \Delta \mathbf{u}_I^i + \mathbf{n}_0 \otimes \mathbf{n}_0 \Delta \mathbf{x}_0 - \mathbf{n}_0 \otimes (\mathbf{x}_I^i - \mathbf{x}_0) \Delta \mathbf{n}_0 \\ &\quad - (\mathbf{x}_I^i - \mathbf{x}_0) \cdot \mathbf{n}_0 \Delta \mathbf{n}_0 = \mathbf{E}_I^i \mathbf{d}_s \end{aligned} \quad (4.106)$$

can also be expressed in dependency of the solution vector together with the matrix $\mathbf{E}_I^i \in \mathbb{R}^{3 \times 24}$

$$\mathbf{E}_I^i = [\mathbf{1} - \mathbf{n}_0 \otimes \mathbf{n}_0] \mathbf{P}_I^i + \mathbf{n}_0 \otimes \mathbf{n}_0 \mathbf{P}_{N_I(\mathbf{0})}^1 - \mathbf{n}_0 \otimes (\mathbf{x}_I^i - \mathbf{x}_0) \mathbf{E}_{n_0} - (\mathbf{x}_I^i - \mathbf{x}_0) \cdot \mathbf{n}_0 \mathbf{E}_{n_0}. \quad (4.107)$$

The eight matrices for all slave and all master nodes have to be stored in the summarized matrix $\mathbf{E} \in \mathbb{R}^{24 \times 24}$ needed for further linearization.

Pallet points

The next step is the determination of the linearization matrix $\mathbf{D}^p \in \mathbb{R}^{9 \times 24}$ of the three pallet points which have to be divided into the linearization of each individual pallet

point $\mathbf{d}_i^p \in \mathbb{R}^{3 \times 24}$

$$\Delta \bar{\mathbf{u}}_{xp=(1,2,3)}^p = \mathbf{D}^p \mathbf{d}_s, \quad \mathbf{D}^p = \begin{bmatrix} \mathbf{d}_1^p \\ \mathbf{d}_2^p \\ \mathbf{d}_3^p \end{bmatrix}. \quad (4.108)$$

The pallet point ($x_p=1,2$) can be a projected slave or master node where the contribution to the matrix corresponds directly to the desired matrix of the projection point

$$\Delta \bar{\mathbf{u}}_{xp}^p = \Delta \bar{\mathbf{x}}_I^i, \quad \mathbf{d}_{xp}^p = \mathbf{E}_I^i, \quad (4.109)$$

or the pallet point is an intersection point where a special matrix $\mathbf{E}_{int} \in \mathbb{R}^{3 \times 24}$ has to be determined

$$\mathbf{d}_{xp}^p = \mathbf{E}_{int} \quad (4.110)$$

which contains the linearization of the Cyrus-Beck algorithm (4.74). Defining some vectors for the distances, the numerator and the denominator using cross matrices (C.6)

$$\begin{aligned} \mathbf{d}^i &:= \bar{\mathbf{x}}_1^1 - \bar{\mathbf{x}}_1^2, \quad \mathbf{d}^1 := \bar{\mathbf{x}}_2^1 - \bar{\mathbf{x}}_1^1, \quad \mathbf{d}^2 := \bar{\mathbf{x}}_2^2 - \bar{\mathbf{x}}_1^2, \\ n_{int}^n &:= \mathbf{n}_0 \Omega(\mathbf{d}^i) \mathbf{d}^2, \quad n_{int}^d := \mathbf{n}_0 \Omega(\mathbf{d}^1) \mathbf{d}^2, \end{aligned} \quad (4.111)$$

the linearized intersection point can be expressed in an abbreviated form

$$\begin{aligned} \Delta \bar{\mathbf{x}}_{int} &= \left[\left(1 + \frac{n_{int}^n}{n_{int}^d} \right) \mathbf{1} + \left(\frac{1}{n_{int}^d} + \frac{n_{int}^n}{(n_{int}^d)^2} \right) \mathbf{d}^1 \otimes \mathbf{n}_0 \Omega(\mathbf{d}^2) \right] \Delta \bar{\mathbf{u}}_1^1 \\ &\quad - \left[\frac{n_{int}^n}{n_{int}^d} \mathbf{1} + \frac{n_{int}^n}{(n_{int}^d)^2} \mathbf{d}^1 \otimes \mathbf{n}_0 \Omega(\mathbf{d}^2) \right] \Delta \bar{\mathbf{u}}_2^1 \\ &\quad + \left[\frac{1}{n_{int}^d} \left(\mathbf{d}^1 \otimes \mathbf{n}_0 \Omega(\mathbf{d}^i) - \mathbf{d}^1 \otimes \mathbf{n}_0 \Omega(\mathbf{d}^2) \right) - \frac{n_{int}^n}{(n_{int}^d)^2} \mathbf{d}^1 \otimes \mathbf{n}_0 \Omega(\mathbf{d}^1) \right] \Delta \bar{\mathbf{u}}_1^2 \\ &\quad + \left[\frac{n_{int}^n}{(n_{int}^d)^2} \mathbf{d}^1 \otimes \mathbf{n}_0 \Omega(\mathbf{d}^1) - \frac{1}{n_{int}^d} \mathbf{d}^1 \otimes \mathbf{n}_0 \Omega(\mathbf{d}^i) \right] \Delta \bar{\mathbf{u}}_2^2 \\ &\quad + \left[\frac{n_{int}^n}{(n_{int}^d)^2} \mathbf{d}^1 \otimes \mathbf{d}^2 \Omega(\mathbf{d}^1)^T - \frac{1}{n_{int}^d} \mathbf{d}^1 \otimes \mathbf{d}^2 \Omega(\mathbf{d}^i)^T \right] \Delta \mathbf{n}_0 = \mathbf{E}_{int} \mathbf{d}_s. \end{aligned} \quad (4.112)$$

In each arrangement of the pallet points, the third point is always the centroid (4.75) and the linearization of that point is the average of the linearization of all the other points

$$\Delta \mathbf{d}_3^p = \frac{1}{n_{pa}} \sum_{q=1}^{n_{pa}} \Delta \mathbf{d}_q^p. \quad (4.113)$$

Integration points

Starting from (4.76), the linearization of the integration point at each surface follows directly from the Newton iteration process (4.77)

$$\Delta \xi_g^{\alpha i} = \left[\sum_{I=1}^3 N_I(\xi_g^p) \Delta \mathbf{x}_I^p - \sum_{I=1}^{n_i} N_I(\xi_g^i) \Delta \bar{\mathbf{x}}_I^i \right] \cdot \bar{\mathbf{a}}_{\beta g}^i \bar{\mathbf{a}}_g^{\alpha \beta i}. \quad (4.114)$$

Together with the known linearization of the pallet and the projection points, (4.114) can be rewritten

$$\Delta \xi_g^{\alpha i} = \bar{\mathbf{a}}_g^{\alpha \beta} \bar{\mathbf{a}}_{\beta g} \left[\mathbf{P}_{N(\xi_g^p)}^p \mathbf{D}^p - \mathbf{P}_{N(\xi_g^i)}^i \mathbf{E} \right] \mathbf{d}_s = \mathbf{B}_{gp}^{i\alpha} \mathbf{d}_s \quad (4.115)$$

where the matrices for the slave (i=1) and the master (i=2) side $\mathbf{B}_{gp}^{i\alpha} \in \mathbb{R}^{2 \times 24}$ include the linearization of the pallet and the projection points.

Jacobian

Additionally, the linearization of the determinant of the Jacobian (4.81)

$$\begin{aligned} \Delta \det \mathbf{j} = & \frac{(\mathbf{x}_2^p - \mathbf{x}_1^p) \times (\mathbf{x}_3^p - \mathbf{x}_1^p)}{2 \|\mathbf{x}_2^p - \mathbf{x}_1^p\| \times \|\mathbf{x}_3^p - \mathbf{x}_1^p\|} \left[(\Delta \mathbf{x}_2^p - \Delta \mathbf{x}_1^p) \times (\mathbf{x}_3^p - \mathbf{x}_1^p) \right. \\ & \left. + (\mathbf{x}_2^p - \mathbf{x}_1^p) \times (\Delta \mathbf{x}_3^p - \Delta \mathbf{x}_1^p) \right] \end{aligned} \quad (4.116)$$

together with the cross product and the introduction of the vector $\mathbf{S}^p \in \mathbb{R}^9$

$$\mathbf{S}^p = \begin{bmatrix} \mathbf{n}_j [\boldsymbol{\Omega}(\mathbf{x}_3^p - \mathbf{x}_1^p) - \boldsymbol{\Omega}(\mathbf{x}_2^p - \mathbf{x}_1^p)] \\ \mathbf{n}_j \boldsymbol{\Omega}(\mathbf{x}_3^p - \mathbf{x}_1^p) \\ \mathbf{n}_j \boldsymbol{\Omega}(\mathbf{x}_2^p - \mathbf{x}_1^p) \end{bmatrix}, \quad \mathbf{n}_j = \frac{\boldsymbol{\Omega}(\mathbf{x}_2^p - \mathbf{x}_1^p)(\mathbf{x}_3^p - \mathbf{x}_1^p)}{2 \|\boldsymbol{\Omega}(\mathbf{x}_2^p - \mathbf{x}_1^p)(\mathbf{x}_3^p - \mathbf{x}_1^p)\|^2} \quad (4.117)$$

can be written in terms of the vector $\mathbf{B}_j \in \mathbb{R}^{24}$

$$\Delta \det \mathbf{j} = \det \mathbf{j} \mathbf{B}_j \mathbf{d}_s, \quad \text{where} \quad \mathbf{B}_j = \mathbf{S}^p \mathbf{D}^p \quad (4.118)$$

Dual shape function

If dual shape functions are used, the coefficient matrix has also to be linearized additional to the linearization of the standard shape functions at each integration point

$$\begin{aligned} \Delta N_A^d(\xi_g^1) &= \sum_{B=1}^{n_s} [\Delta A_{AB} N_B(\xi_g^1) + A_{AB} N_{B,\alpha}(\xi_g^1) \Delta \xi_g^{\alpha 1}] \\ &= \Delta_d N_A^d(\xi_g^1) + N_{A,\alpha}^d(\xi_g^1) \Delta \xi_g^{\alpha 1} \end{aligned} \quad (4.119)$$

where the subscript d indicates the contribution of the coefficient matrix. Using the prescription of the derivative of inverse tensors which can be found for instance in

Holzapfel [2000] and neglecting the summation over the slave nodes, the linearization of the coefficient matrix (4.94) is given as

$$\Delta A_{AB} = \Delta D_{AC} M_{CB}^{-1} - A_{AC} \Delta M_{CD} M_{DB}^{-1} \quad (4.120)$$

where

$$\begin{aligned} \Delta D_{AC} &= \delta_{AC} \sum_{q=1}^{n_{gp}^1} [N_C(\boldsymbol{\xi}_q^1) \Delta \det \mathbf{j} + N_{C,\alpha}(\boldsymbol{\xi}_q^1) \Delta \xi_q^{\alpha 1} \det \mathbf{j}] W_q \\ \Delta M_{CD} &= \sum_{q=1}^{n_{gp}^1} [N_C(\boldsymbol{\xi}_q^1) N_D(\boldsymbol{\xi}_q^1) \Delta \det \mathbf{j} \\ &\quad + (N_{C,\alpha}(\boldsymbol{\xi}_q^1) N_D(\boldsymbol{\xi}_q^1) + N_C(\boldsymbol{\xi}_q^1) N_{D,\alpha}(\boldsymbol{\xi}_q^1)) \Delta \xi_q^{\alpha 1} \det \mathbf{j}] W_q. \end{aligned} \quad (4.121)$$

Using a split of the summation over all integration points of the slave element into a summation over the segments and a summation over the integration points of that segment, the additional linearization part

$$\begin{aligned} \Delta_d N_A^d(\boldsymbol{\xi}_g^1) &= \sum_{t=1}^{n_{seg}} \sum_{p=1}^{n_{gp}^s} \left(\delta_{AC} [N_C(\boldsymbol{\xi}_p^1) \mathbf{B}_j + N_{C,\alpha}(\boldsymbol{\xi}_p^1) \mathbf{B}_{gp}^{1\alpha}] \det \mathbf{j} W_p M_{CB}^{-1} \right. \\ &\quad - A_{AC} [N_C(\boldsymbol{\xi}_p^1) N_D(\boldsymbol{\xi}_p^1) \mathbf{B}_j + (N_{C,\alpha}(\boldsymbol{\xi}_p^1) N_D(\boldsymbol{\xi}_p^1) \\ &\quad \left. + N_C(\boldsymbol{\xi}_p^1) N_{D,\alpha}(\boldsymbol{\xi}_p^1)) \mathbf{B}_{gp}^{1\alpha}] \det \mathbf{j} W_p M_{DB}^{-1} \right) N_B(\boldsymbol{\xi}_p^1) \mathbf{d}_t \end{aligned} \quad (4.122)$$

can be summarized to the new vector $\mathbf{B}_d^t \in \mathbb{R}^{24}$ with an arbitrary length t

$$\Delta_d N_A^d(\boldsymbol{\xi}_g^1) = \sum_{t=1}^{n_{seg}} \mathbf{B}_d^t \mathbf{d}_t. \quad (4.123)$$

Hence an additional loop within the stiffness matrix occur which as for the penalty method slows down the solution process.

Base vectors

For the linearization of the base vectors of one node \bar{I} (4.79), an additional loop over maximal 4 adjacent elements n_{ae}^1 has to be applied. The linearization of the tangential nodal base vector

$$\Delta \mathbf{a}_{\bar{I}\alpha} = \sum_{a=1}^{n_{ae}^1} \sum_{B=1}^{n_s} N_{B,\alpha}(\bar{\boldsymbol{\xi}}_{\bar{I}}^a) \Delta \mathbf{u}_B^1 = \sum_{a=1}^{n_{ae}^1} \mathbf{B}_b^{a\alpha} \mathbf{d}_a, \quad \mathbf{B}_b^{a\alpha} = \mathbf{P}_{N_{B,\alpha}(\bar{\boldsymbol{\xi}}_{\bar{I}}^a)}^1, \quad (4.124)$$

its normalized counterpart

$$\begin{aligned} \Delta \mathbf{t}_{\bar{I}\alpha} &= \left[\frac{\Delta \mathbf{a}_{\bar{I}\alpha}}{\|\mathbf{a}_{\bar{I}\alpha}\|} - \frac{\mathbf{a}_{\bar{I}\alpha} \otimes \mathbf{a}_{\bar{I}\alpha} \Delta \mathbf{a}_{\bar{I}\alpha}}{\|\mathbf{a}_{\bar{I}\alpha}\|^3} \right] \\ &= \left[\frac{\mathbf{1}}{\|\mathbf{a}_{\bar{I}\alpha}\|} - \frac{\mathbf{a}_{\bar{I}\alpha} \otimes \mathbf{a}_{\bar{I}\alpha}}{\|\mathbf{a}_{\bar{I}\alpha}\|^3} \right] \sum_{a=1}^{n_{ae}^1} \mathbf{P}_{N_{\bar{I},\alpha}(\bar{\boldsymbol{\xi}}_{\bar{I}}^a)}^1 \mathbf{d}_a = \sum_{a=1}^{n_{ae}^1} \mathbf{B}_t^{a\alpha} \mathbf{d}_a \end{aligned} \quad (4.125)$$

and the normalized normal vector

$$\begin{aligned}
\Delta \mathbf{n}_{\bar{I}} &= [-\Omega(\mathbf{t}_{\bar{I}2}^1) \Delta \mathbf{t}_{\bar{I}2}^1 + \Omega(\mathbf{t}_{\bar{I}1}^1) \Delta \mathbf{t}_{\bar{I}1}^1] \\
&= \sum_{a=1}^{n_{ae}^1} \left(-\Omega(\mathbf{t}_{\bar{I}2}^1) \left[\frac{\mathbf{1}}{\|\mathbf{a}_{\bar{I}1}\|} - \frac{\mathbf{a}_{\bar{I}1} \otimes \mathbf{a}_{\bar{I}1}}{\|\mathbf{a}_{\bar{I}1}\|^3} \right] \mathbf{P}_{N_{\bar{I},1}}^1(\bar{\xi}_{\bar{I}}^a) \right. \\
&\quad \left. + \Omega(\mathbf{t}_{\bar{I}1}^1) \left[\frac{\mathbf{1}}{\|\mathbf{a}_{\bar{I}2}\|} - \frac{\mathbf{a}_{\bar{I}2} \otimes \mathbf{a}_{\bar{I}2}}{\|\mathbf{a}_{\bar{I}2}\|^3} \right] \mathbf{P}_{N_{\bar{I},2}}^1(\bar{\xi}_{\bar{I}}^a) \right) \mathbf{d}_a = \sum_{a=1}^{n_{ae}^1} \mathbf{B}_n^a \mathbf{d}_a
\end{aligned} \tag{4.126}$$

can also be summarized in terms of the vectors $\mathbf{B}_b^{a\alpha} \in \mathbb{R}^{2 \times 24}$, $\mathbf{B}_t^{a\alpha} \in \mathbb{R}^{2 \times 24}$ and $\mathbf{B}_n^a \in \mathbb{R}^{24}$.

4.3.5.2 Kinematical quantities

Based on the contact vectors of the preceding section, the linearization of the kinematical contact quantities can be represented more precisely. The summation over all integration points of one averaged node is subdivided into the summation over all segments n_{seg}^A of that node and over all integration points of each segment n_{gp}^s which fit to the assembly strategy described at the beginning of this chapter. For the linearization of the gap vector (4.85)

$$\begin{aligned}
\Delta \bar{\mathbf{g}}_A &= \sum_{s=1}^{n_{seg}^A} \left(\mathbf{G}_{\Delta \mathbf{g}}^s \mathbf{d}_s + \sum_{t=1}^{n_{gp}^1} \mathbf{G}_{\Delta \mathbf{d} \mathbf{g}}^{st} \mathbf{d}_s^t \right), \quad \mathbf{G}_{\Delta \mathbf{d} \mathbf{g}}^{st} = \sum_{g=1}^{n_{gp}^s} (\mathbf{x}_g^2 - \mathbf{x}_g^1) \mathbf{B}_d^{tT} \det \mathbf{j} \mathbf{W}_g \in \mathbb{R}^{3 \times 24} \\
\mathbf{G}_{\Delta \mathbf{g}}^s &= \sum_{g=1}^{n_{gp}^s} \left(M_{Ag}^1 \mathbf{B}_{li} + M_{Ag}^1 (\mathbf{x}_g^2 - \mathbf{x}_g^1) \mathbf{B}_j^T + \left[M_{Ag,\alpha}^1 (\mathbf{x}_g^2 - \mathbf{x}_g^1) - M_{Ag}^1 \mathbf{x}_{g,\alpha}^1 \right] \mathbf{B}_{gp}^{1\alpha T} \right. \\
&\quad \left. + M_{Ag}^1 \mathbf{x}_{g,\alpha}^2 \mathbf{B}_{gp}^{2\alpha T} \right) \det \mathbf{j} \mathbf{W}_g \in \mathbb{R}^{3 \times 24},
\end{aligned} \tag{4.127}$$

submatrices are introduced containing all the contributions with regard to the standard displacement term and to the dual shape function part which has only to be added if dual shape functions are used. The matrix \mathbf{B}_{li} and its derivative $\mathbf{B}_{li,\alpha}^\beta$ can be found in (C.4). Additionally, the linearization of all the other kinematical quantities of section 4.3.4 will be listed here for completeness, like the gap vector at the old time step (4.91)

$$\Delta \bar{\mathbf{g}}_A^o = \sum_{s=1}^{n_{seg}^A} \mathbf{G}_{\Delta \mathbf{g}^o}^s \mathbf{d}_s, \quad \mathbf{G}_{\Delta \mathbf{g}^o}^s = \sum_{g=1}^{n_{gp}^s} M_{Ag}^1 \mathbf{B}_{li} \det \mathbf{j} \mathbf{W}_g \in \mathbb{R}^{3 \times 24}, \tag{4.128}$$

the virtual gap (4.97)

$$\delta \bar{\mathbf{g}}_A = \sum_{s=1}^{n_{seg}^A} \delta \mathbf{d}_s \mathbf{G}_{\delta \mathbf{g}}^s, \quad \mathbf{G}_{\delta \mathbf{g}}^s = \sum_{g=1}^{n_{gp}^s} M_{Ag}^1 \mathbf{B}_{li} \det \mathbf{j} \mathbf{W}_g \in \mathbb{R}^{24 \times 3}, \tag{4.129}$$

and its linearization

$$\begin{aligned}\Delta\delta\bar{\mathbf{g}}_A &= \sum_{s=1}^{n_{seg}^A} \delta\mathbf{d}_s \left(\mathbf{G}_{\Delta\delta\mathbf{g}}^s \mathbf{d}_s + \sum_{t=1}^{n_{gp}^1} \mathbf{G}_{\Delta_d\delta\mathbf{g}}^{st} \mathbf{d}_s^t \right), \quad \mathbf{G}_{\Delta_d\delta\mathbf{g}}^{st} = \sum_{g=1}^{n_{gp}^s} \mathbf{B}_{li} \mathbf{B}_d^{tT} \det \mathbf{j}W_g \in \mathbb{R}^{24 \times 24 \times 3} \\ \mathbf{G}_{\Delta\delta\mathbf{g}}^s &= \sum_{g=1}^{n_{gp}^s} \mathbf{B}_{li} \left(M_{Ag}^1 \mathbf{B}_j^T + M_{Ag,\alpha}^1 \mathbf{B}_{gp}^{1\alpha T} \right) \det \mathbf{j}W_g + \mathbf{B}_{li,\alpha}^\beta M_{Ag}^1 \mathbf{B}_{gp}^{\beta\alpha T} \det \mathbf{j}W_g \in \mathbb{R}^{24 \times 24 \times 3}.\end{aligned}\tag{4.130}$$

If no dual shape functions are used, the linearized Lagrange multiplier of (4.98) and the linearized slip increment read

$$\begin{aligned}\Delta\bar{\boldsymbol{\lambda}}_A &= \sum_{s=1}^{n_{seg}^A} \mathbf{G}_{\Delta\boldsymbol{\lambda}}^s \mathbf{d}_s, \quad \Delta\bar{\boldsymbol{\gamma}}_A = \sum_{s=1}^{n_{seg}^A} \mathbf{G}_{\Delta\boldsymbol{\gamma}}^s \mathbf{d}_s \\ \mathbf{G}_{\Delta\boldsymbol{\lambda}}^s &= \sum_{g=1}^{n_{gp}^s} M_{Ag}^1 \boldsymbol{\lambda}_g \mathbf{B}_j^T + \left[M_{Ag,\alpha}^1 \boldsymbol{\lambda}_g + M_{Ag}^1 \boldsymbol{\lambda}_{g,\alpha} \right] \mathbf{B}_{gp}^{1\alpha T} \det \mathbf{j}W_g \in \mathbb{R}^{3 \times 24} \\ \mathbf{G}_{\Delta\boldsymbol{\gamma}}^s &= \sum_{g=1}^{n_{gp}^s} \left(M_{Ag}^1 \boldsymbol{\gamma}_g \mathbf{B}_j + \left[M_{Ag,\alpha}^1 \boldsymbol{\gamma}_g + M_{Ag}^1 \boldsymbol{\gamma}_{g,\alpha} \right] \mathbf{B}_{gp}^{1\alpha} \right) \det \mathbf{j}W_g \in \mathbb{R}^{24}.\end{aligned}\tag{4.131}$$

In addition to the linearization with respect to the displacements, the vectors including the linearized Lagrange multipliers and the linearized slip increment of the slave element of each segment have to be stated

$$\mathbf{l}_s = [\Delta\boldsymbol{\lambda}_1, \dots, \Delta\boldsymbol{\lambda}_4]^T \in \mathbb{R}^{12}, \quad \mathbf{c}_s = [\Delta\boldsymbol{\gamma}_1, \dots, \Delta\boldsymbol{\gamma}_4]^T \in \mathbb{R}^4.\tag{4.132}$$

Within a contact code, normally, both vectors are combined to one, but for the sake of clearness the vectors are considered independently of each other. The linearization leads to the submatrices

$$\begin{aligned}\Delta\bar{\boldsymbol{\lambda}}_A &= \sum_{s=1}^{n_{seg}^A} \mathbf{L}_{\Delta\boldsymbol{\lambda}}^s \mathbf{l}_s, \quad \mathbf{L}_{\Delta\boldsymbol{\lambda}}^s = \sum_{g=1}^{n_{gp}^s} M_{Ag}^1 \mathbf{P}_{NB}^l \det \mathbf{j}W_g \in \mathbb{R}^{3 \times 12}, \\ \Delta\bar{\boldsymbol{\gamma}}_A &= \sum_{s=1}^{n_{seg}^A} \mathbf{C}_{\Delta\boldsymbol{\gamma}}^s \mathbf{c}_s, \quad \mathbf{C}_{\Delta\boldsymbol{\gamma}}^s = \sum_{g=1}^{n_{gp}^s} M_{Ag}^1 \mathbf{P}_{NB}^c \det \mathbf{j}W_g \in \mathbb{R}^4.\end{aligned}\tag{4.133}$$

where the projection tensors for the Lagrange multiplier and the slip increment are given in (C.5). The linearization of the alternative formulation of the kinematical quantities in section 4.3.4 can also be represented in vector form, but now the linearization of the base vectors has to be taken into account which results in two additional loops. Dual shape functions are neglected for the sake of clearness, but they can be added in

the same way as for the gap quantities listed above. For the normal contribution, the linearization of the normal penetration (4.100)

$$\begin{aligned}
\Delta \bar{g}_{NA} &= \sum_{s=1}^{n_{seg}^A} \left(\mathbf{G}_{\Delta \bar{g}_N}^s \mathbf{d}_s + \sum_{B=1}^n \sum_{a=1}^{n_{ae}^1} \mathbf{G}_{\Delta \mathbf{n}B}^{s a} \mathbf{d}_s^{B a} \right) \\
\mathbf{G}_{\Delta \bar{g}_N}^s &= \sum_{g=1}^{n_{gp}} \left(N_{Ag}^1 \mathbf{B}_{li} \mathbf{n}_g^1 + N_{Ag}^1 (\mathbf{x}_g^2 - \mathbf{x}_g^1) \cdot \mathbf{n}_g^1 \mathbf{B}_j + \left[M_{Ag,\alpha}^1 (\mathbf{x}_g^2 - \mathbf{x}_g^1) \cdot \mathbf{n}_g^1 \right. \right. \\
&\quad \left. \left. - N_{Ag}^1 \mathbf{x}_{g,\alpha}^1 \cdot \mathbf{n}_g^1 + N_{Ag}^1 (\mathbf{x}_g^2 - \mathbf{x}_g^1) \cdot \mathbf{n}_{g,\alpha}^1 \right] \mathbf{B}_{gp}^{1\alpha} + N_{Ag}^1 \mathbf{x}_{g,\alpha}^2 \cdot \mathbf{n}_g^1 \mathbf{B}_{gp}^{2\alpha} \right) \det \mathbf{j}W_g \in \mathbb{R}^{24} \\
\mathbf{G}_{\Delta \mathbf{n}B}^{s a} &= \sum_{g=1}^{n_{gp}} N_{Ag}^1 (\mathbf{x}_g^2 - \mathbf{x}_g^1) N_{Bg}^1 \mathbf{B}_{nB}^a \det \mathbf{j}W_g \in \mathbb{R}^{24},
\end{aligned} \tag{4.134}$$

its virtual counterpart (4.100)

$$\delta \bar{g}_{NA} = \sum_{s=1}^{n_{seg}^A} \delta \mathbf{d}_s \mathbf{G}_{\delta \bar{g}_N}^s, \quad \mathbf{G}_{\delta \bar{g}_N}^s = \sum_{g=1}^{n_{gp}} N_{Ag}^1 \mathbf{B}_{li} \mathbf{n}_g^1 \det \mathbf{j}W_g \in \mathbb{R}^{24} \tag{4.135}$$

and the linearization of the virtual normal penetration

$$\begin{aligned}
\Delta \delta \bar{g}_{NA} &= \sum_{s=1}^{n_{seg}^A} \delta \mathbf{d}_s \left(\mathbf{G}_{\Delta \delta \bar{g}_N}^s \mathbf{d}_s + \sum_{B=1}^n \sum_{a=1}^{n_{ae}^1} \mathbf{G}_{\delta \mathbf{n}B}^{s a} \mathbf{d}_s^{B a} \right) \\
\mathbf{G}_{\Delta \delta \bar{g}_N}^s &= \sum_{g=1}^{n_{gp}} \mathbf{B}_{li} \left(N_{Ag}^1 \mathbf{n}_g^1 \mathbf{B}_j^T + \left[M_{Ag,\alpha}^1 \mathbf{n}_g^1 + N_{Ag}^1 \mathbf{n}_{g,\alpha}^1 \right] \mathbf{B}_{gp}^{1\alpha,T} \right) \det \mathbf{j}W_g \\
&\quad + \mathbf{B}_{li,\alpha}^\beta N_{Ag}^1 \mathbf{n}_g^1 \mathbf{B}_{gp}^{\beta\alpha T} \det \mathbf{j}W_g \in \mathbb{R}^{24 \times 24} \\
\mathbf{G}_{\delta \mathbf{n}B}^{s a} &= \sum_{g=1}^{n_{gp}} \mathbf{B}_{li} N_{Ag}^1 N_{Bg}^1 \mathbf{B}_{nB}^{aT} \det \mathbf{j}W_g \in \mathbb{R}^{24 \times 24}
\end{aligned} \tag{4.136}$$

are also specified in vector form. In the same way, the tangential quantities can be discretized. The linearized tangential gap at the actual time step (4.101)

$$\begin{aligned}
\Delta \bar{g}_{T\alpha A} &= \sum_{s=1}^{n_{seg}^A} \left(\mathbf{G}_{\Delta \bar{g}_{T\alpha}}^s \mathbf{d}_s + \sum_{B=1}^n \sum_{a=1}^{n_{ae}^1} \mathbf{G}_{\Delta \mathbf{t}_{\alpha B}}^{s a} \mathbf{d}_s^{B a} \right) \\
\mathbf{G}_{\Delta \bar{g}_{T\alpha}}^s &= \sum_{g=1}^{n_{gp}} \left(N_{Ag}^1 \mathbf{B}_{li} \mathbf{t}_{\alpha g}^1 + N_{Ag}^1 (\mathbf{x}_g^2 - \mathbf{x}_g^1) \cdot \mathbf{t}_{\alpha g}^1 \mathbf{B}_j + \left[M_{Ag,\beta}^1 (\mathbf{x}_g^2 - \mathbf{x}_g^1) \cdot \mathbf{t}_{\alpha g}^1 \right. \right. \\
&\quad \left. \left. - N_{Ag}^1 \mathbf{x}_{g,\beta}^1 \cdot \mathbf{t}_{\alpha g}^1 + N_{Ag}^1 (\mathbf{x}_g^2 - \mathbf{x}_g^1) \cdot \mathbf{t}_{\alpha,\beta g}^1 \right] \mathbf{B}_{gp}^{1\beta} + N_{Ag}^1 \mathbf{x}_{g,\beta}^2 \cdot \mathbf{t}_{\alpha g}^1 \mathbf{B}_{gp}^{2\beta} \right) \det \mathbf{j}W_g \in \mathbb{R}^{2 \times 24} \\
\mathbf{G}_{\Delta \mathbf{t}_{\alpha B}}^{s a} &= \sum_{g=1}^{n_{gp}} N_{Ag}^1 (\mathbf{x}_g^2 - \mathbf{x}_g^1) N_{Bg}^1 \mathbf{B}_{t_{\alpha B}}^{a T} \det \mathbf{j}W_g \in \mathbb{R}^{2 \times 24},
\end{aligned} \tag{4.137}$$

and at the old time step (4.101), respectively, are specified in vector form as

$$\Delta \bar{g}_{T\alpha A}^o = \sum_{s=1}^{n_{seg}^A} \mathbf{G}_{\Delta \bar{g}_{T\alpha}^o}^s \mathbf{d}_s \quad \text{where} \quad \mathbf{G}_{\Delta \bar{g}_{T\alpha}^o}^s = \sum_{g=1}^{n_{gp}} N_{Ag}^1 \mathbf{B}_{li} \mathbf{t}_{\alpha g}^1 \det \mathbf{j}W_g \in \mathbb{R}^{2 \times 24}. \tag{4.138}$$

The virtual form (4.101)

$$\delta \bar{g}_{T\alpha A} = \sum_{s=1}^{n_{seg}^A} \delta \mathbf{d}_s \mathbf{G}_{\delta \bar{g}_{T\alpha}}^s \quad \text{where} \quad \mathbf{G}_{\delta \bar{g}_{T\alpha}}^s = \sum_{g=1}^{n_{gp}} N_{Ag}^1 \mathbf{B}_{li} \mathbf{n}_g^1 \det \mathbf{j}W_g \in \mathbb{R}^{24 \times 2} \tag{4.139}$$

and its linearization read

$$\begin{aligned}
\Delta \delta \bar{g}_{T\alpha A} &= \sum_{s=1}^{n_{seg}^A} \delta \mathbf{d}_s \left(\mathbf{G}_{\Delta \delta \bar{g}_{T\alpha}}^s \mathbf{d}_s + \sum_{B=1}^n \sum_{a=1}^{n_{ae}^1} \mathbf{G}_{\delta \mathbf{t}_{\alpha B}}^{s a} \mathbf{d}_s^{B a} \right) \\
\mathbf{G}_{\Delta \delta \bar{g}_{T\alpha}}^s &= \sum_{g=1}^{n_{gp}} \left[\mathbf{B}_{li} \left(N_{Ag}^1 \mathbf{t}_{\alpha g}^1 \mathbf{B}_j^T + \left[M_{Ag,\beta}^1 \mathbf{t}_{\alpha g}^1 + N_{Ag}^1 \mathbf{t}_{\alpha,\beta g}^1 \right] \mathbf{B}_{gp}^{1\beta T} \right) \right. \\
&\quad \left. + \mathbf{B}_{li,\beta}^\gamma N_{Ag}^1 \mathbf{t}_{\alpha g}^1 \mathbf{B}_{gp}^{\gamma \beta T} \right] \det \mathbf{j}W_g \in \mathbb{R}^{24 \times 24 \times 2} \\
\mathbf{G}_{\delta \mathbf{t}_{\alpha B}}^{s a} &= \sum_{g=1}^{n_{gp}} \mathbf{B}_{li} N_{Ag}^1 N_{Bg}^1 \mathbf{B}_{t_{\alpha B}}^{a T} \det \mathbf{j}W_g \in \mathbb{R}^{24 \times 24 \times 2}.
\end{aligned} \tag{4.140}$$

The last linearized quantities are the averaged normal and tangential Lagrange multipliers

$$\begin{aligned}
\Delta \bar{\lambda}_{NA} &= \sum_{s=1}^{n_{seg}^A} (\mathbf{G}_{\Delta \bar{\lambda}_N}^s \mathbf{d}_s + \mathbf{L}_{\Delta \bar{\lambda}_N}^s \mathbf{l}_s), & \Delta \bar{\lambda}_{T\alpha A} &= \sum_{s=1}^{n_{seg}^A} (\mathbf{G}_{\Delta \bar{\lambda}_{T\alpha}}^s \mathbf{d}_s + \mathbf{L}_{\Delta \bar{\lambda}_{T\alpha}}^s \mathbf{l}_s) \\
\mathbf{G}_{\Delta \bar{\lambda}_N}^s &= \sum_{g=1}^{n_{gp}} \left(N_{Ag}^1 \lambda_{Ng} \mathbf{B}_j + N_{Ag,\alpha}^1 \lambda_{Ng} \mathbf{B}_{gp}^{1\alpha} \right) \det \mathbf{j}W_g \in \mathbb{R}^{24} \\
\mathbf{G}_{\Delta \bar{\lambda}_{T\alpha}}^s &= \sum_{g=1}^{n_{gp}} \left(N_{Ag}^1 \lambda_{T\alpha g} \mathbf{B}_j + N_{Ag,\beta}^1 \lambda_{T\alpha g} \mathbf{B}_{gp}^{1\beta} \right) \det \mathbf{j}W_g \in \mathbb{R}^{2 \times 24} \\
\mathbf{L}_{\Delta \bar{\lambda}_N}^s &= N_{Ag}^1 \mathbf{P}_{N_B^1}^{ln} \det \mathbf{j}W_g \in \mathbb{R}^{12}, & \mathbf{L}_{\Delta \bar{\lambda}_{T\alpha}}^s &= N_{Ag}^1 \mathbf{P}_{N_B^1}^{lt\alpha} \det \mathbf{j}W_g \in \mathbb{R}^{2 \times 12}
\end{aligned} \tag{4.141}$$

where additional vector contributions due to the linearized nodal Lagrange multipliers of the slave surface

$$\mathbf{l}_s = [\Delta \lambda_{N1}, \Delta \lambda_{T11}, \Delta \lambda_{T21}, \dots, \Delta \lambda_{N4}, \Delta \lambda_{T14}, \Delta \lambda_{T24}]^T \in \mathbb{R}^{12} \tag{4.142}$$

have to be taken into account in combination with the projection vectors $\mathbf{P}_{N_B^1}^{ln}$, $\mathbf{P}_{N_B^1}^{lt\alpha}$ of the appendix C.5

4.3.6 Residual vector and tangent matrix

Four different solution methods are presented in this section, namely, the standard penalty formulation and the augmented Lagrangian method and for the first time a pure Lagrange multiplier method and a mixed version consisting of the augmented Lagrangian and the penalty method. The discretized contributions and the linearization of the weak form are indicated with an h and only the nodal contributions

$$G_u^{ch} = \sum_{A=1}^{n_s} G_{uA}^{ch}, \quad DG_u^{ch} = \sum_{A=1}^{n_s} DG_{uA}^{ch} \tag{4.143}$$

will be specified in detail. Additionally, in the Mortar method there can be cases where the slave node lies outside of the master surface. These nodes can be indicated, if the area of the slave node (4.99b) is equal to zero

$$\text{if } a_A = 0 \rightarrow \text{node inactive.} \tag{4.144}$$

In this section the stiffness matrices are determined for the case that a switch is used to distinguish between dual and standard shape functions. If dual shape functions are preferred, the assembling process can be simplified, since the terms with regard to the linearized Lagrange multipliers and to the slip increment are only needed for the actual slave node A , see also (4.99). Hence the vectors \mathbf{l}_s and \mathbf{c}_s can be replaced by the nodal contributions $\Delta \lambda_A$ and $\Delta \gamma_A$, respectively, and the size of the stiffness matrices has to be adjusted.

4.3.6.1 Lagrange multiplier method

The status of each slave node determines the residual vector and the stiffness matrix. For the pure Lagrange multiplier method based on (4.7), the transition from the actual status to the new one takes place, if one of the four possible inequalities

$$\begin{aligned} \text{inactive to active} &\rightarrow \bar{\mathbf{g}}_A \cdot \mathbf{n}_A \leq 0 & \text{active to inactive} &\rightarrow \bar{\boldsymbol{\lambda}}_A \cdot \mathbf{n}_A > 0 \\ \text{stick to slip} &\rightarrow f_c(\bar{\boldsymbol{\lambda}}_A) > 0 & \text{slip to stick} &\rightarrow \Delta_t \bar{\gamma}_A \leq 0 \end{aligned} \quad (4.145)$$

is fulfilled. The discretized form of the virtual contact work (4.8) is based on the formulation without base vectors

$$G_{uA}^{ch} = \delta \bar{\mathbf{g}}_A \cdot \boldsymbol{\lambda}_A = \sum_{s=1}^{n_{seg}^A} \delta \mathbf{d}_s \mathbf{R}_u^s, \quad \mathbf{R}_u^s = \mathbf{G}_{\delta \mathbf{g}}^s \boldsymbol{\lambda}_A \in \mathbb{R}^{24}. \quad (4.146)$$

The derivative of the discretized weak form leads to the stiffness matrix contributions

$$DG_{uA}^{ch} = \Delta \delta \bar{\mathbf{g}}_A \cdot \boldsymbol{\lambda}_A + \delta \bar{\mathbf{g}}_A \cdot \Delta \boldsymbol{\lambda}_A = \sum_{s=1}^{n_{seg}^A} \left(\delta \mathbf{d}_s \mathbf{K}_{uu}^s \mathbf{d}_s + \delta \mathbf{d}_s \sum_{t=1}^{n_{seg}^s} \mathbf{K}_{ut}^s \mathbf{d}_t + \delta \mathbf{d}_s \mathbf{K}_{ul}^s \Delta \boldsymbol{\lambda}_A \right) \quad (4.147)$$

where each tangent is formulated in terms of the contact vectors of section 4.3.5.2

$$\mathbf{K}_{uu}^s = \mathbf{G}_{\Delta \delta \mathbf{g}}^s \boldsymbol{\lambda}_A \in \mathbb{R}^{24 \times 24}, \quad \mathbf{K}_{ul}^s = \mathbf{G}_{\delta \mathbf{g}}^s \in \mathbb{R}^{24 \times 3}, \quad \mathbf{K}_{ut}^s = \mathbf{G}_{\Delta_d \delta \mathbf{g}}^s \boldsymbol{\lambda}_A \in \mathbb{R}^{24 \times 24}. \quad (4.148)$$

The discretization of the linearized contact constraints leads to the generic form

$$\begin{aligned} DG_{lA}^{ch} = \delta \boldsymbol{\lambda}_A \cdot \left[\sum_{s=1}^{n_{seg}^A} \left(\mathbf{K}_{lu}^s \mathbf{d}_s + \sum_{t=1}^{n_{seg}^s} \mathbf{K}_{lut}^s \mathbf{d}_t^t + \mathbf{K}_{ll}^s \mathbf{l}_s + \mathbf{K}_{lc}^s \mathbf{c}_s \right) + \sum_{a=1}^{n_{ae}^1} \mathbf{K}_{lu}^a \mathbf{d}_a \right] \\ + \delta \gamma_A \left(\sum_{s=1}^{n_{seg}^A} \left(\mathbf{K}_{cu}^s \mathbf{d}_s + \sum_{t=1}^{n_{seg}^s} \mathbf{K}_{cut}^s \mathbf{d}_t^t + \mathbf{K}_{cl}^s \mathbf{l}_s + \mathbf{K}_{cc}^s \mathbf{c}_s \right) + \sum_{a=1}^{n_{ae}^1} \mathbf{K}_{cu}^a \mathbf{d}_a \right] \end{aligned} \quad (4.149)$$

where for each status the submatrices have to be specified and matrices which are not formulated explicitly are then equal to zero. If the slave node sticks on the other body, the discretized nodal weak form of (4.9)

$$G_{lA}^{ch} = \delta \boldsymbol{\lambda}_A \cdot \left[\mathbf{n}_A \bar{\mathbf{g}}_A \cdot \mathbf{n}_A + \mathbf{t}_{A\alpha} (\bar{\mathbf{g}}_A - \bar{\mathbf{g}}_A^o) \cdot \mathbf{t}_{A\alpha} \right] + \delta \gamma_A \frac{1}{c_c} \Delta_t \bar{\gamma}_A. \quad (4.150)$$

has not to be modified before it is sent to the global assembly routine. The linearization of the stick equation

$$\begin{aligned} DG_{lA}^{ch} = \delta \boldsymbol{\lambda}_A \cdot \left[\Delta \mathbf{n}_A \bar{\mathbf{g}}_A \cdot \mathbf{n}_A + \delta \boldsymbol{\lambda}_A \cdot \mathbf{n}_A \Delta \bar{\mathbf{g}}_A \cdot \mathbf{n}_A + \delta \boldsymbol{\lambda}_A \cdot \mathbf{n}_A \bar{\mathbf{g}}_A \cdot \Delta \mathbf{n}_A \right. \\ \left. + \Delta \mathbf{t}_{A\alpha} (\bar{\mathbf{g}}_A - \bar{\mathbf{g}}_A^o) \cdot \mathbf{t}_{A\alpha} + \mathbf{t}_{A\alpha} (\Delta \bar{\mathbf{g}}_A - \Delta \bar{\mathbf{g}}_A^o) \cdot \mathbf{t}_{A\alpha} + \mathbf{t}_{A\alpha} (\bar{\mathbf{g}}_A - \bar{\mathbf{g}}_A^o) \cdot \Delta \mathbf{t}_{A\alpha} \right] \\ + \delta \gamma_A \frac{1}{c_c} \Delta \bar{\gamma}_A \end{aligned} \quad (4.151)$$

delivers the matrix contributions

$$\begin{aligned}
\mathbf{K}_{lu}^s &= \left(\mathbf{n}_A \mathbf{G}_{\Delta \mathbf{g}}^s \mathbf{n}_A + \mathbf{t}_{A\alpha} \left(\mathbf{G}_{\Delta \mathbf{g}}^s - \mathbf{G}_{\Delta \mathbf{g}^o} \right) \mathbf{t}_{A\alpha} \right) \in \mathbb{R}^{3 \times 24} \\
\mathbf{K}_{lu}^a &= \left(\mathbf{B}_n^a \bar{\mathbf{g}}_A \cdot \mathbf{n}_A + \mathbf{n}_A \bar{\mathbf{g}}_A \mathbf{B}_n^a + \mathbf{B}_{t_\alpha}^a (\bar{\mathbf{g}}_A - \bar{\mathbf{g}}_A^o) \cdot \mathbf{t}_{A\alpha} + \mathbf{t}_{A\alpha} (\bar{\mathbf{g}}_A - \bar{\mathbf{g}}_A^o) \mathbf{B}_{t_\alpha}^a \right) \in \mathbb{R}^{3 \times 24} \\
\mathbf{K}_{lut}^s &= \left(\mathbf{n}_A \mathbf{G}_{\Delta d \mathbf{g}}^{st} \mathbf{n}_A + \mathbf{t}_{A\alpha} \mathbf{G}_{\Delta d \mathbf{g}}^{st} \mathbf{t}_{A\alpha} \right) \in \mathbb{R}^{3 \times 24}, \quad \mathbf{K}_{cu}^s = \frac{1}{c_C} \mathbf{G}_{\Delta \gamma}^s \in \mathbb{R}^{24}, \quad \mathbf{K}_{cc}^s = \frac{1}{c_C} \mathbf{C}_{\Delta \gamma}^s \in \mathbb{R}^4.
\end{aligned} \tag{4.152}$$

For a slave node which slips on the other surface, the nodal discretized weak form of (4.10) using the norm of the tangential Lagrange multiplier in (4.88)

$$G_{lA}^{ch} = \delta \boldsymbol{\lambda}_A \cdot \left[\mathbf{n}_A \bar{\mathbf{g}}_A \cdot \mathbf{n}_A + \mathbf{t}_{A\alpha} \left[\left(\bar{\mathbf{g}}_A - \bar{\mathbf{g}}_A^o \right) \cdot \mathbf{t}_{A\alpha} - \Delta_t \bar{\gamma}_A \frac{\bar{\boldsymbol{\lambda}}_A \cdot \mathbf{t}_{A\alpha}}{\|\bar{\boldsymbol{\lambda}}_{TA}\|} \right] + \delta \gamma_A f_c(\bar{\boldsymbol{\lambda}}_A) \right] \tag{4.153}$$

and its linearized form

$$\begin{aligned}
DG_{lA} &= \delta \boldsymbol{\lambda}_A \cdot \left[\Delta \mathbf{n}_A \bar{\mathbf{g}}_A \cdot \mathbf{n}_A + \mathbf{n}_A \Delta \bar{\mathbf{g}}_A \cdot \mathbf{n}_A + \mathbf{n}_A \bar{\mathbf{g}}_A \cdot \Delta \mathbf{n}_A \right. \\
&\quad + \Delta \mathbf{t}_{A\alpha} \left[\left(\bar{\mathbf{g}}_A - \bar{\mathbf{g}}_A^o \right) \cdot \mathbf{t}_{A\alpha} - \Delta_t \bar{\gamma}_A \frac{\bar{\boldsymbol{\lambda}}_A \cdot \mathbf{t}_{A\alpha}}{\|\bar{\boldsymbol{\lambda}}_{TA}\|} \right] + \mathbf{t}_{A\alpha} \left[\left(\Delta \bar{\mathbf{g}}_A - \Delta \bar{\mathbf{g}}_A^o \right) \cdot \mathbf{t}_{A\alpha} \right. \\
&\quad + \left(\bar{\mathbf{g}}_A - \bar{\mathbf{g}}_A^o \right) \cdot \Delta \mathbf{t}_{A\alpha} - \Delta \bar{\gamma}_A \frac{\bar{\boldsymbol{\lambda}}_A \cdot \mathbf{t}_{A\alpha}}{\|\bar{\boldsymbol{\lambda}}_{TA}\|} - \Delta_t \bar{\gamma}_A \frac{\Delta \bar{\boldsymbol{\lambda}}_A \cdot \mathbf{t}_{A\alpha} + \bar{\boldsymbol{\lambda}}_A \cdot \Delta \mathbf{t}_{A\alpha}}{\|\bar{\boldsymbol{\lambda}}_{TA}\|} \\
&\quad \left. \left. + \Delta_t \bar{\gamma}_A \frac{[\bar{\boldsymbol{\lambda}}_A \cdot \mathbf{t}_{A\alpha} \Delta \bar{\boldsymbol{\lambda}}_A \cdot \mathbf{t}_{A\beta}] (\Delta \bar{\boldsymbol{\lambda}}_A \cdot \mathbf{t}_{A\beta} + \bar{\boldsymbol{\lambda}}_A \cdot \Delta \mathbf{t}_{A\beta})}{\|\bar{\boldsymbol{\lambda}}_{TA}\|^3} \right] \right. \\
&\quad \left. + \delta \gamma_A \left[\frac{\Delta \bar{\boldsymbol{\lambda}}_A \cdot \mathbf{t}_{A\alpha} + \bar{\boldsymbol{\lambda}}_A \cdot \Delta \mathbf{t}_{A\alpha}}{\|\bar{\boldsymbol{\lambda}}_{TA}\|} - \mu \operatorname{sign}(\bar{\boldsymbol{\lambda}}_A \cdot \mathbf{n}_A) (\Delta \bar{\boldsymbol{\lambda}}_A \cdot \mathbf{n}_A + \bar{\boldsymbol{\lambda}}_A \cdot \Delta \mathbf{n}_A) \right] \right] \tag{4.154}
\end{aligned}$$

lead to the matrix contributions for the slip case where now the standard displacement

$$\begin{aligned}
\mathbf{K}_{lu}^s &= \mathbf{n}_A \mathbf{G}_{\Delta \mathbf{g}}^s \mathbf{n}_A + \mathbf{t}_{A\alpha} \left[\left(\mathbf{G}_{\Delta \mathbf{g}}^s - \mathbf{G}_{\Delta \mathbf{g}^o} \right) \mathbf{t}_{A\alpha} - \frac{\bar{\boldsymbol{\lambda}}_A \cdot \mathbf{t}_{A\alpha}}{\|\bar{\boldsymbol{\lambda}}_{TA}\|} \mathbf{G}_{\Delta \gamma}^s \right. \\
&\quad \left. - \Delta_t \bar{\gamma}_A \left(\frac{\mathbf{1}_{\alpha\beta}}{\|\bar{\boldsymbol{\lambda}}_{TA}\|} - \frac{\bar{\boldsymbol{\lambda}}_A \cdot \mathbf{t}_{A\alpha} \bar{\boldsymbol{\lambda}}_A \cdot \mathbf{t}_{A\beta}}{\|\bar{\boldsymbol{\lambda}}_{TA}\|^3} \right) \mathbf{t}_{A\beta} \mathbf{G}_{\Delta \lambda}^s \right] \in \mathbb{R}^{3 \times 24}, \\
\mathbf{K}_{cu}^s &= \left(\frac{\bar{\boldsymbol{\lambda}}_A \cdot \mathbf{t}_{A\alpha} \mathbf{t}_{A\alpha}}{\|\bar{\boldsymbol{\lambda}}_{TA}\|} - \mu \operatorname{sign}(\bar{\boldsymbol{\lambda}}_A \cdot \mathbf{n}_A) \mathbf{n}_A \right) \mathbf{G}_{\Delta \lambda}^s \in \mathbb{R}^{24},
\end{aligned} \tag{4.155}$$

the dual shape function

$$\begin{aligned} \mathbf{K}_{lut}^s &= \mathbf{n}_A \mathbf{G}_{\Delta d \mathbf{g}}^{st} \mathbf{n}_A + \mathbf{t}_{A\alpha} \left[\mathbf{G}_{\Delta d \mathbf{g}}^{st} \cdot \mathbf{t}_{A\alpha} - \frac{\bar{\boldsymbol{\lambda}}_A \cdot \mathbf{t}_{A\alpha}}{\|\bar{\boldsymbol{\lambda}}_{TA}\|} \mathbf{G}_{\Delta d \gamma}^{st} \right. \\ &\quad \left. - \Delta_t \bar{\gamma}_A \left(\frac{\mathbf{1}_{\alpha\beta}}{\|\bar{\boldsymbol{\lambda}}_{TA}\|} - \frac{\bar{\boldsymbol{\lambda}}_A \cdot \mathbf{t}_{A\alpha} \bar{\boldsymbol{\lambda}}_A \cdot \mathbf{t}_{A\beta}}{\|\bar{\boldsymbol{\lambda}}_{TA}\|^3} \right) \mathbf{t}_{A\beta} \right] \mathbf{G}_{\Delta d \boldsymbol{\lambda}}^{st} \in \mathbb{R}^{3 \times 24}, \\ \mathbf{K}_{cut}^s &= \left(\frac{\bar{\boldsymbol{\lambda}}_A \cdot \mathbf{t}_{A\alpha} \mathbf{t}_{A\alpha}}{\|\bar{\boldsymbol{\lambda}}_{TA}\|} - \mu \operatorname{sign}(\bar{\boldsymbol{\lambda}}_A \cdot \mathbf{n}_A) \mathbf{n}_A \right) \mathbf{G}_{\Delta d \boldsymbol{\lambda}}^{st} \in \mathbb{R}^{24}, \end{aligned} \quad (4.156)$$

the Lagrange multiplier

$$\begin{aligned} \mathbf{K}_{ll}^s &= -\mathbf{t}_{A\alpha} \Delta_t \bar{\gamma}_A \left(\frac{\mathbf{1}_{\alpha\beta}}{\|\bar{\boldsymbol{\lambda}}_{TA}\|} - \frac{\bar{\boldsymbol{\lambda}}_A \cdot \mathbf{t}_{A\alpha} \bar{\boldsymbol{\lambda}}_A \cdot \mathbf{t}_{A\beta}}{\|\bar{\boldsymbol{\lambda}}_{TA}\|^3} \right) \mathbf{t}_{A\beta} \mathbf{G}_{\Delta \boldsymbol{\lambda}}^s \in \mathbb{R}^{3 \times 12} \\ \mathbf{K}_{cl}^s &= \left[\frac{\bar{\boldsymbol{\lambda}}_A \cdot \mathbf{t}_{A\alpha} \mathbf{t}_{A\alpha}}{\|\bar{\boldsymbol{\lambda}}_{TA}\|} - \mu \operatorname{sign}(\bar{\boldsymbol{\lambda}}_A \cdot \mathbf{n}_A) \mathbf{n}_A \right] \mathbf{G}_{\Delta \boldsymbol{\lambda}}^s \in \mathbb{R}^{12}, \end{aligned} \quad (4.157)$$

the slip increment

$$\mathbf{K}_{lc}^s = -\mathbf{t}_{A\alpha} \frac{\bar{\boldsymbol{\lambda}}_A \cdot \mathbf{t}_{A\alpha}}{\|\bar{\boldsymbol{\lambda}}_{TA}\|} \mathbf{G}_{\Delta \gamma}^s \in \mathbb{R}^{3 \times 4} \quad (4.158)$$

and the base vector parts are stated separately

$$\begin{aligned} \mathbf{K}_{lua}^s &= \mathbf{B}_n^a \bar{\mathbf{g}}_A \cdot \mathbf{n}_A + \mathbf{n}_A \bar{\mathbf{g}}_A \cdot \mathbf{B}_n^a + \mathbf{B}_{t_\alpha}^a (\bar{\mathbf{g}}_A - \bar{\mathbf{g}}_A^o) \cdot \mathbf{t}_{A\alpha} + \mathbf{t}_{A\alpha} \left[(\bar{\mathbf{g}}_A - \bar{\mathbf{g}}_A^o) \cdot \mathbf{B}_{t_\alpha}^a \right. \\ &\quad \left. - \Delta_t \bar{\gamma}_A \left(\frac{\mathbf{1}_{\alpha\beta}}{\|\bar{\boldsymbol{\lambda}}_{TA}\|} - \frac{\bar{\boldsymbol{\lambda}}_A \cdot \mathbf{t}_{A\alpha} \bar{\boldsymbol{\lambda}}_A \cdot \mathbf{t}_{A\beta}}{\|\bar{\boldsymbol{\lambda}}_{TA}\|^3} \right) \bar{\boldsymbol{\lambda}}_A \mathbf{B}_{t_\beta}^a \right] \in \mathbb{R}^{3 \times 24} \\ \mathbf{K}_{cua}^s &= \frac{\bar{\boldsymbol{\lambda}}_A \cdot \mathbf{t}_{A\alpha} \bar{\boldsymbol{\lambda}}_A}{\|\bar{\boldsymbol{\lambda}}_{TA}\|} \mathbf{B}_{t_\alpha}^a - \mu \operatorname{sign}(\bar{\boldsymbol{\lambda}}_A \cdot \mathbf{n}_A) \bar{\boldsymbol{\lambda}}_A \mathbf{B}_n^a \in \mathbb{R}^{24}. \end{aligned} \quad (4.159)$$

For nodes which are not in contact, the normal pressure, the tangential stress and the slip increment have to be zero. The discretized nodal weak form of (4.11)

$$G_{lA}^{ch} = \delta \boldsymbol{\lambda}_A \cdot \left[\mathbf{n}_A \frac{1}{c_N} \bar{\boldsymbol{\lambda}}_A \cdot \mathbf{n}_A + \mathbf{t}_{A\alpha} \frac{1}{c_T} \bar{\boldsymbol{\lambda}}_A \cdot \mathbf{t}_{A\alpha} \right] + \delta \gamma_A \frac{1}{c_C} \Delta_t \bar{\gamma}_A \quad (4.160)$$

has also to be linearized

$$\begin{aligned} DG_{lA}^{ch} &= \delta \boldsymbol{\lambda}_A \cdot \left[\Delta \mathbf{n}_A \frac{1}{c_N} \bar{\boldsymbol{\lambda}}_A \cdot \mathbf{n}_A + \mathbf{n}_A \frac{1}{c_N} \Delta \bar{\boldsymbol{\lambda}}_A \cdot \mathbf{n}_A + \mathbf{n}_A \frac{1}{c_N} \bar{\boldsymbol{\lambda}}_A \cdot \Delta \mathbf{n}_A \right. \\ &\quad \left. + \Delta \mathbf{t}_{A\alpha} \frac{1}{c_T} \bar{\boldsymbol{\lambda}}_A \cdot \mathbf{t}_{A\alpha} + \mathbf{t}_{A\alpha} \frac{1}{c_T} \Delta \bar{\boldsymbol{\lambda}}_A \cdot \mathbf{t}_{A\alpha} + \mathbf{t}_{A\alpha} \frac{1}{c_T} \bar{\boldsymbol{\lambda}}_A \cdot \Delta \mathbf{t}_{A\alpha} \right] + \delta \gamma_A \frac{1}{c_C} \Delta \bar{\gamma}_A. \end{aligned} \quad (4.161)$$

leading to the stiffness matrix contributions

$$\begin{aligned}
\mathbf{K}_{lu}^s &= \mathbf{n}_A \frac{1}{c_N} \mathbf{G}_{\Delta\lambda}^s \mathbf{n}_A + \mathbf{t}_{A\alpha} \frac{1}{c_T} \mathbf{G}_{\Delta\lambda}^s \cdot \mathbf{t}_{A\alpha} \in \mathbb{R}^{3 \times 24}, \quad \mathbf{K}_{cu}^s = \frac{1}{c_C} \mathbf{G}_{\Delta\gamma}^s \in \mathbb{R}^{24} \\
\mathbf{K}_{lut}^s &= \mathbf{n}_A \frac{1}{c_N} \mathbf{G}_{\Delta_d\lambda}^{st} \mathbf{n}_A + \mathbf{t}_{A\alpha} \frac{1}{c_T} \mathbf{G}_{\Delta_d\lambda}^{st} \cdot \mathbf{t}_{A\alpha} \in \mathbb{R}^{3 \times 24}, \quad \mathbf{K}_{cut}^s = \frac{1}{c_C} \mathbf{G}_{\Delta_d\gamma}^{st} \in \mathbb{R}^{24} \\
\mathbf{K}_{ll}^s &= \left[\mathbf{n}_A \frac{1}{c_N} \mathbf{n}_A + \mathbf{t}_{A\alpha} \frac{1}{c_T} \mathbf{t}_{A\alpha} \right] \mathbf{L}_{\Delta\lambda}^s \in \mathbb{R}^{3 \times 12} \\
\mathbf{K}_{lua} &= \mathbf{B}_n^a \frac{1}{c_N} \bar{\lambda}_A \cdot \mathbf{n}_A + \mathbf{n}_A \frac{1}{c_N} \bar{\lambda}_A \cdot \mathbf{B}_n^a + \mathbf{B}_{t_\alpha}^a \frac{1}{c_T} \bar{\lambda}_A \cdot \mathbf{t}_{A\alpha} + \mathbf{t}_{A\alpha} \frac{1}{c_T} \bar{\lambda}_A \cdot \mathbf{B}_{t_\alpha}^a \in \mathbb{R}^{3 \times 24}.
\end{aligned} \tag{4.162}$$

4.3.6.2 Penalty method

In the case of the Mortar method, based on a description in terms of the averaged gap vector, the normal and the tangential stress components read for the penalty regularization

$$\begin{aligned}
\bar{\lambda}_{NA} &= c_N \bar{\mathbf{g}}_A \cdot \mathbf{n}_A \\
\bar{\lambda}_{T\alpha A} &= -c_T \left[(\bar{\mathbf{g}}_A - \bar{\mathbf{g}}_A^o) \cdot \mathbf{t}_{A\alpha} + \Delta_t \bar{\gamma}_A \frac{\bar{\lambda}_A \cdot \mathbf{t}_{A\alpha}}{\|\bar{\lambda}_{TA}\|} \right] + \lambda_{T\alpha A} n, \quad \bar{\lambda}_{TA} = \sqrt{(\bar{\lambda}_A \cdot \mathbf{t}_{A\alpha})^2}.
\end{aligned} \tag{4.163}$$

The decision, if the node is active or inactive, depends only on the sign of the gap vector multiplied with the nodal normal vector (4.15)

$$\bar{\mathbf{g}}_A \cdot \mathbf{n}_A \leq \delta \rightarrow \text{node active} \quad \bar{\mathbf{g}}_A \cdot \mathbf{n}_A > \delta \rightarrow \text{node inactive.} \tag{4.164}$$

Depending on the value of the trial slip criterion

$$\begin{aligned}
\bar{\lambda}_{T\alpha A}^{tr} &= -c_T [(\bar{\mathbf{g}}_A - \bar{\mathbf{g}}_A^o) \cdot \mathbf{t}_{A\alpha}] + \bar{\lambda}_{T\alpha A} n, \\
f(\bar{\lambda}_{TA}^{tr}) &= \|\bar{\lambda}_{TA}^{tr}\| - \mu |\bar{\lambda}_{NA}|
\end{aligned} \tag{4.165}$$

and on the tolerance δ , the node either sticks on or slips along the other surface

$$\begin{aligned}
\text{stick : } \bar{\lambda}_{T\alpha A} &= \bar{\lambda}_{T\alpha A}^{tr} & \text{if } \frac{f(\bar{\lambda}_{TA}^{tr})}{c_T} \leq \delta \\
\text{slip : } \bar{\lambda}_{T\alpha A} &= \mu |\bar{\lambda}_{NA}| \frac{\bar{\lambda}_{T\alpha A}^{tr}}{\|\bar{\lambda}_{TA}^{tr}\|} & \text{if } \frac{f(\bar{\lambda}_{TA}^{tr})}{c_T} > \delta.
\end{aligned} \tag{4.166}$$

Since no Lagrange multipliers are applied for the penalty method, no dual shape functions have to be used. Based on (4.16), only one nodal discretized weak form is needed

for the description of the virtual contact work and the enforcement of the contact constraints

$$G_{uA}^{ch} = \delta \bar{\mathbf{g}} \cdot \left[\mathbf{n}_A c_N \bar{\mathbf{g}}_A \cdot \mathbf{n}_A + \mathbf{t}_{A\alpha} \bar{\lambda}_{T\alpha A} \right] = \sum_{s=1}^{n_{seg}^A} \delta \mathbf{d}_s \cdot \mathbf{R}_u^s \quad (4.167)$$

$$\mathbf{R}_u^s = \mathbf{G}_{\delta \mathbf{g}}^s \left[\mathbf{n}_A c_N \bar{\mathbf{g}}_A \cdot \mathbf{n}_A + \mathbf{t}_{A\alpha} \bar{\lambda}_{T\alpha A} \right] \in \mathbb{R}^{24}.$$

The linearization of the contact weak form is also independent of the type of the constraint

$$\begin{aligned} DG_{uA}^{ch} = & \Delta \delta \bar{\mathbf{g}} \cdot \left(\mathbf{n}_A c_N \bar{\mathbf{g}}_A \cdot \mathbf{n}_A + \mathbf{t}_{A\alpha} \bar{\lambda}_{T\alpha A} \right) + \delta \bar{\mathbf{g}} \cdot \left(\Delta \mathbf{n}_A c_N \bar{\mathbf{g}}_A \cdot \mathbf{n}_A \right. \\ & + \mathbf{n}_A c_N \Delta \bar{\mathbf{g}}_A \cdot \mathbf{n}_A + \mathbf{n}_A c_N \bar{\mathbf{g}}_A \cdot \Delta \mathbf{n}_A + \Delta \mathbf{t}_{A\alpha} \bar{\lambda}_{T\alpha A} \\ & + \mathbf{t}_{A\alpha} \bar{D}_{A\alpha\beta} \left[(\Delta \bar{\mathbf{g}}_A - \Delta \bar{\mathbf{g}}_A^o) \cdot \mathbf{t}_{A\beta} + (\bar{\mathbf{g}}_A - \bar{\mathbf{g}}_A^o) \cdot \Delta \mathbf{t}_{A\beta} \right] \\ & \left. + \mathbf{t}_{A\alpha} \bar{L}_{A\alpha} \left[\Delta \bar{\mathbf{g}}_A \cdot \mathbf{n}_A + \bar{\mathbf{g}}_A \cdot \Delta \mathbf{n}_A \right] \right). \end{aligned} \quad (4.168)$$

Only the matrices $\bar{D}_{A\alpha\beta}$ and $\bar{L}_{A\alpha}$ have to be adjusted for the stick

$$\bar{D}_{A\alpha\beta} = -c_T 1_{\alpha\beta}, \quad \bar{L}_{A\alpha} = 0_\alpha \quad (4.169)$$

or for the slip case

$$\bar{D}_{A\alpha\beta} = -\mu |\bar{\lambda}_{NA}| \left[\frac{1_{\alpha\beta}}{\|\bar{\lambda}_{TA}^{tr}\|} - \frac{\bar{\lambda}_{T\alpha A}^{tr} \bar{\lambda}_{T\beta A}^{tr}}{\|\bar{\lambda}_{TA}^{tr}\|^3} \right] c_T, \quad \bar{L}_{A\alpha} = \mu \operatorname{sign}(\bar{\lambda}_{NA}) \frac{\bar{\lambda}_{T\alpha A}^{tr}}{\|\bar{\lambda}_{TA}^{tr}\|}. \quad (4.170)$$

Based on the scheme for the stiffness matrices

$$DG_{uA}^{ch} = \delta \mathbf{d}_s \cdot \sum_{s=1}^{n_{seg}^A} \left(\mathbf{K}_{uu}^s \mathbf{d}_s + \sum_{r=1}^{n_{seg}^A} \mathbf{K}_{ur}^s \mathbf{d}_r + \sum_{a=1}^{n_{ae}^1} \mathbf{K}_{ua}^a \mathbf{d}_a \right), \quad (4.171)$$

the individual contributions are given as

$$\begin{aligned} \mathbf{K}_{uu}^s &= \mathbf{G}_{\Delta \delta \mathbf{g}}^s \left[\mathbf{n}_A c_N \bar{\mathbf{g}}_A \cdot \mathbf{n}_A + \mathbf{t}_{A\alpha} \bar{\lambda}_{T\alpha A} \right] \in \mathbb{R}^{24 \times 24} \\ \mathbf{K}_{ur}^s &= \mathbf{G}_{\delta \mathbf{g}}^s \mathbf{n}_A \left[c_N \mathbf{G}_{\Delta \mathbf{g}}^r \mathbf{n}_A \right] + \mathbf{G}_{\delta \mathbf{g}}^s \mathbf{t}_{A\alpha} \left[\bar{D}_{A\alpha\beta} (\mathbf{G}_{\Delta \mathbf{g}}^r - \mathbf{G}_{\Delta \mathbf{g}^o}^r) \mathbf{t}_{A\beta} + \bar{L}_{A\alpha} \mathbf{G}_{\Delta \mathbf{g}}^r \mathbf{n}_A \right] \in \mathbb{R}^{24 \times 24} \\ \mathbf{K}_{ua}^s &= \left(\mathbf{B}_n^a c_N \bar{\mathbf{g}}_A \cdot \mathbf{n}_A + \mathbf{n}_A c_N \bar{\mathbf{g}}_A \cdot \mathbf{B}_n^a + \mathbf{B}_{t\alpha}^a \bar{\lambda}_{T\alpha A} \right. \\ & \quad \left. + \mathbf{t}_{A\alpha} \bar{D}_{A\alpha\beta} (\bar{\mathbf{g}}_A - \bar{\mathbf{g}}_A^o) \mathbf{B}_{t\beta}^a + \mathbf{t}_{A\alpha} \bar{L}_{A\alpha} \bar{\mathbf{g}}_A \cdot \mathbf{B}_n^a \right) \in \mathbb{R}^{24 \times 24}. \end{aligned} \quad (4.172)$$

The additional loop in (4.171) over all segments (r) of the slave node leads to a coupled matrix of the segments (s) and (r) which rises the effort in the assembly process and slows down the solution process.

4.3.6.3 Augmented Lagrange multiplier method

For the augmented method, the two nonlinear complementarity functions of (4.18) determine the actual state of the slave node

$$\begin{aligned} \text{if } \hat{\lambda}_{NA} &< \delta \rightarrow \text{active else inactive} \\ \text{if } \|\hat{\lambda}_{TA}\| - \mu|\hat{\lambda}_{NA}| &\leq \delta \rightarrow \text{stick else slip} \end{aligned} \quad (4.173)$$

where for the ease of clearness, in the following implementations, the augmented components

$$\begin{aligned} \hat{\lambda}_{NA} &= (\bar{\lambda}_A + c_N \bar{\mathbf{g}}_A) \cdot \mathbf{n}_A \\ \hat{\lambda}_{TA} &= [\bar{\lambda}_A - c_T (\bar{\mathbf{g}}_A - \bar{\mathbf{g}}_A^o)] \cdot \mathbf{t}_{A\alpha}, \quad \|\hat{\lambda}_{TA}\| = \sqrt{\hat{\lambda}_{TA\alpha} \hat{\lambda}_{TA\alpha}} \end{aligned} \quad (4.174)$$

are introduced. The weak form of the virtual contact work remains the same as for the Lagrange multiplier method (4.146)

$$G_{uA}^{ch} = \delta \bar{\mathbf{g}}_A \cdot \lambda_A = \sum_{s=1}^{n_{seg}^A} \delta \mathbf{d}_s \mathbf{R}_u^s, \quad \mathbf{R}_u^s = \mathbf{G}_{\delta \mathbf{g}}^s \lambda_A \in \mathbb{R}^{24}.$$

and hence the linearized form is also equal to (4.147)

$$\begin{aligned} DG_{uA}^{ch} &= \Delta \delta \bar{\mathbf{g}}_A \cdot \lambda_A + \delta \bar{\mathbf{g}}_A \cdot \Delta \lambda_A \\ &= \sum_{s=1}^{n_{seg}^A} \left(\delta \mathbf{d}_s \mathbf{K}_{uu}^s \mathbf{d}_s + \delta \mathbf{d}_s \sum_{t=1}^{n_{seg}^s} \mathbf{K}_{ut}^s \mathbf{d}_t + \delta \mathbf{d}_s \mathbf{K}_{ul}^s \Delta \lambda_A \right) \end{aligned}$$

where the matrices can be taken from (4.148). Additionally, for slave nodes which stick on the master surface, the weak enforcement of the constraint corresponds to the expression of the Lagrange multiplier method (4.150), although the additional part of the slip increment is dropped

$$G_{lA}^{ch} = \delta \lambda_A \cdot \left[\mathbf{n}_A \bar{\mathbf{g}}_A \cdot \mathbf{n}_A + \mathbf{t}_{A\alpha} (\bar{\mathbf{g}}_A - \bar{\mathbf{g}}_A^o) \cdot \mathbf{t}_{A\alpha} \right] \quad (4.175)$$

as can be seen in the nodal weak form of the augmented method (4.22). The linearized expression is then similar to (4.151)

$$\begin{aligned} DG_{lA}^{ch} &= \delta \lambda_A \cdot \left[\Delta \mathbf{n}_A \bar{\mathbf{g}}_A \cdot \mathbf{n}_A + \mathbf{n}_A \Delta \bar{\mathbf{g}}_A \cdot \mathbf{n}_A + \mathbf{n}_A \bar{\mathbf{g}}_A \cdot \Delta \mathbf{n}_A \right. \\ &\quad \left. + \Delta \mathbf{t}_{A\alpha} (\bar{\mathbf{g}}_A - \bar{\mathbf{g}}_A^o) \cdot \mathbf{t}_{A\alpha} + \mathbf{t}_{A\alpha} (\Delta \bar{\mathbf{g}}_A - \Delta \bar{\mathbf{g}}_A^o) \cdot \mathbf{t}_{A\alpha} + \mathbf{t}_{A\alpha} (\bar{\mathbf{g}}_A - \bar{\mathbf{g}}_A^o) \cdot \Delta \mathbf{t}_{A\alpha} \right]. \end{aligned} \quad (4.176)$$

The generic structure of the discretized nodal weak constraints in terms of the stiffness matrices for the stick, the slip and the inactive case is given as

$$DG_{lA}^{ch} = \delta \lambda_A \cdot \left[\sum_{s=1}^{n_{seg}^A} \left(\mathbf{K}_{lu}^s \mathbf{d}_s + \sum_{t=1}^{n_{seg}^s} \mathbf{K}_{ut}^s \mathbf{d}_t + \mathbf{K}_{ll}^s \mathbf{l}_s \right) + \sum_{a=1}^{n_{ae}^1} \mathbf{K}_{lu}^a \mathbf{d}_a \right] \quad (4.177)$$

where for the stick case the matrices are listed in (4.152). In contrast to Popp et al. [2010b], the plastic increment and the norm of the tangential part of the Lagrange multiplier are not comprised leading to a slightly different expression of the stick/slip behavior. In the case of slip, the weak form of the augmented Lagrangian formulation (4.24) at the slave node

$$G_{lA} = \delta \boldsymbol{\lambda}_A \cdot \left[\mathbf{n}_A \bar{\mathbf{g}}_A \cdot \mathbf{n}_A + \mathbf{t}_{A\alpha} \frac{1}{c_T} \left(\bar{\boldsymbol{\lambda}}_A \cdot \mathbf{t}_{A\alpha} - \mu |\hat{\lambda}_{NA}| \frac{\hat{\lambda}_{T\alpha A}}{\|\hat{\boldsymbol{\lambda}}_{TA} \cdot \mathbf{t}_{A\alpha}\|} \right) \right] \quad (4.178)$$

and its linearization

$$\begin{aligned} DG_{lA} = \delta \boldsymbol{\lambda}_A \cdot & \left[\Delta \mathbf{n}_A \bar{\mathbf{g}}_A \cdot \mathbf{n}_A + \mathbf{n}_A \Delta \bar{\mathbf{g}}_A \cdot \mathbf{n}_A + \mathbf{n}_A \bar{\mathbf{g}}_A \cdot \Delta \mathbf{n}_A \right. \\ & + \Delta \mathbf{t}_{A\alpha} \frac{1}{c_T} \left(\bar{\boldsymbol{\lambda}}_A \cdot \mathbf{t}_{A\alpha} - \mu |\hat{\lambda}_{NA}| \frac{\hat{\lambda}_{T\alpha A}}{\|\hat{\boldsymbol{\lambda}}_{TA}\|} \right) + \mathbf{t}_{A\alpha} \frac{1}{c_T} \left(\Delta \bar{\boldsymbol{\lambda}}_A \cdot \mathbf{t}_{A\alpha} + \bar{\boldsymbol{\lambda}}_A \cdot \Delta \mathbf{t}_{A\alpha} \right. \\ & - \mu \operatorname{sign} \left(\hat{\lambda}_{NA} \right) \left(\Delta \bar{\boldsymbol{\lambda}}_A + c_N \Delta \bar{\mathbf{g}}_A \right) \cdot \mathbf{n}_A + \left(\bar{\boldsymbol{\lambda}}_A + c_N \bar{\mathbf{g}}_A \right) \cdot \Delta \mathbf{n}_A \frac{\hat{\lambda}_{T\alpha A}}{\|\hat{\boldsymbol{\lambda}}_{TA}\|} \\ & - \mu |\hat{\lambda}_{NA}| \left[\frac{1_{\alpha\beta}}{\|\hat{\boldsymbol{\lambda}}_{TA}\|} - \frac{\hat{\lambda}_{T\alpha A} \hat{\lambda}_{T\beta A}}{\|\hat{\boldsymbol{\lambda}}_{TA}\|^3} \right] \left[\left[\Delta \bar{\boldsymbol{\lambda}}_A - c_T (\Delta \bar{\mathbf{g}}_A - \Delta \bar{\mathbf{g}}_A^o) \right] \cdot \mathbf{t}_{A\beta} \right. \\ & \left. \left. + \left[\bar{\boldsymbol{\lambda}}_A - c_T (\bar{\mathbf{g}}_A - \bar{\mathbf{g}}_A^o) \right] \cdot \Delta \mathbf{t}_{A\beta} \right] \right) \end{aligned} \quad (4.179)$$

determine the residual vector and the tangent matrix. (4.178) can also be sent without any modifications to the global assembler and (4.179) yields the following matrix contributions for the displacements

$$\begin{aligned} \mathbf{K}_{lu}^s &= \mathbf{n}_A \mathbf{G}_{\Delta \mathbf{g}}^s \mathbf{n}_A - \mathbf{t}_{A\alpha} \frac{1}{c_T} \left(\mathbf{G}_{\Delta \boldsymbol{\lambda}}^s \mathbf{t}_{A\alpha} - \mu \operatorname{sign} \left(\hat{\lambda}_{NA} \right) \frac{\hat{\lambda}_{T\alpha A}}{\|\hat{\boldsymbol{\lambda}}_{TA}\|} \left(\mathbf{G}_{\Delta \boldsymbol{\lambda}}^s + c_N \mathbf{G}_{\Delta \mathbf{g}}^s \right) \mathbf{n}_A \right. \\ & \left. - \mu |\hat{\lambda}_{NA}| \left[\frac{1_{\alpha\beta}}{\|\hat{\boldsymbol{\lambda}}_{TA}\|} - \frac{\hat{\lambda}_{T\alpha A} \hat{\lambda}_{T\beta A}}{\|\hat{\boldsymbol{\lambda}}_{TA}\|^3} \right] \left[\mathbf{G}_{\Delta \boldsymbol{\lambda}}^s - c_T (\mathbf{G}_{\Delta \mathbf{g}} - \mathbf{G}_{\Delta \mathbf{g}}^o) \right] \mathbf{t}_{A\alpha} \right) \in \mathbb{R}^{3 \times 24} \\ \mathbf{K}_{lu}^{st} &= \mathbf{n}_A \mathbf{G}_{\Delta \mathbf{g}}^{st} \mathbf{n}_A + \mathbf{t}_{A\alpha} \frac{1}{c_T} \left(\mathbf{G}_{\Delta \boldsymbol{\lambda}}^{st} \mathbf{t}_{A\alpha} - \mu \operatorname{sign} \left(\hat{\lambda}_{NA} \right) \frac{\hat{\lambda}_{T\alpha A}}{\|\hat{\boldsymbol{\lambda}}_{TA}\|} \left(\mathbf{G}_{\Delta \boldsymbol{\lambda}}^{st} + c_N \mathbf{G}_{\Delta \mathbf{g}}^{st} \right) \mathbf{n}_A \right. \\ & \left. - \mu |\hat{\lambda}_{NA}| \left[\frac{1_{\alpha\beta}}{\|\hat{\boldsymbol{\lambda}}_{TA}\|} - \frac{\hat{\lambda}_{T\alpha A} \hat{\lambda}_{T\beta A}}{\|\hat{\boldsymbol{\lambda}}_{TA}\|^3} \right] \left(\mathbf{G}_{\Delta \boldsymbol{\lambda}}^{st} - c_T \mathbf{G}_{\Delta \mathbf{g}}^{st} \right) \mathbf{t}_{A\alpha} \right) \in \mathbb{R}^{3 \times 24}, \end{aligned} \quad (4.180)$$

the Lagrange multiplier

$$\begin{aligned} \mathbf{K}_{ll}^s = \mathbf{t}_{A\alpha} \frac{1}{c_T} & \left(\mathbf{L}_{\Delta\lambda}^s \mathbf{t}_{A\alpha} - \mu \operatorname{sign}(\hat{\lambda}_{NA}) \frac{\hat{\lambda}_{T\alpha A}}{\|\hat{\lambda}_{TA}\|} \mathbf{L}_{\Delta\lambda}^s \mathbf{n}_A \right. \\ & \left. - \mu |\hat{\lambda}_{NA}| \left[\frac{1_{\alpha\beta}}{\|\hat{\lambda}_{TA}\|} - \frac{\hat{\lambda}_{T\alpha A} \hat{\lambda}_{T\beta A}}{\|\hat{\lambda}_{TA}\|^3} \right] \mathbf{L}_{\Delta\lambda}^s \mathbf{t}_{A\alpha} \right) \in \mathbb{R}^{3 \times 12} \end{aligned} \quad (4.181)$$

and for the displacement part due to the base vectors

$$\begin{aligned} \mathbf{K}_{lua}^s = \mathbf{B}_n^a \bar{\mathbf{g}}_A \cdot \mathbf{n}_A + \mathbf{n}_A \bar{\mathbf{g}}_A \cdot \mathbf{B}_n^a + \mathbf{B}_{t_\alpha}^a \frac{1}{c_T} & \left(\bar{\lambda}_A \cdot \mathbf{t}_{A\alpha} - \mu |\hat{\lambda}_{NA}| \frac{\hat{\lambda}_{T\alpha A}}{\|\hat{\lambda}_{TA}\|} \right) \\ + \mathbf{t}_{A\alpha} \frac{1}{c_T} & \left(\bar{\lambda}_{A\alpha} \mathbf{B}_{t_\alpha}^a - \mu \operatorname{sign}(\hat{\lambda}_{NA}) \frac{\hat{\lambda}_{T\alpha A}}{\|\hat{\lambda}_{TA}\|} (\bar{\lambda}_A + c_N \bar{\mathbf{g}}_A) \mathbf{B}_n^a \right. \\ & \left. - \mu |\hat{\lambda}_{NA}| \left[\frac{1_{\alpha\beta}}{\|\hat{\lambda}_{TA}\|} - \frac{\hat{\lambda}_{T\alpha A} \hat{\lambda}_{T\beta A}}{\|\hat{\lambda}_{TA}\|^3} \right] [\bar{\lambda}_A - c_T (\bar{\mathbf{g}}_A - \bar{\mathbf{g}}_A^o)] \mathbf{B}_{t_\alpha}^a \right) \in \mathbb{R}^{3 \times 24}. \end{aligned} \quad (4.182)$$

Slave nodes which are inactive have to fulfill nearly the same constraint as for the weak form of the Lagrange multiplier method (4.160), only without the additional constraint of a zero slip increment

$$G_{lA}^{ch} = \delta \lambda_A \cdot \left[\mathbf{n}_A \frac{1}{c_N} \bar{\lambda}_A \cdot \mathbf{n}_A + \mathbf{t}_{A\alpha} \frac{1}{c_T} \bar{\lambda}_A \cdot \mathbf{t}_{A\alpha} \right]. \quad (4.183)$$

Additionally, the linearized form corresponds to the Lagrange multiplier case (4.161) neglecting the slip increment part

$$\begin{aligned} DG_{lA}^{ch} = \delta \lambda_A \cdot & \left[\Delta \mathbf{n}_A \frac{1}{c_N} \bar{\lambda}_A \cdot \mathbf{n}_A + \mathbf{n}_A \frac{1}{c_N} \Delta \bar{\lambda}_A \cdot \mathbf{n}_A + \mathbf{n}_A \frac{1}{c_N} \bar{\lambda}_A \cdot \Delta \mathbf{n}_A \right. \\ & \left. + \Delta \mathbf{t}_{A\alpha} \frac{1}{c_T} \bar{\lambda}_A \cdot \mathbf{t}_{A\alpha} + \mathbf{t}_{A\alpha} \frac{1}{c_T} \Delta \bar{\lambda}_A \cdot \mathbf{t}_{A\alpha} + \mathbf{t}_{A\alpha} \frac{1}{c_T} \bar{\lambda}_A \cdot \Delta \mathbf{t}_{A\alpha} \right] \end{aligned} \quad (4.184)$$

where the matrix contributions can be found in (4.162).

4.3.6.4 Mixed method

The mixed method combines the augmented Lagrangian method applied for the non penetration condition with the penalty regularization for the stick-slip behavior where now the normal penetration and the tangential movement are averaged directly. Dual shape functions are not considered, but can be implemented easily following sections 4.3.6.1, 4.3.6.2 and 4.3.6.3. To reduce the CPU time, the Hellinger-Reissner formulation (3.19) is used for the tangential part

$$\delta \lambda_{T\alpha A} \frac{1}{c_T} [\bar{\lambda}_{T\alpha A} - \bar{t}_{T\alpha A}], \quad (4.185)$$

introducing additional Lagrange multipliers $\bar{\lambda}_{T\alpha A}$. The formulation states that the Lagrange multipliers have to be equal to the tangential stress components $\bar{t}_{T\alpha A}$ resulting from the implicit return mapping algorithm. For the linear Coulomb law, the determination of the actual stress is equivalent to (4.59) or (4.166)

$$\begin{aligned} \text{stick : } \bar{t}_{T\alpha A} &= \bar{t}_{T\alpha A}^{tr} & \text{if } \frac{f(\bar{\mathbf{t}}_{TA}^{tr})}{c_T} \leq \delta \\ \text{slip : } \bar{t}_{T\alpha A} &= \mu |\bar{\lambda}_{NA}| \frac{\bar{t}_{T\alpha A}^{tr}}{\|\bar{\mathbf{t}}_{TA}^{tr}\|} & \text{if } \frac{f(\bar{\mathbf{t}}_{TA}^{tr})}{c_T} > \delta \end{aligned} \quad (4.186)$$

and based on the tolerance δ , the trial stress components and the trial slip criterion

$$\begin{aligned} \bar{t}_{T\alpha A}^{tr} &= -c_T (\bar{g}_{T\alpha A} - \bar{g}_{T\alpha A}^o) + \bar{t}_{T\alpha A} n \\ f(\bar{\mathbf{t}}_{TA}^{tr}) &= \|\bar{\mathbf{t}}_{TA}^{tr}\| - \mu |\bar{\lambda}_{NA}|, \quad \|\bar{\mathbf{t}}_{TA}^{tr}\| = \sqrt{\bar{t}_{T\alpha A}^{tr} \bar{t}_{T\alpha A}^{tr}}. \end{aligned} \quad (4.187)$$

The nonlinear complementarity function (4.18) determines, if the slave node is active or inactive

$$\text{if } \bar{\lambda}_{NA} + c_N \bar{g}_{NA} < \delta \rightarrow \text{active else inactive.} \quad (4.188)$$

In contrast to the other solution methods, the contribution of the Lagrange multipliers to the virtual contact work is now subdivided into a normal and a tangential part

$$\begin{aligned} G_{uA}^{ch} &= \delta \bar{g}_{NA} \lambda_{NA} + \delta \bar{g}_{T\alpha A} \lambda_{T\alpha A} = \sum_{s=1}^{n_{seg}^A} \delta \mathbf{d}_s \cdot \mathbf{R}_u^s \\ \mathbf{R}_u^s &= \mathbf{G}_{\delta \bar{g}_N}^s \lambda_{NA} + \mathbf{G}_{\delta \bar{g}_{T\alpha}}^s \lambda_{T\alpha A} \in \mathbb{R}^{24}. \end{aligned} \quad (4.189)$$

The linearization of (4.189)

$$\begin{aligned} DG_{uA}^{ch} &= \Delta \delta \bar{g}_{NA} \lambda_{NA} + \Delta \delta \bar{g}_{T\alpha A} \lambda_{T\alpha A} + \delta \bar{g}_{NA} \Delta \lambda_{NA} + \delta \bar{g}_{T\alpha A} \Delta \lambda_{T\alpha A} \\ &= \sum_{s=1}^{n_{seg}^A} \delta \mathbf{d}_s \cdot \left[\mathbf{K}_{uu}^s \mathbf{d}_s + \sum_{B=1}^{n_s} \sum_{a=1}^{n_{ae}^1} \mathbf{K}_{uu a B}^s \mathbf{d}_s^{aB} + \mathbf{K}_{ul}^s \boldsymbol{\lambda}_A \right] \end{aligned} \quad (4.190)$$

leads to the matrices

$$\begin{aligned} \mathbf{K}_{uu}^s &= \mathbf{G}_{\Delta \delta \bar{g}_N} \lambda_{NA} + \mathbf{G}_{\Delta \delta \bar{g}_{T\alpha}} \lambda_{T\alpha A} \in \mathbb{R}^{24 \times 24} \\ \mathbf{K}_{uu a}^s &= \mathbf{G}_{\delta \mathbf{n} B}^a \lambda_{NA} + \mathbf{G}_{\delta \mathbf{t}_\alpha B}^a \lambda_{T\alpha A} \in \mathbb{R}^{24 \times 24} \\ \mathbf{K}_{ul}^s &= \mathbf{G}_{\delta \bar{g}_N}^s \mathbf{1}_N + \mathbf{G}_{\delta \bar{g}_{T\alpha}}^s \mathbf{1}_\alpha \in \mathbb{R}^{24 \times 3} \end{aligned} \quad (4.191)$$

where $\mathbf{1}_N = [1 \ 0 \ 0]^T$, $\mathbf{1}_1 = [0 \ 1 \ 0]^T$ and $\mathbf{1}_2 = [0 \ 0 \ 1]^T$ are vectors locating the multipliers in the matrix. The nodal contact constraint equation consists of the standard non

penetration condition in the weak form and of the Hellinger-Reissner description for the tangential part

$$G_{lA}^{ch} = \delta\lambda_{NA}\bar{g}_{NA} + \delta\lambda_{T\alpha A}\frac{1}{c_T} [\bar{\lambda}_{T\alpha A} - \bar{t}_{T\alpha A}] = 0 \quad (4.192)$$

which can be sent without any modifications to the global residual vector. For the linearized form of the constraint equation

$$\begin{aligned} DG_{lA}^{ch} &= \delta\lambda_{NA}\Delta\bar{g}_{NA} + \delta\lambda_{T\alpha A}\frac{1}{c_T} [\Delta\bar{\lambda}_{T\alpha A} - \bar{D}_{A\alpha\beta} (\Delta\bar{g}_{T\beta A} - \Delta\bar{g}_{T\beta A}^o) - \bar{L}_{A\alpha}\Delta\bar{\lambda}_{NA}] \\ &= \delta\lambda_A \cdot \sum_{s=1}^{n_{seg}^A} \left[\mathbf{K}_{lu}^s \mathbf{d}_s + \sum_{B=1}^{n_s} \sum_{a=1}^{n_{ae}^1} \mathbf{K}_{lu a B}^s \mathbf{d}_s^{aB} + \mathbf{K}_{ll}^s \mathbf{l}_s \right], \end{aligned} \quad (4.193)$$

as for the penalty regularization, the matrices $\bar{D}_{A\alpha\beta}$ and $\bar{L}_{A\alpha}$ have to be determined for the stick case

$$\bar{D}_{A\alpha\beta} = -c_T 1_{\alpha\beta}, \quad \bar{L}_{A\alpha} = 0_\alpha \quad (4.194)$$

and for the slip case where the vector $\bar{L}_{A\alpha}$ links the tangential stress components to the normal Lagrange multiplier

$$\bar{D}_{A\alpha\beta} = -\mu |\bar{\lambda}_{NA}| \left[\frac{1_{\alpha\beta}}{\|\bar{\mathbf{t}}_{TA}^{tr}\|} - \frac{\bar{\mathbf{t}}_{T\alpha A}^{tr} \bar{\mathbf{t}}_{T\beta A}^{tr}}{\|\bar{\mathbf{t}}_{TA}^{tr}\|^2} \right] c_T, \quad \bar{L}_{A\alpha} = \mu \text{sign}(\bar{\lambda}_{NA}) \frac{\bar{\mathbf{t}}_{T\alpha A}^{tr}}{\|\bar{\mathbf{t}}_{TA}^{tr}\|}. \quad (4.195)$$

The individual tangent matrices of (4.193) are written in detail as

$$\begin{aligned} \mathbf{K}_{lu}^s &= \mathbf{1}_N \mathbf{G}_{\Delta\bar{g}_N}^s + \mathbf{1}_\alpha \frac{1}{c_T} \left[\mathbf{G}_{\Delta\bar{\lambda}_{T\alpha}}^s - \bar{D}_{A\alpha\beta} \left(\mathbf{G}_{\Delta\bar{g}_{T\beta}}^s - \mathbf{G}_{\Delta\bar{g}_{T\beta}^o}^s \right) - \bar{L}_{A\alpha} \mathbf{G}_{\Delta\bar{\lambda}_N}^s \right] \in \mathbb{R}^{3 \times 24} \\ \mathbf{K}_{lu a}^s &= \mathbf{1}_N \mathbf{G}_{\Delta\mathbf{n}B}^a - \mathbf{1}_\alpha \frac{1}{c_T} \bar{D}_{A\alpha\beta} \left(\mathbf{G}_{\Delta\mathbf{t}_{\beta B}}^a - \mathbf{G}_{\Delta\mathbf{t}_{\beta B}^o}^a \right) \in \mathbb{R}^{3 \times 24} \\ \mathbf{K}_{ll}^s &= \mathbf{1}_\alpha \frac{1}{c_T} \left[\mathbf{L}_{\Delta\bar{\lambda}_{T\alpha}}^s - \bar{L}_{A\alpha} \mathbf{L}_{\Delta\bar{\lambda}_N}^s \right] \in \mathbb{R}^{3 \times 12}. \end{aligned} \quad (4.196)$$

For inactive nodes the constraint of zero normal and tangential Lagrange multiplier components has to be enforced leading to the weak form and its linearization

$$\begin{aligned} G_{lA}^{ch} &= \delta\lambda_{NA} \frac{1}{c_N} \bar{\lambda}_{NA} + \delta\lambda_{T\alpha A} \frac{1}{c_T} \bar{\lambda}_{T\alpha A} = 0 \\ DG_{lA}^{ch} &= \delta\lambda_{NA} \frac{1}{c_N} \Delta\bar{\lambda}_{NA} + \delta\lambda_{T\alpha A} \frac{1}{c_T} \Delta\bar{\lambda}_{T\alpha A} = \delta\lambda_A \cdot \sum_{s=1}^{n_{seg}^A} \left[\mathbf{K}_{lu}^s \mathbf{d}_s + \mathbf{K}_{ll}^s \mathbf{l}_s \right] \end{aligned} \quad (4.197)$$

where the matrix contributions are specified as

$$\mathbf{K}_{lu}^s = \mathbf{1}_N \frac{1}{c_N} \mathbf{G}_{\Delta\bar{\lambda}_N}^s + \mathbf{1}_\alpha \frac{1}{c_T} \mathbf{G}_{\Delta\bar{\lambda}_{T\alpha}}^s \in \mathbb{R}^{3 \times 24}, \quad \mathbf{K}_{ll}^s = \mathbf{1}_N \frac{1}{c_N} \mathbf{L}_{\Delta\bar{\lambda}_T}^s + \mathbf{1}_\alpha \frac{1}{c_T} \mathbf{L}_{\Delta\bar{\lambda}_{T\alpha}}^s \in \mathbb{R}^{3 \times 12}. \quad (4.198)$$

Comparing the mixed version with the augmented Lagrangian method, the only difference is that instead of the trial the augmented tangential stress is used in the latter method, but both variants are formulated in Hellinger-Reissner form. Explaining in more detail, the tangential stress at the old time step is replaced by the actual tangential stress leading to the exact fulfillment of the stick constraint, but also to a larger effort in computing the tangent matrix.

4.4 Numerical solutions

The Mortar method is claimed in the literature as an improvement regarding the robustness of the algorithm, the accuracy and the smoothness of the reaction forces compared to the node to surface approaches. Three different examples are selected to demonstrate the mentioned behavior of the Mortar method. The results are also compared to the results of the node to segment approach to show the difference of the two contact discretization techniques. The tests selected are very popular in the literature and a comparison with these results also validates the implementation into the finite element code. All the examples are thereby given in fundamental units.

4.4.1 Hertzian contact

Analytical solutions of contact problems are only available for some simple examples. The most popular one is the Hertzian contact (Hertz [1881]). A short overview of the theory applied to different cases can also be found in Johnson [1985] or Timoshenko and Goodier [1970]. Here only the performance of the Mortar method for the frictionless contact case is tested. The same test with the same result is accomplished in Popp et al. [2010b]. For the three-dimensional case a hemisphere ($E = 200$, $\nu = 0.3$), loaded with a constant pressure $p = 0.2$ on top, is pressed on a rigid plane where the standard linear elastic material model is used to model the hemisphere. The rigidity is realized by means of a block with a sufficiently high Young's modulus ($E = 100000$, $\nu = 0.3$). The geometrical measurements and the boundary conditions are given in figure 4.9. The

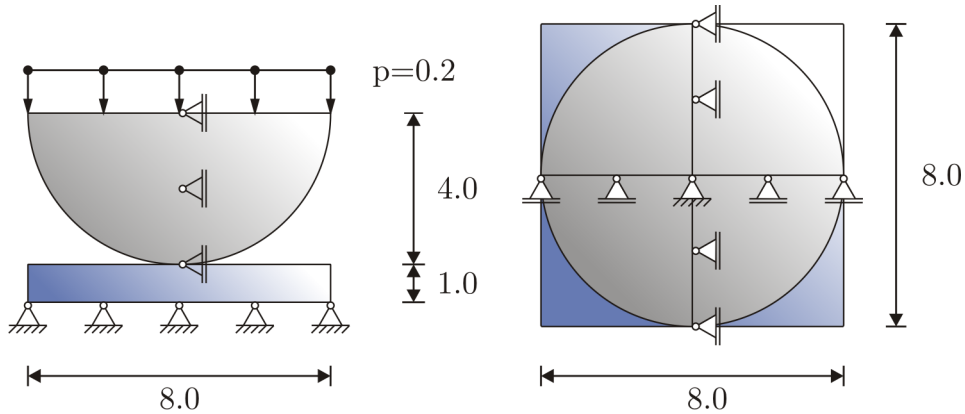


Figure 4.9: Side view (left) and top view (right) of the Hertzian contact example

numerical results evaluated at the cut plane $y = 0$ are compared with the analytical solutions. The pressure distribution along the x -axis can be stated as a function in dependency of the distance x to the center of the hemisphere

$$p(x) = p_0 \sqrt{1 - \frac{x^2}{a^2}}. \quad (4.199)$$

The maximal contact pressure p_0 and the length of the contact zone a

$$p_0 = 0.388 \sqrt[3]{4 p \pi E^2}, \quad a = 1.109 \sqrt[3]{\frac{p R^3 \pi}{2 E}} \quad (4.200)$$

are determined therein in terms of the radius R , the pressure p and Young's modulus E . The initial mesh and the vertical stress distribution is shown in figure 4.10. The

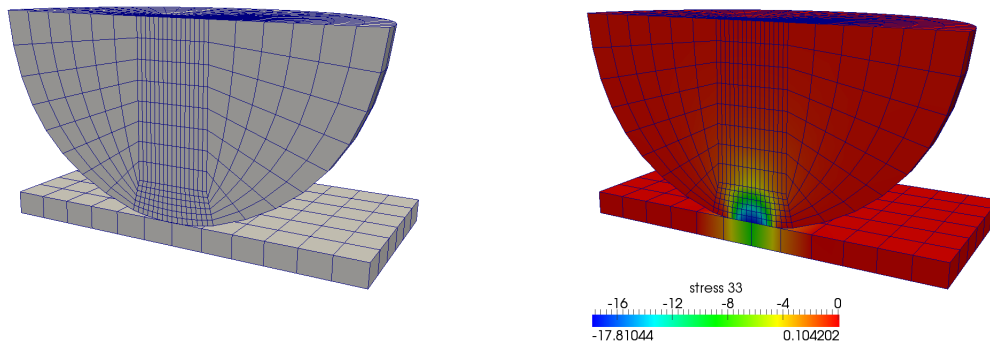


Figure 4.10: Initial mesh (left) and σ_{33} stress distribution (right) in the cutting plane ($y=0$)

comparison of the analytical and the numerical results (figure 4.11) for the augmented formulation with dual shape functions ($c_N = 10^1$, $c_T = 10^1$) and for the mixed formulation with standard shape functions ($c_N = 10^1$, $c_T = 10^1$) shows for both cases only small differences to the analytical solution. Only at the boundary of the contact zone a larger discrepancy of the numerical solution is obvious due to the use of linear shape functions and the coarse mesh where the finite element nodes do not coincide with the boundary of the contact zone. An adaptive h- and p- refinement can improve the results even at the outmost of the contact zone (Franke et al. [2010]). With regard to the results, the convergence behavior and the computation time of all test cases, no differences between dual and standard shape functions can be found and hence in the following examples only standard shape functions are applied. Also comparing the CPU time between dual and standard shape functions no large differences are obvious for the examples with a low number of degrees of freedom as ben used in this work. The advantage of a reduced number of unknowns in the overall tangent to be solved is equalized by the additional loop in the tangent and the elimination and update of the Lagrange multiplier.

4.4.2 Rotating blocks

To show the smoothness of the reacting forces using the Mortar method compared to the node to segment formulation, an elastic cube ($E = 1.0$, $\nu = 0.3$) rotates (and

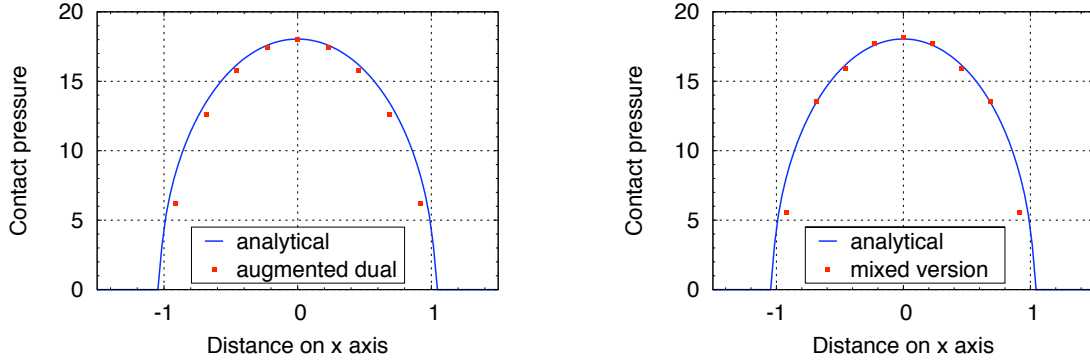


Figure 4.11: Comparison of the analytical and the numerical contact pressure for the augmented method with dual shape functions (left) and for the mixed formulation with standard shape functions (right)

slides) on another elastic cube ($E = 1.0$, $\nu = 0.3$) with the same material behavior and the same geometry (figure 4.12) where the Neo-Hookian material model (2.45) is used for both cubes. First the upper block is loaded with a prescribed displacement of

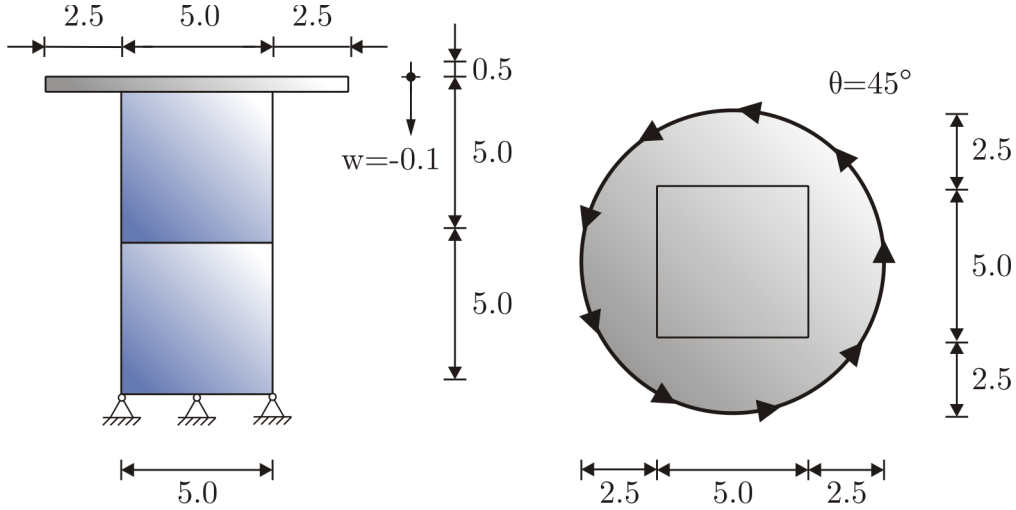


Figure 4.12: Side view (left) and top view (right) of the rotating blocks example

$w = -0.1$ which is applied within 8 steps. Afterwards, the upper block rotates on the lower one where at each step the increment of the angle consists of 5° . The results in figure 4.13 show a smooth behavior of the axial force for the Mortar method even for a coarse mesh. For the evaluation of this example, the mixed version ($c_N = 10^1$, $c_T = 10^1$) is selected, but all the other solution methods within the Mortar framework lead to the same outcome. Only the node to segment formulation fails after 5 steps and the resulting axial force changes significantly compared to the load step before, but it has to be noted that for smaller angle increments the node to segment formulation converges at each step as well. Only the significant change of the axial force between

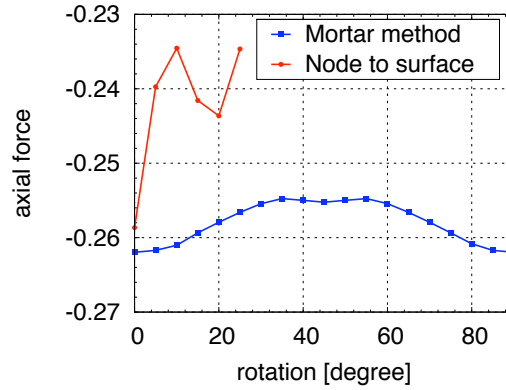


Figure 4.13: Rotating blocks: Axial force distribution of the node to segment formulation and of the Mortar method

the steps remains. Due to the stronger deformation at the corners of the upper block at angles around 45° , the axial pressure has to decrease. A more detailed evaluation

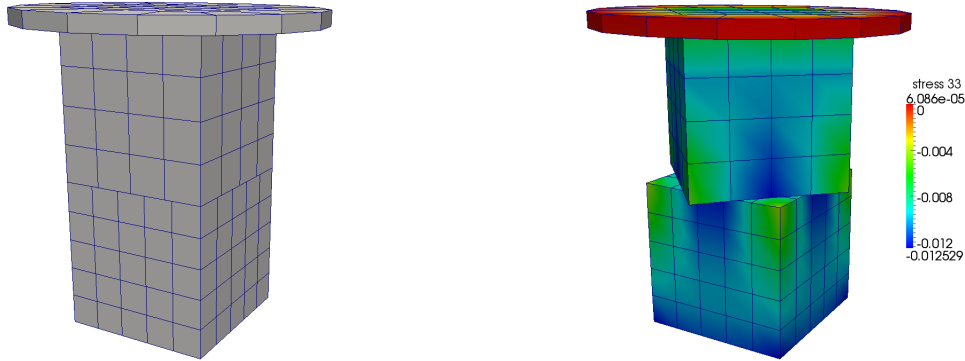


Figure 4.14: Rotating blocks: Initial mesh (left) and stress σ_{33} distribution at an angle of 46° (right)

on the behavior of rotating blocks with different integration rules and a patch test performance can be found in Puso and Laursen [2004a].

4.4.3 Ironing

The last example reveals the frictional behavior of different solution techniques at finite deformations. An elastic half tube ($E = 1000$, $\nu = 0.3$) is first pressed ($w = 1.4$) into a softer elastic block ($E = 1$, $\nu = 0.3$) within 1 time unit and afterwards, the tube slides along the block over a distance of $u = 4.0$ within 4 time units (figure 4.15). As for the example before, the Neo-Hookian material model (2.45) is used for both contact members. Figure 4.16 displays the initial mesh and the vertical displacement u_3 at the solution time $t = 4.0$. The maximal time step size and the corresponding CPU time

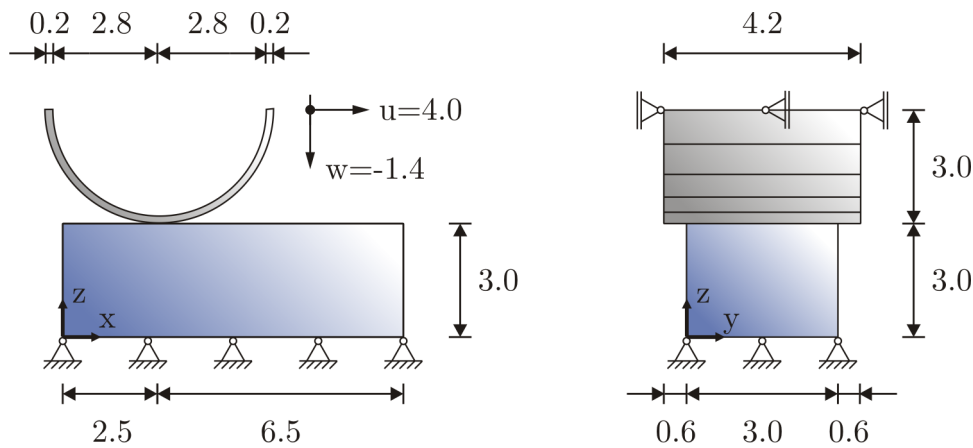


Figure 4.15: Side view (left) and top view (right) of the ironing example

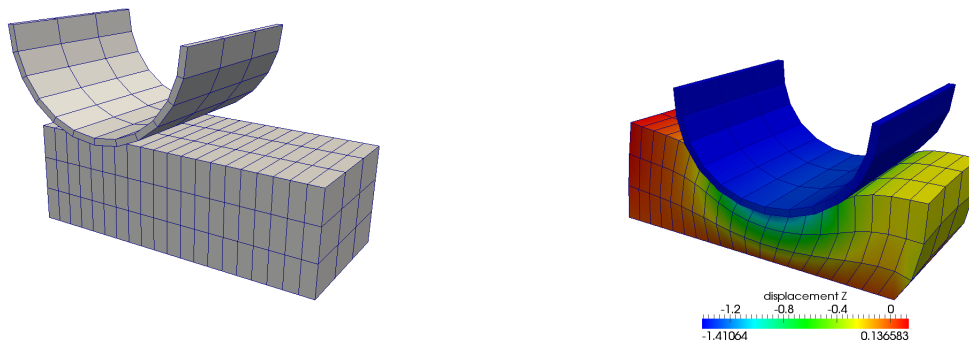


Figure 4.16: Ironing test: Initial mesh (left) and vertical displacement u_3 at $t = 4.0$ (right)

for each solution method (all with the parameters $c_N = 10^2$, $c_T = 10^2$ which lead to a stable simulation) are listed in table 4.6. For a detailed investigation of the influence of different penalty parameters in the context of the augmented Lagrangian method, see Popp et al. [2010b]. For the penetration process, the penalty and the augmented

	normal direction		tangential direction	
solution typ	Δt	CPU time	Δt	CPU time
Lagrange	0.05 s	23.86 s	0.02 s	61.94 s
Penalty	0.1 s	45.75 s	0.02 s	289.12 s
Augmented	0.1 s	10.17 s	0.02 s	48.38 s
Mixed	0.02 s	68.11 s	0.02 s	69.87 s

Table 4.6: Ironing test: Time step size and CPU time for different contact solution methods

method have the maximal increment size and conversely, the mixed method formulated on the basis of an averaged normal penetration and an averaged tangential movement needs a smaller load step to converge. Looking at the CPU time (standard desktop computer with 4GB RAM and computation on one core), due to the intrinsic loop over all integration points of the corresponding node (see section 4.3.6.2), the penalty

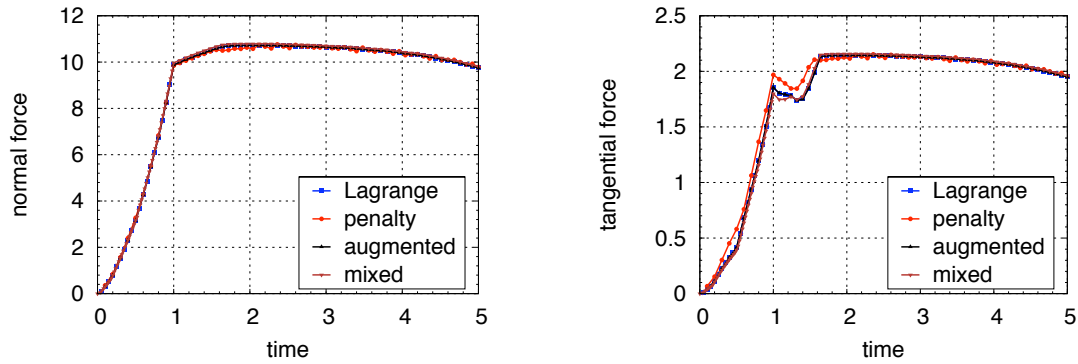


Figure 4.17: Ironing test: Normal (left) and tangential (right) reaction force at the contact zone for different solution types

method takes four to five times longer than all the other formulations. The normal and

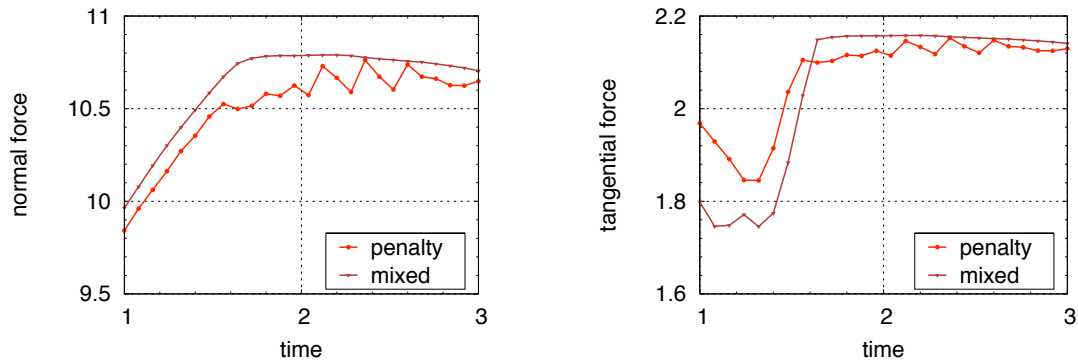


Figure 4.18: Ironing test: Normal (left) and tangential (right) reaction force at the contact zone for the penalty and the mixed method at the time interval 1-3

the tangential reaction force (figure 4.17) at the contact zone is almost the same for each solution type. Only for the penalty method, the normal and the tangential force distributions oscillate (figure 4.18) which is also the case in the 2D ironing example regularized with the penalty method in Fischer and Wriggers [2006]. The node to segment approach can not accomplish this example and fails after a few time steps. The simulation of this ironing example is also conducted for the frictionless case in Popp et al. [2010b] and for the case of friction similar results of a slightly different ironing example can be found in Puso and Laursen [2004b]. At the end, it has to be highlighted that the solution depends strongly on the mesh topology. For a coarse mesh and large load steps sometimes the penetration of a slave node into the master body is too large leading independent of the formulation to a divergence of the solution and finally to a failure of the computation. Additionally, the penalty method fails earlier for coarsening

the mesh and at different mesh sizes or different incremental time steps, the Lagrange multiplier method oscillates. Hence as an outcome, the augmented method fulfills the contact constraints with the same accuracy as the Lagrange multiplier method, but with less iteration and no oscillations at each time step. Additionally, if the overlap is not too large, it leads to a robust and fast regularization type compared to the other methods. At last comparing the augmented Lagrangian method with the mixed version which are very similar, see section 4.3.6.4, formulations based on the averaged gap $\bar{\mathbf{g}}_A$ instead of the averaged normal penetration $\bar{\mathbf{g}}_{NA}$ and the averaged tangential movement $\bar{\mathbf{g}}_{T\alpha A} - \bar{\mathbf{g}}_{T\alpha A}^o$ seems to be more robust within the Mortar framework. An explanation could be that averaging only the gap leads to a smoother transition behavior of the penetration and the tangential movement between the slave nodes compared to the second kinematical formulation.

Chapter 5

Soil mechanics

The development of mechanical models which can be used to predict the material behavior of soils under loading is still an ongoing process. The difficulty with such models arises from the variety of components of the soil. Different rock materials broken and changed in size and shape over the years and liquids and gas filling the space between the grains characterizes the assembly. At different locations the properties of the soil assembly can be changed strongly challenging the reliable prediction of the soil behavior. Granular materials can also not be classified uniquely into fluid or solid materials. The grains have a higher mobility than the atoms of a solid material but due to its large weight the mobility of the grains is not as high as it is for fluids. This challenges especially the selection of the appropriate numerical solution method (Eulerian/Lagrangian FEM, DEM or meshless methods).

5.1 Classification of the soil

Before any construction can be planned, the soil on which the building should be founded has to be classified which is also necessary for the determination of the material parameters of the soil model. The soil can be classified regarding the

- **Grain size distribution:** Within the sieve curve (figure 5.1) the grain size which contains 10% of the mass (d_{10}) is a good indicator of the permeability of the soil and the coefficient of uniformity $C_u = d_{60}/d_{10}$ specifies the fluctuation of the grain size. If 85 % of the grains have a diameter $d \leq 0.06$ mm, the soil is called non cohesive and is unsuitable for a foundation.
- **Shapes of grains:** Each grain of an assembly can be distinguished with regard to its roundness, its sphericity and its size (figure 5.2). The roundness characterizes the sharpness on the edges and the sphericity the deflection of the grain compared to a sphere. This kind of classification is too expensive to be integrated directly into a soil model, however the shape of the grains limits the maximal and the minimal space in a solid skeleton which are important parameters in soil mechanics.

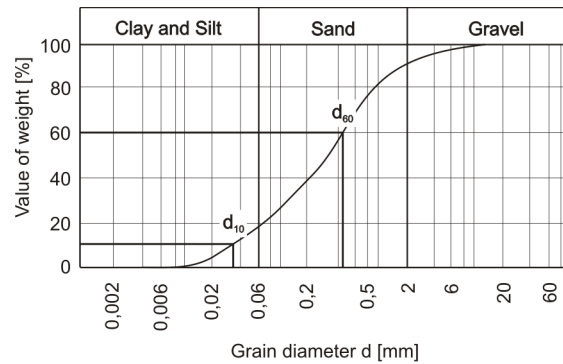


Figure 5.1: Typical sieve curve of a soil specimen



Figure 5.2: Grain characteristic of Karlsruhe (left) and Schlabendorf sand with a higher sphericity (right) given in Herle [1997]

- **Compactness of the packing:** Each assembly has a certain void ratio e which can be determined on the basis of the relative compactness (Terzaghi et al. [1996]) and divides the soil into dense $e \approx < 0.5$ or loose $e \approx > 0.5$ (figure 5.3 left).

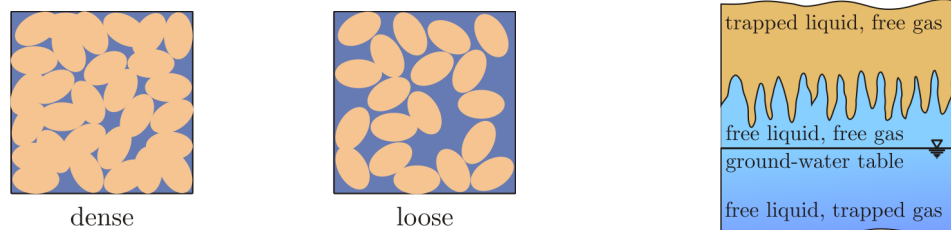


Figure 5.3: Dense and loose distribution of soil particles (left) and different layers near the groundwater table (right)

- **Water content:** Different phases of the soil with regard to the water content can be distinguished. In the saturated phase (below the groundwater table) water flows through the pores and gas is trapped whereas in the vadose zone above the groundwater table only gas flows through the pores. Close above the groundwater table a partly saturated domain (capillary fringe) exists where water seeps up due to the surface tension between water and gas. The capillary height depends thereby on the diameter of the pores. Above the partly saturated zone water adheres at the grains (figure 5.3).

- **Physical-chemical activity:** Electrostatic or van der Waals forces can also influence the material behavior especially for non cohesive materials, but can be neglected for a cohesive soil.

Whilst only some important classifications have been highlighted, it should be emphasized that the modeling of the soil behavior can only be based on rough and averaged properties leading normally to a huge number of parameters. A more detailed description of the soil behavior and its classification can be found for instance in Terzaghi et al. [1996]

5.2 Behavior under loading

The special structure of the soil consisting of a solid skeleton, liquids and gas leads to special effects which have to be taken into account in the development of soil models. Additionally, the soil can only carry compression loads since the load transfer takes place mostly in terms of contact forces between the grains. Experiments and further investigations on the behavior of a soil under loading can be found in Schanz [1998].

5.2.1 Plastic behavior

Even with small loads leading to strains larger than $\epsilon \geq 10^{-6}$, the grains get rearranged which is an irreversible process and hence the soil behavior has to be viewed as completely plastic. On the other hand during unloading (figure 5.4) a nonlinear behavior is also shown in experiments which is very challenging for models based on the elasto-plastic theory.

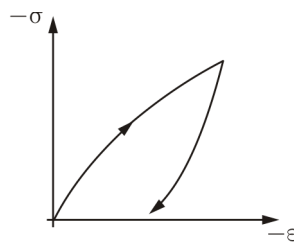


Figure 5.4: Nonlinear stress strain relation of a soil specimen under loading and unloading

5.2.2 Change of volume

Under hydrostatic compression, due to the rearrangements of the grains, the volume can decrease to a certain compression point although the solid skeleton, the water and the gas are normally viewed as incompressible (Eipper [1998]) and a very compact structure of the grains can be realized by means of small cyclic loadings. However, under a shear load the volume can increase (dilatancy) or decrease (contractancy) due to the rearrangement of the particles, see figure 5.5. Additionally, within partially or

fully saturated domains where an undrained situation exists, i.e. if the loading is faster than the water can flow through the pores, in the case of dilatancy the water is sucked into the pores and a negative pressure occurs. Conversely under contractancy, water is squeezed out and a positive pressure arises. Furthermore after monotonic shearing the soil gets into a critical state where the porosity and the stress strain relationship remains constant and no dilatancy or contractancy effects occur ($\dot{\sigma} = 0, \dot{\epsilon} = 0$).

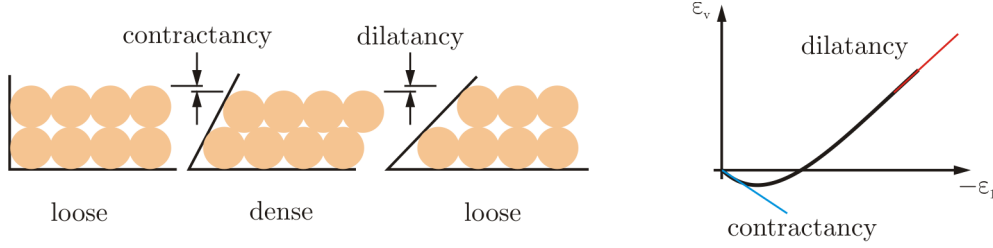


Figure 5.5: Dilatancy/contractancy effect at a sample of spheres (left) and the same effect in a volumetric strain curve (right)

5.2.3 Dependency on pressure and porosity

In experiments a dense or a loose sand show a completely different shear and volumetric strain behavior at the onset of loading. At the beginning the dense sand gets packed more closely and reaches the maximal shear stress, afterwards the soil dilates and the shear stress decreases. Conversely for a loose sand the void ratio decreases and the shear stress increases during loading (see figure 5.6). The normalized shear stress curve also varies strongly, if the soil specimen is loaded with different pressures (figure 5.6). Models taking into account the pressure and the porosity dependency, for instance of the friction angle, can be found in Bauer [1996] and in Hettler and Gudehus [1988], respectively. An additional outcome of experiments shows that the stiffness (Young's

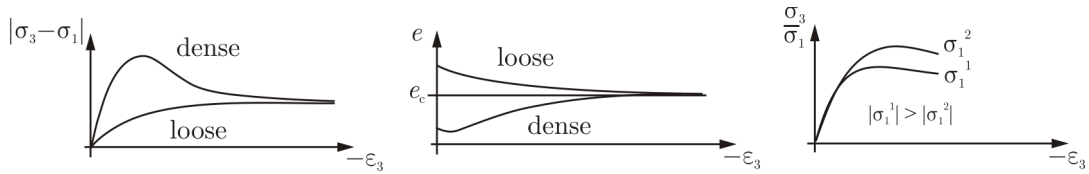


Figure 5.6: Behavior of dense and loose sand in triaxial test: shear stress (left) and volumetric strain (middle) and shear stress with different cell pressures (right)

modulus) has to depend on the pressure as well. In Herle [1997] an explanation of this observation is given based on the Hertzian contact theory (Timoshenko and Goodier [1970]).

5.2.4 Localization

Loading beyond the maximal stiffness of the soil leads to shear bands where even under homogeneous conditions locally the material gets unstable and the deformation increases until failure (figure 5.7). This phenomena is observed mainly in ductile ma-



Figure 5.7: Slope stability of a sand specimen under loading on the top (Ehlers and Avci [2012])

terials which include also granular materials where the grains within the localization zone slip along a given surface. Thereby the location of the zone and the slip direction are a priori unknown and a value of approximately two to three times the mean grain size diameter is a good estimate for the localization height. Numerical investigations of the localization phenomena can be found for instance in Leppin [1999].

5.2.5 Shakedown and runaway ratcheting

Under cyclic loading soil can either reach a limited (shakedown) or an unlimited state. In the case of shakedown, soil gradually goes from the plastic to an almost elastic state with only small particle movements and a small volume change. On the other hand under cyclic loadings with a constant stress being applied, the strain can increase at each cycle. This phenomena is called ratcheting and can lead to an incremental collapse of the structure (figure 5.8). A special model for the accumulation of the strains under

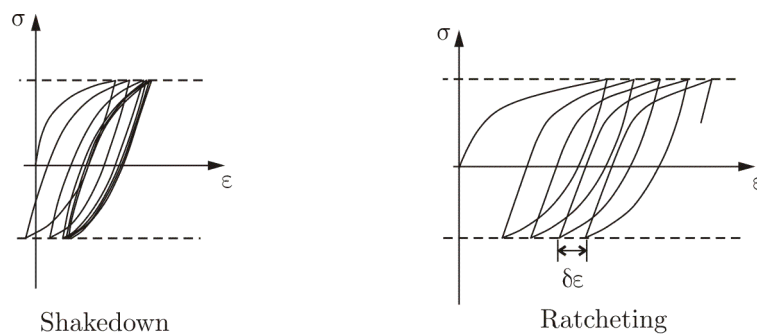


Figure 5.8: Stress-strain curve for shakedown (left) and ratcheting (right) at constant stress cycles

a high-cyclic loading can be found in Niemunis et al. [2005]

5.2.6 Liquefaction and consolidation

Liquefaction is mainly observed in saturated soils with a low permeability (undrained or mainly undrained situation) where at high cyclic loadings, like earthquakes, the pore water can not move to zones with a lower pressure. Hence the pore water pressure increases and the grains lose the contact with each other leading to a decrease of the shear resistance until the soil behaves like a liquid (figure 5.9).

On the other hand consolidation can be observed if the load is increased with a moderate velocity. At the beginning mainly the water resists the applied pressure, but later the solid skeleton takes over the resistance and the pore water drains out leading to a volume decrease of the soil. This observation is similar to creep and a strict distinction is often hard to make.



Figure 5.9: Liquefaction phenomena below a dam under a high cycle loading

5.3 Modeling strategies

A lot of models used in geotechnical simulations are based on elasto-plasticity where the underlying concept is described in section 3.3. Since some soil characteristics can be only hardly included into the elasto-plastic framework, recently hypoplastic models were developed where the material behavior is considered as inelastic from the onset of loading. In the hypoplastic framework the stress strain behavior is written in rate form

$$\dot{\boldsymbol{\sigma}} = \mathbb{L}\dot{\boldsymbol{\epsilon}} + \mathbf{N}\|\dot{\boldsymbol{\epsilon}}\|, \quad \dot{e} = (1 + e) \dot{\boldsymbol{\epsilon}} \cdot \mathbf{1} \quad (5.1)$$

where the tensors \mathbb{L} and \mathbf{N} have to be specified for each material. Often the evolution equation for the porosity e is integrated analytically. Kolymbas [2000] gives a general introduction into hypoplasticity and von Wolffersdorff [1996] proposes a simple but accurate model where the material parameters can be determined by standard experimental tests (Herle [1997]).

In this work only an elasto-plastic soil model will be used being based on Ehlers [1995] and often extended to its actual form (Ehlers and Scholz [2007]). Nevertheless other elasto-plastic soil models are also available in the literature, like the simple Mohr Coulomb or Drucker Prager model. Additionally, Cam Clay models based on the critical state concept are also used quite often. An introduction to these three models can be found in Desai and Siriwardane [1984] and a numerical realization of the Mohr Coulomb and the Drucker Prager model is given in de Souza Neto et al. [2008]. A recent extension of the critical soil state concept applicable to cyclic loadings is proposed by

means of the SANISAND model (Taiebat and Dafalias [2008]). Other elasto-plastic soil models can be found for example in Leppin [1999] and the references therein.

For frictional materials the corresponding elasto-plastic models are based mostly on the Coulomb slip rule

$$f^c = \|\mathbf{\lambda}_T\| - |\lambda_N| \tan \varphi - c = 0 \quad (5.2)$$

which has been extended and reformulated towards new yield criteria. Therein $\mathbf{\lambda}_T$ is the tangential part of the contact stress vector, λ_N the contact pressure, φ the friction angle and c the cohesion which is normally neglected at contact cases. In triaxial tests the tangential and the normal stress vector contribution can be reformulated in terms of the maximal σ_1 and the minimal σ_3 principle stress (see figure 5.10)

$$f = \frac{1}{2} (\sigma_1 - \sigma_3) \sec \varphi - \frac{1}{2} (\sigma_1 + \sigma_3) \tan \varphi - c = 0. \quad (5.3)$$

Following Nayak and Zienkiewicz [1972], see also the explanation in appendix A, the

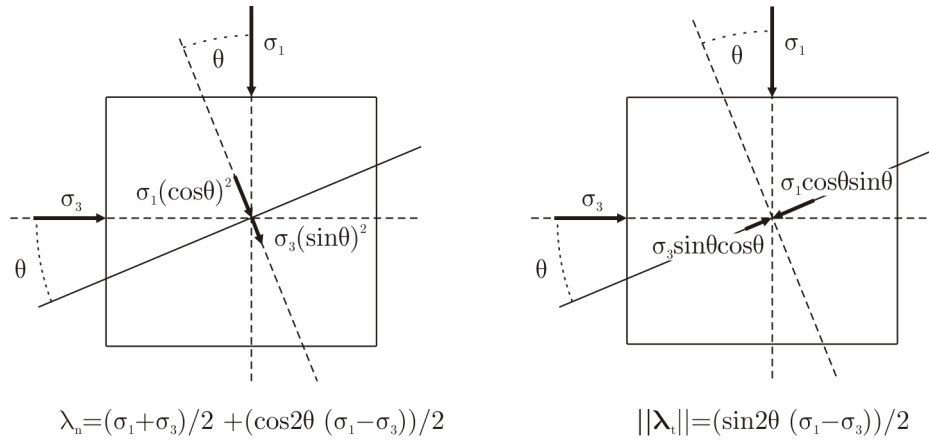


Figure 5.10: Derivation of the normal and tangential stress in terms of principal stresses

principle stresses can be expressed in terms of the stress invariants

$$\sigma_1 = \frac{2\sqrt{\text{II}_s}}{\sqrt{3}} \sin \left(\Theta + \frac{2\pi}{3} \right) + \frac{\text{I}_\sigma}{3}, \quad \sigma_3 = \frac{2\sqrt{\text{II}_s}}{\sqrt{3}} \sin \left(\Theta - \frac{2\pi}{3} \right) + \frac{\text{I}_\sigma}{3} \quad (5.4)$$

where I_σ is the first stress invariant and II_s , III_s the second and the third invariant of the deviatoric stress \mathbf{s} , respectively

$$\text{I}_\sigma = \boldsymbol{\sigma} \cdot \mathbf{1}, \quad \text{II}_s = \frac{1}{2} \mathbf{s} \cdot \mathbf{s}, \quad \text{III}_s = \frac{1}{3} \mathbf{s} \mathbf{s} \cdot \mathbf{s}, \quad \mathbf{s} = \boldsymbol{\sigma} - \frac{1}{3} \boldsymbol{\sigma} \cdot \mathbf{1}. \quad (5.5)$$

The Lode angle can also be linked to the invariants of the deviatoric stress via

$$\Theta = -\frac{1}{3} \arcsin \left(\frac{\sqrt{27}}{2} \frac{\text{III}_s}{\text{II}_s^{\frac{3}{2}}} \right). \quad (5.6)$$

Exploiting the trigonometric relations for the summation and the difference of the sinus (see Abramovitz and Stegun [1972]), the Mohr Coulomb yield criterion can now be rewritten by means of the stress invariants

$$f^{mc}(\boldsymbol{\sigma}) = \sqrt{\Pi_s} \cos(\Theta) \sec \varphi + \left[\frac{1}{3} \text{I}_{\boldsymbol{\sigma}} - \sqrt{\frac{\Pi_s}{3}} \sin(\Theta) \right] \tan \varphi - c = 0 \quad (5.7)$$

which serves as a basis for more advanced soil models.

5.4 Ehlers soil models

Experimental tests show a decrease of the friction angle at an increased pressure (Gudehus [1973]) and a strong dependency of the admissible elastic domain on the Lode angle Θ (Yamada and Ishihara [1979]). In Yamada and Ishihara [1979] a change of the shape on the π -plane from a cycle to a rounded triangle was also discovered during the loading process. And contrary to metals plastic response is observed even during pure hydrostatic compression. Based on these experimental observations a nonlinear yield criterion in stress space together with a parameter hardening concept which covers all the mentioned experimental outcomes is developed and can be found for instance in Ehlers and Scholz [2007] or in a more detailed form in Scholz [2007]. The main idea behind this yield criterion was to formulate a convex single yield surface which is differentiable at each point of the surface. This feature should guarantee a unique back projection within the return mapping algorithm.

5.4.1 Stress strain relation

The porous structure of the soil is captured within the linear elastic stress strain relation by means of the porosity factor c^v

$$\boldsymbol{\sigma} = \lambda \text{tr} \boldsymbol{\epsilon}^e c^v + 2\mu \boldsymbol{\epsilon}^e \quad (5.8)$$

which includes the influence of the solid volume ratio limited by its initial value n_0^s and its upper bound n_{max}^s (Ehlers and Scholz [2007])

$$c^v = \frac{\text{tr} \boldsymbol{\epsilon}^c}{(\text{tr} \boldsymbol{\epsilon}^c - \text{tr} \boldsymbol{\epsilon}^e)}, \quad \text{tr} \boldsymbol{\epsilon}^c = \frac{n_p^s}{n_{max}^s} - 1 = \frac{n_0^s}{n_{max}^s (1 + \text{tr} \boldsymbol{\epsilon}^p)} - 1. \quad (5.9)$$

The solid volume ratio can also be linked to the void ratio which is a common variable in geomechanics

$$n_0^s = \frac{1}{1 + e}, \quad e_0 = \frac{1 - n_0^s}{n_0^s}, \quad e_{max} = \frac{1 - n_{max}^s}{n_{max}^s}. \quad (5.10)$$

5.4.2 Yield criterion and evolution equation

The seven parametric yield criterion of Ehlers [1995] written in terms of the invariants $f(\boldsymbol{\sigma}) = f(\text{I}_{\boldsymbol{\sigma}}, \text{II}_{\text{s}}, \text{III}_{\text{s}})$ has a closed shape

$$f(\boldsymbol{\sigma}) = \sqrt{\left(1 + \gamma \text{III}_{\text{s}} \text{II}_{\text{s}}^{-\frac{3}{2}}\right)^m \text{II}_{\text{s}} + \frac{1}{2} \alpha \text{I}_{\boldsymbol{\sigma}}^2 + \delta^2 \text{I}_{\boldsymbol{\sigma}}^4 + \beta \text{I}_{\boldsymbol{\sigma}} + \epsilon \text{I}_{\boldsymbol{\sigma}}^2 - \kappa} = 0 \quad (5.11)$$

and the standard parameters, like friction angle and cohesion, can be linked to the model via

$$\kappa = c \cos \varphi, \quad \beta = \frac{1}{3} \sin \varphi. \quad (5.12)$$

Most of the materials exhibit a conical structure of the yield surface and a description in cylindrical coordinates is advantageous especially for the graphical representation. Now the Ehlers yield criterion can be decomposed additively into a deviatoric and a volumetric part

$$f(\text{I}_{\boldsymbol{\sigma}}, \text{II}_{\text{s}}, \Theta) = f^d(\text{II}_{\text{s}}, \Theta) + f^v(\text{I}_{\boldsymbol{\sigma}}) = 0 \quad (5.13)$$

where the first one depends on the second invariant of the deviatoric stress and on the Lode angle

$$f^d(\text{II}_{\text{s}}, \Theta) = \sqrt{\left(1 + \frac{2}{\sqrt{27}} \gamma \sin(3\Theta)\right)^m \text{II}_{\text{s}}} \quad (5.14)$$

and the second one can be formulated only by the first stress invariant

$$f^v(\text{I}_{\boldsymbol{\sigma}}) = \sqrt{(\epsilon^2 - \delta^2) \text{I}_{\boldsymbol{\sigma}}^4 + 2\beta\epsilon \text{I}_{\boldsymbol{\sigma}}^3 + \left(\beta^2 - \frac{1}{2} \alpha - 2\epsilon\kappa\right) \text{I}_{\boldsymbol{\sigma}}^2 - 2\beta\kappa \text{I}_{\boldsymbol{\sigma}} + \kappa^2}. \quad (5.15)$$

For a graphical representation of the yield surface the radius of the cone

$$r = \sqrt{2\text{II}_{\text{s}}} = \frac{\sqrt{2\text{II}_{\text{s}}}}{f^d(\text{II}_{\text{s}}, \Theta)} f^v(\text{I}_{\boldsymbol{\sigma}}) \quad (5.16)$$

varies not only on the π -plane but also along the hydrostatic axis (figure 5.11). Additionally, to represent dilatancy and contractancy effects, a plastic potential is introduced

$$g(\boldsymbol{\sigma}) = \sqrt{\Psi_1 \text{II}_{\text{s}} + \frac{1}{2} \alpha \text{I}_{\boldsymbol{\sigma}}^2 + \delta^2 \text{I}_{\boldsymbol{\sigma}}^4 + \Psi_2 \beta \text{I}_{\boldsymbol{\sigma}} + \epsilon \text{I}_{\boldsymbol{\sigma}}^2} \quad (5.17)$$

leading to a non-associated description of the soil behavior (figure 5.12). Since plasticity is path dependent, an evolution equation for the plastic strain is needed

$$\begin{aligned} \dot{\boldsymbol{\epsilon}}^p &= \dot{\lambda} \frac{\partial g(\boldsymbol{\sigma})}{\partial \boldsymbol{\sigma}} = \frac{1}{2g_{rt}} \left[\Psi_1 \frac{\partial \text{II}_{\text{s}}}{\partial \boldsymbol{\sigma}} + (\alpha \text{I}_{\boldsymbol{\sigma}} + 4\delta^2 \text{I}_{\boldsymbol{\sigma}}^3) \frac{\partial \text{I}_{\boldsymbol{\sigma}}}{\partial \boldsymbol{\sigma}} \right] + (\Psi_2 \beta + 2\epsilon \text{I}_{\boldsymbol{\sigma}}) \frac{\partial \text{I}_{\boldsymbol{\sigma}}}{\partial \boldsymbol{\sigma}} \\ g_{rt} &= \sqrt{\Psi_1 \text{II}_{\text{s}} + \frac{1}{2} \alpha \text{I}_{\boldsymbol{\sigma}}^2 + \delta^2 \text{I}_{\boldsymbol{\sigma}}^4} \end{aligned} \quad (5.18)$$

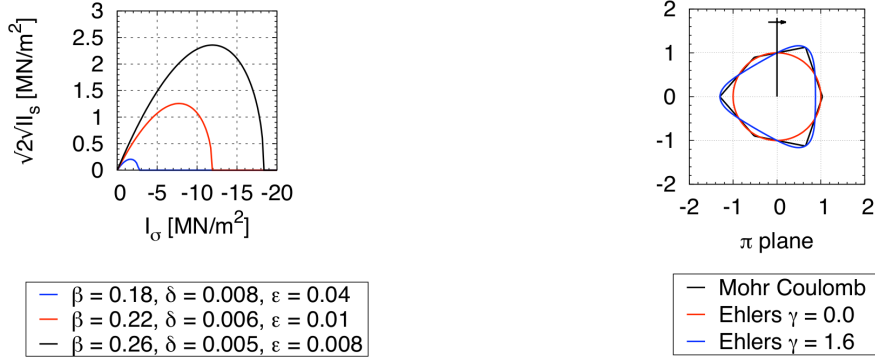


Figure 5.11: Distribution of the Ehlers soil model along the hydrostatic axis (left) and on the π -plane where the zero Lode angle Θ is indicated by an arrow (right)

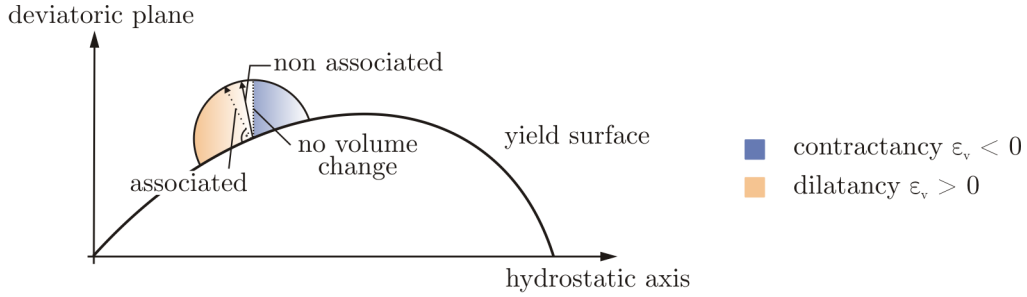


Figure 5.12: Assignment of contractancy and dilatancy effects along the hydrostatic axis of the Ehlers yield surface

where the abbreviation of the root of the potential g_{rt} is used to simplify the notation. With the definition of the dilatancy angle as the ratio between the volumetric and the deviatoric plastic deformation

$$\tan \nu^p = \frac{\dot{\epsilon}^p \cdot \mathbf{1}}{3 \|e(\epsilon^p)\|} = \frac{1}{\sqrt{2} \Pi_s} \left[\frac{\partial g}{\partial \Pi_s} \right]^{-1} \frac{\partial g}{\partial I_\sigma} \quad (5.19)$$

the flow rule (5.18) can now be reformulated in terms of the dilatancy angle

$$\dot{\epsilon}^p = \dot{\lambda} \left[\frac{1}{\sqrt{2} \Pi_s} + \tan \nu^p \frac{\partial I_\sigma}{\partial \sigma} \right], \quad \dot{\lambda} = \sqrt{2} \Pi_s \frac{\partial g}{\partial \Pi_s} \dot{\lambda} \quad (5.20)$$

where the operator in (5.19)

$$e(\bullet) = \bullet - \frac{1}{3} \bullet \cdot \mathbf{1} \quad (5.21)$$

indicates the deviatoric expression of the desired second order tensor \bullet . For the Ehlers soil model, the tangent of the dilatancy angle can be specified as

$$\tan \nu^p = \frac{1}{\Psi_1 \sqrt{2} \Pi_s} \left[\alpha I_\sigma + 4 \delta^2 I_\sigma^3 + 2 \sqrt{\Psi_1 \Pi_s + \frac{1}{2} I_\sigma^2 + \delta^2 I_\sigma^4 (\Psi_2 \beta + 2 \epsilon I_\sigma)} \right] \quad (5.22)$$

5.4.3 Hardening concept

Even at the onset of loading the soil shows a plastic deformation behavior and at further loading the soil can harden or soften. Different concepts of hardening are possible (Desai and Siriwardane [1984]) and in the Ehlers soil model the concept of a parameter hardening is realized where the actual version is given in Ehlers and Scholz [2007]. The evolution equation for the selected parameters $\mathbf{h} = [\beta, \delta, \epsilon, \gamma]^T$

$$\dot{\mathbf{h}} = \dot{\lambda} (\mathbf{h}_{max} - \mathbf{h}) \left[\mathbf{C}_h^v \text{tr} \frac{\partial g(\boldsymbol{\sigma}, \mathbf{h})}{\partial \boldsymbol{\sigma}} + \mathbf{C}_h^d e \left(\frac{\partial g(\boldsymbol{\sigma}, \mathbf{h})}{\partial \boldsymbol{\sigma}} \right) \parallel \right] = 0 \quad (5.23)$$

ensures that the complete deviatoric strain and the contractant part of the volumetric strain leads to a hardening and the dilatant part of the volumetric strain to a softening. The parameters β, δ, ϵ change the shape of the yield surface along the hydrostatic axis and γ is responsible for the conversion from a cycle to a rounded triangle. If the hardening concept is used for the Ehlers model, the dependency of the yield criterion and of the potential on the hardening variables have to be extended leading to $f = f(\boldsymbol{\sigma}, \mathbf{h})$, $g = g(\boldsymbol{\sigma}, \mathbf{h})$. Figure 5.13 shows the yield surface for GEBA sand (table 5.1) at the initial and at the final position where the z-axis corresponds to the hydrostatic

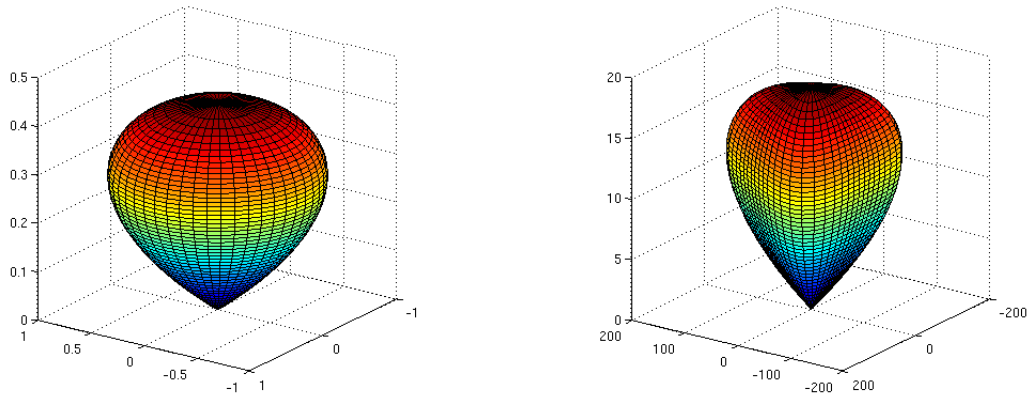


Figure 5.13: Starting (left) and final (right) yield surface for GEBA sand

axis and the units are significantly larger at the final yield surface.

5.4.4 Derivatives

For the tangent matrix some derivatives of the yield criterion and of the potential are needed which will be stated in the following. With the derivatives of the invariants (see also B.5)

$$\frac{\partial I_{\boldsymbol{\sigma}}}{\partial \boldsymbol{\sigma}} = \mathbf{1}, \quad \frac{\partial II_{\mathbf{s}}}{\partial \boldsymbol{\sigma}} = \mathbf{s}, \quad \frac{\partial III_{\mathbf{s}}}{\partial \boldsymbol{\sigma}} = \mathbf{s} \mathbf{s} - \frac{1}{3} \mathbf{s} \cdot \mathbf{s} \mathbf{1}, \quad \frac{\partial^2 II_{\mathbf{s}}}{\partial \boldsymbol{\sigma} \partial \boldsymbol{\sigma}} = \mathbf{1} \mathbf{1} - \frac{1}{3} \mathbf{1} \otimes \mathbf{1}, \quad (5.24)$$

the second derivative of the potential with respect to the stress

$$\begin{aligned} \frac{\partial^2 g}{\partial \boldsymbol{\sigma} \partial \boldsymbol{\sigma}} &= \frac{1}{2g_{rt}} \left[\Psi_1 \frac{\partial^2 \Pi_s}{\partial \boldsymbol{\sigma} \partial \boldsymbol{\sigma}} + (\alpha + 12\delta^2 I_\sigma^2) \frac{\partial I_\sigma}{\partial \boldsymbol{\sigma}} \otimes \frac{\partial I_\sigma}{\partial \boldsymbol{\sigma}} \right] \\ &\quad - \frac{1}{4g_{rt}^3} \left[\Psi_1^2 \frac{\partial \Pi_s}{\partial \boldsymbol{\sigma}} \otimes \frac{\partial \Pi_s}{\partial \boldsymbol{\sigma}} + (\alpha I_\sigma + 4\delta^2 I_\sigma^3)^2 \frac{\partial I_\sigma}{\partial \boldsymbol{\sigma}} \otimes \frac{\partial I_\sigma}{\partial \boldsymbol{\sigma}} \right. \\ &\quad \left. + \Psi_1 (\alpha I_\sigma + 4\delta^2 I_\sigma^3) \left(\frac{\partial \Pi_s}{\partial \boldsymbol{\sigma}} \otimes \frac{\partial I_\sigma}{\partial \boldsymbol{\sigma}} + \frac{\partial I_\sigma}{\partial \boldsymbol{\sigma}} \otimes \frac{\partial \Pi_s}{\partial \boldsymbol{\sigma}} \right) \right] + 2\epsilon \frac{\partial I_\sigma}{\partial \boldsymbol{\sigma}} \otimes \frac{\partial I_\sigma}{\partial \boldsymbol{\sigma}} \end{aligned} \quad (5.25)$$

can be specified. Using the abbreviations

$$\Gamma = \left(1 + \gamma \text{III}_s \text{II}_s^{-\frac{3}{2}} \right) \quad f_{rt} = \sqrt{\Gamma^m \text{II}_s + \frac{1}{2} \alpha I_\sigma^2 + \delta^2 I_\sigma^4}, \quad (5.26)$$

the derivative of the yield criterion with respect to the stress

$$\begin{aligned} \frac{\partial f}{\partial \boldsymbol{\sigma}} &= \frac{1}{2f_{rt}} \left[m\Gamma^{m-1}\gamma \left(\frac{\partial \text{III}_s}{\partial \boldsymbol{\sigma}} \text{II}_s^{-\frac{1}{2}} - \frac{3}{2} \text{III}_s \text{II}_s^{-\frac{3}{2}} \frac{\partial \text{II}_s}{\partial \boldsymbol{\sigma}} \right) + \Gamma^m \frac{\partial \text{II}_s}{\partial \boldsymbol{\sigma}} \right. \\ &\quad \left. + (\alpha I_\sigma + 4\delta^2 I_\sigma^3) \frac{\partial I_\sigma}{\partial \boldsymbol{\sigma}} \right] + (\beta + 2\epsilon I_\sigma) \frac{\partial I_\sigma}{\partial \boldsymbol{\sigma}} \end{aligned} \quad (5.27)$$

can be written in a compact form. Additionally, the derivative of the flow rule (5.18) with respect to the hardening parameters

$$\begin{aligned} \frac{\partial^2 g}{\partial \boldsymbol{\sigma} \partial \beta} &= \Psi_2 \frac{\partial I_\sigma}{\partial \boldsymbol{\sigma}}, \quad \frac{\partial^2 g}{\partial \boldsymbol{\sigma} \partial \gamma} = 0, \quad \frac{\partial^2 g}{\partial \boldsymbol{\sigma} \partial \epsilon} = 2I_\sigma \frac{\partial I_\sigma}{\partial \boldsymbol{\sigma}} \\ \frac{\partial^2 g}{\partial \boldsymbol{\sigma} \partial \delta} &= \frac{1}{2g_{rt}} 4I_\sigma^3 \frac{\partial I_\sigma}{\partial \boldsymbol{\sigma}} 2\delta - \frac{1}{4g_{rt}^3} \left[\Psi_1 \frac{\partial \text{II}_s}{\partial \boldsymbol{\sigma}} + (\alpha I_\sigma + 4\delta I_\sigma^3) \frac{\partial I_\sigma}{\partial \boldsymbol{\sigma}} \right] I_\sigma^4 2\delta \end{aligned} \quad (5.28)$$

as well as the derivative of the yield criterion (5.11) with respect to β, γ, δ and ϵ

$$\frac{\partial f}{\partial \beta} = I_\sigma, \quad \frac{\partial f}{\partial \gamma} = \frac{1}{2f_{rt}} m \Gamma^{m-1} \text{III}_s \text{II}_s^{-\frac{1}{2}}, \quad \frac{\partial f}{\partial \delta} = \frac{1}{2f_{rt}} 2\delta I_\sigma^4, \quad \frac{\partial f}{\partial \epsilon} = I_\sigma^2 \quad (5.29)$$

are needed for the solution process.

5.4.5 Algorithmic implementation

Using the implicit backward Euler time integration scheme for the evolution equation of the plastic strain (3.33), the linear elastic strain can be modified to

$$\boldsymbol{\epsilon}_{n+1}^e = \boldsymbol{\epsilon}_{n+1} - \boldsymbol{\epsilon}_{n+1}^p = \boldsymbol{\epsilon}_{n+1}^{tr} - \gamma_{n+1} \frac{\partial g}{\partial \boldsymbol{\sigma}} \Big|_{n+1}. \quad (5.30)$$

Together with the porosity factor c_{n+1}^v and its trial state c_{n+1}^{vtr} at the actual time step

$$\begin{aligned} c_{n+1}^v &= \frac{\text{tr } \boldsymbol{\varepsilon}_{n+1}^c}{\text{tr } \boldsymbol{\varepsilon}_{n+1}^c - \text{tr } \boldsymbol{\varepsilon}_{n+1} + \text{tr } \boldsymbol{\varepsilon}_{n+1}^p}, & \text{tr } \boldsymbol{\varepsilon}_{n+1}^c &= \frac{n_0^s}{n_{max}^s (1 + \text{tr } \boldsymbol{\varepsilon}_{n+1}^p)} - 1 \\ c_{n+1}^{vtr} &= \frac{\text{tr } \boldsymbol{\varepsilon}_{n+1}^{ctr}}{\text{tr } \boldsymbol{\varepsilon}_{n+1}^{ctr} - \text{tr } \boldsymbol{\varepsilon}_{n+1} + \text{tr } \boldsymbol{\varepsilon}_n^p}, & \text{tr } \boldsymbol{\varepsilon}_{n+1}^{ctr} &= \frac{n_0^s}{n_{max}^s (1 + \text{tr } \boldsymbol{\varepsilon}_n^p)} - 1, \end{aligned} \quad (5.31)$$

the trial stress and also the trial hardening parameters can be formulated

$$\boldsymbol{\sigma}_{n+1}^{tr} = \lambda \text{tr } \boldsymbol{\varepsilon}^{tr} c_{n+1}^{vtr} + 2\mu \boldsymbol{\varepsilon}^{tr}, \quad \mathbf{h}_{n+1}^{tr} = \mathbf{h}_n. \quad (5.32)$$

The trial yield criterion determines whether the integration point behaves elastic or plastic

$$\begin{aligned} \text{if } f(\boldsymbol{\sigma}_{n+1}^{tr}, \mathbf{h}_{n+1}^{tr}) &\leq 0 \quad \rightarrow \quad \text{elastic} \\ \text{if } f(\boldsymbol{\sigma}_{n+1}^{tr}, \mathbf{h}_{n+1}^{tr}) &> 0 \quad \rightarrow \quad \text{plastic.} \end{aligned} \quad (5.33)$$

In the case of an elastic response, the stress, the strain and the porosity factor are equal to the corresponding trial state and the material tangent is equivalent to the derivative of the stress with respect to the elastic strain

$$\begin{aligned} \boldsymbol{\sigma}_{n+1} &= \boldsymbol{\sigma}_{n+1}^{tr}, \\ \mathbf{D}_{n+1} &= \mathbf{D}_{n+1}^e = 2\mu \mathbf{1} + \lambda \left(c_{n+1}^v + \text{tr } \boldsymbol{\varepsilon}^e \frac{\text{tr } \boldsymbol{\varepsilon}_{n+1}^e \text{tr } \boldsymbol{\varepsilon}_{n+1}^c}{(\text{tr } \boldsymbol{\varepsilon}_{n+1}^c - \text{tr } \boldsymbol{\varepsilon}_{n+1}^e)^2} \right) \mathbf{1} \otimes \mathbf{1}. \end{aligned} \quad (5.34)$$

For a plastic response, the three equations

$$\begin{aligned} \mathbf{R}_{\sigma n+1} &= \boldsymbol{\sigma}_{n+1} - 2\mu \boldsymbol{\varepsilon}_{n+1}^e - \lambda \text{tr } \boldsymbol{\varepsilon}_{n+1}^e c_{n+1}^v = 0 \\ \mathbf{R}_{h n+1} &= \mathbf{h}_{n+1} - \mathbf{h}_n + \gamma_{n+1} (\mathbf{h}_{n+1} - \mathbf{h}_{max}) \left[\mathbf{C}_h^v \mathbf{n}_{n+1}^{vp} + \mathbf{C}_h^d \|\mathbf{n}_{n+1}^{ep}\| \right] = 0 \\ \mathbf{R}_{\gamma n+1} &= f(\boldsymbol{\sigma}_{n+1}, \mathbf{h}_{n+1}) = 0 \end{aligned} \quad (5.35)$$

have to be solved using the abbreviations

$$\begin{aligned} \gamma_{n+1} \mathbf{n}_{n+1}^{vp} &= \gamma_{n+1} \frac{\partial g}{\partial \boldsymbol{\sigma}_{n+1}} \cdot \mathbf{1} = \text{tr } \boldsymbol{\varepsilon}_{n+1}^p - \text{tr } \boldsymbol{\varepsilon}_n^p \\ \gamma_{n+1} \mathbf{n}_{n+1}^{ep} &= \gamma_{n+1} \left(\frac{\partial g}{\partial \boldsymbol{\sigma}_{n+1}} - \frac{1}{3} \left[\frac{\partial g}{\partial \boldsymbol{\sigma}_{n+1}} \cdot \mathbf{1} \right] \mathbf{1} \right) = \mathbf{e}_{n+1}^p - \mathbf{e}_n^p. \end{aligned} \quad (5.36)$$

Due to the nonlinearity of (5.35), the Newton iteration is applied leading to the coupled matrix

$$\begin{bmatrix} \mathbf{K}_{\sigma \gamma n+1} & \mathbf{K}_{\sigma h n+1} & \mathbf{K}_{\sigma \gamma n+1} \\ \mathbf{K}_{h \sigma n+1} & \mathbf{K}_{h h n+1} & \mathbf{K}_{h \gamma n+1}^g \\ \mathbf{K}_{\gamma \sigma n+1} & \mathbf{K}_{\gamma h n+1} & 0 \end{bmatrix} \begin{bmatrix} \Delta \boldsymbol{\sigma}_{n+1} \\ \Delta \mathbf{h}_{n+1} \\ \Delta \gamma_{n+1} \end{bmatrix} = \begin{bmatrix} \mathbf{R}_{\sigma n+1} \\ \mathbf{R}_{h n+1} \\ \mathbf{R}_{\gamma n+1} \end{bmatrix}. \quad (5.37)$$

The individual matrix contributions of the first row of the tangent matrix

$$\begin{aligned}
\mathbf{K}_{\sigma\sigma n+1} &= \left[2\mu \mathbf{1} + \lambda \left(c^v + \text{tr} \boldsymbol{\epsilon}_{n+1}^e \frac{\partial c_{n+1}^v}{\partial \text{tr} \boldsymbol{\epsilon}_{n+1}^p} \right) \mathbf{1} \otimes \mathbf{1} \right] \frac{\partial^2 g}{\partial^2 \boldsymbol{\sigma}} \Big|_{n+1} \\
\mathbf{K}_{\sigma h n+1} &= \left[2\mu \mathbf{1} + \lambda \left(c^v + \text{tr} \boldsymbol{\epsilon}_{n+1}^e \frac{\partial c_{n+1}^v}{\partial \text{tr} \boldsymbol{\epsilon}_{n+1}^p} \right) \mathbf{1} \otimes \mathbf{1} \right] \frac{\partial^2 g}{\partial \boldsymbol{\sigma} \partial \mathbf{h}} \Big|_{n+1} \\
\mathbf{K}_{\sigma\gamma n+1} &= \left[2\mu \mathbf{1} + \lambda \left(c^v + \text{tr} \boldsymbol{\epsilon}_{n+1}^e \frac{\partial c_{n+1}^v}{\partial \text{tr} \boldsymbol{\epsilon}_{n+1}^p} \right) \mathbf{1} \otimes \mathbf{1} \right] \frac{\partial g}{\partial \boldsymbol{\sigma}} \Big|_{n+1}
\end{aligned} \tag{5.38}$$

are based on the derivative of the porosity factor with respect to the plastic strain tensor

$$\begin{aligned}
\frac{\partial c_{n+1}^v}{\partial \text{tr} \boldsymbol{\epsilon}_{n+1}^p} &= \frac{\text{tr} \boldsymbol{\epsilon}_{n+1}^c}{(\text{tr} \boldsymbol{\epsilon}_{n+1}^c - \text{tr} \boldsymbol{\epsilon}_{n+1}^e)^2} \left(1 - \frac{n_0^s}{n_{max}^s (1 + \text{tr} \boldsymbol{\epsilon}_{n+1}^p)^2} \right) \\
&\quad - \frac{n_0^s}{n_{max}^s (1 + \text{tr} \boldsymbol{\epsilon}_{n+1}^p)^2}.
\end{aligned} \tag{5.39}$$

The second row indicates the derivatives of the hardening evolution equation

$$\begin{aligned}
\mathbf{K}_{h\sigma n+1} &= \gamma_{n+1} \left[\mathbf{C}_h^v \mathbf{1} + \mathbf{C}_h^d \frac{\mathbf{n}_{n+1}^{ep}}{\|\mathbf{n}_{n+1}^{ep}\|} \right] \frac{\partial^2 g}{\partial \boldsymbol{\sigma} \partial \boldsymbol{\sigma}} \Big|_{n+1} \\
\mathbf{K}_{hh n+1} &= \mathbf{1}^h + \gamma_{n+1} \left(\left[\mathbf{C}_h^v \mathbf{n}_{n+1}^{vp} + \mathbf{C}_h^d \|\mathbf{n}_{n+1}^{ep}\| \right] + \left[\mathbf{C}_h^v \mathbf{1} + \mathbf{C}_h^d \frac{\mathbf{n}_{n+1}^{ep}}{\|\mathbf{n}_{n+1}^{ep}\|} \right] \frac{\partial^2 g}{\partial \boldsymbol{\sigma} \partial \mathbf{h}} \Big|_{n+1} \right) \\
\mathbf{K}_{h\gamma n+1} &= (\mathbf{h}_{n+1} - \mathbf{h}_{max}) \left[\mathbf{C}_h^v \mathbf{n}_{n+1}^{vp} + \mathbf{C}_h^d \|\mathbf{n}_{n+1}^{ep}\| \right]
\end{aligned} \tag{5.40}$$

and in the last row, the derivatives of the yield criterion with respect to the stress and to the hardening parameters are conducted

$$\mathbf{K}_{\gamma\sigma n+1} = \frac{\partial f}{\partial \boldsymbol{\sigma}} \Big|_{n+1}, \quad \mathbf{K}_{\gamma h n+1} = \frac{\partial f}{\partial \mathbf{h}} \Big|_{n+1}. \tag{5.41}$$

The linearization of the stress, the hardening parameters and the plastic increment can also be written in matrix notation equivalent to (5.37), but now the first row has to be multiplied with the inverse of the updated elastic tangent \mathbf{D}_{n+1}^e

$$\begin{bmatrix} \mathbf{D}_{n+1}^{e-1} \mathbf{K}_{\sigma\gamma n+1} & \mathbf{D}_{n+1}^{e-1} \mathbf{K}_{\sigma h n+1} & \mathbf{D}_{n+1}^{e-1} \mathbf{K}_{\sigma\gamma n+1} \\ \mathbf{K}_{h\sigma n+1} & \mathbf{K}_{hh n+1} & \mathbf{K}_{h\gamma n+1}^g \\ \mathbf{K}_{\gamma\sigma n+1} & \mathbf{K}_{\gamma h n+1} & 0 \end{bmatrix} \begin{bmatrix} \Delta \boldsymbol{\sigma}_{n+1} \\ \Delta \mathbf{h}_{n+1} \\ \Delta \gamma_{n+1} \end{bmatrix} = \begin{bmatrix} \Delta \boldsymbol{\epsilon}_{n+1} \\ \mathbf{0} \\ 0 \end{bmatrix} \tag{5.42}$$

in order to use the scheme in (3.39) and (3.40) for the computation of the material tensor

$$\mathbf{D}_{n+1} = \mathbf{A}_{\sigma\sigma n+1}. \tag{5.43}$$

5.4.6 Substepping scheme

If the trial stress and the trial hardening parameters are far away from the projection point, the Newton iteration can fail. Especially close to the apex often a backprojec-

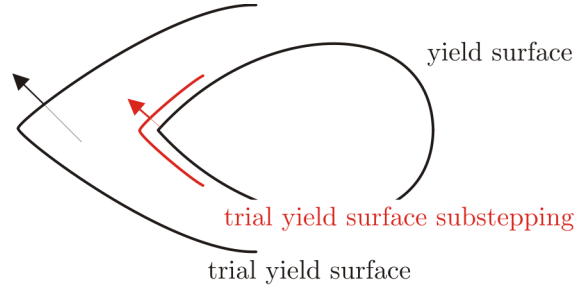


Figure 5.14: Derivation of the Mohr Coulomb normal stress and tangential stress in principal stress

tion is not possible (see figure 5.14), or due to the highly nonlinear yield criterion, a projection to different solutions can occur leading to a non convergence of the algorithm. A possibility to improve the closest point projection is the use of a substepping scheme (Sloan [1987], and figure 5.14) which is based on line search techniques. There at each integration point, the trial elastic strain is subdivided into a number of increments which ensures that the trial value remains always closely to the projection point. Within an additional loop $k = 1, \text{steps}$ the residuals of (5.35)

$$\begin{aligned} \mathbf{R}_{\sigma n+1}^{(k)} &= \boldsymbol{\sigma}_{n+1}^{(k)} - \tilde{\boldsymbol{\sigma}} \left(\boldsymbol{\epsilon}_{n+1}^{(k)}, \boldsymbol{\epsilon}_{n+1}^{p(k)} \right) = 0 \\ \mathbf{R}_{h n+1}^{(k)} &= \mathbf{h}_{n+1} - \mathbf{h}_n + \gamma_{n+1} (\mathbf{h}_{n+1} - \mathbf{h}_{max}) \left[\mathbf{C}_h^v \mathbf{n}_{n+1}^{vp(k)} + \mathbf{C}_h^d \|\mathbf{n}_{n+1}^{ep(k)}\| \right] = 0 \\ \mathbf{R}_{\gamma n+1}^{(k)} &= f_{n+1}^{s(k)} = 0 \end{aligned} \quad (5.44)$$

have to be solved at each step k where the strain and the plastic part

$$q^{(k)} = \sum_{i=1}^k s^{(k)}, \quad \boldsymbol{\epsilon}_{n+1}^{(k)} = q^{(k)} \boldsymbol{\epsilon}_{n+1}, \quad \boldsymbol{\epsilon}_{n+1}^{p(k)} = s^{(k)} \boldsymbol{\epsilon}_n^p + \gamma_{n+1}^{(k)} \frac{\partial \mathbf{g}}{\partial \boldsymbol{\sigma}} \bigg|_{n+1}^{(k)} + \boldsymbol{\epsilon}^{p(k-1)}, \quad (5.45)$$

have to be updated at each step. For the linearization within the substepping scheme (Perez-Foguet et al. [2001]), the tangent of (5.42) (at the end of the substepping loop) can be used

$$\begin{bmatrix} \bar{\mathbf{D}}_{n+1}^{e-1} \mathbf{K}_{\sigma \gamma n+1} & \bar{\mathbf{D}}_{n+1}^{e-1} \mathbf{K}_{\sigma h n+1} & \bar{\mathbf{D}}_{n+1}^{e-1} \mathbf{K}_{\sigma \gamma n+1} \\ \mathbf{K}_{h \sigma n+1} & \mathbf{K}_{h h n+1} & \mathbf{K}_{h \gamma n+1}^g \\ \mathbf{K}_{\gamma \sigma n+1} & \mathbf{K}_{\gamma h n+1} & 0 \end{bmatrix} \begin{bmatrix} \Delta \boldsymbol{\sigma}_{n+1} \\ \Delta \mathbf{h}_{n+1} \\ \Delta \gamma_{n+1} \end{bmatrix} = \begin{bmatrix} \Delta \boldsymbol{\epsilon}_{n+1} \\ \mathbf{0} \\ 0 \end{bmatrix}, \quad (5.46)$$

but now at each step k , the modified elastic material tensor has to be updated

$$\begin{aligned}\bar{\mathbf{D}}_{n+1}^{e(k)} &= q^{(k)} \mathbf{D}_{n+1}^{e(k)} - \mathbf{D}_{n+1}^{p(k)} \mathbf{D}_{n+1}^{p(k-1)-1} \left[q^{(k-1)} \mathbf{D}_{n+1}^{e(k-1)} - \mathbf{D}_{n+1}^{(k-1)} \right] \\ \mathbf{D}_{n+1}^{p(k)} &= \frac{\partial \boldsymbol{\sigma}_{n+1}}{\partial \boldsymbol{\varepsilon}_{n+1}^p}\end{aligned}\tag{5.47}$$

where the tangents $\mathbf{D}_{n+1}^{p(k)}$, $\mathbf{D}_{n+1}^{e(k)}$ and $\mathbf{D}_{n+1}^{(k)}$ have to be stored for the next step. For the determination of the number of steps, two possibilities are used in the literature. One is based on the truncation error of the Newton iteration (Sloan [1987]) and the other one adapts automatically the number of steps based on the convergence behavior of the Newton iteration (Perez-Foguet et al. [2001]) which is preferred in this work. If the Newton iteration takes more than 5 steps, the number of substeps is increased by 5 loops.

5.4.7 Viscoplastic regularization

Another numerical instability can occur by means of oscillations in the backprojection algorithm, if the solution lies closely between the elastic or plastic state (change of the active set) and a possible improvement is a viscoplastic regularization which smoothens the transition from elastic to plastic. One variant of this kind of regularization is formulated in Duvaut and Lions [1976] and numerically realized in Simo [1998]. A viscous damper η is introduced leading to an extension of the elastic domain which relaxes with time. So called overstresses

$$\begin{aligned}\boldsymbol{\sigma}_{n+1} &= \boldsymbol{\sigma}_{n+1}^* + \frac{\eta/\Delta t}{1 + \eta/\Delta t} (\boldsymbol{\sigma}_{n+1}^{tr} - \boldsymbol{\sigma}_{n+1}^*) \\ \mathbf{D}_{n+1} &= \frac{\eta/\Delta t}{1 + \eta/\Delta t} \mathbf{D}_{n+1}^*\end{aligned}\tag{5.48}$$

occur where $\boldsymbol{\sigma}_{n+1}^*$ and \mathbf{D}_{n+1}^* are the back projected stress and material tangent, respectively.

5.4.8 Numerical triaxial and footing test

A standard experiment in soil mechanics is the triaxial test where a cylindrical specimen is loaded in axial and radial direction leading to a homogeneous strain and stress distribution. All the tests are performed with GEBA fine sand of the Gebenbacher pit (Hirschau) with a grain diameter of 0.03 - 0.3 mm, a sieve retention of $d_{10} = 0.09$ mm, $d_{60} = 0.11$ mm and a coefficient of uniformity of $C_u = 1.22$. The complete set of parameters for the GEBA fine sand is specified in table 5.1 where the material parameters are determined by a fitting process on experimental data. (cf. Scholz [2007]). The first test is the triaxial compression test which characterizes the shearing behavior of the soil sample. Therefore the specimen is loaded with a variable radial

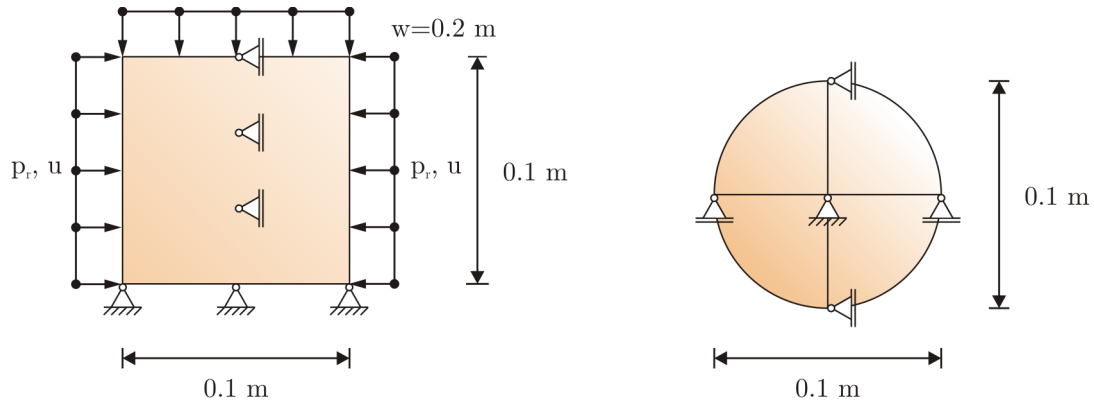


Figure 5.15: Side view (left) and top view (right) of the soil specimen in the triaxial test

stress p_r and an axial displacement of $w = 0.02$ m. To avoid a rotation around the z -axis, the displacements perpendicular to the x - and y -axis are kept fixed (figure 5.15). First the loads in axial and radial direction are increased hydrostatically in 10 steps until the limit of the radial stress is reached where the relationship between the axial displacement and the radial stress is given as

$$\epsilon_{33} = \frac{w}{h} = \frac{1 - 2\nu}{E} p_r. \quad (5.49)$$

Afterwards, the axial displacement is increased in 500 steps to its maximal value where the radial stress remains constant. The shear stress and the volumetric strain distribu-

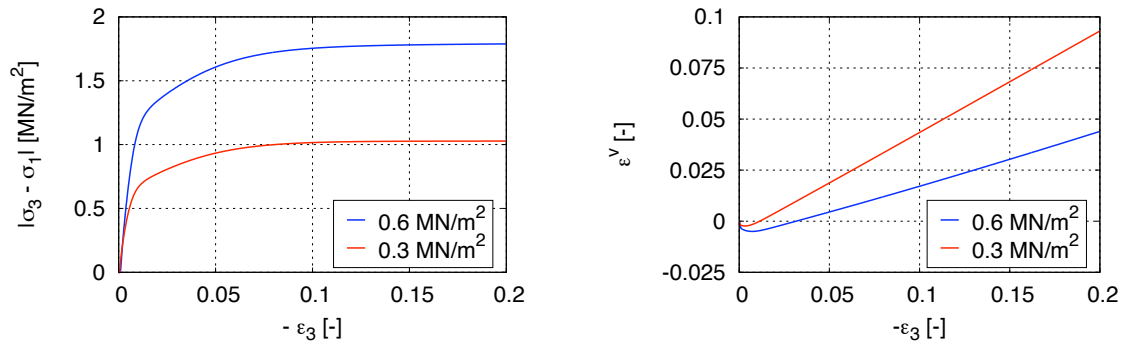


Figure 5.16: Triaxial compression test: Shear stress (left) and volumetric strain (right)

tion of the test are evaluated for two different radial stresses $p_r = 0.3$ MN/m² and $p_r = 0.6$ MN/m² showing the typical behavior of a dense sand where first the specimen compacts and afterwards dilates, see figure 5.16 right side. Only the shear stress shows no peak for the GEBA fine sand (5.16 left side) in the triaxial test.

The second test is an indicator for the behavior of the sand under a pure hydrostatic loading where also a plastic reaction of the material is observed in experimental

measurements. Therefore the cylindrical specimen (figure 5.15) is loaded with a displacement in axial as well as in radial direction of $u = w = 0.12$ m. Figure 5.17 shows

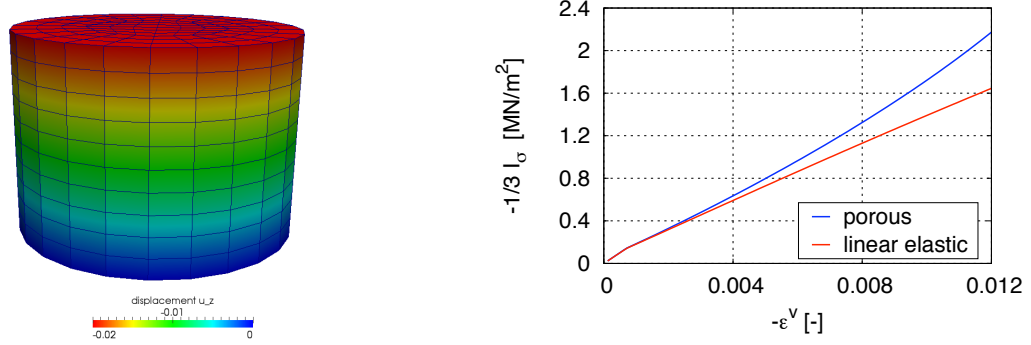


Figure 5.17: Final displacements of the shear compression test (left) and pressure distribution of the hydrostatic compression test (right)

a nonlinear distribution of the first stress invariant in the case of a porous stress strain relationship (5.8) compared to the usage of the standard linear elastic material tensor. The same test procedures with the same material parameters are also performed in Ehlers et al. [2011].

The second example is a large scale test where the pressure distribution under a footing is investigated. Due to the symmetry, only a quarter of the footing is considered where

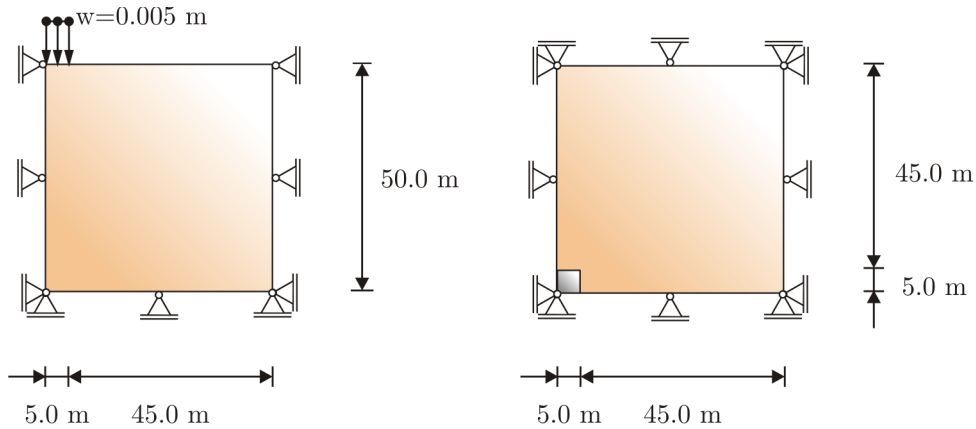


Figure 5.18: Side view (left) and top view (right) of the soil specimen in the footing test

a cube specimen of 50 m length is loaded at a quadratic area of 5 m length with a vertical displacement ($w = 0.005$ m) applied in 100 steps (see figure 5.18). Hence positive hydrostatic pressures occur around the outmost of the footing which is also a good test for the quality of the substepping algorithm. The right side of figure 5.19 shows that the pressure reaches a maximum value around $w = 0.0043$ m and decreases

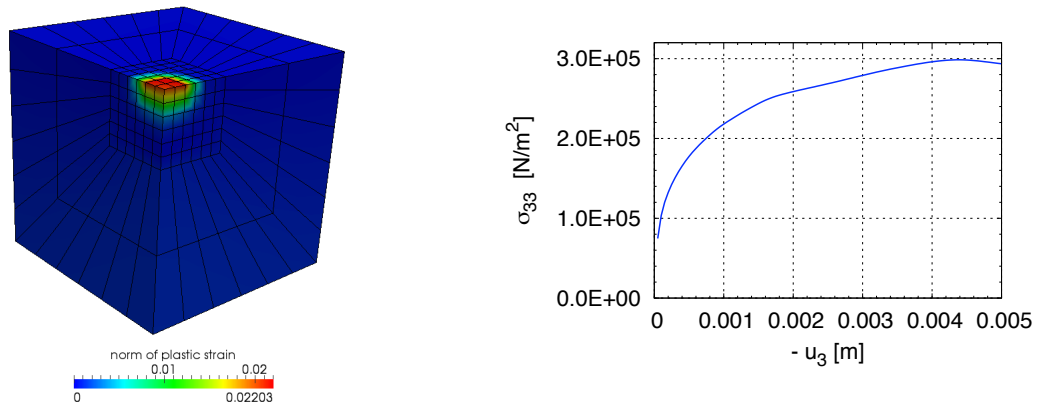


Figure 5.19: Norm of plastic strain (left) and pressure σ_{33} under the footing (right)

afterwards which is very similar to the shear behavior of a dense sand. On the left side of figure 5.19, it can be seen that the plastic strain is strongly localized closely under the footing and decreases quickly at larger distances in the case of a GEBA fine sand.

$\lambda = 100 \frac{\text{MN}}{\text{m}^2}$	$\mu = 150 \frac{\text{MN}}{\text{m}^2}$	$n_0^s = 0.585$	$n_{max}^s = 0.595$
$\beta_0 = 0.105$	$\beta_{max} = 0.263$	$C_\beta^v = -58$	$C_\beta^d = 350$
$\gamma_0 = 0.0$	$\gamma_{max} = 1.6$	$C_\gamma^v = -10$	$C_\gamma^d = 35$
$\delta_0 = 0.01 \frac{\text{m}^2}{\text{MN}}$	$\delta_{max} = 0.005 \frac{\text{m}^2}{\text{MN}}$	$C_\delta^v = 90$	$C_\beta^d = -15.9$
$\epsilon_0 = 0.0805 \frac{\text{m}^2}{\text{MN}}$	$\epsilon_{max} = 0.008 \frac{\text{m}^2}{\text{MN}}$	$C_\epsilon^v = -300$	$C_\epsilon^d = 300$
$\alpha = 0.01$	$\kappa = 0.0001 \frac{\text{MN}}{\text{m}^2}$	$m = 0.5454$	$\eta = 0.005$
$\Psi_1 = 0.97$	$\Psi_2 = 0.48$		

Table 5.1: Material data for GEBA sand

Chapter 6

Theory of porous media

Many industrial materials like polymeric or metallic foams, biomaterials or as seen in the previous chapter the soil have a porous structure consisting on different aggregates. Describing the interactions between the constituents on a macroscopic level the theory of porous media (TPM) was developed combining the theory of mixtures (Truesdell and Toupin [1960] or Truesdell [1984]) with the concept of volume fractions. Since the influence of water or gas at the contact surface are considered only in a theoretical form a brief description of the theory and the numerical implementation will be presented. A detailed introduction to the TPM is given in Ehlers [2002] or de Boer [2005].

6.1 Concept of volume fractions

The whole volume V of the desired body is the sum over all volumes of each constituent V^α

$$V = \int_{\varphi(B)} dv = \sum_{\alpha=1}^n V^\alpha = \sum_{\alpha=1}^n \int_{\varphi(B)} dv^\alpha = \sum_{\alpha=1}^n \int_{\varphi(B)} n^\alpha dv \quad (6.1)$$

where each volume fraction n^α is specified as

$$n^\alpha = \frac{dv^\alpha}{dv}, \quad \sum_{\alpha=1}^n n^\alpha = 1. \quad (6.2)$$

The saturation condition, i.e. the sum over all volume fractions has to be 1, has also to be fulfilled within the whole domain and at each local point. Within the concept of volume fractions the statistical distribution of the constituents is smeared out and instead a representative element volume (REV, see figure 6.1) is considered (Ehlers [2002]). A material and a partial density

$$\rho_0^\alpha = \frac{dm^\alpha}{dv^\alpha}, \quad \rho^\alpha = \frac{dm^\alpha}{dv}, \quad (6.3)$$

respectively, can be defined which are linked over the volume of fractions

$$\rho^\alpha = n^\alpha \rho_0^\alpha. \quad (6.4)$$

As a consequence, if a constituent is incompressible ($\rho_0^\alpha = \text{const.}$) the partial density is not necessarily constant.

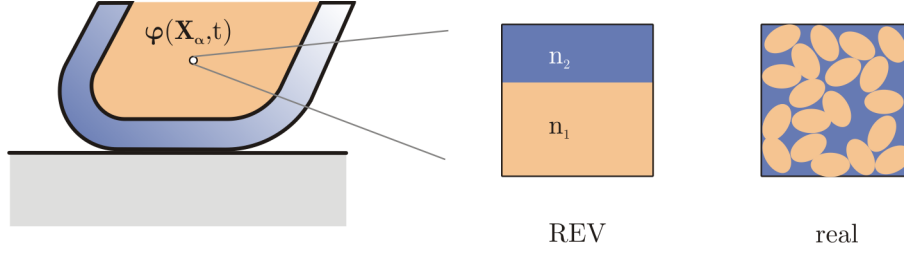


Figure 6.1: REV element

6.2 Kinematics of the mixture

The basic idea of the theory of mixtures is to superimpose different continuous media at each local point in the current configuration. Each media has thereby its own motion path (figure 6.2)

$$\mathbf{x} = \varphi_\alpha(\mathbf{X}_\alpha, t) \quad (6.5)$$

which leads to different velocities for each medium

$$\mathbf{x}'_\alpha = \frac{d_\alpha \mathbf{x}}{dt}. \quad (6.6)$$

The index ' indicates thereby the material derivative of the constituent and for values given in the Eulerian description the derivative follows accordingly to (2.4)

$$(\bullet)'_\alpha = \frac{\partial(\bullet)}{\partial t} + \text{grad}(\bullet) \cdot \mathbf{x}'_\alpha. \quad (6.7)$$

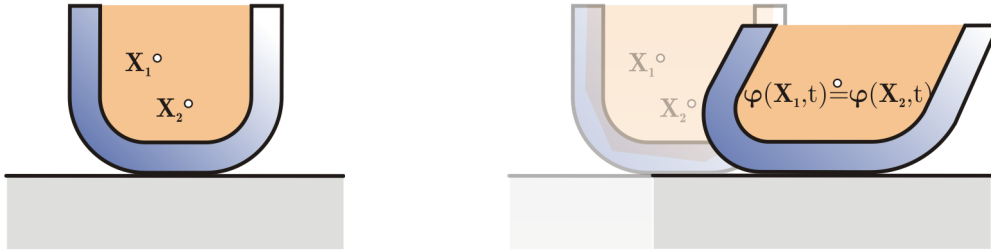


Figure 6.2: Initial configuration (left) and current configuration (right)

6.3 Balance of mass and momentum of the mixture

The theoretical framework of the theory of mixtures is based upon Truesdell [1984] who states three principles

- All properties of the mixture must be mathematical consequences of the properties of the constituents

- So as to describe the motion of a constituent we may in imagination isolate it from the the rest of the mixture provided we allow properly for the actions of the other constituent
- The motion of the mixture is governed by the same equations as is a single body

Consequently, the balance principles of each material should have a similar structure as the classical balance principles of the continuum. Only so called production terms can be added for each phase incorporating the interaction between the constituents, but after summation over all phases these interaction terms have to vanish. The balance of mass of each material

$$(\rho^\alpha)'_\alpha + \rho^\alpha \operatorname{div} \mathbf{x}'_\alpha = \hat{\rho}^\alpha \quad (6.8)$$

and the balance of momentum corresponds to the balance principles of the continuum (2.16), (2.23)

$$\rho^\alpha \mathbf{x}''_\alpha = \operatorname{div} \boldsymbol{\sigma}^\alpha + \rho^\alpha \bar{\mathbf{b}}^\alpha + \hat{\mathbf{p}}^\alpha \quad (6.9)$$

where now only the production terms for the mass ($\hat{\rho}^\alpha$) and for the momentum ($\hat{\mathbf{p}}^\alpha$) are added to the equations. Fulfilling the statement of Truesdell, after the summation over all constituents n

$$\sum_{\alpha=1}^n \hat{\rho}^\alpha = 0, \quad \sum_{\alpha=1}^n \hat{\mathbf{p}}^\alpha = \mathbf{0} \quad (6.10)$$

the production terms have to be equal to zero.

6.4 Incompressible biphasic model

For a lot of materials the solid skeleton of the porous media and the fluid can be assumed being incompressible. Neglecting the mass production term and considering the incompressibility assumption ($\rho_0^\alpha = \text{const.}$) the balance of mass (6.8) can be reduced to the continuity equation of the volume fractions

$$(n^\alpha)'_\alpha + n^\alpha \operatorname{div} \dot{\mathbf{x}}_\alpha = 0. \quad (6.11)$$

For the solid skeleton $\alpha = s$ and for the fluid $\alpha = f$ will be used in the following statements. The continuity equation for the solid skeleton can be integrated analytically leading to a relation between the initial and the current solid volume of fraction n_0^s and n^s , respectively. In the finite deformation regime the relation is based on the determinant of the solid deformation gradient \mathbf{F}_s

$$n^s = n_0^s (1 - \det \mathbf{F}_s^{-1}) \quad (6.12)$$

and in the linear case it depends on the divergence of the solid displacement

$$n^s = n_0^s (1 - \operatorname{div} \mathbf{u}_s), \quad n^f = 1 - n_0^s (1 - \operatorname{div} \mathbf{u}_s). \quad (6.13)$$

With the definition of the seepage velocity \mathbf{w}_f as the difference between the fluid and the solid velocity

$$\mathbf{w}_f = \mathbf{v}_f - \mathbf{v}_s \quad (6.14)$$

it is possible to rewrite the fluid time derivative in terms of the solid time derivative

$$(n^f)'_f = (n^f)'_s + \text{grad } n^f \mathbf{w}_f. \quad (6.15)$$

Using also the saturation condition in the derivative of (6.15)

$$(n^s)'_s = (1 - n^f)'_s = - (n^f)'_s \quad (6.16)$$

the continuity equation (6.11) of the whole mixture can be rewritten into the final form

$$\begin{aligned} (n^s)'_f + n^s \text{div } \mathbf{v}_s + (n^f)'_f + n^f \text{div } \mathbf{v}_f &= \text{grad } n^f \mathbf{w}_f + n^f \text{div } \mathbf{w}_f + \text{div } \mathbf{v}_s \\ &= \text{div } (n^f \mathbf{w}_f + \mathbf{v}_s) = 0. \end{aligned} \quad (6.17)$$

As a remark, due to the seepage velocity the Eulerian description of the fluid phase is now related to the Lagrangian form of the solid displacement which is also called a modified Eulerian setting (Ehlers [2002]) and at each material point the fluid is taken into account due to its relative motion. The fluid time derivative of the fluid velocity can also be represented by means of the solid time derivative

$$\mathbf{a}_f = (\mathbf{v}_f)'_f = (\mathbf{v}_s + \mathbf{w}_f)'_f = (\mathbf{v}_s + \mathbf{w}_f)'_s + \text{grad } (\mathbf{v}_s + \mathbf{w}_f) \mathbf{w}_f. \quad (6.18)$$

For the balance of momentum (6.9) the constitutive equations of each phase of the mixture have to be specified. The stress of the solid phase $\boldsymbol{\sigma}^s$ and of the fluid phase $\boldsymbol{\sigma}^f$

$$\boldsymbol{\sigma}^s = -n^s p \mathbf{1}, \quad \boldsymbol{\sigma}^f = -n^f p \mathbf{1}, \quad \boldsymbol{\sigma}^s + \boldsymbol{\sigma}^f = \boldsymbol{\sigma} - p \mathbf{1} \quad (6.19)$$

are subdivided such that the sum corresponds to the effective stress defined by Terzaghi (see Terzaghi et al. [1996]). $\boldsymbol{\sigma}$ can be determined by standard constitutive relations of section 2 or 5, for instance. The momentum production term of the fluid phase

$$\hat{\mathbf{p}}^f = -\hat{\mathbf{p}}^s = p \text{grad } n^f - \frac{(n^f)^2 \gamma_0^f}{k^f} \mathbf{1} \mathbf{w}_f \quad (6.20)$$

is specified in such a way that the balance of momentum of the fluid yields to an dynamic extension of Darcys law of flow in the case of an isotropic permeability coefficient k_f (for a derivation of the law, see Bear [1972])

$$n^f \rho_0^f \mathbf{a}_f = -n^f \text{grad } p - \frac{(n^f)^2 \gamma_0^f}{k^f} \mathbf{w}_f + \rho^f \mathbf{b}. \quad (6.21)$$

For the quasi static case using (6.21) the unknown seepage velocity can be eliminated from the continuity equation of the mixture (6.18)

$$\text{div } \mathbf{v}_s - \frac{k_f}{\gamma_0^f} \text{div } \left(\text{grad } p - \rho_0^f \bar{\mathbf{b}} \right) = 0. \quad (6.22)$$

The balance of momentum (6.9) of the whole mixture in the case of incompressibility leads to

$$n^s \rho_0^s \mathbf{a}_s + n^f \rho_0^f \mathbf{a}_f = \text{div } (\boldsymbol{\sigma} - p \mathbf{1}) + \left(n^s \rho_0^s + n^f \rho_0^f \right) \bar{\mathbf{b}} \quad (6.23)$$

where the gravitational acceleration $\bar{\mathbf{b}}$ is the same for all phases.

6.5 Weak form of porous media

The primal variables of the incompressible two phase model are the solid displacement \mathbf{u}_s , the seepage velocity \mathbf{w}_f and the pressure p where for each variable the corresponding weak form has to be stated. For the displacements the balance of momentum of the whole mixture has to be weighted and set to zero

$$\begin{aligned} \int_{\varphi(B)} [\boldsymbol{\eta}_s \cdot (\rho^s \mathbf{a}_s + \rho^f \mathbf{a}_f) + \text{grad } \boldsymbol{\eta}_s (\boldsymbol{\sigma} - p \mathbf{1}) - \boldsymbol{\eta}_s \cdot (\rho^s + \rho^f) \bar{\mathbf{b}}] \, dv = \\ \int_{\varphi(\partial B_\sigma)} \boldsymbol{\eta}_s \cdot \bar{\mathbf{t}}^m \, da \end{aligned} \quad (6.24)$$

together with the prescribed stress vector $\bar{\mathbf{t}}^m = (-p \mathbf{1} + \boldsymbol{\sigma}) \cdot \mathbf{n}$. For the seepage velocity the balance of momentum of the fluid phase

$$\begin{aligned} \int_{\varphi(B)} \left[\delta \mathbf{w}_f \cdot \rho^f \mathbf{a}_f - \text{div} (\delta \mathbf{w}_f) n^f p + \delta \mathbf{w}_f \cdot \left(\frac{(n^f)^2 \gamma_0^f}{k^f} \mathbf{w}_f - \rho^f \bar{\mathbf{b}} \right) \right] \, dv = \\ \int_{\varphi(\partial B_\sigma)} \delta \mathbf{w}_f \cdot \bar{\mathbf{t}}^f \, da \end{aligned} \quad (6.25)$$

and for the pressure the continuity equation of the whole mixture has to be weighted

$$\int_{\varphi(B)} [\text{grad } \delta p \cdot n^f \mathbf{w}_f - \delta p \text{div } \mathbf{v}_s] \, dv = \int_{\varphi(\partial B_\sigma)} \delta p \bar{v} \, da \quad (6.26)$$

where the Neumann boundary condition $\bar{\mathbf{t}}^f = -n^f \bar{p} \mathbf{n}$ displays the stress vector of the fluid and $\bar{v} = n^f \bar{\mathbf{w}}_f \cdot \mathbf{n}$ the volume flux at the boundary, respectively. Using Darcys constitutive relationship for the seepage velocity (6.21) the weak form of the continuity equation of the mixture can be rewritten

$$\begin{aligned} \int_{\varphi(B)} \left[- \text{grad } \delta p \cdot \frac{k^f}{\gamma_0^f} \text{grad } p - \text{grad } \delta p \cdot \rho_0^f (\mathbf{a}_f - \bar{\mathbf{b}}) - \delta p \text{div } \mathbf{v}_s \right] \, dv = \\ \int_{\varphi(\partial B_\sigma)} \delta p \bar{v} \, da \end{aligned} \quad (6.27)$$

decreasing the index of the DAE form 2 to 1 which leads to a more stable formulation (Ellsiepen [1999]). In the quasi static case the balance of momentum (6.24) and the continuity equation (6.27) do not depend on the seepage velocity and hence the balance of momentum of the fluid phase (6.25) can be neglected. The balance of momentum (6.24)

$$\int_{\varphi(B)} [\text{grad } \boldsymbol{\eta}_s (\boldsymbol{\sigma} - p \mathbf{1}) - (\rho^s + \rho^f) \bar{\mathbf{b}}] \, dv = \int_{\varphi(\partial B_\sigma)} \boldsymbol{\eta}_s \cdot \bar{\mathbf{t}}^m \, da \quad (6.28)$$

as well as the weak form of the continuity equation (6.27) simplifies to

$$\begin{aligned} \int_{\varphi(B)} \left[-\operatorname{grad} \delta p \cdot \frac{k^f}{\gamma_0^f} \operatorname{grad} p + \operatorname{grad} \delta p \cdot \rho_0^f \bar{\mathbf{b}} - \delta p \operatorname{div} \mathbf{v}_s \right] dv = \\ \int_{\varphi(\partial B_\sigma)} \delta p \bar{v} da. \end{aligned} \quad (6.29)$$

6.6 Discretization of porous media

Normally, within the discretization process dealing with incompressibility constraints mixed formulations are preferred. Since the displacement gradient (stress) is added to the pressure quadratic shape functions are applied for the displacement and the seepage velocity and linear shape functions are used for the pressure. For these type of elements mathematically the inf-sup condition (Babushka Brezzi condition Braess [2007]) is fulfilled. For more details see Ellsiepen [1999] and the references therein. Here for simplicity only linear shape functions are applied for all unknowns and only the quasi static formulation is used. An extension to the dynamic case can be found in Ellsiepen [1999]. For the quasi static case the nodal solution vector $\mathbf{d}_J = [\mathbf{u}_{sJ}, p_J]$ and the element contributions to the overall tangent simplify to

$$\sum_{g=1}^{n_{gp}} \left\{ \sum_{I=1}^n \left(\sum_{J=1}^n [\mathbf{C}_{IJ} \mathbf{d}_J + \mathbf{K}_{IJ} \mathbf{d}_J] \right) = -\mathbf{R}_I \right\}. \quad (6.30)$$

The residual vector of the two fields (6.28), (6.29) are given in detail as

$$\begin{aligned} \mathbf{R}_I^u &= \mathbf{B}_I^T (\boldsymbol{\sigma} - p \mathbf{1}) - N_I (\rho^s + \rho^f) \bar{\mathbf{b}} \\ \mathbf{R}_I^p &= -\mathbf{B}_{vI} \cdot \frac{k^f}{\gamma_0^f} \operatorname{grad} p + \mathbf{B}_{vI} \cdot \rho_0^f \bar{\mathbf{b}} - N_I \operatorname{div} \mathbf{v}_s. \end{aligned} \quad (6.31)$$

where the matrices \mathbf{B}_I , \mathbf{B}_{vI} can be found in the appendix B.1. The contributions of the damping and of the stiffness matrix

$$\mathbf{C}_{IJ} = \begin{bmatrix} \mathbf{0} & \mathbf{0} \\ \mathbf{C}_{pu} & 0 \end{bmatrix}, \quad \mathbf{K}_{IJ} = \begin{bmatrix} \mathbf{K}_{uu} & \mathbf{K}_{up} \\ \mathbf{0} & K_{pp} \end{bmatrix} \quad (6.32)$$

can also be specified as

$$\begin{aligned} \mathbf{C}_{pu} &= N_I \mathbf{B}_{vJ}, & \mathbf{K}_{uu} &= \mathbf{B}_I^T \mathbf{D} \mathbf{B}_J + N_I n_0^S (\rho_0^S - \rho_0^F) \bar{\mathbf{b}} \mathbf{B}_{vJ}^T \\ \mathbf{K}_{up} &= -\mathbf{B}_{vI} N_J, & K_{pp} &= \mathbf{B}_{vI} \frac{k^F}{\gamma_0^F} \cdot \mathbf{B}_{vJ}. \end{aligned} \quad (6.33)$$

6.7 Consolidation test

A simple consolidation test shows the influence of the coupled Darcy's law within the TPM framework on the properties of an elastic block ($E = 2.65 \cdot 10^5 \text{ N/m}^2$, $\nu = 0.3$, $\rho^s = 2.72 \cdot 10^3 \text{ kg/m}^3$) where a linear elastic material description is used. The block is loaded with a prescribed pressure of $1.25 \cdot 10^5 \text{ N/m}^2$ on top which is applied completely at $t = 0 \text{ s}$. The top side is also perfectly drained ($p = 0 \text{ N/m}^2$) whereas all the other surfaces are kept fixed and are water impermeable (figure 6.3). The volume

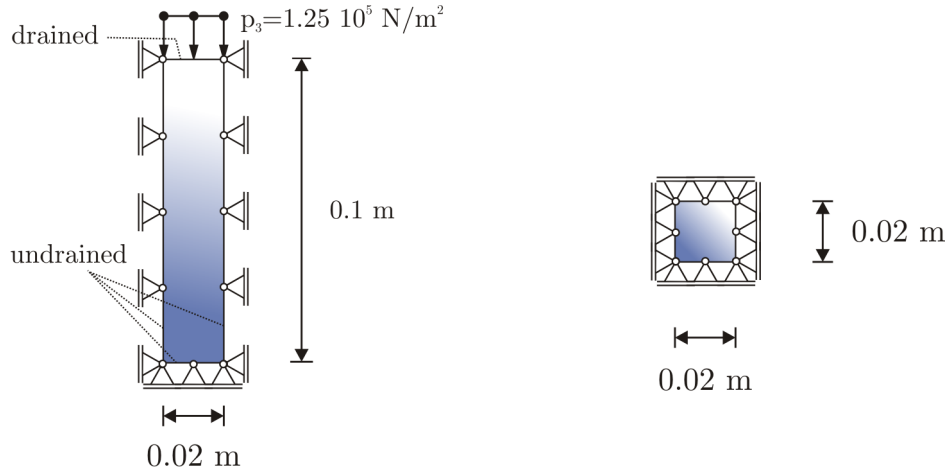


Figure 6.3: Side view (left) and top view (right) of the consolidation example

ratio of the solid skeleton is chosen as $n^s = 0.67$ and the density of the water is given as $\rho^f = 1.0 \cdot 10^3 \text{ kg/m}^3$. The numerical results of the consolidation test with different

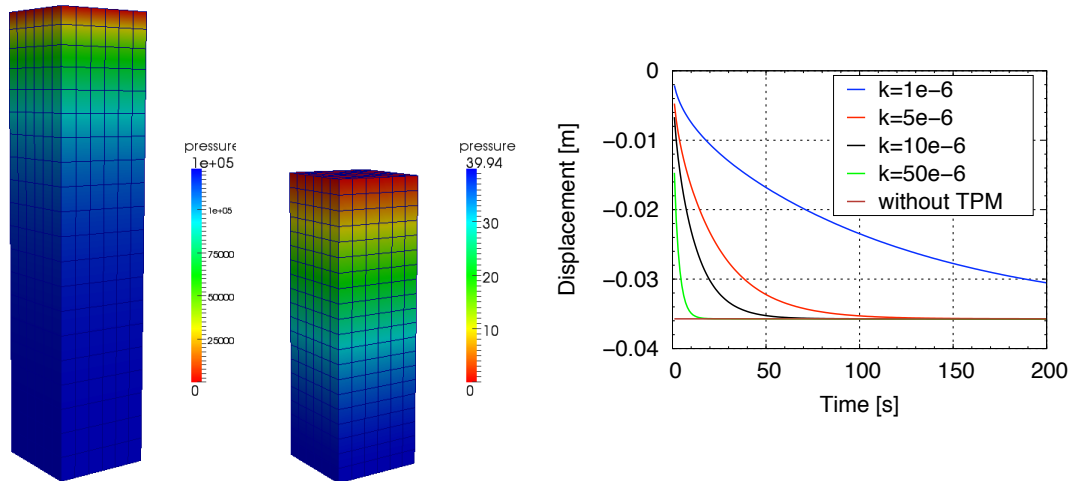


Figure 6.4: Pressure distribution at $t = 1 \text{ s}$ and $t = 100 \text{ s}$ (left) and vertical displacements of the specimen over time with different permeability's (right)

permeability coefficients $k_f = 1.0 \cdot 10^{-6}$, $5.0 \cdot 10^{-6}$, $10.0 \cdot 10^{-6}$, $50.0 \cdot 10^{-6} \text{ m/s}$ is evaluated during the first 200 seconds ($\Delta_t = 1 \text{ s}$) where the implicit Euler scheme is used for

the time integration. The consolidation process depends almost exponentially on the permeability coefficient where for larger values the behavior corresponds nearly to the pure elastic case, see figure 6.4 (right side). The left side of figure 6.4 shows the pressure distribution inside the deformed specimen (for $k_f = 10.0 \cdot 10^{-6}$ m/s) at time $t = 1$ s and $t = 100$ s where the maximum pressure is decreased rapidly after 100 seconds.

Chapter 7

Projection strategies

As can be seen within section 5.3, a natural connection between slip and yield criteria for frictional materials exists, but a direct application of a yield criterion in a contact formulation is not possible, since the dilatancy effect would separate the contacting bodies although contact takes place. Consequently, a cap structure of the yield criterion can not be translated directly into a slip criterion, since the back projection of the tangential stress component to the slip surface is not possible, if the normal pressure exceeds the limit of the yield surface. Hence novel concepts are necessary to project plasticity models onto the contact surface. The first concept is based on the incorporation of the stress into the coefficient of friction and a second variant introduces an additional contact stress component which makes it possible to find a direct relation between a yield criterion and a friction law. The implementation of both concepts is thereby based on the Mortar method, but can also be combined with all other contact discretization techniques.

7.1 Projection over the coefficient of friction

Within the description of contact mechanics the classical Coulomb slip criterion

$$f^c = \|\bar{\boldsymbol{\lambda}}_{\text{T}An+1}\| + \mu_{An+1}|\bar{\lambda}_{\text{N}An+1}| = 0 \quad (7.1)$$

is only a rough estimate of the real physical behavior. Introductory works on the frictional contact behavior can be found in Tabor [1981], Kragelsky et al. [1982], Oden and Martins [1985] or as a bottom up approach starting from the atomistical range in Mate [2008]. Experimental contact tests show a dependency of the frictional behavior on the actual velocity $\dot{\mathbf{g}}_{\text{T}An+1}$, on the pressure $\bar{\lambda}_{\text{N}An+1}$, on the temperature Θ_{An+1} and on the surface roughness $z_{n+1}(x, y)$ given mostly in terms of the autocorrelation function and the frequency densities (Patir [1978]). Two different strategies can be pursued to incorporate these dependencies. One is to use special slip criteria and the other one is to formulate the coefficient of friction as a function of its underlying quantities

$$\mu_{An+1} := \tilde{\mu}(\dot{\mathbf{g}}_{\text{T}An+1}, \bar{\lambda}_{\text{N}An+1}, \Theta_{An+1}, z_{n+1}(x, y)) . \quad (7.2)$$

A detailed description of different frictional formulations can be found in Wriggers [2006] and a numerical implementation of a pressure and velocity dependent coefficient of friction within a multi-scale framework in Wriggers and Reinelt [2009]. An alternative way is proposed in the following statements where the complete plastic behavior of the underlying structure is taken into account by means of a dependency of μ_{An+1} on the three-dimensional elastic stress

$$\mu_{An+1} := \tilde{\mu}(\boldsymbol{\sigma}_{An+1}). \quad (7.3)$$

At each node an equivalent continuum model is set up where the kinematical contact quantities are linked to the classical continuum kinematics. The concept is independent

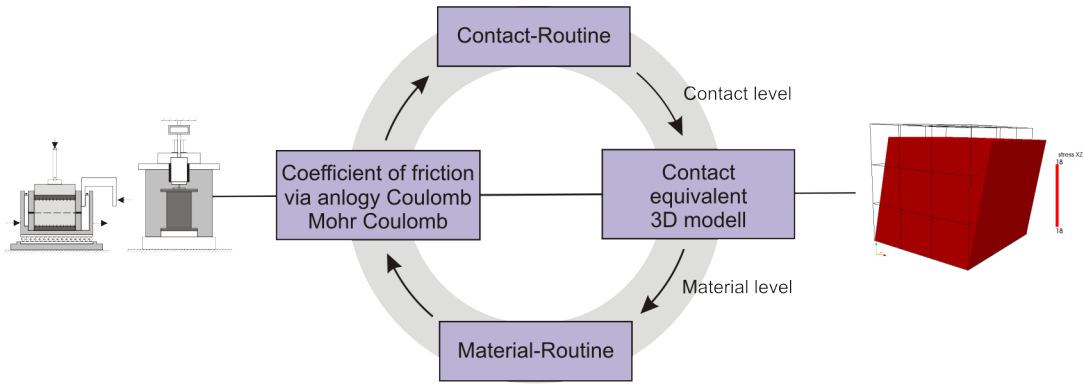


Figure 7.1: Projection algorithm

of the global contact solution algorithm fulfilling the contact constraints. It can be coupled with the pure Lagrange multiplier, the penalty or the augmented method. Within this work, the mixed version in combination with the Mortar method (see section 4.3.6.4) is chosen as the global contact solution algorithm.

7.1.1 Link between contact and continuum

Using the penalty regularization, the elasto-plastic stress strain relation at each node can be written in matrix notation with regards to the derivations of section 2.4.2

$$\begin{bmatrix} 0 \\ 0 \\ \bar{\sigma}_{33An+1} \\ 0 \\ \bar{\sigma}_{23An+1} \\ \bar{\sigma}_{13An+1} \end{bmatrix} = \begin{bmatrix} c_N & 0 & 0 & 0 & 0 & 0 \\ 0 & c_N & 0 & 0 & 0 & 0 \\ 0 & 0 & c_N & 0 & 0 & 0 \\ 0 & 0 & 0 & c_T & 0 & 0 \\ 0 & 0 & 0 & 0 & c_T & 0 \\ 0 & 0 & 0 & 0 & 0 & c_T \end{bmatrix} \begin{bmatrix} 0 \\ 0 \\ \bar{g}_{NA n+1} \\ 0 \\ -\bar{g}_{T1A n+1}^e \\ -\bar{g}_{T2A n+1}^e \end{bmatrix} \quad (7.4)$$

where the bar over the quantities indicates averaged values due to the Mortar method. A comparison with the linear elastic material tensor leads to a connection of the penalty parameters c_N, c_T to the elastic material data E, ν by means of a given influence height h

$$\nu = 0, \quad E = 2 c_T h = 2 c_N h \quad (7.5)$$

where the connection between the normal strain and the normal penetration (2.84) as well as the connection between the shear strain and the tangential movement (2.81) have to be taken into account. To be in line with the continuum description, the normal and the tangential penalty parameters have to be equal $c_N = c_T$. Modifying the standard description of the elastic strain (3.33) in order to be similar to the elastic tangential movement of the penalty contact formulation

$$\begin{aligned}\bar{\epsilon}_{An+1}^e &= \Delta_t \bar{\epsilon}_{An+1} + \bar{\epsilon}_{An}^e - \gamma_{An+1} \frac{\partial g}{\partial \sigma} \Big|_{An+1} \\ \bar{g}_{T\alpha An+1}^e &= -\Delta_t \bar{g}_{T\alpha An+1} - \bar{g}_{T\alpha An}^e - \gamma_{An+1} \frac{\bar{\lambda}_{T\alpha An+1}}{\|\bar{\lambda}_{TAn+1}\|},\end{aligned}\tag{7.6}$$

the standard description of the strain can be achieved by summing up the incremental strain

$$\begin{aligned}\bar{\epsilon}_{An+1}^e &= \bar{\epsilon}_{An+1} - \bar{\epsilon}_{An}^p - \gamma_{An+1} \frac{\partial g}{\partial \sigma} \Big|_{An+1} \\ \bar{\epsilon}_{An+1} &= \bar{\epsilon}_{An} + \Delta_t \bar{\epsilon}_{An+1}, \quad \bar{\epsilon}_{A0} = \mathbf{0}.\end{aligned}\tag{7.7}$$

The incremental shearing strain can now be linked directly to the incremental tangential movement (2.81)

$$2\Delta \bar{\epsilon}_{\alpha 3An+1} = \frac{1}{h a_{An+1}} (-\bar{g}_{TAn+1} + \bar{g}_{TAn+1}^o).\tag{7.8}$$

On the contrary, the actual normal component (2.84)

$$\bar{\epsilon}_{33An+1} = \frac{1}{h a_{An+1}} \frac{\bar{\lambda}_{NAn+1}}{2 c_n}\tag{7.9}$$

follows directly from the normal pressure and needs not to be accumulated during the computation. All the other values are equal to zero, see (2.78)

$$\bar{\epsilon}_{11An+1} = \bar{\epsilon}_{22An+1} = \bar{\epsilon}_{12An+1} = 0.\tag{7.10}$$

Now the actual strain is defined and together with the nodal plastic strain at the old time step they can be sent to the standard continuum plasticity routine. Getting a pure elastic response, the actual node is in stick and the standard no-tangential-movement constraint has to be fulfilled. Otherwise the slave node slips along the master surface. The analogy between the Coulomb friction law (5.2) and the Mohr-Coulomb yield criterion (5.7) without cohesion

$$\begin{aligned}f^c &= \|\bar{\mathbf{t}}_{TA}\| - |\bar{\lambda}_{NA}| \tan \varphi = 0 \\ f^m &= \sqrt{\Pi_s} \cos(\Theta) + \left[\frac{1}{3} \mathbf{I}_\sigma - \sqrt{\frac{\Pi_s}{3}} \sin(\Theta) \right] \sin(\varphi) = 0\end{aligned}\tag{7.11}$$

determines the actual coefficient of friction

$$\mu_A = |\tan \varphi| = \left| \tan \left(\arcsin \left(\frac{\sqrt{\Pi_s} \cos(\Theta)}{\frac{1}{3} I_\sigma - \sqrt{\frac{\Pi_s}{3}} \sin(\Theta)} \right) \right) \right| \quad (7.12)$$

where the invariants are due to (5.5), (5.6). To ease the notation, the subscript $n+1$ is dropped within the derivation of the coefficient of friction and in the following section, since all values depend on the actual time step. Additionally, in the case of a plastic response of the 3D plasticity routine, the actual plastic strain with all 6 components has to be stored at each node.

7.1.2 Linearization

Within the linearization process of the contact stress components in the case of slip, an additional term due to the coefficient of friction has to be considered in the overall linearization (4.193)

$$\begin{aligned} \Delta \bar{t}_{T\alpha A} = & \mu_A \operatorname{sign}(\bar{\lambda}_{NA}) \Delta \bar{\lambda}_{NA} \frac{\bar{t}_{T\alpha A}^{tr}}{\|\bar{\mathbf{t}}_{TA}^{tr}\|} + \mu_A |\bar{\lambda}_{NA}| \frac{\Delta \bar{t}_{T\alpha A}^{tr}}{\|\bar{\mathbf{t}}_{TA}^{tr}\|} \\ & - \mu_A |\bar{\lambda}_{NA}| \frac{\bar{t}_{T\alpha A}^{tr} \bar{t}_{T\beta A}^{tr} \Delta \bar{t}_{T\beta A}^{tr}}{\|\bar{\mathbf{t}}_{TA}^{tr}\|^3} + \Delta \mu_A |\bar{\lambda}_{NA}| \frac{\bar{t}_{T\alpha A}^{tr}}{\|\bar{\mathbf{t}}_{TA}^{tr}\|}. \end{aligned} \quad (7.13)$$

The coefficient of friction is linearized with respect to the elastic stress of the underlying continuum

$$\begin{aligned} \Delta \mu_A = & \frac{\operatorname{sign}(\tan \varphi)}{\cos^2 \varphi} \frac{1}{\sqrt{1 - \left(\frac{\sqrt{\Pi_s} \cos(\Theta)}{\frac{1}{3} I_\sigma - \sqrt{\frac{\Pi_s}{3}} \sin(\Theta)} \right)^2}} \left[\frac{\cos(\Theta)}{2 \sqrt{\Pi_s} \left(\frac{1}{3} I_\sigma - \sqrt{\frac{\Pi_s}{3}} \sin(\Theta) \right)} \frac{\partial \Pi_s}{\partial \sigma} \right. \\ & - \frac{\sqrt{\Pi_s} \sin(\Theta)}{\frac{1}{3} I_\sigma - \sqrt{\frac{\Pi_s}{3}} \sin(\Theta)} \frac{\partial \Theta}{\partial \sigma} - \frac{\sqrt{\Pi_s} \cos(\Theta)}{2 \left(\frac{1}{3} I_\sigma - \sqrt{\frac{\Pi_s}{3}} \sin(\Theta) \right)^3} \\ & \left. \left[\frac{1}{3} \frac{\partial I_\sigma}{\partial \sigma} - \frac{\sin(\Theta)}{2 \sqrt{3} \Pi_s} \frac{\partial \Pi_s}{\partial \sigma} - \sqrt{\frac{\Pi_s}{3}} \cos(\Theta) \frac{\partial \Theta}{\partial \sigma} \right] \right] \Delta \sigma_A \end{aligned} \quad (7.14)$$

where the linearization of the Lode angle with respect to the stress is specified as

$$\frac{\partial \Theta}{\partial \sigma} = -\frac{1}{3} \frac{1}{\sqrt{1 - \left(\frac{\sqrt{27}}{2} III_s II_s^{-3/2} \right)^2}} \frac{\sqrt{27}}{2} \left(\frac{\partial III_s}{\partial \sigma} II_s^{-3/2} - \frac{3}{2} III_s II_s^{-5/2} \frac{\partial II_s}{\partial \sigma} \right). \quad (7.15)$$

The linearization of the elastic stress components σ_{iA} given in Voigt notation is linked to the linearization of the contact quantities through

$$\Delta\sigma_{iA} = \begin{bmatrix} A_{13} & A_{15} & A_{16} \\ A_{23} & A_{25} & A_{26} \\ A_{33} & A_{35} & A_{36} \\ A_{43} & A_{45} & A_{46} \\ A_{53} & A_{55} & A_{56} \\ A_{63} & A_{65} & A_{66} \end{bmatrix} \begin{bmatrix} \Delta\bar{\lambda}_{NA}/c_N \\ -(\Delta\bar{g}_{T1A} - \Delta\bar{g}_{T1A}^o) \\ -(\Delta\bar{g}_{T2A} - \Delta\bar{g}_{T2A}^o) \end{bmatrix} \quad (7.16)$$

where the inverse of the algorithmic tangent (3.39) is applied. The contribution to the nodal tangential contact matrix in the case of slip (4.195) is now extended by the additional parts $\bar{D}_{\alpha\beta}$ and \bar{L}_α due to the stress dependent coefficient of friction

$$\Delta\bar{t}_{t\alpha} = \left(\bar{D}_{\alpha\beta} + \tilde{D}_{\alpha\beta}\right) (\Delta\bar{g}_{T\beta A n+1} - \Delta\bar{g}_{T\beta A n+1}^o) + \left[\bar{L}_\alpha + \tilde{L}_\alpha\right] \Delta\bar{\lambda}_{NA n+1} \quad (7.17)$$

where the additional matrices follow in detail exploiting (7.13), (7.14) and (7.16) to

$$\tilde{D}_{\alpha\beta} = -|\bar{\lambda}_{NA}| \frac{\bar{t}_{T\alpha A}^{tr}}{\|\bar{\mathbf{t}}_{TA}^{tr}\|} \left[\frac{\partial\mu_A}{\partial\sigma_i} A_{i(4+\alpha)} \right], \quad \tilde{L}_\alpha = |\bar{\lambda}_{NA}| \frac{\bar{t}_{T\alpha A}^{tr}}{\|\bar{\mathbf{t}}_{TA}^{tr}\|} \left[\frac{\partial\mu_A}{\partial\sigma_i} A_{i3} \frac{1}{c_N} \right]. \quad (7.18)$$

7.2 Direct link between yield and slip criterion

Before this concept is applied to the soil model of Ehlers, a generic description of the proposed algorithm is presented. Comparing again the standard contact slip criterion with its three-dimensional extension (7.11) in a slightly different form

$$\begin{aligned} f^c &= \|\bar{\mathbf{t}}_T\| - |\bar{\lambda}_N| \tan \varphi = 0 \\ f^m &= \sqrt{\Pi_s} \cos(\Theta) + \left[\frac{1}{3} \mathbf{I}_\sigma - \sqrt{\frac{\Pi_s}{3}} \sin(\Theta) \right] \cos \varphi \tan \varphi = 0 \end{aligned} \quad (7.19)$$

where in the second equation the sinus is replaced by the tangent multiplied with the cosine, the two invariants of the Coulomb slip criterion are faced with the three invariants of the Mohr-Coulomb yield criterion. This makes it impossible to link both descriptions directly, but since the tangential contact motion is equivalent to shearing with a load on top, the Lode angle has a value close to zero and the assumption $\Theta = 0^\circ$ can be stated. Now it is possible to link the invariants of the contact formulation to the continuum description in (7.19)

$$\begin{aligned} \sqrt{\Pi_s} &= \|\bar{\mathbf{t}}_T\|, \quad \text{or} \quad \Pi_s = \bar{\mathbf{t}}_T \cdot \bar{\mathbf{t}}_T \\ \mathbf{I}_\sigma &= 3 \bar{\lambda}_N \cos \varphi \\ \Theta &= 0^\circ, \quad \text{or} \quad \text{III}_s = 0. \end{aligned} \quad (7.20)$$

The second challenge of this contact formulation is to include the influence of dilatancy or contractancy effects into the model leading not to gap between the contacting bodies.

This can be realized by means of an additional normal stress component. Based on (7.20), the flow rule (2.51) can also be transformed to an evolution equation of the gap subdivided into a normal and a tangential part

$$\begin{aligned}\dot{\mathbf{g}}_T &= \dot{\gamma} \frac{\partial \|\bar{\mathbf{t}}_T\|}{\partial \bar{\mathbf{t}}_T} = \dot{\gamma} \frac{\bar{\mathbf{t}}_T}{\|\bar{\mathbf{t}}_T\|} \\ \dot{\mathbf{g}}_N &= \dot{\gamma} \left[\frac{\partial g}{\partial \|\bar{\mathbf{t}}_T\|} \right]^{-1} \frac{\partial g}{\partial \bar{\lambda}_N} = \dot{\gamma} \tan \nu^p\end{aligned}\quad (7.21)$$

where the evolution equation is transformed such that the tangential part corresponds to the classical evolution equation of the tangential movement. The ratio of the normal and the tangential part is thereby equivalent to the tangent of the dilatancy angle ν^p

$$\frac{\dot{\mathbf{g}}_N^p}{\|\dot{\mathbf{g}}_T^p\|} = \tan \nu^p =: \frac{-\bar{t}_D}{\|\bar{\mathbf{t}}_T\|}. \quad (7.22)$$

A new quantity is now defined which is proportional to the negative normal gap ($\bar{t}_D \sim -\dot{\mathbf{g}}_N^p$). Since the norm of the tangential stress $\|\bar{\mathbf{t}}_T\|$ is also proportional to the norm of the plastic tangential movement $\|\dot{\mathbf{g}}_T^p\|$, the tangent of the dilatancy angle is proposed as the ratio of the new dilatancy stress component \bar{t}_D to the norm of the tangential stress vector written as

$$\bar{t}_D = -\tan \nu^p \|\bar{\mathbf{t}}_T\|. \quad (7.23)$$

Due to the new dilatancy stress quantity \bar{t}_D a backprojection in the normal direction is now also possible which ensures the backprojection similar to the standard return mapping algorithm known in plasticity (figure 7.2). In figure 7.2 also the distribution of the tangent of the dilatancy angle $\tan \nu^p$ shows a strong increase of its value and hence a stronger backprojection in normal direction, if the normal pressure lies outside of the friction law. Now the relation of the invariants (7.20) has to be modified only

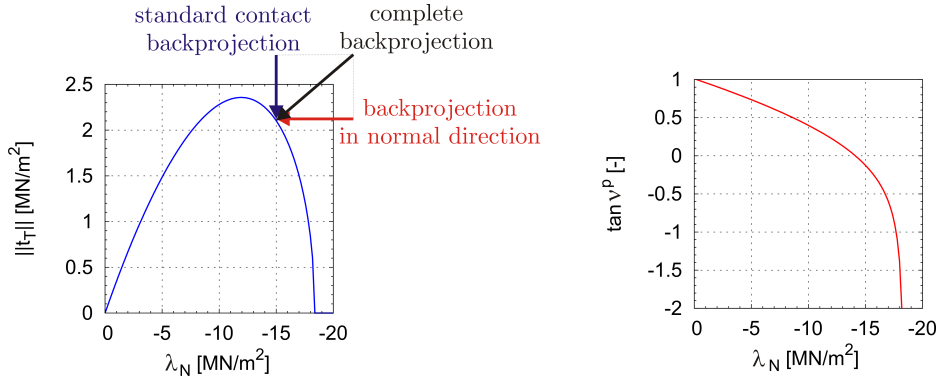


Figure 7.2: Schematic representation of the new backprojection algorithm (left) and tangent of the dilatancy angle versus normal pressure (right)

for the case of a projected yield criterion

$$\begin{aligned}\sqrt{\Pi_s} &= \|\bar{\mathbf{t}}_T\| \quad \text{or} \quad \Pi_s = \bar{\mathbf{t}}_T \cdot \bar{\mathbf{t}}_T \\ I_\sigma &= 3\bar{\lambda}_N \cos \varphi - \bar{t}_D.\end{aligned}\quad (7.24)$$

Normally, the whole procedure delivers a nonlinear slip criterion where the solution of the admissible tangent stress vector has to be solved by an implicit return mapping algorithm together with a Newton iteration. In the next section, this method is applied to the Ehlers soil model of section 5.4, but it can be also adopted to other yield criteria and evolution equations.

7.2.1 Projection of Ehlers yield criterion

The first step within the projection process is to determine the dilatancy stress component. For a given set of material parameters the potential g of (5.17) results in the contact potential exploiting (7.20)

$$g = \sqrt{\Psi_1 \|\bar{\mathbf{t}}_{TA n+1}\|^2 + \frac{1}{2} \alpha (I_{\sigma}^g)^2 + \delta^2 (I_{\sigma}^g)^4 + \Psi_2 \beta I_{\sigma}^g + \epsilon (I_{\sigma}^g)^2} \quad (7.25)$$

$$I_{\sigma}^g = 3\bar{\lambda}_{NA n+1} \cos \varphi, \quad \|\bar{\mathbf{t}}_{TA n+1}\| = \sqrt{\bar{t}_{T\alpha A n+1} \bar{t}_{T\alpha A n+1}}$$

where the cosine of the friction angle can be deduced from the material parameter β , see Ehlers [1995]

$$\cos \varphi = \cos (\arcsin (3\beta)) \quad (7.26)$$

and the term I_{σ}^g indicates the first contact invariant applied within the potential g . Using the abbreviation for the root of the potential

$$g_{rt} = \sqrt{\Psi_1 \|\bar{\mathbf{t}}_{TA n+1}\|^2 + \frac{1}{2} \alpha (I_{\sigma}^g)^2 + \delta^2 (I_{\sigma}^g)^4} \quad (7.27)$$

the tangent of the dilatancy angle

$$\tan \nu^p = \frac{1}{2 \Psi_1 \|\bar{\mathbf{t}}_{TA n+1}\|} \left[\alpha I_{\sigma}^g + 4\delta^2 (I_{\sigma}^g)^3 + 2g_{rt} (\Psi_2 \beta + 2\epsilon (I_{\sigma}^g)) \right] \quad (7.28)$$

and following (7.23) the dilatancy stress component

$$\bar{t}_{DA n+1} = -\frac{1}{2 \Psi_1} \left[\alpha (I_{\sigma}^g) + 4\delta^2 (I_{\sigma}^g)^3 + 2g_{rt} (\Psi_2 \beta + 2\epsilon (I_{\sigma}^g)) \right] \quad (7.29)$$

can be written in a more compact form. The projected slip criterion of Ehlers (5.11) is based on the modified first invariant I_{σ}^f (7.24)

$$f^{ec} = \sqrt{\|\bar{\mathbf{t}}_{TA n+1}\|^2 + \frac{1}{2} \alpha (I_{\sigma}^f)^2 + \delta^2 (I_{\sigma}^f)^4 + \beta I_{\sigma}^f + \epsilon (I_{\sigma}^f)^2} - \kappa = 0 \quad (7.30)$$

$$I_{\sigma}^f = 3\bar{\lambda}_{NA n+1} \cos \varphi - \bar{t}_{DA n+1}$$

which renders the influence of the dilatancy part. The incorporation of the hardening effects leads to the integrated form of the evolution equation (5.23) for the contact case

$$\mathbf{h}_{n+1} - \mathbf{h}_n^c + \Delta t \gamma_{n+1} (\mathbf{h}_{n+1}^c - \mathbf{h}_{max}) \left[\mathbf{C}_h^v \frac{\partial g}{\partial \bar{\lambda}_{NA n+1}} + \mathbf{C}_h^d \frac{\partial g}{\partial \|\bar{\mathbf{t}}_{TA n+1}\|} \right] = 0 \quad (7.31)$$

where the derivatives of the potential in the direction of the normal and the tangential contact stress vector are

$$\begin{aligned} \frac{\partial g}{\partial \bar{\lambda}_{NA n+1}} &= \left[\frac{1}{2 g_{rt}} \left(\alpha I_{\sigma}^g + 4 \delta^2 (I_{\sigma}^g)^3 \right) + \Psi_2 \beta + 2 \epsilon I_{\sigma}^g \right] 3 \cos \varphi \\ \frac{\partial g}{\partial \|\bar{\mathbf{t}}_{TA n+1}\|} &= \frac{\Psi_1}{g_{rt}} \|\bar{\mathbf{t}}_{TA n+1}\|. \end{aligned} \quad (7.32)$$

Using the trial stress value given in (4.187) and the trial hardening parameters

$$\bar{\mathbf{t}}_{T\alpha A n+1}^{tr} = -c_T \left(\bar{g}_{T\alpha A n+1} - \bar{g}_{T\alpha A n+1}^o \right) + \bar{\mathbf{t}}_{T\alpha A n}, \quad \mathbf{h}_{n+1}^{tr} = \mathbf{h}_n \quad (7.33)$$

the trial slip criterion decides whether the node sticks or slips

$$\begin{aligned} f^{ec} \left(\bar{\mathbf{t}}_{T\alpha A n+1}^{tr}, \mathbf{h}_{n+1}^{tr} \right) &\leq 0 \quad \rightarrow \quad \text{stick} \\ f^{ec} \left(\bar{\mathbf{t}}_{T\alpha A n+1}^{tr}, \mathbf{h}_{n+1}^{tr} \right) &> 0 \quad \rightarrow \quad \text{slip.} \end{aligned} \quad (7.34)$$

For the stick case, the desired nodal tangential stress vector and the actual hardening values

$$\begin{aligned} \bar{\mathbf{t}}_{T\alpha A n+1} &= \bar{\mathbf{t}}_{T\alpha A n+1}^{tr} \\ \mathbf{h}_{n+1} &= \mathbf{h}_{n+1}^{tr} \end{aligned} \quad (7.35)$$

are equal to their trial counterparts. In the case of slip, a set of algebraic equations has to be solved to determine the unknown tangential stress components $\bar{\mathbf{t}}_{T\alpha A n+1}$ and the actual hardening values \mathbf{h}_{n+1} . For the solution of the nonlinear equation, the Newton iteration is applied and the loop is finished until the norm of the slip criterion $|\mathbf{R}_{\gamma n+1}|$ is lower than a prescribed tolerance δ . As usual in the other sections, the index $n+1$ is neglected within the linearization process to shorten the notation. Only values at the old time step will be indicated further with n .

$$\begin{bmatrix} K_{t_\alpha t_\beta} & \mathbf{0} & K_{t_\alpha \gamma} \\ K_{h_i t_\beta} & K_{h_i h_j} & K_{h_i \gamma} \\ K_{\gamma t_\beta} & K_{\gamma h_j} & 0 \end{bmatrix} \begin{bmatrix} \Delta t_{T\alpha A} \\ \Delta h_{iA} \\ \Delta \gamma_A \end{bmatrix} = \begin{bmatrix} R_{t_\alpha} \\ R_{ih} \\ R_\gamma \end{bmatrix}. \quad (7.36)$$

The residual vectors can be specified for the tangential stress contribution, the hardening parameters and the slip criterion

$$\begin{aligned} R_{t_\alpha} &= \frac{1}{c_T} \left(\bar{\mathbf{t}}_{T\alpha A} - \bar{\mathbf{t}}_{T\alpha A}^{tr} \right) + \Delta t \gamma_A \frac{\bar{\mathbf{t}}_{T\alpha A}}{\|\bar{\mathbf{t}}_{TA}\|} \\ R_{h_i} &= h_{iA} - h_{iA n} + \Delta t \gamma_A \left(h_{iA} - h_{i \max} \right) \left[C_{ih}^v \frac{\partial g}{\partial \bar{\lambda}_{NA}} + C_{ih}^d \frac{\partial g}{\partial \|\bar{\mathbf{t}}_{TA}\|} \right] \\ R_\gamma &= f^{ec}. \end{aligned} \quad (7.37)$$

The contributions of the submatrices are split into contributions regarding the tangential stress part

$$\begin{aligned} K_{t_\alpha t_\beta} &= \frac{1}{c_T} 1_{\alpha\beta} + \frac{\Delta_t \gamma_A}{\|\bar{\mathbf{t}}_{TA}\|} \left[1_{\alpha\beta} - \frac{\bar{t}_{T\alpha A}}{\|\bar{\mathbf{t}}_{TA}\|} \frac{\bar{t}_{T\beta A}}{\|\bar{\mathbf{t}}_{TA}\|} \right] \\ K_{t_\alpha \gamma} &= \frac{\bar{t}_{T\alpha A}}{\|\bar{\mathbf{t}}_{TA}\|} \end{aligned} \quad (7.38)$$

and the hardening part

$$\begin{aligned} K_{h_i \bar{t}_\beta} &= \Delta_t \gamma_A (h_{iA} - h_{imax}) \left[C_{ih}^v \frac{\partial^2 g}{\partial \bar{\lambda}_{NA} \partial \bar{t}_{T\beta A}} + C_{ih}^d \frac{\partial^2 g}{\partial \|\bar{\mathbf{t}}_{TA}\| \partial \bar{t}_{T\beta A}} \right] \\ K_{h_i h_j} &= 1_{ij} + \Delta_t \gamma_A 1_{ij} \left[C_{ih}^v \frac{\partial g}{\partial \bar{\lambda}_{NA}} + C_{ih}^d \frac{\partial g}{\partial \|\bar{\mathbf{t}}_{TA}\|} \right] \\ &\quad + \Delta_t \gamma_A (h_{iA} - h_{imax}) \left[C_{ih}^v \frac{\partial^2 g}{\partial \bar{\lambda}_{NA} \partial h_{jA}} + C_{ih}^d \frac{\partial^2 g}{\partial \|\bar{\mathbf{t}}_{TA}\| \partial h_{jA}} \right] \\ K_{h_i \gamma} &= (h_{iA} - h_{imax}) \left[C_{ih}^v \frac{\partial g}{\partial \bar{\lambda}_{NA}} + C_{ih}^d \frac{\partial g}{\partial \|\bar{\mathbf{t}}_{TA}\|} \right]. \end{aligned} \quad (7.39)$$

The derivatives inside the matrices can be further stated as

$$\begin{aligned} \frac{\partial^2 g}{\partial \bar{\lambda}_{NA} \partial \bar{t}_{T\beta A}} &= -\frac{3 \cos \varphi}{2 g_{rt}^3} \left[\alpha I_\sigma^g + 4 \delta^2 (I_\sigma^g)^3 \right] \Psi_1 \|\bar{\mathbf{t}}_{TA}\| \\ \frac{\partial^2 g}{\partial \|\bar{\mathbf{t}}_{TA}\| \partial \bar{t}_{T\beta A}} &= \left[\frac{\Psi_1}{g_{rt}} - \frac{\Psi_1^2 \|\bar{\mathbf{t}}_{TA}\|^2}{g_{rt}^3} \right] \frac{\bar{t}_{T\beta A}}{\|\bar{\mathbf{t}}_{TA}\|}. \end{aligned} \quad (7.40)$$

The derivatives of the slip criterion lead to the contributions

$$K_{\gamma t_\beta} = \frac{\partial f^{ec}}{\partial \bar{t}_{T\beta A}}, \quad K_{\gamma h_j} = \frac{\partial f^{ec}}{\partial h_{jA}} \quad (7.41)$$

where the derivative of the slip criterion with respect to the tangential stress component

$$\frac{\partial f^{ec}}{\partial \bar{t}_{T\beta A}} = \left[\frac{\partial f}{\partial \|\bar{\mathbf{t}}_{TA}\|} + \frac{\partial f}{\partial I_\sigma^f} \frac{\partial I_\sigma^f}{\partial \|\bar{\mathbf{t}}_{TA}\|} \right] \frac{\bar{t}_{T\beta A}}{\|\bar{\mathbf{t}}_{TA}\|} = a_1 \frac{\bar{t}_{T\beta A}}{\|\bar{\mathbf{t}}_{TA}\|} \quad (7.42)$$

can be related to the standard slip direction using an additional constant

$$\begin{aligned} a_1 &= \frac{1}{f_{rt}^{ec}} \|\bar{\mathbf{t}}_{TA}\| - \left[\frac{1}{2 f_{rt}^{ec}} \left(\alpha I_\sigma^f + 4 \delta^2 (I_\sigma^f)^2 \right) + \beta + 2 \epsilon I_\sigma^f \right] \frac{1}{g_{rt}^{ec}} (\Psi_2 \beta + 2 \epsilon I_\sigma^g) \|\bar{\mathbf{t}}_{TA}\| \\ f_{rt}^{ec} &= \sqrt{\|\bar{\mathbf{t}}_{TA}\|^2 + \frac{1}{2} \alpha (I_\sigma^f)^2 + \delta^2 (I_\sigma^f)^4}. \end{aligned} \quad (7.43)$$

At last, the derivatives of the normal and tangential directions of the hardening evolution equation

$$\begin{aligned} \frac{\partial^2 g}{\partial \|\bar{\mathbf{t}}_{TA}\| \partial \beta} &= 0 \quad \frac{\partial^2 g}{\partial \|\bar{\mathbf{t}}_{TA}\| \partial \epsilon} = 0 \quad \frac{\partial^2 g}{\partial \|\bar{\mathbf{t}}_{TA}\| \partial \delta} = -\frac{\Psi_1 \|\bar{\mathbf{t}}_{TA}\|}{2 g_{rt}^3} (\mathbf{I}_{\sigma}^4)^4 2\delta \\ \frac{\partial^2 g}{\partial \bar{\lambda}_{NA} \partial \beta} &= \Psi_2 3 \cos \varphi \quad \frac{\partial^2 g}{\partial \bar{\lambda}_{NA} \partial \epsilon} = 6 \mathbf{I}_{\sigma}^g \cos \varphi \\ \frac{\partial^2 g}{\partial \bar{\lambda}_{NA} \partial \delta} &= \left[\frac{3 \cos \varphi}{2 g_{rt}^3} 4 (\mathbf{I}_{\sigma}^g)^3 - \frac{3 \cos \varphi}{4 g_{rt}^3} \left[\alpha \mathbf{I}_{\sigma}^g + 4 \delta^2 (\mathbf{I}_{\sigma}^g)^3 \right] (\mathbf{I}_{\sigma}^4)^4 \right] 2\delta \end{aligned} \quad (7.44)$$

as well as the slip criterion have to be differentiated with respect to the hardening variables

$$\frac{\partial f}{\partial \beta} = \mathbf{I}_{\sigma}^f \quad \frac{\partial f}{\partial \epsilon} = (\mathbf{I}_{\sigma}^f)^2 \quad \frac{\partial f}{\partial \delta} = \frac{1}{2 f_{rt}} (\mathbf{I}_{\sigma}^f)^4 2\delta. \quad (7.45)$$

7.2.2 Linearization

Similar to the plasticity case, the linearized tangential stress components follow directly from the solution of (7.36) where only the residual vector has to be adjusted

$$\begin{bmatrix} \mathbf{K}_{t_{\alpha} t_{\beta}} & \mathbf{0} & \mathbf{K}_{t_{\alpha} \gamma} \\ \mathbf{K}_{h_i t_{\beta}} & \mathbf{K}_{h_i h_j} & \mathbf{K}_{h_i \gamma} \\ \mathbf{K}_{\gamma t_{\beta}} & \mathbf{K}_{\gamma h_j} & 0 \end{bmatrix} \begin{bmatrix} \Delta \bar{t}_{T\alpha A} \\ \Delta h_{iA} \\ \Delta \gamma_A \end{bmatrix} = \begin{bmatrix} -(\Delta \bar{g}_{T\alpha A} - \Delta \bar{g}_{T\alpha A}^o) \\ 0_i \\ -\frac{\partial f^{ec}}{\partial \bar{\lambda}_{NA}} \Delta \bar{\lambda}_{NA} \end{bmatrix}. \quad (7.46)$$

Inverting the tangent matrix

$$\begin{bmatrix} \mathbf{D}_{t_{\alpha} t_{\beta}} & \mathbf{D}_{t_{\alpha} h_j} & \mathbf{D}_{t_{\alpha} \gamma} \\ \mathbf{D}_{h_i t_{\beta}} & \mathbf{D}_{h_i h_j} & \mathbf{K}_{h_i \gamma} \\ \mathbf{D}_{\gamma t_{\beta}} & \mathbf{D}_{\gamma h_j} & \mathbf{D}_{\gamma \gamma} \end{bmatrix} = \begin{bmatrix} \mathbf{K}_{t_{\alpha} t_{\beta}} & \mathbf{0} & \mathbf{K}_{t_{\alpha} \gamma} \\ \mathbf{K}_{h_i t_{\beta}} & \mathbf{K}_{h_i h_j} & \mathbf{K}_{h_i \gamma} \\ \mathbf{K}_{\gamma t_{\beta}} & \mathbf{K}_{\gamma h_j} & 0 \end{bmatrix}^{-1}, \quad (7.47)$$

the complete linearized tangential stress components can be obtained

$$\Delta \bar{t}_{T\alpha A} = -\mathbf{D}_{t_{\alpha} t_{\beta}} (\Delta \bar{g}_{T\alpha A} - \Delta \bar{g}_{T\alpha A}^o) - \mathbf{D}_{t_{\alpha} \gamma} \frac{\partial f^{ec}}{\partial \bar{\lambda}_{NA}} \Delta \bar{\lambda}_{NA} \quad (7.48)$$

where the derivative of the slip criterion with respect to the normal stress component is specified as

$$\begin{aligned} \frac{\partial f^{ec}}{\partial \bar{\lambda}_{NA}} &= \left[\frac{1}{2 f_{rt}} \left(\alpha \mathbf{I}_{\sigma}^f + 4 \delta^2 (\mathbf{I}_{\sigma}^f)^3 \right) + \beta + 2 \epsilon \mathbf{I}_{\sigma}^f \right] \left(3 \cos \varphi \right. \\ &\quad \left. - \frac{3 \cos \varphi}{2 \Psi_1} \left[\alpha + 12 \delta^2 (\mathbf{I}_{\sigma}^g)^2 + 4 \epsilon g_{rt} + (\Psi_2 \beta + 2 \epsilon \mathbf{I}_{\sigma}^g) \frac{1}{g_{rt}} \left(\alpha \mathbf{I}_{\sigma}^g + 4 \delta^2 (\mathbf{I}_{\sigma}^g)^3 \right) \right] \right). \end{aligned} \quad (7.49)$$

7.3 Connection to the theory of porous media

Since in the case of contact there is no height between the two bodies, no fluid can flow in between. Only the influence of the fluid pressure can be taken into account where the pressure on both sides of the contact zone is set to be equal. The discretized weak forms of the mixed method (4.189) and (4.192) have to be supplemented by the fluid pressure in the virtual contact work

$$\begin{aligned} G_{uA}^{ch} &= \delta \bar{g}_{NA n+1} (\lambda_{NA n+1} + p_{A n+1}) + \delta \bar{g}_{T\alpha A n+1} \lambda_{T\alpha A n+1} \\ G_{lA}^{ch} &= \delta \lambda_{NA n+1} \bar{g}_{NA n+1} + \delta \lambda_{T\alpha A n+1} \frac{1}{c_T} [\bar{\lambda}_{T\alpha A n+1} - \bar{t}_{T\alpha A n+1}] = 0. \end{aligned} \quad (7.50)$$

If the soil is modeled on the master side in the contact formulation, the pressure at the slave node corresponds to

$$p_{A n+1} = \frac{1}{a_{A n+1}} \sum_g \sum_C N_{A n+1} N_{C n+1} p_{C n+1} \det \mathbf{j}_{n+1} W_g. \quad (7.51)$$

7.4 Numerical tests

Two different shear test cases are considered which highlight the behavior of the developed projected friction laws. In the first one, the direct shear test, the contact behavior under different loads applied to the specimen is investigated. The second test case is the demonstrator of the research group FOR 1136 GeoTech of the DFG where this work is applied to and compares the numerical results with experimental observations.

7.4.1 Direct shear test

A block of steel ($E = \text{MN/m}^2$, $\nu = 0.2$) with a rough surface is sheared on a soil specimen where for the steel block a linear elastic material model and for the soil specimen the Ehlers model with GEBA fine sand (table 5.1) are used. The apparatus is loaded with different normal forces which are continuously distributed on top of the upper block. To neglect positive stress values within the soil specimen during the

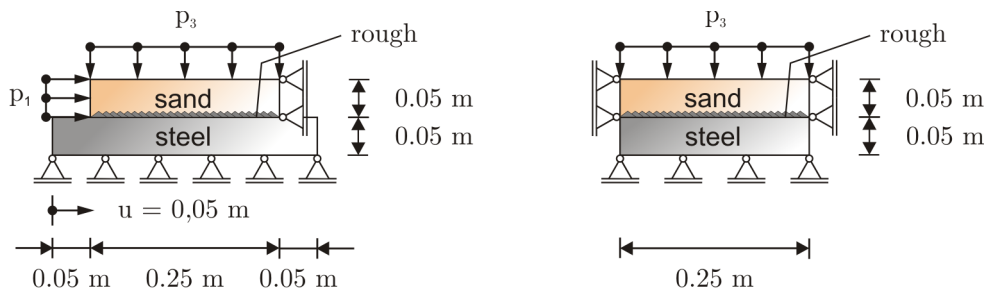


Figure 7.3: Direct shear test: Side view (left) and front view (right)

shearing process, instead of Dirichlet boundary conditions on both sides, only one side

is fixed and the other one is loaded with a continuous distributed force $p_1 = 0.5 \text{ kN/m}^2$. The geometrical measurements and the boundary conditions applied can be found in figure 7.3. A series of different pressure values $p_3 = (5, 10, 50, 100, 250, 500) \text{ kN/m}^2$ and different intrinsic heights $h = (5, 10, 15) \text{ mm}$ are conducted where the initial mesh and the final position of the shear test are depicted in figure 7.4. Thereby the normal pressure is applied in 10 steps and the tangential displacement in 100 steps. First the

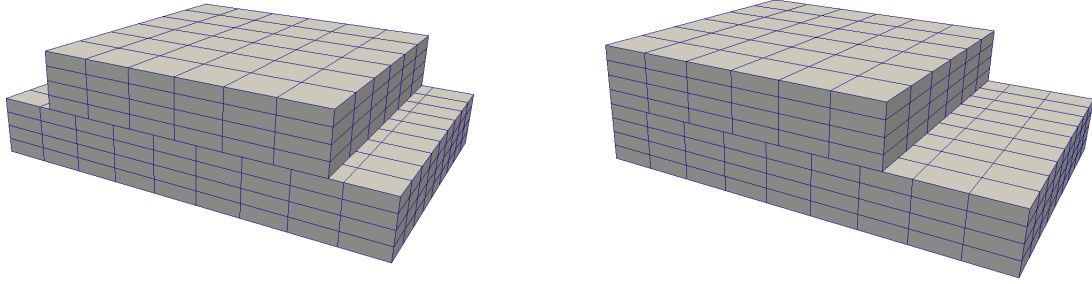


Figure 7.4: Direct shear test: Initial mesh (left) and final position (right)

projection over the coefficient of friction is investigated. Neglecting the influence of hardening effects, the evaluations show that, due to a large coefficient of friction in the transition phase between stick and slip, a peak evolves, see figure 7.5. The amount of the peak decreases with larger pressures or with smaller influence heights (figure 7.5). Using the subroutine which includes the hardening effects for the determination of the

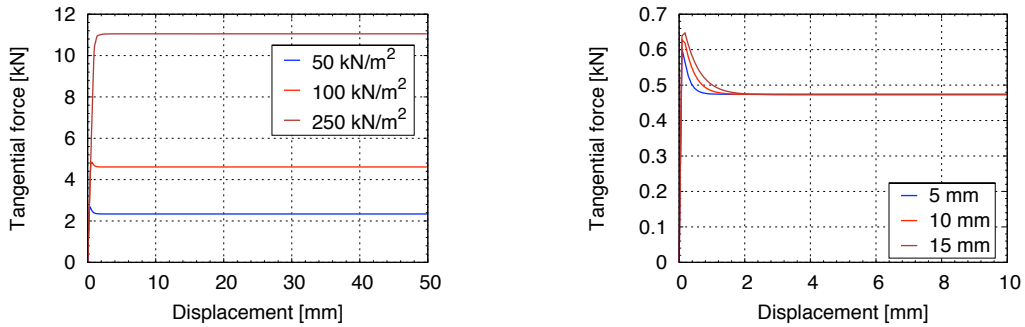


Figure 7.5: Direct shear test without hardening: Tangential force versus sliding distance at a constant influence height $h = 10 \text{ mm}$ (left) and at a constant pressure $p = 10 \text{ kN/m}^2$ (right)

coefficient of friction, a smoother transition from stick to slip evolves due to a slow increase of the yield surface. The qualitative distribution of the tangential force over the distance (figure 7.6) is very similar to the shear force distribution in the triaxial test (compare figure 5.16), and hence the initial goal of this work is reached and a projection of the soil model onto the contact surface is performed. Especially, a peak

evolves in the tangential force distribution which highlights the dense behavior of the GEBA fine sand (compare figure 5.6) The comparison of figure 7.5 with figure 7.7 shows

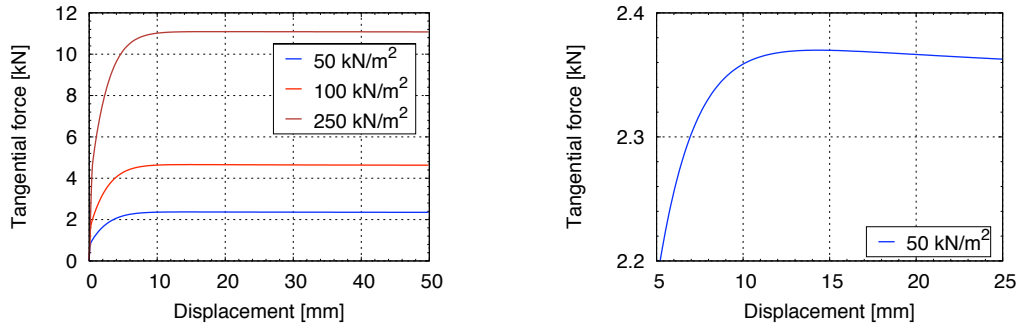


Figure 7.6: Direct shear test with hardening: Tangential force versus sliding distance at a constant influence height $h = 10\text{mm}$ (left) and zoom into the distribution of a constant pressure of $p=50\text{ kN/m}^2$ (right)

that the final tangential force and hence the final friction angle do no depend on the intrinsic height in the case of the Ehlers soil model without hardening. Similar to the

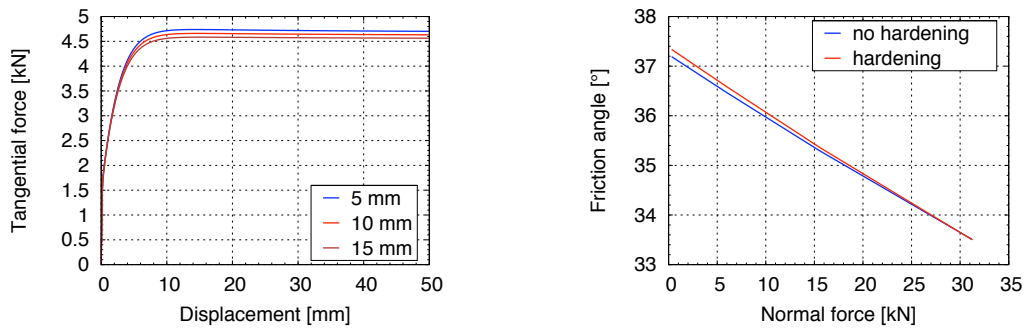


Figure 7.7: Direct shear test: Tangential force versus sliding distance at a constant pressure of $p = 100\text{ kN/m}^2$ (left) and comparison between hardening and no hardening at different normal pressures (right)

triaxial test (see for instance Herle [1997] page 63 for an experimental investigation), the friction angle depends on the normal pressure applied where the amount decreases for larger pressures (figure 7.7).

The second projection concept which uses the link between the yield and slip criterion is also evaluated at the direct shear test. This concept is independent of an intrinsic height and shows no peak at the transition between stick and slip in the case of no hardening, but for the hardening case qualitatively the same distribution evolves as for the first concept. Only the maximum tangential force is smaller as for the projection

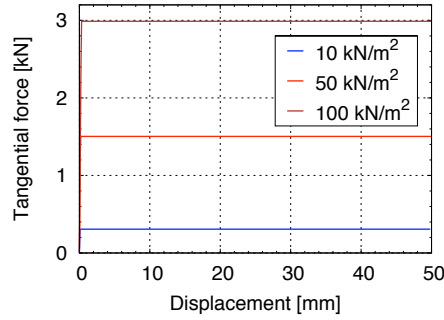


Figure 7.8: Direct shear test: Comparison of tangential force versus sliding distance with no hardening

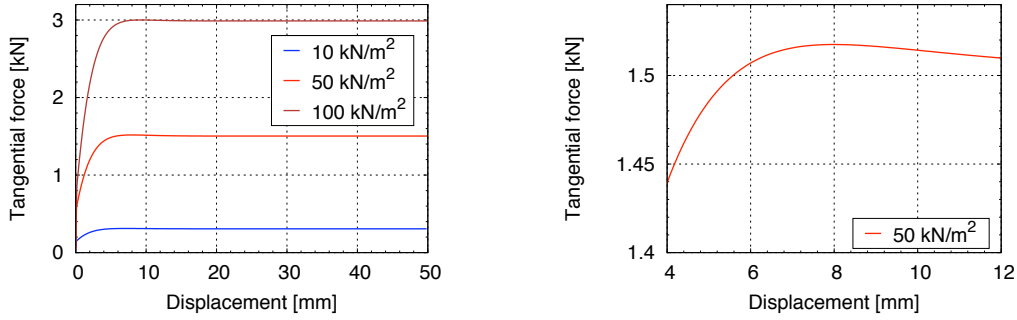


Figure 7.9: Direct shear test: Comparison of tangential force versus sliding distance with hardening (left) and zoom into the distribution at a constant pressure of 50 kN/m² (right)

over the coefficient of friction in the case of hardening as well as in the case of no hardening (comparing figure 7.8 and 7.9 with figures 7.5 and 7.6). In figure 7.10, the distribution of the friction angle versus the normal force at the final position is equal for the case with or without hardening. The almost negative exponential distribution of the friction angle corresponds well to the experimental measurements in Herle [1997], see figure 7.10.

7.4.2 Pull out of a wall

In the research group where this thesis is applied to, an experimental demonstrator test with Karlsruhe sand was conducted to validate the projected friction laws of the soil models where the soil models are developed by the other project partners. Since the material data of the Karlsruhe sand was not available at the time this thesis was written, only a qualitative comparison is possible. For the test case, sand was filled slowly into a box. Thereby the wall on the front side can be moved in vertical direction

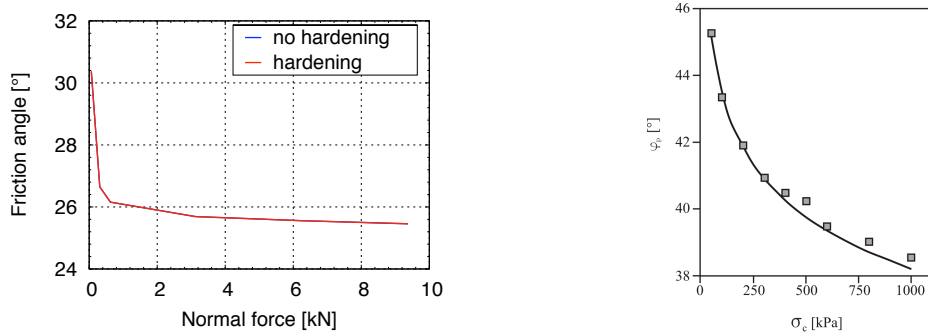


Figure 7.10: Direct shear test: Comparison between hardening and no hardening of different normal pressures (left) and experimental investigations of a triaxial test in Herle [1997] page 63

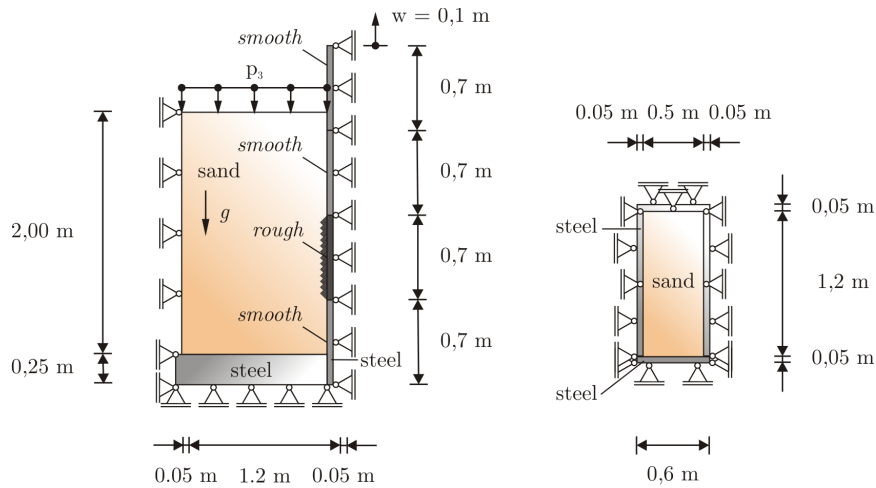


Figure 7.11: Side view (left) and top view (right) of the pull out test

and it is also subdivided into four equal segments where on the second one beginning from the bottom sand particles are glued to introduce a rough surface into the system, see figure 7.11. On each of the four segments, the normal and the tangential force can be measured leading to four individual distributions of the friction angles. The only load which is applied to the system is the gravity of the sand and of the steel components. Instead of the Karlsruhe sand, the GEBA fine sand (table 5.1) was chosen and for the steel specimen, the material parameters are set to $E = 210 \cdot 10^9 \text{ N/m}^2$, $\nu = 0.3$ and $\rho = 8 \cdot 10^3 \text{ kg/m}^3$ where the same material models are used as for the direct shear test. After the gravity is applied in 10 steps, the wall is pulled out in z -direction ($w = 0.1 \text{ m}$, $\Delta t = 0.01$). To guarantee almost positive first invariant (pressure) inside the soil specimen, a sand layer of 0.05 m on the top of the box was taken out and a normal pressure of $p_3 = 10 \cdot 10^3 \text{ N/m}^2$ is applied instead (figure 7.11). Four pictures (figures 7.12) show a concentration of the plastic strain close to the rough segment and a strong dilatant behavior below that rough segment. Comparing the experimental

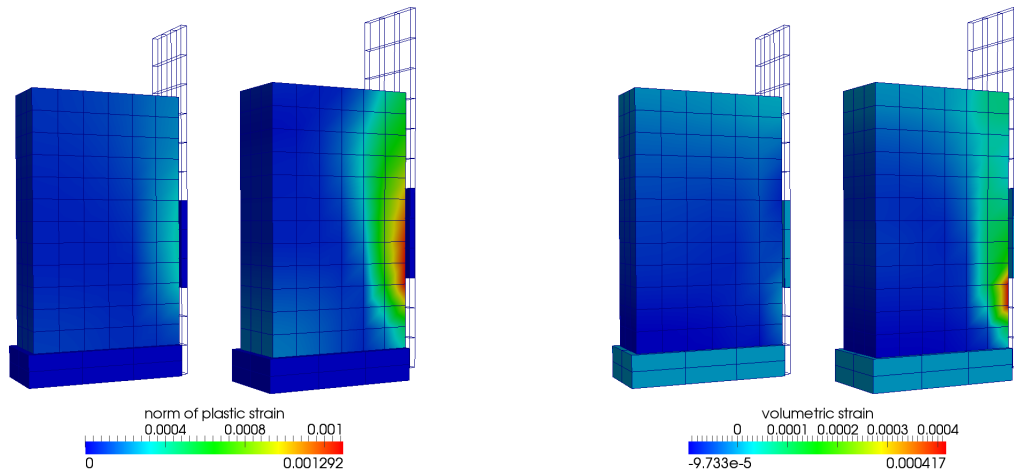


Figure 7.12: Norm of plastic strain after 15 mm and 100 mm (left) and volumetric strain after 15 mm and 100 mm (right)

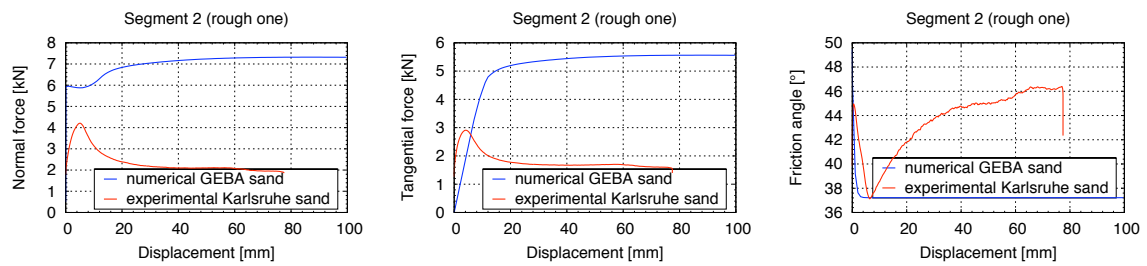


Figure 7.13: Pull out test: Comparison between experimental and numerical results for segment 2 (rough segment): Normal force (left), tangential force (middle) and friction angle (right)

data (Rebstock [2011]) with the numerical results, only the tangential distribution of the segment below (figure 7.14) and above the rough segment (figure 7.15) show an almost useful accordance with the experiments. Since this test case in combination with the Ehlers soil model is very challenging, only the projection concept over the coefficient of friction was applied in this example.

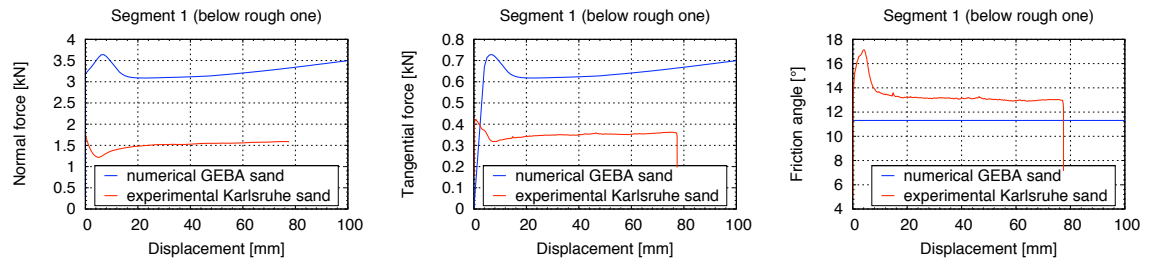


Figure 7.14: Pull out test: Comparison between experimental and numerical results for segment 1 (below rough segment): Normal force (left), tangential force (middle) and friction angle (right)

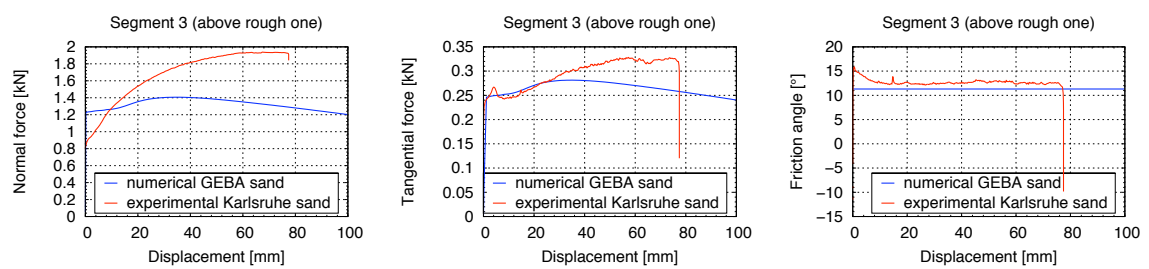


Figure 7.15: Pull out test: Comparison between experimental and numerical results for segment 3 (above rough segment): Normal force (left), tangential force (middle) and friction angle (right)

Chapter 8

3D contact element

Following the derivations of the contact kinematics in section 2.4.2, a three-dimensional contact element can be deduced assigning the contact zone a specific height. The advantage of a three-dimensional consideration of the contact zone is that not only the force transition but also the whole behavior at the interface can be modeled and the plasticity models of the continuum can be integrated directly. Especially for soil structure interactions where the contact zone lies completely within the soil, contact corresponds to a forced localization where the height of the localization zone is approximately two to three times the grain diameter.

In summary, the 3D contact element can essentially be viewed as a combination of the solid-shell theory (Schoop [1986] and modern forms in Parisch [1995], Hauptmann and Schweizerhof [1998] or Klinkel et al. [1999]) with a contact formulation, here the Mortar method, regularized by a penalty formulation (Belgacem et al. [1998], Puso and Laursen [2004b]). Due to the natural connection between yielding and slip for frictional materials, plasticity models (for soil structure interactions Ehlers et al. [2011] for example) are also combined to incorporate the frictional behavior within the contact model.

To improve the computational effort, the 3D contact formulation is based on the Hellinger-Reissner principle where Lagrange multipliers are introduced as additional unknowns.

In addition, it has to be highlighted that the derivation of the classical Reynolds equation can also be viewed as a combination of the shell kinematics with an integration over the height. An alternative derivation of the Reynolds equation based on shell kinematics is given explicitly in the appendix D.

8.1 3D contact kinematical relations

Based on the concept of the Mortar method (see also section 4.3.4), all the kinematical quantities of each slave node are averaged over its adjacent elements. Usually, in shell theory the formulation is based on the initial configuration and hence will be used here as well. Since in the component form (2.14) there is no difference between the configurations, the formulations hold also for the current configuration. As an

alternative to the standard form, the elasto-plastic stress strain relation can also be written as

$$\dot{\bar{\mathbf{E}}}_A - \dot{\lambda}_A \frac{\partial g}{\partial \bar{\mathbf{S}}} \Big|_A = \mathbf{D}^{-1} \dot{\bar{\mathbf{S}}}_A. \quad (8.1)$$

Using an implicit time integration scheme where $\gamma_{A n+1} = \Delta_t \lambda_{A n+1}$

$$\Delta_t \bar{\mathbf{E}}_{A n+1} - \gamma_{A n+1} \frac{\partial g}{\partial \bar{\mathbf{S}}} \Big|_{A n+1} = \mathbf{D}^{-1} [\bar{\mathbf{S}}_{A n+1} - \bar{\mathbf{S}}_{A n}], \quad (8.2)$$

the incremental Green Lagrange strain tensor $\Delta_t \bar{\mathbf{E}}_{A n+1}$ can be further specified. Writing the components of the incremental Green Lagrange strain tensor in terms of the components of the incremental metric tensor

$$\begin{aligned} \Delta_t \bar{\mathbf{E}}_{A i j n+1} &= \frac{1}{2} (\Delta_t \bar{g}_{A \alpha \beta n+1} + 2 \Delta_t \bar{g}_{A \alpha 3 n+1} + \Delta_t \bar{g}_{A 33 n+1}) \\ &= \frac{1}{2} \left[(\bar{g}_{\alpha \beta} - \bar{G}_{A \alpha \beta}) + 2 (\bar{g}_{A \alpha 3} - \bar{G}_{A \alpha 3}) + (\bar{g}_{A 33} - \bar{G}_{A 33}) \right], \end{aligned} \quad (8.3)$$

the metric at the old time step can be interpreted as the initial metric of the loading within this time step. Latin letters ($i, j = 1, 3$) represent thereby the continuum formulation and greek letters ($\alpha, \beta = 1, 2$) indicate shell or contact quantities. The base vectors of the actual time step correspond to the one of the current configuration (2.5)

$$\begin{aligned} \mathbf{g}_\alpha &= \frac{\partial \mathbf{x}(\boldsymbol{\xi}_{n+1})}{\partial \xi^\alpha} = \left(1 - \frac{\xi}{h}\right) \mathbf{x}_{,\alpha}^1(\boldsymbol{\xi}_{n+1}) + \frac{\xi}{h} \mathbf{x}_{,\alpha}^2(\boldsymbol{\xi}_{n+1}) \\ \mathbf{g}_3 &= \mathbf{g}^3 = \frac{\partial \mathbf{x}(\boldsymbol{\xi}_{n+1})}{\partial \xi} = \frac{1}{h} [\mathbf{x}^2(\boldsymbol{\xi}_{n+1}) - \mathbf{x}^1(\boldsymbol{\xi}_{n+1})]. \end{aligned} \quad (8.4)$$

To be in line with the Mortar method where an objective derivative of the tangential movement is obtained by means of the derivative at the integration point (equation (4.90) or Yang et al. [2005]), this concept is also applied leading to the base vectors at the old time step

$$\begin{aligned} \mathbf{G}_\alpha &= \frac{\partial \mathbf{x}(\boldsymbol{\xi}_n)}{\partial \xi^\alpha} = \left(1 - \frac{\xi}{h}\right) \mathbf{x}_{,\alpha}^1(\boldsymbol{\xi}_n) + \frac{\xi}{h} \mathbf{x}_{,\alpha}^2(\boldsymbol{\xi}_n) \\ \mathbf{G}_3 &= \mathbf{g}^3 = \frac{\partial \mathbf{x}(\boldsymbol{\xi}_n)}{\partial \xi} = \frac{1}{h} [\mathbf{x}^2(\boldsymbol{\xi}_n) - \mathbf{x}^1(\boldsymbol{\xi}_n)]. \end{aligned} \quad (8.5)$$

To set up the 3D contact element, first the actual metric components are integrated over the height (see section 2.4.2) and averaged afterwards. For the membrane part (2.77), the nodal equivalent form is given as

$$\begin{aligned} \bar{g}_{\alpha \beta A} &= \sum_{g=1}^{n_{gp}} M_A(\boldsymbol{\xi}_{g n+1}^1) \left[\frac{h}{3} \left(\mathbf{x}_{,\alpha n+1}^1(\boldsymbol{\xi}_{g n+1}^1) \cdot \mathbf{a}_{\beta n+1}^1(\boldsymbol{\xi}_{g n+1}^1) \right. \right. \\ &\quad \left. \left. + \mathbf{x}_{,\alpha n+1}^2(\boldsymbol{\xi}_{g n+1}^2) \cdot \mathbf{a}_{\beta n+1}^2(\boldsymbol{\xi}_{g n+1}^2) \right) + \frac{h}{6} \left(\mathbf{x}_{,\alpha n+1}^1(\boldsymbol{\xi}_{g n+1}^1) \cdot \mathbf{a}_{\beta n+1}^2(\boldsymbol{\xi}_{g n+1}^2) \right. \right. \\ &\quad \left. \left. + \mathbf{x}_{,\alpha n+1}^2(\boldsymbol{\xi}_{g n+1}^2) \cdot \mathbf{a}_{\beta n+1}^1(\boldsymbol{\xi}_{g n+1}^1) \right) \right] \det \mathbf{j}_{n+1} W_g \end{aligned} \quad (8.6)$$

where correspondingly to the Mortar method, two different types of base vectors are applied. The one indicated with an \mathbf{a} , e.g. \mathbf{a}_α^i , are nodal averaged base vectors (4.79) to guarantee a smooth transition between the elements. The other type of base vectors indicated as the derivative of the position vector $\mathbf{x}_{,\alpha}^i$ correspond to the actual base vectors at that point. In the same way, the shearing part (2.79)

$$\bar{g}_{\alpha 3A} = - \sum_{g=1}^{n_{gp}} M_A (\boldsymbol{\xi}_{g n+1}^1) \left(\mathbf{x}_{n+1}^2 (\boldsymbol{\xi}_{g n+1}^2) - \mathbf{x}_{n+1}^1 (\boldsymbol{\xi}_{g n+1}^1) \right) \cdot \frac{1}{2} \left(\mathbf{a}_{\alpha n+1}^1 (\boldsymbol{\xi}_{g n+1}^1) + \mathbf{a}_{\alpha n+1}^2 (\boldsymbol{\xi}_{g n+1}^2) \right) \det \mathbf{j}_{n+1} W_g \quad (8.7)$$

and the normal part (2.82)

$$\bar{g}_{33A} = \sum_{g=1}^{n_{gp}} M_A (\boldsymbol{\xi}_{g n+1}^1) \left(\mathbf{x}_{n+1}^2 (\boldsymbol{\xi}_{g n+1}^2) - \mathbf{x}_{n+1}^1 (\boldsymbol{\xi}_{g n+1}^1) \right) \cdot \mathbf{n}_{n+1}^1 (\boldsymbol{\xi}_{g n+1}^1) \det \mathbf{j}_{n+1} W_g \quad (8.8)$$

are averaged where the minus sign in the shearing contributions stems from the contact difference vector \mathbf{w} which points towards the opposite direction compared to the shell

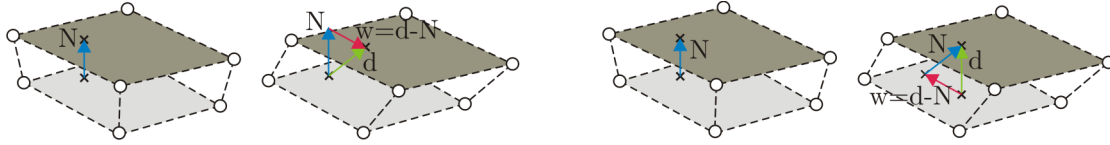


Figure 8.1: Difference vector determined within the shell theory (left) and within a contact formulation (right)

theory (see figure 8.1 or section 2.4.2). The averaged quantities at the old time step in (8.3) are also subdivided into a membrane

$$\begin{aligned} \bar{G}_{\alpha\beta A} = \sum_{g=1}^{n_{gp}} M_A (\boldsymbol{\xi}_{g n}^1) & \left[\frac{h}{3} \left(\mathbf{x}_{,\alpha n+1}^1 (\boldsymbol{\xi}_{g n}^1) \cdot \mathbf{a}_{\beta n+1}^1 (\boldsymbol{\xi}_{g n}^1) \right. \right. \\ & + \mathbf{x}_{,\alpha n+1}^2 (\boldsymbol{\xi}_{g n}^2) \cdot \mathbf{a}_{\beta n+1}^2 (\boldsymbol{\xi}_{g n}^2) \Big) + \frac{h}{6} \left(\mathbf{x}_{,\alpha n+1}^1 (\boldsymbol{\xi}_{g n}^1) \cdot \mathbf{a}_{\beta n+1}^2 (\boldsymbol{\xi}_{g n}^2) \right. \\ & \left. \left. + \mathbf{x}_{,\alpha n+1}^2 (\boldsymbol{\xi}_{g n}^2) \cdot \mathbf{a}_{\beta n+1}^1 (\boldsymbol{\xi}_{g n}^1) \right) \right] \det \mathbf{j}_n W_g, \end{aligned} \quad (8.9)$$

a shearing

$$\bar{G}_{\alpha 3A} = - \sum_{g=1}^{n_{gp}} M_A (\boldsymbol{\xi}_{g n}^1) \left(\mathbf{x}_{n+1}^2 (\boldsymbol{\xi}_{g n}^2) - \mathbf{x}_{n+1}^1 (\boldsymbol{\xi}_{g n}^1) \right) \cdot \frac{1}{2} \left(\mathbf{a}_{\alpha n+1}^1 (\boldsymbol{\xi}_{g n}^1) + \mathbf{a}_{\alpha n+1}^2 (\boldsymbol{\xi}_{g n}^2) \right) \det \mathbf{j}_n W_g \quad (8.10)$$

and a normal part

$$\bar{G}_{33A} = \sum_{g=1}^{n_{gp}} M_A (\boldsymbol{\xi}_{g n}^1) h_n \det \mathbf{j}_n W_g. \quad (8.11)$$

The normal contribution is thereby equivalent to the averaged height at the old time step and has to be used since the integration points can only account for movements in the tangential and not in the normal direction. Additionally, the virtual Green Lagrange strain components can be formulated in terms of the integrated and averaged virtual metric components

$$\delta \bar{E}_{ij\,n+1} = \frac{1}{2} (\delta \bar{g}_{\alpha\beta} + 2 \delta \bar{g}_{\alpha 3} + \delta \bar{g}_{33}). \quad (8.12)$$

Accordingly to section 2.4.2, in (8.12) the contributions of the virtual averaged nodal base vectors are neglected in the membrane part of (2.77)

$$\begin{aligned} \delta \bar{g}_{\alpha\beta A} = & \sum_{g=1}^{n_{gp}} M_A (\boldsymbol{\xi}_{g\,n+1}^1) \left[\frac{h}{3} \left(\boldsymbol{\eta}_{,\alpha\,n+1}^1 (\boldsymbol{\xi}_{g\,n+1}^1) \cdot \mathbf{a}_{\beta\,n+1}^1 (\boldsymbol{\xi}_{g\,n+1}^1) \right. \right. \\ & + \boldsymbol{\eta}_{,\alpha\,n+1}^2 (\boldsymbol{\xi}_{g\,n+1}^2) \cdot \mathbf{a}_{\beta\,n+1}^2 (\boldsymbol{\xi}_{g\,n+1}^2) \Big) + \frac{h}{6} \left(\boldsymbol{\eta}_{,\alpha\,n+1}^1 (\boldsymbol{\xi}_{g\,n+1}^1) \cdot \mathbf{a}_{\beta\,n+1}^2 (\boldsymbol{\xi}_{g\,n+1}^2) \right. \\ & \left. \left. + \boldsymbol{\eta}_{,\alpha\,n+1}^2 (\boldsymbol{\xi}_{g\,n+1}^2) \cdot \mathbf{a}_{\beta\,n+1}^1 (\boldsymbol{\xi}_{g\,n+1}^1) \right) \right] \det \mathbf{j}_{n+1} W_g \end{aligned} \quad (8.13)$$

and in the shearing part (2.79)

$$\begin{aligned} \delta \bar{g}_{\alpha 3 A} = & \sum_{g=1}^{n_{gp}} M_A (\boldsymbol{\xi}_{g\,n+1}^1) \left(\boldsymbol{\eta}_{n+1}^2 (\boldsymbol{\xi}_{g\,n+1}^2) - \boldsymbol{\eta}_{n+1}^1 (\boldsymbol{\xi}_{g\,n+1}^1) \right) \\ & \cdot \frac{1}{2} \left(\mathbf{a}_{\alpha\,n+1}^1 (\boldsymbol{\xi}_{g\,n+1}^1) + \mathbf{a}_{\alpha\,n+1}^2 (\boldsymbol{\xi}_{g\,n+1}^2) \right) \det \mathbf{j}_{n+1} W_g, \end{aligned} \quad (8.14)$$

but not in the the normal part (2.82) where also equation (2.83) is used

$$\delta \bar{g}_{33 A} = \sum_{g=1}^{n_{gp}} M_A (\boldsymbol{\xi}_{g\,n+1}^1) \left(\boldsymbol{\eta}_{n+1}^2 (\boldsymbol{\xi}_{g\,n+1}^2) - \boldsymbol{\eta}_{n+1}^1 (\boldsymbol{\xi}_{g\,n+1}^1) \right) \cdot \mathbf{n}_{n+1}^1 (\boldsymbol{\xi}_{g\,n+1}^1) \det \mathbf{j}_{n+1} W_g. \quad (8.15)$$

Additionally, the actual 2nd Piola Kirchhoff stress tensor and the Lagrange multipliers are needed in an averaged form in the solution scheme

$$\begin{aligned} \bar{S}_{ij\,A} &= \sum_{g=1}^{n_{gp}} M_A (\boldsymbol{\xi}_{g\,n+1}^1) S_{ij\,n+1} (\boldsymbol{\xi}_{g\,n+1}^1) \det \mathbf{j}_{n+1} W_g \\ \bar{\lambda}_{ij\,A} &= \sum_{g=1}^{n_{gp}} M_A (\boldsymbol{\xi}_{g\,n+1}^1) \lambda_{ij\,n+1} (\boldsymbol{\xi}_{g\,n+1}^1) \det \mathbf{j}_{n+1} W_g. \end{aligned} \quad (8.16)$$

8.2 Linearized quantities

Only standard shape functions are used and the averaged base vectors of each slave node are only updated at the beginning of each time step which simplifies the linearization

process and facilitates the solution process since no extra loops occur. To neglect the update of the nodal base vectors within the Newton iteration is acceptable, if the deformation of the slave body within one time step is considerably small. Analogously to section 4.3.5.2, the summation over all integration points of one averaged node is subdivided into the summation over all segments n_{seg}^A of that node and over all integrations points of that segment n_{gp}^s which suits to the assembling strategy proposed in section 4.3. The linearization of the current membrane part

$$\begin{aligned} \Delta \bar{\mathbf{g}}_{\alpha\beta A} &= \sum_{s=1}^{n_{seg}^A} \mathbf{G}_{\Delta \bar{\mathbf{g}}_{\alpha\beta}}^s \mathbf{d}_s, \quad \mathbf{G}_{\Delta \bar{\mathbf{g}}_{\alpha\beta}}^s = \sum_{g=1}^{n_{gp}^s} \left(M_{Ag}^1 \frac{h}{3} \left(\mathbf{B}_{li,\alpha}^1 \mathbf{a}_{\beta g}^1 + \mathbf{B}_{li,\alpha}^2 \mathbf{a}_{\beta g}^2 \right) + \frac{h}{6} \left(\mathbf{B}_{li,\alpha}^1 \mathbf{a}_{\beta g}^2 \right. \right. \\ &\quad \left. \left. + \mathbf{B}_{li,\alpha}^2 \mathbf{a}_{\beta g}^1 \right) + \left[M_{Ag}^1 \frac{h}{3} \left(\mathbf{x}_{,\alpha g}^1 \cdot \mathbf{a}_{\beta g}^1 + \mathbf{x}_{,\alpha g}^2 \cdot \mathbf{a}_{\beta g}^2 \right) + \frac{h}{6} \left(\mathbf{x}_{,\alpha g}^1 \cdot \mathbf{a}_{\beta g}^2 + \mathbf{x}_{,\alpha g}^2 \cdot \mathbf{a}_{\beta g}^1 \right) \right] \mathbf{B}_j \right. \\ &\quad \left. + \left(M_{A,\gamma g}^1 \left[\frac{h}{3} \left(\mathbf{x}_{,\alpha g}^1 \cdot \mathbf{a}_{\beta g}^1 + \mathbf{x}_{,\alpha g}^2 \cdot \mathbf{a}_{\beta g}^2 \right) + \frac{h}{6} \left(\mathbf{x}_{,\alpha g}^1 \cdot \mathbf{a}_{\beta g}^2 + \mathbf{x}_{,\alpha g}^2 \cdot \mathbf{a}_{\beta g}^1 \right) \right] \right. \right. \\ &\quad \left. \left. + M_{Ag}^1 \left[\frac{h}{3} \left(\mathbf{x}_{,\alpha \gamma g}^1 \cdot \mathbf{a}_{\beta g}^1 + \mathbf{x}_{,\alpha g}^1 \cdot \mathbf{a}_{\beta, \gamma g}^1 \right) + \frac{h}{6} \left(\mathbf{x}_{,\alpha \gamma g}^1 \cdot \mathbf{a}_{\beta g}^2 + \mathbf{x}_{,\alpha g}^2 \cdot \mathbf{a}_{\beta, \gamma g}^1 \right) \right] \right) \mathbf{B}_{gp}^{1\gamma} \right. \right. \\ &\quad \left. \left. + M_{Ag}^1 \left[\frac{h}{3} \left(\mathbf{x}_{,\alpha \gamma g}^2 \cdot \mathbf{a}_{\beta g}^2 + \mathbf{x}_{,\alpha g}^2 \cdot \mathbf{a}_{\beta, \gamma g}^2 \right) + \frac{h}{6} \left(\mathbf{x}_{,\alpha \gamma g}^2 \cdot \mathbf{a}_{\beta g}^1 + \mathbf{x}_{,\alpha g}^1 \cdot \mathbf{a}_{\beta, \gamma g}^2 \right) \right] \mathbf{B}_{gp}^{2\gamma} \right) \det \mathbf{j} \mathbf{W}_g \right. \end{aligned} \quad (8.17)$$

and the current shearing part

$$\begin{aligned} \Delta \bar{\mathbf{g}}_{\alpha 3 A} &= \sum_{s=1}^{n_{seg}^A} \mathbf{G}_{\Delta \bar{\mathbf{g}}_{\alpha 3}}^s \mathbf{d}_s, \quad \mathbf{G}_{\Delta \bar{\mathbf{g}}_{\alpha 3}}^s = \sum_{g=1}^{n_{gp}^s} \left(M_{Ag}^1 \mathbf{B}_{li} \frac{1}{2} (\mathbf{a}_{\alpha g}^1 + \mathbf{a}_{\alpha g}^2) \right. \\ &\quad \left. + M_{Ag}^1 (\mathbf{x}_g^2 - \mathbf{x}_g^1) \cdot \frac{1}{2} (\mathbf{a}_{\alpha g}^1 + \mathbf{a}_{\alpha g}^2) \mathbf{B}_j + \left[M_{A,\beta g}^1 (\mathbf{x}_g^2 - \mathbf{x}_g^1) \cdot \frac{1}{2} (\mathbf{a}_{\alpha g}^1 + \mathbf{a}_{\alpha g}^2) \right. \right. \\ &\quad \left. \left. - M_{Ag}^1 \mathbf{x}_{g,\beta}^1 \cdot \frac{1}{2} (\mathbf{a}_{\alpha g}^1 + \mathbf{a}_{\alpha g}^2) + M_{Ag}^1 (\mathbf{x}_g^2 - \mathbf{x}_g^1) \cdot \frac{1}{2} (\mathbf{a}_{\alpha,\beta g}^1 + \mathbf{a}_{\alpha,\beta g}^2) \right] \mathbf{B}_{gp}^{1\beta} \right. \\ &\quad \left. + M_{Ag}^1 \mathbf{x}_{g,\beta}^2 \cdot \frac{1}{2} (\mathbf{a}_{\alpha g}^1 + \mathbf{a}_{\alpha g}^2) \mathbf{B}_{gp}^{2\beta} \right) \det \mathbf{j} \mathbf{W}_g \end{aligned} \quad (8.18)$$

can be summarized by means of the individual linearization vectors of each segment $\mathbf{G}_{\Delta \bar{\mathbf{g}}_{\alpha\beta}}^s \in \mathbb{R}^{3 \times 24}$ and $\mathbf{G}_{\Delta \bar{\mathbf{g}}_{\alpha 3}}^s \in \mathbb{R}^{2 \times 24}$ written in Voigt notation. All the Mortar B matrices and their derivatives can be found in the appendix C.4. The linearization of the normal component is thereby equivalent to the linearization of the normal penetration in (4.134)

$$\Delta \bar{\mathbf{g}}_{33 A} = \sum_{s=1}^{n_{seg}^A} \mathbf{G}_{\Delta \bar{\mathbf{g}}_{33}} \mathbf{d}_s, \quad \mathbf{G}_{\Delta \bar{\mathbf{g}}_{33}} = \mathbf{G}_{\Delta \bar{\mathbf{g}}_N}. \quad (8.19)$$

The linearization of quantities at the old time step simplifies to a linearization of the current position vectors as can be seen for the membrane

$$\begin{aligned} \Delta \bar{G}_{\alpha\beta A} &= \sum_{s=1}^{n_{seg}^A} \mathbf{G}_{\Delta \bar{G}_{\alpha\beta}}^s \mathbf{d}_s, \quad \mathbf{G}_{\Delta \bar{G}_{\alpha\beta}}^s = \sum_{g=1}^{n_{gp}^s} M_{Ag}^1 \left[\frac{h}{3} \left(\mathbf{B}_{li,\alpha n}^1 \mathbf{a}_{\beta g n}^1 + \mathbf{B}_{li,\alpha n}^2 \mathbf{a}_{\beta g n}^2 \right) \right. \\ &\quad \left. + \frac{h}{6} \left(\mathbf{B}_{li,\alpha n}^1 \mathbf{a}_{\beta g n}^2 + \mathbf{B}_{li,\alpha n}^2 \mathbf{a}_{\beta g n}^1 \right) \right] \det \mathbf{j}_n W_g \in \mathbb{R}^{3 \times 24} \end{aligned} \quad (8.20)$$

and for the shearing part

$$\Delta \bar{G}_{\alpha 3 A} = \sum_{s=1}^{n_{seg}^A} \mathbf{G}_{\Delta \bar{G}_{\alpha 3}}^s \mathbf{d}_s, \quad \mathbf{G}_{\Delta \bar{G}_{\alpha 3}}^s = \sum_{g=1}^{n_{gp}^s} M_{Ag}^1 \mathbf{B}_{li n} \frac{1}{2} (\mathbf{a}_{\alpha g n}^1 + \mathbf{a}_{\alpha g n}^2) \det \mathbf{j}_n W_g \in \mathbb{R}^{2 \times 24}. \quad (8.21)$$

The linearization of the normal component is equal to zero, since all quantities depend only on the old time step. The variations of the components can also be displayed in vector form for each segment where the membrane part is

$$\begin{aligned} \delta \bar{G}_{\alpha\beta A} &= \sum_{s=1}^{n_{seg}^A} \delta \mathbf{d}_s \mathbf{G}_{\delta \bar{G}_{\alpha\beta}}^s, \quad \mathbf{G}_{\delta \bar{G}_{\alpha\beta}}^s = \sum_{g=1}^{n_{gp}^s} M_{Ag}^1 \left[\frac{h}{3} \left(\mathbf{B}_{li,\alpha}^1 \mathbf{a}_{\beta g}^1 + \mathbf{B}_{li,\alpha}^2 \mathbf{a}_{\beta g}^2 \right) \right. \\ &\quad \left. + \frac{h}{6} \left(\mathbf{B}_{li,\alpha}^1 \mathbf{a}_{\beta g}^2 + \mathbf{B}_{li,\alpha}^2 \mathbf{a}_{\beta g}^1 \right) \right] \det \mathbf{j} W_g \in \mathbb{R}^{24 \times 3} \end{aligned} \quad (8.22)$$

and the linearization follows to

$$\begin{aligned} \Delta \delta \bar{G}_{\alpha\beta A} &= \sum_{s=1}^{n_{seg}^A} \delta \mathbf{d}_s \mathbf{G}_{\Delta \delta \bar{G}_{\alpha\beta}}^s \mathbf{d}_s, \quad \mathbf{G}_{\Delta \delta \bar{G}_{\alpha\beta}}^s = \sum_{g=1}^{n_{gp}^s} \left[\mathbf{B}_{li,\alpha}^1 \left(M_{Ag}^1 \left[\frac{h}{3} \mathbf{a}_{\beta g}^1 + \frac{h}{6} \mathbf{a}_{\beta g}^2 \right] \mathbf{B}_j^T \right. \right. \\ &\quad \left. \left. + \left(M_{A,\gamma g}^1 \left[\frac{h}{3} \mathbf{a}_{\beta g}^1 + \frac{h}{6} \mathbf{a}_{\beta g}^2 \right] + M_{Ag}^1 \frac{h}{3} \mathbf{a}_{\beta,\gamma g}^1 \right) \mathbf{B}_{gp}^{1\gamma T} + M_{Ag}^1 \frac{h}{6} \mathbf{a}_{\beta,\gamma g}^2 \mathbf{B}_{gp}^{2\gamma T} \right) \right. \\ &\quad \left. + \mathbf{B}_{li,\alpha}^2 \left(M_{Ag}^1 \left[\frac{h}{3} \mathbf{a}_{\beta g}^2 + \frac{h}{6} \mathbf{a}_{\beta g}^1 \right] \mathbf{B}_j^T + \left(M_{A,\gamma g}^1 \left[\frac{h}{3} \mathbf{a}_{\beta g}^2 + \frac{h}{6} \mathbf{a}_{\beta g}^1 \right] \right. \right. \right. \\ &\quad \left. \left. + M_{Ag}^1 \frac{h}{6} \mathbf{a}_{\beta,\gamma g}^1 \right) \mathbf{B}_{gp}^{1\gamma T} + M_{Ag}^1 \frac{h}{3} \mathbf{a}_{\beta,\gamma g}^2 \mathbf{B}_{gp}^{2\gamma T} \right) + \mathbf{B}_{li,\alpha\gamma}^1 M_{Ag}^1 \left[\frac{h}{3} \mathbf{a}_{\beta g}^1 + \frac{h}{6} \mathbf{a}_{\beta g}^2 \right] \mathbf{B}_{gp}^{1\gamma T} \right. \\ &\quad \left. + \mathbf{B}_{li,\alpha\gamma}^2 M_{Ag}^1 \left[\frac{h}{3} \mathbf{a}_{\beta g}^2 + \frac{h}{6} \mathbf{a}_{\beta g}^1 \right] \mathbf{B}_{gp}^{2\gamma T} \right] \det \mathbf{j} W_g \in \mathbb{R}^{24 \times 24}. \end{aligned} \quad (8.23)$$

For the shearing part

$$\delta \bar{G}_{\alpha 3 A} = \sum_{s=1}^{n_{seg}^A} \delta \mathbf{d}_s \mathbf{G}_{\delta \bar{G}_{\alpha 3 A}}^s \quad \mathbf{G}_{\delta \bar{G}_{\alpha 3 A}}^s = \sum_{g=1}^{n_{gp}^s} M_{Ag}^1 \mathbf{B}_{li} \frac{1}{2} (\mathbf{a}_{\alpha g}^1 + \mathbf{a}_{\alpha g}^2) \det \mathbf{j} W_g \in \mathbb{R}^{24 \times 2} \quad (8.24)$$

the linearization reads

$$\begin{aligned} \Delta \delta \bar{g}_{\alpha 3 A} &= \sum_{s=1}^{n_{seg}^A} \mathbf{G}_{\Delta \delta \bar{g}_{\alpha 3}}^s \mathbf{d}_s \quad \mathbf{G}_{\Delta \delta \bar{g}_{\alpha 3}}^s = \sum_{g=1}^{n_{gp}^s} \left[\mathbf{B}_{li} \left(M_{Ag}^1 \frac{1}{2} (\mathbf{a}_{\alpha g}^1 + \mathbf{a}_{\alpha g}^2) \mathbf{B}_j^T \right. \right. \\ &\quad \left. \left. + \left[M_{A,\beta g}^1 \frac{1}{2} (\mathbf{a}_{\alpha g}^1 + \mathbf{a}_{\alpha g}^2) + M_{Ag}^1 \frac{1}{2} \mathbf{a}_{\alpha,\beta g}^1 \right] \mathbf{B}_{gp}^{1\beta T} + M_{Ag}^1 \frac{1}{2} \mathbf{a}_{\alpha,\beta g}^2 \mathbf{B}_{gp}^{2\beta T} \right) \right. \\ &\quad \left. + \mathbf{B}_{li,\beta}^\gamma M_{Ag}^1 \frac{1}{2} (\mathbf{a}_{\alpha g}^1 + \mathbf{a}_{\alpha g}^2) \mathbf{B}_{gp}^{\gamma\beta T} \right] \det \mathbf{j}W_g \in \mathbb{R}^{24 \times 24}. \end{aligned} \quad (8.25)$$

The variation of the normal contribution and its linearization is thereby again equivalent to (4.135) and (4.136)

$$\begin{aligned} \delta \bar{g}_{33A} &= \sum_{s=1}^{n_{seg}^A} \delta \mathbf{d}_s \mathbf{G}_{\delta \bar{g}_{33}}^s, \quad \mathbf{G}_{\delta \bar{g}_{33}}^s = \mathbf{G}_{\delta \bar{g}_N}^s \\ \Delta \delta \bar{g}_{33A} &= \sum_{g=1}^{n_{gp}} \mathbf{G}_{\Delta \delta \bar{g}_{33A}} \mathbf{d}^c, \quad \mathbf{G}_{\Delta \delta \bar{g}_{33A}} = \mathbf{G}_{\Delta \delta \bar{g}_N}. \end{aligned} \quad (8.26)$$

With all the individual components of the metric tensor, the linearization of the Green Lagrange strain tensor in Voigt notation can be summarized to

$$\Delta \bar{\mathbf{E}} = \sum_{s=1}^{n_{seg}^A} \mathbf{E}_{\Delta \bar{\mathbf{E}}}^s, \quad \mathbf{E}_{\Delta \bar{\mathbf{E}}}^s = \frac{1}{2} \begin{bmatrix} \mathbf{G}_{\Delta \bar{g}_{\alpha\beta A}}^s & -\mathbf{G}_{\Delta \bar{G}_{\alpha\beta A}}^s \\ 2\mathbf{G}_{\Delta \bar{g}_{\alpha 3 A}}^s & -2\mathbf{G}_{\Delta \bar{G}_{\alpha 3 A}}^s \\ & \mathbf{G}_{\Delta \bar{g}_{33 A}}^s \end{bmatrix} \in \mathbb{R}^{6 \times 24} \quad (8.27)$$

as well as its variation

$$\delta \bar{\mathbf{E}} = \sum_{s=1}^{n_{seg}^A} \mathbf{E}_{\delta \bar{\mathbf{E}}}^s, \quad \mathbf{E}_{\delta \bar{\mathbf{E}}}^s = \frac{1}{2} \begin{bmatrix} \mathbf{G}_{\delta \bar{g}_{\alpha\beta A}}^s \\ 2\mathbf{G}_{\delta \bar{g}_{\alpha 3 A}}^s \\ \mathbf{G}_{\delta \bar{g}_{33 A}}^s \end{bmatrix} \in \mathbb{R}^{6 \times 24} \quad (8.28)$$

and the linearized variation

$$\Delta \delta \bar{\mathbf{E}} = \sum_{s=1}^{n_{seg}^A} \mathbf{E}_{\Delta \delta \bar{\mathbf{E}}}^s, \quad \mathbf{E}_{\Delta \delta \bar{\mathbf{E}}}^s = \frac{1}{2} \left[\mathbf{G}_{\Delta \delta \bar{g}_{\alpha\beta A}}^s + 2\mathbf{G}_{\Delta \delta \bar{g}_{\alpha 3 A}}^s + \mathbf{G}_{\Delta \delta \bar{g}_{33 A}}^s \right] \in \mathbb{R}^{24 \times 24}. \quad (8.29)$$

At last, the contributions of the Lagrange multipliers have to be linearized

$$\Delta \bar{\lambda}_{iA} = \sum_{s=1}^{n_{seg}^A} (\mathbf{G}_{\Delta \bar{\lambda}}^s \mathbf{d}_s + \mathbf{L}_{\Delta \bar{\lambda}} \mathbf{l}_s) \quad (8.30)$$

leading to the vectors

$$\begin{aligned} \mathbf{G}_{\Delta \bar{\lambda}} &= \left(M_{Ag}^1 \lambda_{ig} \mathbf{B}_j + \left[M_{A,\alpha g}^1 \lambda_{ig} + M_{Ag}^1 \lambda_{i,\alpha g} \right] \mathbf{B}_{gp}^{1\alpha} \right) \det \mathbf{j}W_g \in \mathbb{R}^{6 \times 24} \\ \mathbf{L}_{\Delta \bar{\lambda}} &= M_{Ag}^1 \mathbf{P}_{N_B^1}^{l3d} \det \mathbf{j}W_g \in \mathbb{R}^{6 \times 24} \end{aligned} \quad (8.31)$$

where the projection tensor $\mathbf{P}_{N_B^1}^{l3d}$ can be found in the appendix C.5.

8.3 Residual vector and tangent matrix

For the active set of each contact node, instead of the normal penetration as for the classical penalty method, now a critical height has to be introduced which indicates if contact takes place or not. Due to dilatancy effects, the height

$$h_{An+1} = \mathbf{x}_{An+1}^1 - \frac{1}{a_{An+1}} M_A (\boldsymbol{\xi}_{gn+1}^1) \mathbf{x}^2 (\boldsymbol{\xi}_{gn+1}^2) \det \mathbf{j}_{n+1} W_g \quad (8.32)$$

can go above the initial critical value. Hence two different limits have to be chosen

$$\begin{array}{llll} \text{inactive} & \rightarrow & \text{active} & h_{An+1} \leq h^{ic} \\ \text{active} & \rightarrow & \text{inactive} & h_{An+1} \geq h^{ac} \end{array} \quad (8.33)$$

to determine the status of the node where h^{ac} has to be slightly larger than h^{ic} . For an incorporation of standard plasticity models into the concept of the shell theory, a transformation of the base vectors from the local to the global framework can be performed. This concept was successfully applied to shells in Klinkel et al. [1999] and extended to the case of plasticity in Sprenger et al. [2000]. The quantities, as for instance the Green Lagrange strain tensor, can be transformed to the Cartesian coordinate system using the fourth order tensor \mathbb{T}_A

$$\begin{aligned} \tilde{\mathbf{E}}_A &= \mathbb{T}_A \bar{\mathbf{E}}_A & \tilde{\mathbf{E}}_{Aij} &= \mathbb{T}_{Aijkl} \bar{\mathbf{E}}_{Akl} \\ \mathbb{T}_{Aijkl} &= \mathbf{e}_{Ai} \cdot \mathbf{G}_A^k \mathbf{e}_{Aj} \cdot \mathbf{G}_A^l \end{aligned} \quad (8.34)$$

where values in the Cartesian framework are denoted with a tilde on top. Due to the symmetry of the strain and of the stress tensor, the Voigt notation is used and the explicit description of the transformation tensor in matrix notation can be found in the appendix (B.7). Summing up the incremental strain components (8.3), the current Green Lagrange strain tensor $\tilde{\mathbf{E}}_{An+1}$ can be computed leading to the standard solution procedure for plasticity models where the trial state

$$\tilde{\mathbf{S}}_{An+1}^{tr} = \tilde{\mathbf{D}}^e \left[\tilde{\mathbf{E}}_{An+1} - \tilde{\mathbf{E}}_{An}^p \right] \quad (8.35)$$

determines the actual stick-slip state of the contact node. If the trial yield criterion $f(\tilde{\mathbf{S}}_{An+1}^{tr}) \leq 0$ is fulfilled, the elastic stress is given as

$$\begin{aligned} \tilde{\mathbf{S}}_{An+1} &= \tilde{\mathbf{S}}_{An+1}^{tr} \\ \tilde{\mathbf{D}}_{An+1} &= \tilde{\mathbf{D}}^e \\ \tilde{\mathbf{E}}_{An+1}^p &= \tilde{\mathbf{E}}_{An}^p \end{aligned} \quad (8.36)$$

and $\tilde{\mathbf{D}}_{An+1}$ corresponds to the standard linear elastic material tensor (B.3). For nodes violating the yield criterion $f(\tilde{\mathbf{S}}_{An+1}^{tr}) > 0$, the back projection algorithm, as in (3.38),

has to be performed until the two equations

$$\begin{aligned} \mathbf{R}_{\tilde{\mathbf{S}}_{An+1}} &= \tilde{\mathbf{D}}^{e-1} \tilde{\mathbf{S}}_{An+1} - \tilde{\mathbf{E}}_{An+1} - \tilde{\mathbf{E}}_{An}^p - \gamma_{An+1} \frac{\partial g(\tilde{\mathbf{S}})}{\partial \tilde{\mathbf{S}}} \Big|_{An+1} = \mathbf{0} \\ \mathbf{R}_{\gamma_{An+1}} &= f(\tilde{\mathbf{S}}_{An+1}) = 0 \end{aligned} \quad (8.37)$$

hold. As in (3.39) and (3.40), the tangent matrix follows from the converged and inverted tangent matrix of the Newton iteration

$$\begin{aligned} \tilde{\mathbf{D}}_{An+1} &= \tilde{\mathbf{A}}_{\tilde{\mathbf{S}}\tilde{\mathbf{S}}}^{-1} \\ \tilde{\mathbf{E}}_{An+1}^p &= \tilde{\mathbf{E}}_{An}^p + \gamma_{An+1} \frac{\partial g(\tilde{\mathbf{S}})}{\partial \tilde{\mathbf{S}}} \Big|_{An+1}. \end{aligned} \quad (8.38)$$

Afterwards, the stress and the material matrix have to be back projected to the local coordinate system which can be performed in terms of the transformation matrix

$$\begin{aligned} \bar{\mathbf{S}}_{An+1} &= \mathbf{T}_{An+1} \tilde{\mathbf{S}}_{\alpha n+1} \\ \bar{\mathbf{D}}_{An+1} &= \mathbf{T}_{An+1}^T \tilde{\mathbf{D}}_{An+1} \mathbf{T}_{An+1} \\ \bar{\mathbf{E}}_{An+1}^p &= \mathbf{T}_{An+1}^{-1} \tilde{\mathbf{E}}_{An+1}^p. \end{aligned} \quad (8.39)$$

The algorithm above can also be extended to cases with a hardening evolution equation, as in (5.23) or (5.35). Alternatively, instead of the base vectors \mathbf{a}_α^i of the slave and the master side, its normalized counterparts \mathbf{t}_α^i can also be used within the computation which simplifies the process. As shown in the numerical examples for the Mortar method (4.4.3), the classical penalty formulation leads to an increase in the CPU time due to the additional loop over all integration points. A remedy to decrease the CPU time is to introduce additional unknowns which can be applied to overcome the additional loop leading to a Hellinger-Reissner formulation for this contact shell version. The weak form is then subdivided into the virtual contact work

$$G_{uA}^{ch} = \delta \bar{\mathbf{E}}_A \cdot \boldsymbol{\lambda}_A = \sum_{s=1}^{n_{seg}^A} \delta \mathbf{d}_s \mathbf{R}_u^s, \quad \mathbf{R}_u^s = \mathbf{E}_{\delta \bar{\mathbf{E}}}^s \boldsymbol{\lambda}_A \in \mathbb{R}^{24} \quad (8.40)$$

and a second equation which forces the unknown Lagrange multiplier to be equal to the 2nd Piola Kirchhoff stress tensor

$$G_{lA}^{ch} = \delta \boldsymbol{\lambda}_A \mathbf{R}_l^A, \quad \mathbf{R}_l^A = \mathbf{D}^{e-1} [\bar{\boldsymbol{\lambda}}_A - \bar{\mathbf{S}}_A] \in \mathbb{R}^6. \quad (8.41)$$

As in the Mortar method, the Lagrange multiplier part can also be sent directly to the assembler. The linearization of the virtual contact work

$$DG_{uA}^{ch} = \Delta \delta \bar{\mathbf{E}}_A \cdot \boldsymbol{\lambda}_A + \delta \bar{\mathbf{E}}_A \cdot \Delta \boldsymbol{\lambda}_A = \sum_{s=1}^{n_{seg}^A} \left(\delta \mathbf{d}_s \mathbf{K}_{uu}^s \mathbf{d}_s + \delta \mathbf{d}_s \mathbf{K}_{ul}^s \Delta \boldsymbol{\lambda}_A \right) \quad (8.42)$$

and of the enforcement of the stress

$$DG_{lA}^{ch} = \delta \lambda_A \cdot \mathbf{D}_A^{e-1} [\Delta \bar{\lambda}_A - \mathbf{D}_A \Delta \bar{\mathbf{E}}_A] = \sum_{s=1}^{n_{seg}^A} \left(\delta \lambda_A \mathbf{K}_{lu}^s \mathbf{d}_s + \delta \lambda_A \mathbf{K}_{ll}^s \mathbf{l}_s \right) \quad (8.43)$$

can be further subdivided into tangent matrices given in detail as

$$\begin{aligned} \mathbf{K}_{uu}^s &= \mathbf{E}_{\Delta \delta \bar{\mathbf{E}}}^s \lambda_A \in \mathbb{R}^{24 \times 24}, & \mathbf{K}_{ul}^s &= \mathbf{E}_{\delta \bar{\mathbf{E}}}^s \in \mathbb{R}^{24 \times 6} \\ \mathbf{K}_{lu}^s &= \mathbf{D}^{e-1} [\mathbf{G}_{\Delta \bar{\lambda}}^s - \bar{\mathbf{D}}_A \mathbf{E}_{\Delta \bar{\mathbf{E}}}^s] \in \mathbb{R}^{6 \times 24}, & \mathbf{K}_{ll}^s &= \sum_{g=1}^{n_{gp}^s} \mathbf{D}^{e-1} \mathbf{L}_{\Delta \bar{\lambda}}^s \in \mathbb{R}^{6 \times 24}. \end{aligned} \quad (8.44)$$

Different versions of this 3D model are also possible, but the focus of this approach was the smooth transition to the penalty version of the classical Mortar method. With a zero height ($h = 0$) and no Poisson ratio ($\nu = 0$) the penalty version can be reached where the additional unknowns $\bar{\lambda}_{11}$, $\bar{\lambda}_{22}$ and $\bar{\lambda}_{12}$ are forced to be zero automatically within the computation.

8.4 Connection to the theory of porous media

On the basis of the integrated shell concept, the three-dimensional contact formulation can be easily extended towards the theory of porous media. In accordance with chapter 6, for the quasi-static case, the weak form of the contact node leads to

$$G_A^c(\mathbf{u}) = \delta \bar{\mathbf{E}}_A^s \cdot \mathbf{S}_A^s - \text{div } \delta \bar{\mathbf{u}}_A^s p_A + \delta p_A \text{div } \bar{\mathbf{v}}_A^s + \frac{k_f}{\gamma_0} \text{grad } \delta \bar{p}_A \cdot \text{grad } \bar{p}_A = 0 \quad (8.45)$$

where the superscript s indicates the solid and f the fluid components. In (8.45), the nodal averaged divergence of the fluid velocity

$$\begin{aligned} \text{div } \bar{\mathbf{v}}_A^s &= \frac{h}{6} M_A(\boldsymbol{\xi}_{g n+1}^1) \sum_{i=1}^2 \sum_{j=1}^2 \mathbf{x}_{\alpha n+1}^i(\boldsymbol{\xi}_{g n+1}^i) \cdot \mathbf{a}_{\beta n+1}^j(\boldsymbol{\xi}_{g n+1}^j) \det \mathbf{j}_{n+1} W_g \\ &+ M_A(\boldsymbol{\xi}_{g n+1}^1) \left[\mathbf{x}_{n+1}^2(\boldsymbol{\xi}_{g n+1}^2) - \mathbf{x}_{n+1}^1(\boldsymbol{\xi}_{g n+1}^1) \right] \cdot \mathbf{n}_{n+1}^1(\boldsymbol{\xi}_{g n+1}^1) \det \mathbf{j}_{n+1} W_g \end{aligned} \quad (8.46)$$

and analogously, the variation of the solid displacements $\text{div } \delta \mathbf{u}_A^s$ can be determined by usage of the solid-shell concept. The gradient of the fluid pressure

$$\begin{aligned} \text{grad } \bar{p}_A &= \frac{h}{2 a_A} g_{\alpha \beta A}^{-1} M_A(\boldsymbol{\xi}_{g n+1}^1) \sum_{i=1}^2 p_{\alpha n+1}(\boldsymbol{\xi}_{g n+1}^1) \mathbf{a}_{\beta n+1}^i(\boldsymbol{\xi}_{g n+1}^i) \det \mathbf{j}_{n+1} W_g \\ \text{grad } \delta \bar{p}_A &= \frac{h}{2} M_A(\boldsymbol{\xi}_{g n+1}^1) \sum_{i=1}^2 \delta p_{\alpha n+1}(\boldsymbol{\xi}_{g n+1}^1) \mathbf{a}_{\alpha n+1}^i(\boldsymbol{\xi}_{g n+1}^i) \det \mathbf{j}_{n+1} W_g \end{aligned} \quad (8.47)$$

is also formulated by an average where now the distribution of the pressure over the height is assumed to be constant at the contact zone.

8.5 Numerical direct shear test

The investigation of the 3D contact element is also performed at the direct shear test of section 7.4.1, but now a height between the contacting bodies is introduced into the system as can be seen in figure 8.2 where also the complete measurements and boundary conditions are depicted. All the evaluations are performed on the basis of the Ehlers

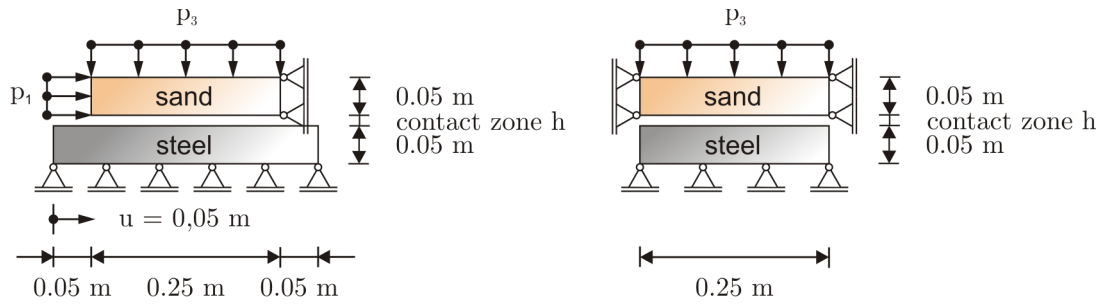


Figure 8.2: Side view (left) and front view (right) of the direct shear test

soil model with hardening which is described in detail in section 5.4. The tangential force distribution (figure 8.3) shows now a larger peak than in section 7.4.1 and also the final values are larger than in the projected version. In contrast to figure 7.6, the tangential force does not depend on the height, but the maximum value increases and the length of the peak zone decreases with a smaller contact height (figure 8.3). The

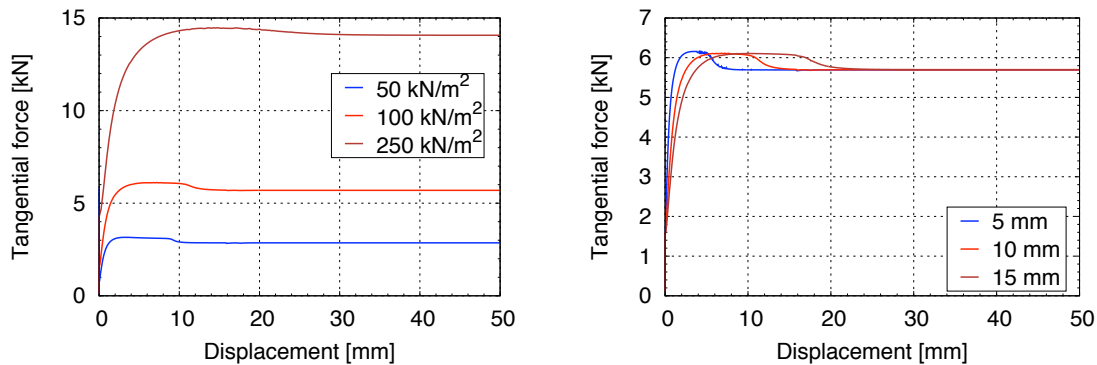


Figure 8.3: Direct shear test: Tangential force versus sliding distance at a constant height $h = 10\text{ mm}$ (left) and at a constant pressure of $p = 100\text{ kN/m}^2$ (right)

evaluation of the interface height (figure 8.4) for the dense GEBA sand is quite similar to the corresponding distribution of the volumetric strain in a triaxial test. First the height decreases (contractancy) and afterwards increases (dilatancy) beyond the initial height. For a small initial height also a peak evolves which decreases asymptotically to a constant final value. At the end, figure 8.5 and especially the side view in figure 8.6 show the initial and the final mesh of the direct shear test where no mesh distortion

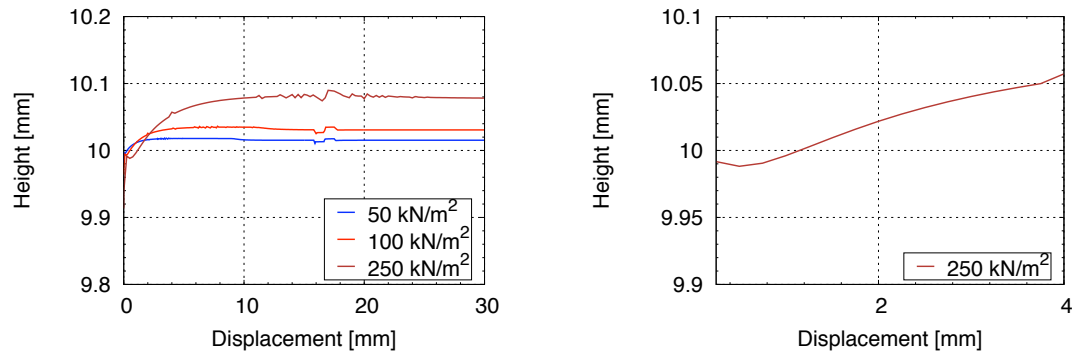


Figure 8.4: Direct shear test: Height versus sliding distance at a constant contact height of $h = 10\text{mm}$ (left) and zoom into the distribution at a constant pressure of $p = 250\text{ kN/m}^2$ and at a contact height of $h = 10\text{mm}$ (right)

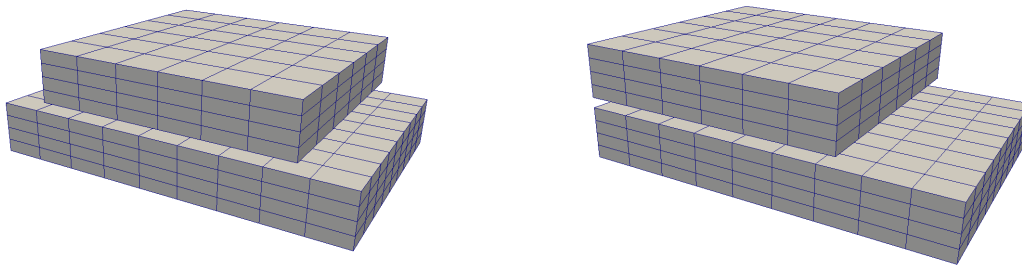


Figure 8.5: Initial mesh (left) and end position (right) of the direct shear test with a 3D contact element in between

evolves, since the interface element is mainly based on the contact formulation which allows arbitrarily large deformations.



Figure 8.6: Side view of the initial mesh (left) and the end position (right) of the direct shear test with a 3D contact element in between

Chapter 9

XFEM contact element

In the case of simulating special phenomena like cracks or other dislocations with the Finite Element Method, normally, an adaptive remeshing is necessary. Additionally, within fluid structure interactions special tools, like the Arbitrary Lagrangian Eulerian (ALE) method, are often applied. An alternative way to model these cases is based on the eXtended Finite Element Method (XFEM) where on the initial mesh another domain is overlapped. This can be another mesh as for fluid structure interactions (Gerstenberger and Wall [2008]) or a line indicating the interface between two materials (Moes et al. [2003]) or a crack line through the material (Moes et al. [1999]). The overlapped domain can be viewed as fixed or moving with regards to the underlying mesh where for the latter one proper evolution equations have to be defined. The interface or the discontinuity can be modeled as weak or strong where the former one is used for material interfaces where no jump of the displacement is allowed and the latter one is applied to model holes within the mesh, for instance. A detailed description of the XFEM can be found in Fries and Belytschko [2010]. Here due to the focus on contact or Dirichlet boundary conditions within an element only strong discontinuities will be discussed and the interfaces are fixed within the elements which simplifies the modeling process.

9.1 Description of elements with interfaces

The idea of the XFEM is to introduce additional unknowns within the elements which are cut by an interface instead of introducing new nodes along the interface. First an algorithm has to be chosen which determines all cut elements. Afterwards, the displacements of these elements are enriched

$$\mathbf{u}(\mathbf{x}) = \sum_{I=1}^n N_I(\mathbf{x}) \mathbf{u}_I + \sum_{I=1}^n \bar{N}_I(\mathbf{x}) \bar{\mathbf{u}}_I \quad (9.1)$$

where proper shape functions \bar{N}_I have to be defined. An explanation of the underlying idea of the XFEM on a simple example can be found in Moes et al. [1999]. The simplest strategy to deal with the different DOFs at each node is to enrich all nodes and to

fix the nodes which are not enriched afterwards. To model a strong discontinuity, the Heavyside function is multiplied to the standard discretization N_I forming the enriched shape functions

$$\bar{N}_I = N_I(\mathbf{x}) V(\mathbf{x}), \quad V(\mathbf{x}) = \begin{cases} 1 & \text{if } \phi(\mathbf{x}) \leq 0 \\ 0 & \text{if } \phi(\mathbf{x}) > 0 \end{cases} \quad (9.2)$$

where the function $\phi(\mathbf{x})$ determines, if a point lies inside or outside of the body. Figure 9.1 shows the distribution of all four enriched linear shape functions of a bilinear element where the strong discontinuity is located along the η -axis and the left domain indicates the material. In the case of crack tips, additional unknowns and special shape functions

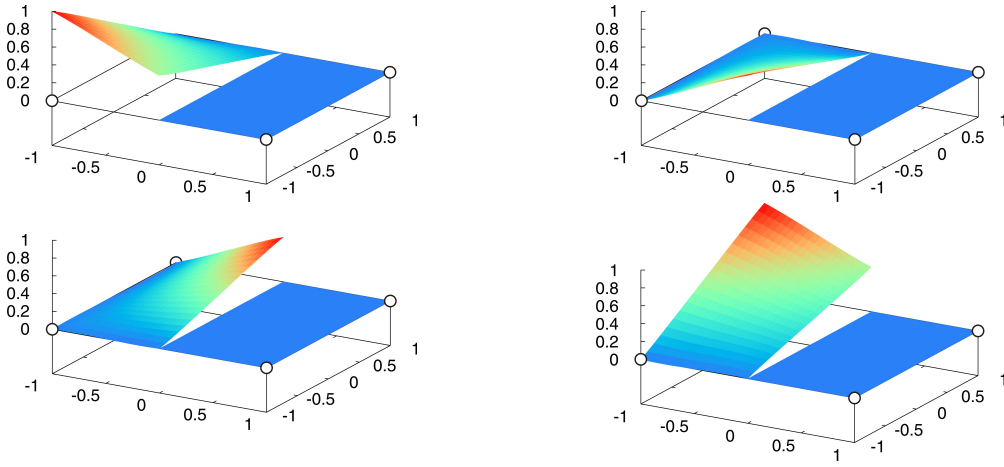


Figure 9.1: Enriched shape functions for a 2D bilinear element with a strong discontinuity

have to be defined (Fries and Belytschko [2010]). Mainly the signed distance function is used to determine $\phi(\mathbf{x})$ computing the distance of an arbitrary point of the mesh to the interface line $\bar{\mathbf{x}}$

$$\phi^h(\mathbf{x}) = \sum_{I=1}^n N_I(\mathbf{x}) \phi_I, \quad \phi_I = \pm \min \|\mathbf{x}_I - \bar{\mathbf{x}}\| \quad (9.3)$$

which fits well to the concept of finite elements. If kinks are located within an element

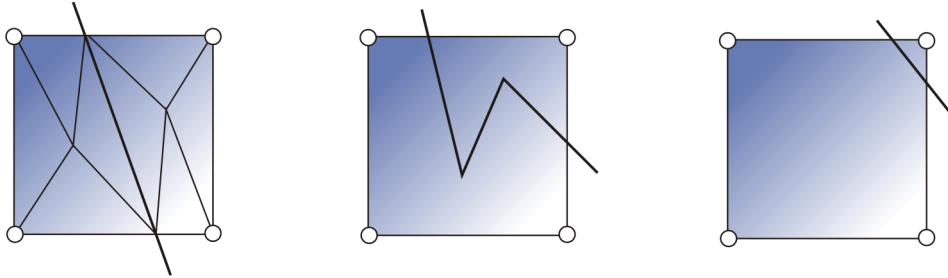


Figure 9.2: Standard interface element (left), interface element with no convex subdomains (middle) and interface close to a node (right)

(figure 9.2), the computation of the signed distance function can be very complicated. Another way is to determine the intersection points \mathbf{x}^p of the interface with the element edges using standard clipping algorithms, like of the one of section 4.3 known from computer graphics (Foley et al. [1996]) and computational geometry (de Berg et al. [2010]). Afterwards, the intersection points are transformed to the local coordinates of the element

$$\sum_{I=1}^n N_I(\boldsymbol{\xi}^p) \mathbf{x}_I - \mathbf{x}^p = 0 \quad (9.4)$$

where this nonlinear equation with respect to the local coordinates $\boldsymbol{\xi}^p$ can be solved using a Newton iteration. At the end, the convex hull, the bubble sort (de Berg et al. [2010] or Sedgewick [1992]) and the centroid point algorithm (4.75) can be applied to subdivide each side of the element into triangles (figure 9.2). Due to the storage of the local coordinates of each triangle, the displacements at the integration point on the material side

$$\mathbf{u}(\boldsymbol{\xi}) = \sum_{I=1}^n N_I \left(\sum_{J=1}^3 \boldsymbol{\xi}_J^p \right) \mathbf{u}_I + \sum_{I=1}^n \bar{N}_I \left(\sum_{J=1}^3 \boldsymbol{\xi}_J^p \right) \bar{\mathbf{u}}_I \quad (9.5)$$

and outside of the material

$$\mathbf{u}(\boldsymbol{\xi}) = \sum_{I=1}^n N_I \left(\sum_{J=1}^3 \boldsymbol{\xi}_J^p \right) \mathbf{u}_I \quad (9.6)$$

can be identified directly, conversely to the formulation in section 4.3. In addition, discontinuities close to the finite element node (figure 9.2) have to be avoided, since the equations (9.5) and (9.6) are then too similar leading to a rank decay of the tangent matrix. In this work, the intersections lie completely inside the elements. Additionally, some elements are not cut into convex parts so that for this case, the domain is further subdivided until each part is convex. Since the position of the discontinuities inside each element is fixed, equation (9.4) has not to be linearized. Further, so called blending elements are necessary for elements surrounding the cut ones. Formulations and open issues regarding these blending elements can be found in Fries and Belytschko [2010].

In the next sections, the focus lies on the formulation of elements with an embedded Dirichlet or contact boundary inside the element. In the surrounding, blending elements are necessary and in the far field, standard elements are used. For programming the last two mentioned elements, it is referred to the literature (Fries and Belytschko [2010], Zienkiewicz and Taylor [1989], Zienkiewicz and Taylor [1991]).

9.2 Linear embedded element

The first step in the development process of appropriate contact formulations within the XFEM framework is to find a way imposing boundary conditions inside an element. The classical formulations, like Lagrange multiplier method or penalty regularization, need a stabilization scheme (see Zilian and Fries [2009] and the references therein) and an improvement is based on the Hellinger-Reissner principle (3.19) where the Lagrange

multiplier enforcing the constraints is identified as the stress vector (Zilian and Fries [2009] and Gerstenberger and Wall [2010]). Since the complementary potential needed within the Hellinger-Reissner principle is hard to formulate in the nonlinear regime, the method is reformulated on the basis of the Hu-Washizu principle (Washizu [1975]).

9.2.1 Weak form

Since the development of an embedded element is only used for imposing Dirichlet boundary conditions, the Neumann part and for simplicity the body force term and the acceleration are neglected within the three field functional (3.18)

$$\Pi(\boldsymbol{\varphi}, \boldsymbol{\epsilon}, \boldsymbol{\sigma}) = \int_B [\mathcal{W}(\boldsymbol{\epsilon}) + \boldsymbol{\sigma} \cdot (\text{grad}^s \mathbf{x} - \boldsymbol{\epsilon})] dv - \int_{\partial B_u} \boldsymbol{\sigma} \mathbf{n} \cdot (\mathbf{u} - \bar{\mathbf{u}}) da \rightarrow \text{stat} \quad (9.7)$$

written in the linear elastic framework with the potential

$$\mathcal{W}(\boldsymbol{\epsilon}) = \frac{1}{2} \boldsymbol{\epsilon} \cdot \mathbb{C} \boldsymbol{\epsilon}. \quad (9.8)$$

The domain close to the intersection is subdivided into a material B^+ and a non material B^- domain and hence the inner potential is split into a positive Π_B^+ and a negative Π_B^- part

$$\begin{aligned} \Pi_B^+ &= \int_{B^+} [\mathcal{W}(\boldsymbol{\epsilon}) + \boldsymbol{\sigma} \cdot (\text{grad}^s \mathbf{x} - \boldsymbol{\epsilon})] dv \\ \Pi_B^- &= \int_{B^-} [\mathcal{W}(\boldsymbol{\epsilon}) + \boldsymbol{\sigma} \cdot (\text{grad}^s \mathbf{x} - \boldsymbol{\epsilon})] dv. \end{aligned} \quad (9.9)$$

Additionally, the boundary part is subdivided into

$$\begin{aligned} \Pi_{\partial B_u}^+ &= - \int_{\partial B_u^+} \boldsymbol{\sigma} \mathbf{n} \cdot (\mathbf{u} - \bar{\mathbf{u}}) da \\ \Pi_{\partial B_u}^- &= - \int_{\partial B_u^-} \boldsymbol{\sigma} \mathbf{n} \cdot (\mathbf{u} - \bar{\mathbf{u}}_0) da \end{aligned} \quad (9.10)$$

where at the positive surface ∂B_u^+ the boundary condition $\bar{\mathbf{u}}$ is enforced and at the negative surface ∂B_u^- the constraint of a zero relative displacement ($\bar{\mathbf{u}}_0 = 0$) has to be fulfilled which ensures that the field outside of the material is not taken into account within the modeling process. The distinction into a positive and a negative boundary surface is different to Zilian and Fries [2009] or Gerstenberger and Wall [2010], but leads to a very robust formulation and accurate results. To be in equilibrium, the functional has to be stationary and the derivatives with respect to three field quantities have to be equal to zero. The displacement part

$$\begin{aligned} D\Pi \cdot \delta \mathbf{u} &= \int_{B^+} \text{grad}^s \delta \mathbf{u} \cdot \boldsymbol{\sigma} dv + \int_{B^-} \text{grad}^s \delta \mathbf{u} \cdot \boldsymbol{\sigma} dv \\ &\quad - \int_{\partial B_u^+} \delta \mathbf{u} \cdot \boldsymbol{\sigma} \mathbf{n} da - \int_{\partial B_u^-} \delta \mathbf{u} \cdot \boldsymbol{\sigma} \mathbf{n} da = 0 \end{aligned} \quad (9.11)$$

leads to the virtual work and the strain part to the formulation of the constitutive equation in a weak sense

$$D\Pi \cdot \delta\epsilon = \int_{B^+} \delta\epsilon \cdot [\mathbb{C}\epsilon - \sigma] \cdot dv + \int_{B^-} \delta\epsilon \cdot [\mathbb{C}\epsilon - \sigma] \cdot dv = 0. \quad (9.12)$$

The last derivative enforces thereby the geometrical constraints

$$\begin{aligned} D\Pi \cdot \delta\sigma &= \int_{B^+} \delta\sigma \cdot [\text{grad } {}^s\mathbf{x} - \epsilon] \cdot dv + \int_{B^-} \delta\sigma \cdot [\text{grad } {}^s\mathbf{x} - \epsilon] \cdot dv \\ &\quad - \int_{\partial B_u^+} \delta\sigma \mathbf{n} \cdot (\mathbf{u} - \bar{\mathbf{u}}) \cdot da - \int_{\partial B_u^-} \delta\sigma \mathbf{n} \cdot (\mathbf{u} - \bar{\mathbf{u}}_0) \cdot da = 0. \end{aligned} \quad (9.13)$$

9.2.2 Discretization

Since the Heavyside function is used, all the unknowns and their virtual counterparts at the integration points inside the material are equal to the sum of the standard and the enriched DOFs. For the integration points outside of the material, the standard interpolation is used

$$\begin{aligned} \mathbf{u}_g^+ &= \sum_{I=1}^{n^u} N_I(\xi_g) [\mathbf{u}_I + \bar{\mathbf{u}}_I], & \mathbf{u}_g^- &= \sum_{I=1}^{n^u} N_I(\xi_g) \mathbf{u}_I \\ \epsilon_g^+ &= \sum_{I=1}^{n^\sigma} N_I(\xi_g) [\epsilon_I + \bar{\epsilon}_I], & \epsilon_g^- &= \sum_{I=1}^{n^\sigma} N_I(\xi_g) \epsilon_I \\ \sigma_g^+ &= \sum_{I=1}^{n^\sigma} N_I(\xi_g) [\sigma_I + \bar{\sigma}_I], & \sigma_g^- &= \sum_{I=1}^{n^\sigma} N_I(\xi_g) \sigma_I. \end{aligned} \quad (9.14)$$

For the displacement and the stress at the boundary, a distinction is also made between points on the positive side $b+$ and on the negative side $b-$ of the boundary, respectively,

$$\begin{aligned} \mathbf{u}_p^{b+} &= \sum_{K=1}^{n^s} N_K^s(\xi_p) \sum_{I=1}^n N_I(\bar{\xi}_K) [\mathbf{u}_I + \bar{\mathbf{u}}_I], & \mathbf{u}_p^{b-} &= \sum_{K=1}^{n^s} N_K^s(\xi_p) \sum_{I=1}^n N_I(\bar{\xi}_K) \mathbf{u}_I \\ \sigma_p^{b+} &= \sum_{K=1}^{n^s} N_K^s(\xi_p) \sum_{I=1}^n N_I(\bar{\xi}_K) [\sigma_I + \bar{\sigma}_I], & \sigma_p^{b-} &= \sum_{K=1}^{n^s} N_K^s(\xi_p) \sum_{I=1}^n N_I(\bar{\xi}_K) \sigma_I. \end{aligned} \quad (9.15)$$

To simplify the notation, the algebraic system on the element level

$$\begin{bmatrix} \mathbf{0} & \mathbf{0} & \tilde{\mathbf{K}}_{u\sigma} \\ \mathbf{0} & \tilde{\mathbf{K}}_{\epsilon\epsilon} & \tilde{\mathbf{K}}_{\epsilon\sigma} \\ \mathbf{K}_{\sigma u} & \tilde{\mathbf{K}}_{\sigma\epsilon} & \mathbf{0} \end{bmatrix} \begin{bmatrix} \Delta \tilde{\mathbf{u}} \\ \Delta \tilde{\epsilon} \\ \Delta \tilde{\sigma} \end{bmatrix} = - \begin{bmatrix} \tilde{\mathbf{R}}_u \\ \tilde{\mathbf{R}}_\epsilon \\ \tilde{\mathbf{R}}_\sigma \end{bmatrix} \quad (9.16)$$

is written in terms of a tilde over the quantities containing an intrinsic vector of the standard and of the enriched quantites as for the primary variables

$$\Delta \tilde{\mathbf{u}} = \begin{bmatrix} \Delta \mathbf{u} \\ \Delta \bar{\mathbf{u}} \end{bmatrix}, \quad \Delta \tilde{\boldsymbol{\epsilon}} = \begin{bmatrix} \Delta \boldsymbol{\epsilon} \\ \Delta \bar{\boldsymbol{\epsilon}} \end{bmatrix}, \quad \Delta \tilde{\boldsymbol{\sigma}} = \begin{bmatrix} \Delta \boldsymbol{\sigma} \\ \Delta \bar{\boldsymbol{\sigma}} \end{bmatrix}. \quad (9.17)$$

The residual vector with a tilde can also be further subdivided into a positive and a negative part each depending on standard and enriched contributions

$$\tilde{\mathbf{R}}_x = \begin{bmatrix} \mathbf{R}_x^+ \\ \mathbf{R}_x^- \end{bmatrix} + \begin{bmatrix} \mathbf{R}_x^- \\ 0 \end{bmatrix} \quad (9.18)$$

where the subscript x indicates the contribution of the desired field. Within the residual vector of the displacements

$$\begin{aligned} \mathbf{R}_u^+ &= \sum_{g=1}^{n_{gp}^+} \sum_{I=1}^n \mathbf{B}_I \boldsymbol{\sigma}_g \det \mathbf{j}_g W_g - \sum_{p=1}^{n_{gp}^s} \sum_{I=1}^n \sum_{K=1}^{n^s} N_K^s N_I^K \boldsymbol{\sigma}_p^s \hat{\mathbf{n}}_p W_p \\ \mathbf{R}_u^- &= \sum_{g=1}^{n_{gp}^-} \sum_{I=1}^n \mathbf{B}_I \boldsymbol{\sigma}_g \det \mathbf{j}_g W_g - \sum_{p=1}^{n_{gp}^s} \sum_{I=1}^n \sum_{K=1}^{n^s} N_K^s N_I^K \boldsymbol{\sigma}_p^s \hat{\mathbf{n}}_p W_p, \end{aligned} \quad (9.19)$$

the second term indicates the surface contribution where the determinant of the Jacobian can be reformulated. For the 2D case, the contribution of the normalized normal vector and the Jacobian

$$\det \mathbf{j}^a = \|\mathbf{a}_\xi\|, \quad \mathbf{n} \det \mathbf{j}^a = \frac{\mathbf{e}_3 \times \mathbf{a}_\xi}{\|\mathbf{a}_\xi\|} \|\mathbf{a}_\xi\| = \hat{\mathbf{n}} \quad (9.20)$$

simplifies to the normal vector $\hat{\mathbf{n}}$

$$\hat{\mathbf{n}} = \mathbf{e}_3 \times \mathbf{a}_\xi, \quad \begin{bmatrix} \hat{n}_1 \\ \hat{n}_2 \end{bmatrix} = \sum_{A=1}^m N_{A,\xi}(\xi) \begin{bmatrix} -x_{2A} \\ x_{1A} \end{bmatrix}. \quad (9.21)$$

The residual vector of the strain contains the constitutive equation in a weak sense

$$\begin{aligned} \mathbf{R}_\epsilon^+ &= \sum_{g=1}^{n_{gp}^+} \sum_{I=1}^n N_I (\mathbb{C} \boldsymbol{\epsilon}_g - \boldsymbol{\sigma}_g) \det \mathbf{j}_g W_g \\ \mathbf{R}_\epsilon^- &= \sum_{g=1}^{n_{gp}^-} \sum_{I=1}^n N_I (\mathbb{C} \boldsymbol{\epsilon}_g - \boldsymbol{\sigma}_g) \det \mathbf{j}_g W_g \end{aligned} \quad (9.22)$$

whereas the residual vector of the stress displays the enforcement of the geometrical equations

$$\begin{aligned}\mathbf{R}_\sigma^+ &= \sum_{g=1}^{n_{gp}^+} \sum_{I=1}^n N_I (\text{grad}^s \mathbf{u}_g - \boldsymbol{\epsilon}_g) \det \mathbf{j}_g W_g - \sum_{p=1}^{n_{gp}^s} \sum_{I=1}^n \sum_{K=1}^{n^s} N_K^s \mathbf{B}_{nI}^{KT} (\mathbf{u}_p - \bar{\mathbf{u}}_p) W_p \\ \mathbf{R}_\sigma^- &= \sum_{g=1}^{n_{gp}^-} \sum_{I=1}^n N_I (\text{grad}^s \mathbf{u}_g - \boldsymbol{\epsilon}_g) \det \mathbf{j}_g W_g - \sum_{p=1}^{n_{gp}^s} \sum_{I=1}^n \sum_{K=1}^{n^s} N_K^s \mathbf{B}_{nI}^{KT} (\mathbf{u}_p - \bar{\mathbf{u}}_p) W_p\end{aligned}\quad (9.23)$$

where the matrices \mathbf{B}_I and \mathbf{B}_{nI} can be found in the appendix B.2. The non zero tangent entries can also be decomposed into positive and negative parts

$$\tilde{\mathbf{K}}_{xy} = \begin{bmatrix} \mathbf{K}_{xy}^+ & \mathbf{K}_{xy}^+ \\ \mathbf{K}_{xy}^+ & \mathbf{K}_{xy}^+ \end{bmatrix} + \begin{bmatrix} \mathbf{K}_{xy}^- & 0 \\ 0 & 0 \end{bmatrix}. \quad (9.24)$$

The tangent on the strain diagonal contains the linear elastic material tensor

$$\begin{aligned}\mathbf{K}_{\epsilon\epsilon}^+ &= \sum_{g=1}^{n_{gp}^+} \sum_{I=1}^n \sum_{J=1}^n N_I \mathbf{D}^e N_J \det \mathbf{j}_g W_g \\ \mathbf{K}_{\epsilon\epsilon}^- &= \sum_{g=1}^{n_{gp}^-} \sum_{I=1}^n \sum_{J=1}^n N_I \mathbf{D}^e N_J \det \mathbf{j}_g W_g\end{aligned}\quad (9.25)$$

and is coupled to the stress part through

$$\begin{aligned}\mathbf{K}_{\epsilon\sigma}^+ &= - \sum_{g=1}^{n_{gp}^+} \sum_{I=1}^n \sum_{J=1}^n N_I \mathbf{1} N_J \det \mathbf{j}_g W_g \\ \mathbf{K}_{\sigma\epsilon}^- &= - \sum_{g=1}^{n_{gp}^-} \sum_{I=1}^n \sum_{J=1}^n N_I \mathbf{1} N_J \det \mathbf{j}_g W_g.\end{aligned}\quad (9.26)$$

The displacement part coupled to the stress can be specified as

$$\begin{aligned}\mathbf{K}_{u\sigma}^+ &= \sum_{g=1}^{n_{gp}^+} \sum_{I=1}^n \sum_{J=1}^n \mathbf{B}_I^T N_J \det \mathbf{j}_g W_g - \sum_{p=1}^{n_{gp}^s} \sum_{I=1}^n \sum_{J=1}^n \sum_{K=1}^{n^s} \sum_{L=1}^{n^s} N_K^s N_I^K N_L^s \mathbf{B}_{nJ}^L W_p \\ \mathbf{K}_{u\sigma}^- &= \sum_{g=1}^{n_{gp}^-} \sum_{I=1}^n \sum_{J=1}^n \mathbf{B}_I^T N_J \det \mathbf{j}_g W_g - \sum_{p=1}^{n_{gp}^s} \sum_{I=1}^n \sum_{J=1}^n \sum_{K=1}^{n^s} \sum_{L=1}^{n^s} N_K^s N_I^K N_L^s \mathbf{B}_{nJ}^L W_p.\end{aligned}\quad (9.27)$$

Since the matrix is symmetric, the remaining contributions to the tangent are the transpose of the corresponding matrices

$$\begin{aligned}\mathbf{K}_{\sigma\epsilon}^+ &= \mathbf{K}_{\epsilon\sigma}^{+T}, & \mathbf{K}_{\sigma\epsilon}^- &= \mathbf{K}_{\epsilon\sigma}^{-T} \\ \mathbf{K}_{\sigma u}^+ &= \mathbf{K}_{u\sigma}^{+T}, & \mathbf{K}_{\sigma u}^- &= \mathbf{K}_{u\sigma}^{-T}.\end{aligned}\quad (9.28)$$

In (9.24), it can be seen that, if the matrix contribution \mathbf{K}_{xy}^- is very small, the first and the second row is almost equal leading to a bad condition number or, if \mathbf{K}_{xy}^- is close to zero, a rank loss of the global tangent occurs.

9.2.3 Solution algorithm

Avoiding the solution of the stress and of the strain contributions within the global algebraic equation, both contributions can be condensed from (9.16). First, the linearized strain tensor of the element can be written in dependency of the linearized stress tensor

$$\Delta \tilde{\epsilon} = -\tilde{\mathbf{K}}_{\epsilon\epsilon}^{-1} \left[\tilde{\mathbf{R}}_{\epsilon} + \tilde{\mathbf{K}}_{\epsilon\sigma} \Delta \tilde{\sigma} \right] \quad (9.29)$$

leading to the reduced system

$$\begin{bmatrix} \mathbf{0} & \tilde{\mathbf{K}}_{u\sigma} \\ \tilde{\mathbf{K}}_{\sigma u} & -\tilde{\mathbf{K}}_{\sigma\sigma} \end{bmatrix} \begin{bmatrix} \Delta \tilde{\mathbf{u}} \\ \Delta \tilde{\sigma} \end{bmatrix} = - \begin{bmatrix} \tilde{\mathbf{R}}_u \\ \tilde{\mathbf{R}}_{\sigma} \end{bmatrix} \quad (9.30)$$

which corresponds to a Hellinger-Reissner formulation with the expressions

$$\bar{\mathbf{K}}_{\sigma\sigma} = \tilde{\mathbf{K}}_{\sigma\epsilon} \tilde{\mathbf{K}}_{\epsilon\epsilon}^{-1} \tilde{\mathbf{K}}_{\epsilon\sigma}, \quad \bar{\mathbf{R}}_{\sigma} = \tilde{\mathbf{R}}_{\sigma} - \tilde{\mathbf{K}}_{\sigma\epsilon} \tilde{\mathbf{K}}_{\epsilon\epsilon}^{-1} \tilde{\mathbf{R}}_{\epsilon}. \quad (9.31)$$

In (9.30), the diagonal contribution of the stress is non zero and the stress can be condensed

$$\Delta \tilde{\sigma} = \bar{\mathbf{K}}_{\sigma\sigma}^{-1} \left[\tilde{\mathbf{R}}_{\sigma} + \tilde{\mathbf{K}}_{\sigma u} \Delta \tilde{\mathbf{u}} \right] \quad (9.32)$$

resulting in the matrix contribution for the unknown displacements

$$\tilde{\mathbf{K}}_{u\sigma} \bar{\mathbf{K}}_{\sigma\sigma}^{-1} \tilde{\mathbf{K}}_{\sigma u} \Delta \tilde{\mathbf{u}} = -\tilde{\mathbf{R}}_u - \tilde{\mathbf{K}}_{u\sigma} \bar{\mathbf{K}}_{\sigma\sigma}^{-1} \tilde{\mathbf{R}}_{\sigma}. \quad (9.33)$$

The drawback of the condensation is the storage of all the tangent matrices and residual vectors in (9.29) and (9.32) and before the next iteration step can be conducted, the strain and stress have to be updated.

9.3 Linear embedded contact element

Solving contact problems within an element using the XFEM strategy together with a standard contact formulation (Kim et al. [2007]), the same drawbacks as for the imposition of Dirichlet boundary conditions evolve, see Sanders et al. [2009]. Hence a XFEM contact element based on the Hu-Washizu principle is proposed to enforce the contact constraints. In the subsequent part, only a simple scheme of solving contact problems within the Hu-Washizu framework is presented.

9.3.1 Weak form

Since two bodies are coupled inside an element, the components of the functional are increased to six

$$\Pi := \Pi(\mathbf{x}^1, \mathbf{x}^2, \boldsymbol{\epsilon}^1, \boldsymbol{\epsilon}^2, \boldsymbol{\sigma}^1, \boldsymbol{\sigma}^2) \rightarrow \text{stat.} \quad (9.34)$$

Neglecting body and external forces as well as the accelerations, the potential can be subdivided into five different parts

$$\Pi = \Pi_{B_1}^+ + \Pi_{B_1}^- + \Pi_{B_2}^+ + \Pi_{B_2}^- + \Pi_c \quad (9.35)$$

where the potentials of each material, $\Pi_{B_1}^+, \Pi_{B_1}^-$ and $\Pi_{B_2}^+, \Pi_{B_2}^-$, correspond exactly to equation (9.9). The additional contact term consists of a positive and a negative part

$$\begin{aligned} \Pi_c = & - \int_{\partial B_c^{1+}} \boldsymbol{\sigma}^1 \mathbf{n}^1 \cdot [\mathbf{x}^1 - \mathbf{x}^2] \, da - \int_{\partial B_c^{1-}} \boldsymbol{\sigma}^1 \mathbf{n}^1 \cdot [\mathbf{u}^1 - \mathbf{u}^2] \, da \\ & - \int_{\partial B_c^{2-}} \boldsymbol{\sigma}^2 \mathbf{n}^2 \cdot [\mathbf{u}^2 - \bar{\mathbf{u}}_0] \, da. \end{aligned} \quad (9.36)$$

The first term indicates the standard stick constraint which is enforced in terms of the slave stress ($i=1$) and the first integral on the negative slave side ensures that the displacements \mathbf{u}^1 and \mathbf{u}^2 outside of the material are equal to zero. (The zero displacement term $\bar{\mathbf{u}}_0$ is thereby removed from the equation.) The last term provides that depending on the master stress, the displacement \mathbf{u}^2 is also equal to zero. Within the derivatives of the functional, only the additional contact term will be considered. The remaining parts can be found in section 9.2. The derivative of the functional with respect to the variational displacements

$$\begin{aligned} D\Pi_c \cdot \delta \mathbf{u} = & - \int_{\partial B_c^{1+}} \delta \mathbf{u}^1 \cdot \boldsymbol{\sigma}^1 \mathbf{n}^1 \, da - \int_{\partial B_c^{1-}} \delta \mathbf{u}^1 \cdot \boldsymbol{\sigma}^1 \mathbf{n}^1 \, da + \int_{\partial B_c^{1+}} \delta \mathbf{u}^2 \cdot \boldsymbol{\sigma}^1 \mathbf{n}^1 \, da \\ & + \int_{\partial B_c^{1-}} \delta \mathbf{u}^2 \cdot \boldsymbol{\sigma}^1 \mathbf{n}^1 \, da - \int_{\partial B_c^{2-}} \delta \mathbf{u}^2 \cdot \boldsymbol{\sigma}^2 \mathbf{n}^2 \, da \end{aligned} \quad (9.37)$$

yields the virtual contact work and the derivative with respect to the variational stress leads to the weak enforcement of the contact constraints

$$\begin{aligned} D\Pi_c \cdot \delta \boldsymbol{\sigma} = & - \int_{\partial B_c^{1+}} \delta \boldsymbol{\sigma}^1 \mathbf{n}^1 \cdot [\mathbf{x}^1 - \mathbf{x}^2] \, da - \int_{\partial B_c^{1-}} \delta \boldsymbol{\sigma}^1 \mathbf{n}^1 \cdot [\mathbf{u}^1 - \mathbf{u}^2] \, da \\ & - \int_{\partial B_c^{2-}} \delta \boldsymbol{\sigma}^2 \mathbf{n}^2 \cdot [\mathbf{u}^2 - \bar{\mathbf{u}}_0] \, da. \end{aligned} \quad (9.38)$$

9.3.2 Segmentation

For each slave boundary segment, the corresponding master segment has to be specified (figure 9.3). The algorithm for the detection of the intersection of one slave segment with the master segment is similar to the algorithm in Yang et al. [2005] where instead of the cross product the scalar product is used which facilitates the linearization process.

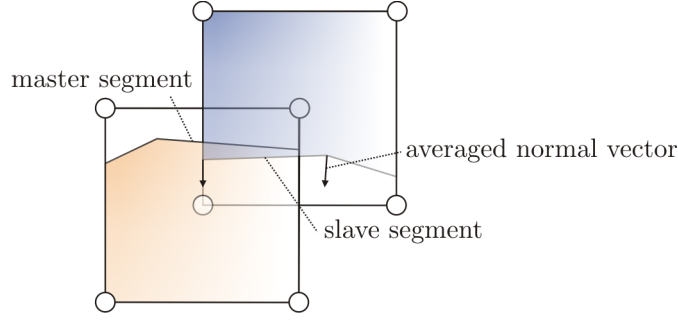


Figure 9.3: Contact element within the XFEM framework

First, the base vector and the normalized normal vector are averaged at each end point \bar{I} of the slave segment correspondingly to the Mortar method (4.79)

$$\mathbf{a}_{\bar{I}}^1 = \sum_{a=1}^{n_{ae}} \sum_{I=1}^2 N_{I,\xi}(\bar{\xi}_{\bar{I}}) \mathbf{x}_I^1, \quad \mathbf{n}_{\bar{I}}^1 = \frac{\mathbf{e}_3 \times \mathbf{a}_{\bar{I}}^1}{\|\mathbf{e}_3 \times \mathbf{a}_{\bar{I}}^1\|} \quad (9.39)$$

where $n_{ae}^1 \leq 2$. Writing down the above formulation explicitly in matrix notation, the normalized tangential vector can be related to the normalized normal vector via

$$\mathbf{t}_A^1 = \begin{bmatrix} t_{A1}^1 \\ t_{A2}^1 \end{bmatrix} = \begin{bmatrix} -n_{A2}^1 \\ n_{A1}^1 \end{bmatrix}. \quad (9.40)$$

For the derivation of the contact element, the projection points of the slave and of the master nodes onto the opposite surface have to be determined by means of the minimal distance algorithm. For the slave node \mathbf{x}_A^1 , the local coordinate on the master segment $\bar{\xi}_A^2$ follows from

$$\left[\sum_{I=1}^{n_{me}} N_I^2(\bar{\xi}_A^2) \mathbf{x}_I^2 - \mathbf{x}_A^1 \right] \cdot \mathbf{t}_A^1 = 0 \quad (9.41)$$

and the projection point on the slave segment $\bar{\xi}_B^1$ of the master node \mathbf{x}_B^2 can be derived by

$$\left[\sum_{I=1}^{n_{se}} N_I^1(\bar{\xi}_B^1) \mathbf{x}_I^1 - \mathbf{x}_B^2 \right] \cdot \sum_{I=1}^{n_{se}} N_I^1(\bar{\xi}_B^1) \mathbf{t}_I^1 = 0. \quad (9.42)$$

9.3.3 Discretization

The displacement, the strain and the stress inside and outside of each material will be discretized equivalently to the previous section, see (9.14). The discretization of the stress and the strain part on the contact boundary corresponds to (9.15). The complete

algebraic system of one contact element consists of

$$\begin{bmatrix} 0 & 0 & 0 & 0 & \tilde{\mathbf{K}}_{u^1\sigma^1} & 0 \\ 0 & 0 & 0 & 0 & \tilde{\mathbf{K}}_{u^2\sigma^1} & \tilde{\mathbf{K}}_{u^2\sigma^2} \\ 0 & 0 & \tilde{\mathbf{K}}_{\epsilon^1\epsilon^1} & 0 & \tilde{\mathbf{K}}_{\epsilon^1\sigma^1} & 0 \\ 0 & 0 & 0 & \tilde{\mathbf{K}}_{\epsilon^2\epsilon^2} & 0 & \tilde{\mathbf{K}}_{\epsilon^2\sigma^2} \\ \tilde{\mathbf{K}}_{\sigma^1u^1} & \tilde{\mathbf{K}}_{\sigma^1u^2} & \tilde{\mathbf{K}}_{\sigma^1\epsilon^1} & 0 & 0 & 0 \\ 0 & \tilde{\mathbf{K}}_{\sigma^2u^2} & 0 & \tilde{\mathbf{K}}_{\sigma^2\epsilon^2} & 0 & 0 \end{bmatrix} \begin{bmatrix} \Delta\tilde{\mathbf{u}}^1 \\ \Delta\tilde{\mathbf{u}}^2 \\ \Delta\tilde{\epsilon}^1 \\ \Delta\tilde{\epsilon}^2 \\ \Delta\tilde{\sigma}^1 \\ \Delta\tilde{\sigma}^2 \end{bmatrix} = - \begin{bmatrix} \tilde{\mathbf{R}}_{u^1} \\ \tilde{\mathbf{R}}_{u^2} \\ \tilde{\mathbf{R}}_{\epsilon^1} \\ \tilde{\mathbf{R}}_{\epsilon^2} \\ \tilde{\mathbf{R}}_{\sigma^1} \\ \tilde{\mathbf{R}}_{\sigma^2} \end{bmatrix}. \quad (9.43)$$

The contributions to the strain residual vector of both materials $\tilde{\mathbf{R}}_{\epsilon^1}$, $\tilde{\mathbf{R}}_{\epsilon^2}$ are unchanged compared to section 9.2 and correspond to (9.22). The weak form of the displacement part is discretized for the slave side as

$$\begin{aligned} \mathbf{R}_{u^1}^+ &= \sum_{g=1}^{n_{gp}^{1+}} \sum_{I=1}^n \mathbf{B}_I \boldsymbol{\sigma}_g^1 \det \mathbf{j}_g W_g - \sum_{p=1}^{n_{gp}^s} \sum_{I=1}^n \sum_{K=1}^{n^s} N_K^s N_I^{K1} \boldsymbol{\sigma}_p^{s1} \hat{\mathbf{n}}_p^1 W_p \\ \mathbf{R}_{u^1}^- &= \sum_{g=1}^{n_{gp}^{1-}} \sum_{I=1}^n \mathbf{B}_I \boldsymbol{\sigma}_g^1 \det \mathbf{j}_g W_g - \sum_{p=1}^{n_{gp}^s} \sum_{I=1}^n \sum_{K=1}^{n^s} N_K^s N_I^{K1} \boldsymbol{\sigma}_p^{s1} \hat{\mathbf{n}}_p^1 W_p \end{aligned} \quad (9.44)$$

and for the master side as

$$\begin{aligned} \mathbf{R}_{u^2}^+ &= \sum_{g=1}^{n_{gp}^{2+}} \sum_{I=1}^n \mathbf{B}_I \boldsymbol{\sigma}_g^2 \det \mathbf{j}_g W_g + \sum_{p=1}^{n_{gp}^s} \sum_{I=1}^n \sum_{K=1}^{n^s} N_K^s N_I^{K2} \boldsymbol{\sigma}_p^{s1} \hat{\mathbf{n}}_p^1 W_p \\ \mathbf{R}_{u^2}^- &= \sum_{g=1}^{n_{gp}^{2-}} \sum_{I=1}^n \mathbf{B}_I \boldsymbol{\sigma}_g^2 \det \mathbf{j}_g W_g + \sum_{p=1}^{n_{gp}^s} \sum_{I=1}^n \sum_{K=1}^{n^s} N_K^s N_I^{K2} [\boldsymbol{\sigma}_p^{s1} \hat{\mathbf{n}}_p^1 - \boldsymbol{\sigma}_p^{s2} \hat{\mathbf{n}}_p^2] W_p. \end{aligned} \quad (9.45)$$

The residual vector enforcing the geometrical equations can now be subdivided into a part for the slave stress

$$\begin{aligned} \mathbf{R}_{\sigma^1}^+ &= \sum_{g=1}^{n_{gp}^{1+}} \sum_{I=1}^n N_I (\text{grad}^s \mathbf{u}_g^1 - \boldsymbol{\epsilon}_g^1) \det \mathbf{j}_g W_g - \sum_{p=1}^{n_{gp}^s} \sum_{I=1}^n \sum_{K=1}^{n^s} N_K^s \mathbf{B}_{n^1 I}^{KT} (\mathbf{x}_p^1 - \mathbf{x}_p^2) W_p \\ \mathbf{R}_{\sigma^1}^- &= \sum_{g=1}^{n_{gp}^{1-}} \sum_{I=1}^n N_I (\text{grad}^s \mathbf{u}_g^1 - \boldsymbol{\epsilon}_g^1) \det \mathbf{j}_g W_g - \sum_{p=1}^{n_{gp}^s} \sum_{I=1}^n \sum_{K=1}^{n^s} N_K^s \mathbf{B}_{n^1 I}^{KT} (\mathbf{u}_p^1 - \mathbf{u}_p^2) W_p \end{aligned} \quad (9.46)$$

and a part regarding the master stress

$$\begin{aligned} \mathbf{R}_{\sigma^2}^+ &= \sum_{g=1}^{n_{gp}^{2+}} \sum_{I=1}^n N_I (\text{grad}^s \mathbf{u}_g^1 - \boldsymbol{\epsilon}_g^1) \det \mathbf{j}_g W_g \\ \mathbf{R}_{\sigma^2}^- &= \sum_{g=1}^{n_{gp}^{2-}} \sum_{I=1}^n N_I (\text{grad}^s \mathbf{u}_g^1 - \boldsymbol{\epsilon}_g^1) \det \mathbf{j}_g W_g - \sum_{p=1}^{n_{gp}^s} \sum_{I=1}^n \sum_{K=1}^{n^s} N_K^s \mathbf{B}_{n^2 I}^{KT} (\mathbf{u}_p^2 - \bar{\mathbf{u}}_{0p}) W_p. \end{aligned} \quad (9.47)$$

The strain tangent matrices $\tilde{\mathbf{K}}_{\epsilon^1\epsilon^1}$, $\tilde{\mathbf{K}}_{\epsilon^2\epsilon^2}$ and $\tilde{\mathbf{K}}_{\sigma^1\epsilon^1}$, $\tilde{\mathbf{K}}_{\sigma^2\epsilon^2}$ correspond to (9.25) and (9.26). The coupling part of the displacement to the stress can also be decomposed into a contribution of the positive and of the negative side of the slave element

$$\begin{aligned} \mathbf{K}_{u^1\sigma^1}^+ &= \sum_{g=1}^{n_{gp}^{1+}} \sum_{I=1}^n \sum_{J=1}^n \mathbf{B}_I^T N_J \det \mathbf{j}_g W_g - \sum_{p=1}^{n_{gp}^s} \sum_{I=1}^n \sum_{J=1}^n \sum_{K=1}^{n^s} \sum_{L=1}^{n^s} N_K^s N_I^{K1} N_L^s \mathbf{B}_{n^1J}^L W_p \\ \mathbf{K}_{u^1\sigma^1}^- &= \sum_{g=1}^{n_{gp}^{1-}} \sum_{I=1}^n \sum_{J=1}^n \mathbf{B}_I^T N_J \det \mathbf{j}_g W_g - \sum_{p=1}^{n_{gp}^s} \sum_{I=1}^n \sum_{J=1}^n \sum_{K=1}^{n^s} \sum_{L=1}^{n^s} N_K^s N_I^{K1} N_L^s \mathbf{B}_{n^1J}^L W_p. \end{aligned} \quad (9.48)$$

The contributions of the positive and the negative side of the master element are given as

$$\begin{aligned} \mathbf{K}_{u^2\sigma^2}^+ &= \sum_{g=1}^{n_{gp}^{2+}} \sum_{I=1}^n \sum_{J=1}^n \mathbf{B}_I^T N_J \det \mathbf{j}_g W_g \\ \mathbf{K}_{u^2\sigma^2}^- &= \sum_{g=1}^{n_{gp}^{2-}} \sum_{I=1}^n \sum_{J=1}^n \mathbf{B}_I^T N_J \det \mathbf{j}_g W_g - \sum_{p=1}^{n_{gp}^s} \sum_{I=1}^n \sum_{J=1}^n \sum_{K=1}^{n^s} \sum_{L=1}^{n^s} N_K^s N_I^{K2} N_L^s \mathbf{B}_{n^2J}^L W_p \end{aligned} \quad (9.49)$$

and the part of the coupled contact contributions reads

$$\begin{aligned} \mathbf{K}_{u^2\sigma^1}^+ &= - \sum_{p=1}^{n_{gp}^s} \sum_{I=1}^n \sum_{J=1}^n \sum_{K=1}^{n^s} \sum_{L=1}^{n^s} N_K^s N_I^{K2} N_L^s \mathbf{B}_{n^1J}^L W_p \\ \mathbf{K}_{u^2\sigma^1}^- &= - \sum_{p=1}^{n_{gp}^s} \sum_{I=1}^n \sum_{J=1}^n \sum_{K=1}^{n^s} \sum_{L=1}^{n^s} N_K^s N_I^{K2} N_L^s \mathbf{B}_{n^1J}^L W_p. \end{aligned} \quad (9.50)$$

Since the formulation is derived from a potential, the tangent is symmetric and all the missing matrix contributions are exactly the transpose of the corresponding matrices.

9.3.4 Solution algorithm

Analogous to the imposition of Dirichlet boundary conditions, the tangent size can be reduced. Eliminating the strain contributions of both materials in (9.43)

$$\begin{bmatrix} \Delta \tilde{\epsilon}^1 \\ \Delta \tilde{\epsilon}^2 \end{bmatrix} = - \begin{bmatrix} \tilde{\mathbf{K}}_{\epsilon^1\epsilon^1}^{-1} & \mathbf{0} \\ \mathbf{0} & \tilde{\mathbf{K}}_{\epsilon^2\epsilon^2}^{-1} \end{bmatrix} \left\{ \begin{bmatrix} \tilde{\mathbf{R}}_{\epsilon^1} \\ \tilde{\mathbf{R}}_{\epsilon^2} \end{bmatrix} + \begin{bmatrix} \tilde{\mathbf{K}}_{\epsilon^1\sigma^1} & \mathbf{0} \\ \mathbf{0} & \tilde{\mathbf{K}}_{\epsilon^2\sigma^2} \end{bmatrix} \begin{bmatrix} \Delta \tilde{\sigma}^1 \\ \Delta \tilde{\sigma}^2 \end{bmatrix} \right\}, \quad (9.51)$$

the set of equations can be rewritten

$$\begin{bmatrix} \mathbf{0} & \mathbf{0} & \tilde{\mathbf{K}}_{u^1\sigma^1} & \mathbf{0} \\ \mathbf{0} & \mathbf{0} & \tilde{\mathbf{K}}_{u^2\sigma^1} & \tilde{\mathbf{K}}_{u^2\sigma^2} \\ \tilde{\mathbf{K}}_{\sigma^1u^1} & \tilde{\mathbf{K}}_{\sigma^1u^2} & -\tilde{\mathbf{K}}_{\sigma^1\sigma^1} & \mathbf{0} \\ \mathbf{0} & \tilde{\mathbf{K}}_{\sigma^2u^2} & \mathbf{0} & -\tilde{\mathbf{K}}_{\sigma^2\sigma^2} \end{bmatrix} \begin{bmatrix} \Delta \tilde{\mathbf{u}}^1 \\ \Delta \tilde{\mathbf{u}}^2 \\ \Delta \tilde{\sigma}^1 \\ \Delta \tilde{\sigma}^2 \end{bmatrix} = - \begin{bmatrix} \tilde{\mathbf{R}}_{u^1} \\ \tilde{\mathbf{R}}_{u^2} \\ \tilde{\mathbf{R}}_{\sigma^1} \\ \tilde{\mathbf{R}}_{\sigma^2} \end{bmatrix} \quad (9.52)$$

together with the tangent contributions

$$\begin{bmatrix} \bar{\mathbf{K}}_{\sigma^1 \sigma^1}^{-1} \\ \bar{\mathbf{K}}_{\sigma^2 \sigma^2}^{-1} \end{bmatrix} = \begin{bmatrix} \tilde{\mathbf{K}}_{\sigma^1 \epsilon^1} \tilde{\mathbf{K}}_{\epsilon^1 \epsilon^1}^{-1} \tilde{\mathbf{K}}_{\epsilon^1 \sigma^1} \\ \tilde{\mathbf{K}}_{\sigma^2 \epsilon^2} \tilde{\mathbf{K}}_{\epsilon^2 \epsilon^2}^{-1} \tilde{\mathbf{K}}_{\epsilon^2 \sigma^2} \end{bmatrix}, \quad \begin{bmatrix} \bar{\mathbf{R}}_{\sigma^1} \\ \bar{\mathbf{R}}_{\sigma^2} \end{bmatrix} = \begin{bmatrix} \tilde{\mathbf{R}}_{\sigma^1} - \tilde{\mathbf{K}}_{\sigma^1 \epsilon^1} \tilde{\mathbf{K}}_{\epsilon^1 \epsilon^1}^{-1} \tilde{\mathbf{R}}_{\epsilon^1} \\ \tilde{\mathbf{R}}_{\sigma^2} - \tilde{\mathbf{K}}_{\sigma^2 \epsilon^2} \tilde{\mathbf{K}}_{\epsilon^2 \epsilon^2}^{-1} \tilde{\mathbf{R}}_{\epsilon^2} \end{bmatrix}. \quad (9.53)$$

In case of a node to node contact formulation, the stress can also be condensed from the tangent

$$\begin{bmatrix} \Delta \tilde{\boldsymbol{\sigma}}^1 \\ \Delta \tilde{\boldsymbol{\sigma}}^2 \end{bmatrix} = \begin{bmatrix} \bar{\mathbf{K}}_{\sigma^1 \sigma^1}^{-1} \left(\bar{\mathbf{R}}_{\sigma^1} + \tilde{\mathbf{K}}_{\sigma^1 u^1} \Delta \tilde{\mathbf{u}}^1 + \tilde{\mathbf{K}}_{\sigma^1 u^2} \Delta \tilde{\mathbf{u}}^2 \right) \\ \bar{\mathbf{K}}_{\sigma^1 \sigma^1}^{-1} \left(\bar{\mathbf{R}}_{\sigma^2} + \tilde{\mathbf{K}}_{\sigma^2 u^2} \Delta \tilde{\mathbf{u}}^2 \right) \end{bmatrix} \quad (9.54)$$

leading to the final set of equations of the contact element

$$\begin{bmatrix} \tilde{\mathbf{K}}_{u^1 \sigma^1} \bar{\mathbf{K}}_{\sigma^1 \sigma^1}^{-1} \tilde{\mathbf{K}}_{\sigma^1 u^1} & \tilde{\mathbf{K}}_{u^1 \sigma^1} \bar{\mathbf{K}}_{\sigma^1 \sigma^1}^{-1} \tilde{\mathbf{K}}_{\sigma^1 u^2} \\ \tilde{\mathbf{K}}_{u^2 \sigma^1} \bar{\mathbf{K}}_{\sigma^1 \sigma^1}^{-1} \tilde{\mathbf{K}}_{\sigma^1 u^1} & \tilde{\mathbf{K}}_{u^2 \sigma^1} \bar{\mathbf{K}}_{\sigma^1 \sigma^1}^{-1} \tilde{\mathbf{K}}_{\sigma^1 u^2} \\ & + \tilde{\mathbf{K}}_{u^2 \sigma^2} \bar{\mathbf{K}}_{\sigma^2 \sigma^2}^{-1} \tilde{\mathbf{K}}_{\sigma^2 u^2} \end{bmatrix} \begin{bmatrix} \Delta \tilde{\mathbf{u}}^1 \\ \Delta \tilde{\mathbf{u}}^2 \end{bmatrix} = - \begin{bmatrix} \tilde{\mathbf{R}}_{u^1} + \tilde{\mathbf{K}}_{u^1 \sigma^1} \bar{\mathbf{K}}_{\sigma^1 \sigma^1}^{-1} \bar{\mathbf{R}}_{\sigma^1} \\ \tilde{\mathbf{R}}_{u^2} + \tilde{\mathbf{K}}_{u^2 \sigma^1} \bar{\mathbf{K}}_{\sigma^1 \sigma^1}^{-1} \bar{\mathbf{R}}_{\sigma^1} \\ \quad + \tilde{\mathbf{K}}_{u^2 \sigma^2} \bar{\mathbf{K}}_{\sigma^2 \sigma^2}^{-1} \bar{\mathbf{R}}_{\sigma^2} \end{bmatrix}. \quad (9.55)$$

9.4 Numerical examples

Two examples show the displacement distribution inside a body where the Dirichlet and the contact boundary conditions are imposed inside the element. All dimensions and all material parameters are thereby given in fundamental units.

In the first case, an elastic block ($E = 3 \cdot 10^{10}$, $\nu = 0.2$) is loaded with a prescribed vertical displacement on top ($w = 0.01$) and fixed at the bottom side (figure 9.4). The mesh does not fit to the geometry of the block leading to interfaces inside the

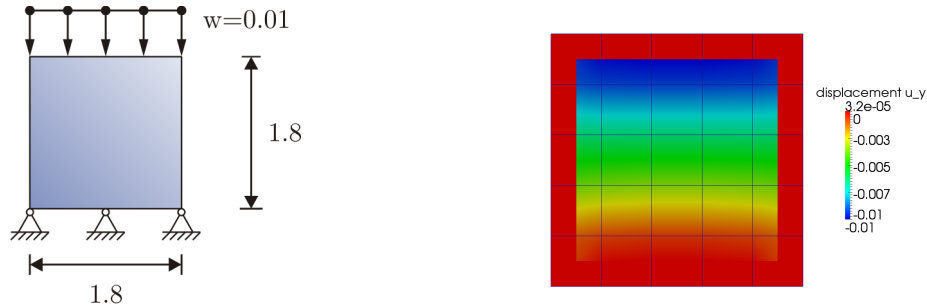


Figure 9.4: Geometry and boundary conditions of the boundary test case (left) and vertical displacements inside and outside of the material (right)

element where the boundary conditions have to be fulfilled. Additionally, the corners of the block are located inside of the element which renders the subdivision of the element into a material and non material part more difficult. A comparison of the vertical displacements computed with the XFEM and with the standard FEM shows no differences (figure 9.5) and the constraint of zero displacements outside of the material is also fulfilled (figure 9.4).

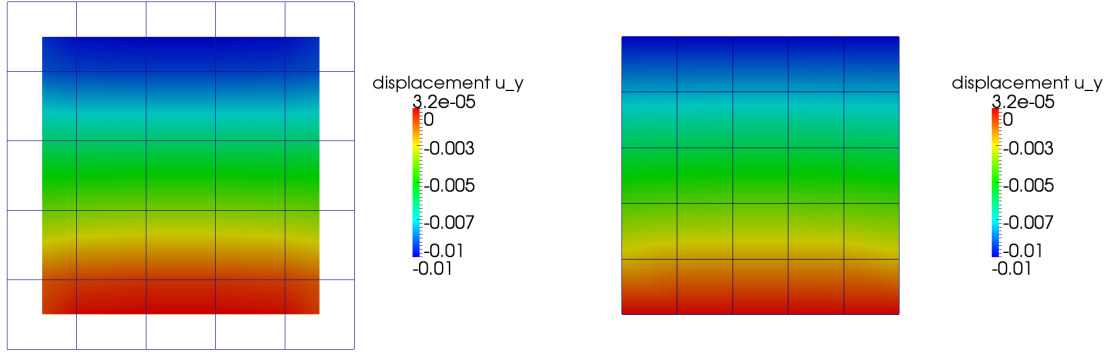


Figure 9.5: Comparison of the vertical displacements between the XFEM element with embedded boundaries (left) and the standard FEM solution (right)

In the second example, two elastic blocks with the same dimensions and the same material parameters ($E = 3 \cdot 10^{10}$, $\nu = 0.2$) as in the first example are pressed together with a prescribed vertical displacement on top ($w = 0.01$) and fixed at the bottom side (figure 9.6). A comparison of the vertical displacements shows a smooth transition

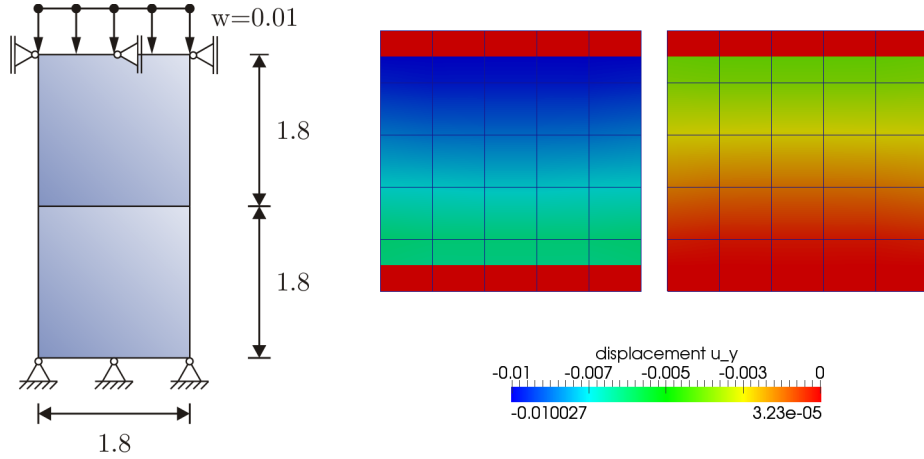


Figure 9.6: Geometry and boundary conditions of the contact test case (left) and vertical displacements inside and outside of the contacting bodies (right)

between both bodies in the case of the XFEM contact element, but a small jump across the contact interface occurs (figure 9.7) compared to the standard node to segment solution where the constraints are enforced using Lagrange multipliers (figure 9.7). Hence the method using the Hu-Washizu formulation to enforce the contact constraints behaves more like the classical penalty formulation where now due to the three-field functional no additional stabilization term is needed. As for the former example, the constraint of zero displacements outside of both bodies is also fulfilled (figure 9.6).

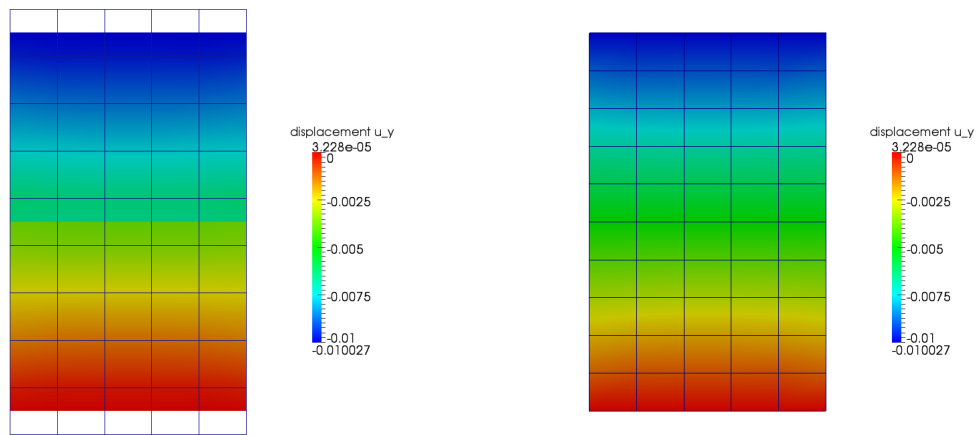


Figure 9.7: Comparison of the vertical displacements of the XFEM contact element with embedded boundaries (left) and the standard FEM solution of a node to surface contact element with Lagrange multipliers (right)

Chapter 10

Conclusion and Outlook

Within this work novel concepts of including three-dimensional plasticity models into a contact algorithm are developed based on a projection and on an extension strategy. The first one projects the plasticity models onto the contact surface and the second one extends the contact formulation towards the third direction which enables the contact algorithm to include the three-dimensional plasticity models directly.

In order to achieve this projection or extension method to be allowed, it is shown that a link between the continuum description and the contact formulation exists. Therefore the solid-shell concept is used to reformulate the three-dimensional strain in terms of an upper and a lower surface. Afterwards, the strain is integrated over the height and then the limit of the height towards zero is applied yielding the standard contact kinematics.

The numerical implementation of the projected friction laws is based on the Mortar method. Beside the standard penalty regularization and the augmented Lagrangian method, a new mixed version and for the first time a pure Lagrange multiplier method is also implemented into the Mortar code. Comparing all four methods on a typical ironing test with large deformations, the augmented Lagrangian method shows the best numerical behavior. The Lagrange multiplier version tends to oscillate and the penalty version takes a long computation time due to the intrinsic loop over all integration points of each contact node. The mixed version which is based on the averaged normal penetration needs smaller time steps to converge during the normal loading. Since in the theory the mixed version and the augmented Lagrangian method are only different in formulating the tangential stress, the discrepancy in the robustness can only be explained in the different kinematical discretization. Hence the mixed version can be improved, if for the normal penetration $\mathbf{g}_A \cdot \mathbf{n}_A$ is used instead of g_{nA} and for the tangential movement $\mathbf{g}_A \cdot \mathbf{t}_{\alpha A} - \mathbf{g}_A^o \cdot \mathbf{t}_{\alpha A}$ is applied instead of $g_{t\alpha A} - g_{t\alpha A}^o$. Dual shape functions show no improvement regarding the computation time in the considered examples, so that in conclusion with regard to the robustness, the computation time and the effort on implementation, the Mortar method regularized with the augmented Lagrangian or the mixed method and based on standard shape functions and on the averaged gap \mathbf{g}_A should be used in contact algorithms.

To evaluate the projected friction laws, the Ehlers soil model is implemented into FEAP. This model is based on the linear elasto-plastic concept where a special stress-

strain relation is used covering the porous structure of the soil. To capture the almost plastic behavior of the soil during loading, the concept of a parameter hardening is applied. The Ehlers soil model has 4 roots on the hydrostatic axis where the domain between the two inner roots determines the yield surface. The solution between the inner and the outer roots is complex and outside, it goes to infinity. The yield surface is also nonlinear with respect to the stress invariants and has a cap structure at both ends. All together, this makes it computationally difficult for the closest point algorithm to find a unique solution on the yield surface especially for the back projection to the rounded apex. Even a substepping algorithm which ensures that the trial yield surface remains close to the actual yield surface does not guarantee a unique solution. Also a viscoplastic regularization is needed to avoid oscillations of the active set introducing a viscosity into the soil model although the soil does not behave viscous.

For the projection strategy, two different concepts were developed. The first one integrates the soil model into the coefficient of friction, as a result, based on the link between the three-dimensional strain and the contact kinematics, the standard subroutine of the continuum soil model can be applied, and together with the resulting stress, the coefficient of friction can be determined. The second concept projects the yield criterion directly onto the contact surface where two reformulations have to be taken into account. Since the Lode angle is approximately zero for contact cases, the three stress invariants of the soil model reduce to two which can then be linked to the normal and to the tangential contact stress components. On the other hand, since an evolution equation for the normal penetration is not allowed, a new stress component is introduced into the contact formulation covering the dilatancy or contractancy effects of the three-dimensional flow rule. A comparison between the triaxial and the direct shear test shows that the projection onto the contact surface was successful for both variants, since all cases have almost the same outcome. Only the first concept of integrating the soil characteristics into the coefficient of friction is more robust, since the back projection onto the slip surface fails for very large normal forces at the second concept.

Neglecting the limit in the link between the three-dimensional strain measure and the contact kinematics a 3D contact element can be stated where the incremental update of the integration points has to be taken into account. Now it is possible to call the desired soil model routine directly to compute the stress state of each active contact node. To speed up the computation time, the weak form of the balance equations is based on the Hellinger-Reissner principle avoiding extra loops at each integration point in the Mortar framework. The numerical results show that the soil characteristics can be represented successfully with the 3D contact element where now a varying height is also allowed which shows the influence of the dilatancy effect at the contact zone. A very robust soil model is needed for this concept, since extreme loadings have to be endured by the system.

For the projection and the extension strategy, a realistic comparison with experimental results is missing which is needed to validate the developed concepts.

For simulations of the material separation within a hammered pile installation process with finite elements, a new strategy, for example the eXtended Finite Element

Method (XFEM), has to be applied. To integrate the contact constraints into this method, a new contact formulation based on the Hu-Washizu principle is developed. Evaluated at a simple example, it shows a smooth transition behavior between the contacting bodies and it needs no extra stabilization scheme. On the other hand, the determination of the correct integration domain inside cut elements can be very complex and the effort can also be enormous especially for contact cases which renders this method unattractive for such kind of simulations.

To conclude this work, it has to be mentioned that models which are based on the active set strategy like contact or elasto-plastic material models are not very convenient from the computational point of view, since a jump is introduced into the solution algorithm which cannot be treated properly. If a point is close to the transition zone between active and inactive or stick and slip for contact cases or between elastic and plastic for material models, the system has a tendency to oscillate or the solution algorithm fails. Therefore a robust contact algorithm which is able to handle large loadsteps, if no discontinuities have to be considered, and plasticity models without any back projection algorithm are still important goals within the research field of computational mechanics.

Appendix A

Principle stresses

The three-dimensional principle stresses are the solutions of the characteristic equation

$$\sigma^3 - \text{I}_{\sigma}\sigma^2 + \text{II}_{\sigma}\sigma - \text{III}_{\sigma} = 0 \quad (\text{A.1})$$

in terms of the three invariants of the actual stress state σ

$$\text{I}_{\sigma} = \text{tr } \sigma, \quad \text{II}_{\sigma} = \frac{1}{2} [(\text{tr } \sigma)^2 - \text{tr } \sigma^2], \quad \text{III}_{\sigma} = \det \sigma. \quad (\text{A.2})$$

Exploiting the connection between the invariants of the stress and its deviator

$$\text{II}_s = - \left(\text{II}_{\sigma} - \frac{1}{3} \text{I}_{\sigma}^2 \right), \quad \text{III}_s = \frac{2}{27} \text{I}_{\sigma}^3 - \frac{1}{3} \text{I}_{\sigma} \text{II}_{\sigma}^2 + \text{III}_{\sigma}, \quad (\text{A.3})$$

the characteristic equation can be rewritten using the substitution $\sigma = \bar{\sigma} + \frac{1}{3} \text{I}_{\sigma}$

$$\bar{\sigma}^3 - \text{II}_s \bar{\sigma} - \text{III}_s = 0. \quad (\text{A.4})$$

Since the discriminant is always negative

$$D = \left(\frac{\text{III}_s}{2} \right)^2 - \left(\frac{\text{II}_s}{2} \right)^3 < 0, \quad (\text{A.5})$$

three real solutions exist

$$\begin{aligned} \sigma_1 &= \frac{2\sqrt{\text{II}_s}}{\sqrt{3}} \cos(\Theta) + \frac{1}{3} \text{I}_{\sigma}, \quad \sigma_2 = \frac{2\sqrt{\text{II}_s}}{\sqrt{3}} \cos\left(\Theta - \frac{2\pi}{3}\right) + \frac{1}{3} \text{I}_{\sigma} \\ \sigma_3 &= \frac{2\sqrt{\text{II}_s}}{\sqrt{3}} \cos\left(\Theta + \frac{2\pi}{3}\right) + \frac{1}{3} \text{I}_{\sigma}, \quad \Theta = \frac{1}{3} \arccos\left(\frac{\sqrt{27}}{2} \text{III}_s \text{II}_s^{-\frac{3}{2}}\right). \end{aligned} \quad (\text{A.6})$$

Using some trigonometric relations (Abramovitz and Stegun [1972])

$$\begin{aligned} \sin(x) &= \cos\left(\frac{\pi}{2} - x\right), \quad \arcsin x = \arccos \sqrt{1 - x^2} \\ \cos(x - y) &= \cos(x) \cos(y) + \sin(x) \sin(y), \end{aligned} \quad (\text{A.7})$$

the principle stresses can be rewritten in terms of the sinus instead of the cosinus in (A.6)

$$\begin{aligned}\sigma_1 &= \frac{2\sqrt{\Pi_s}}{\sqrt{3}}\sin\left(\Theta + \frac{2\pi}{3}\right) + \frac{1}{3}I_\sigma, & \sigma_2 &= \frac{2\sqrt{\Pi_s}}{\sqrt{3}}\sin(\Theta) + \frac{1}{3}I_\sigma \\ \sigma_3 &= \frac{2\sqrt{\Pi_s}}{\sqrt{3}}\sin\left(\Theta - \frac{2\pi}{3}\right) + \frac{1}{3}I_\sigma, & \Theta &= -\frac{1}{3}\arcsin\left(\frac{\sqrt{27}}{2}III_sII_s^{-\frac{3}{2}}\right).\end{aligned}\tag{A.8}$$

Appendix B

Voigt notation

Within the Voigt notation, the symmetry of the stress and the strain tensor is used to formulate the tensors as vector or matrix quantities which saves time within a solution process. The stress-strain relation simplifies then to

$$\sigma_{ij} = \mathbf{C}_{ijkl} \epsilon_{kl} \quad \rightarrow \quad \sigma_i = \mathbf{D}_{ij} \epsilon_j$$

where the specific quantities are defined as

$$\sigma_i = \begin{bmatrix} \sigma_{11} \\ \sigma_{22} \\ \sigma_{33} \\ \sigma_{12} \\ \sigma_{23} \\ \sigma_{13} \end{bmatrix}, \quad \epsilon_j = \begin{bmatrix} \epsilon_{11} \\ \epsilon_{22} \\ \epsilon_{33} \\ 2\epsilon_{12} \\ 2\epsilon_{23} \\ 2\epsilon_{13} \end{bmatrix}, \quad \mathbf{D}_{ij} = \begin{bmatrix} \mathbf{C}_{1111} & \mathbf{C}_{1122} & \mathbf{C}_{1133} & \mathbf{C}_{1112} & \mathbf{C}_{1123} & \mathbf{C}_{1113} \\ \mathbf{C}_{2211} & \mathbf{C}_{2222} & \mathbf{C}_{2233} & \mathbf{C}_{2212} & \mathbf{C}_{2223} & \mathbf{C}_{2213} \\ \mathbf{C}_{3311} & \mathbf{C}_{3322} & \mathbf{C}_{3333} & \mathbf{C}_{3312} & \mathbf{C}_{3323} & \mathbf{C}_{3313} \\ \mathbf{C}_{1211} & \mathbf{C}_{1222} & \mathbf{C}_{1233} & \mathbf{C}_{1212} & \mathbf{C}_{1223} & \mathbf{C}_{1213} \\ \mathbf{C}_{2311} & \mathbf{C}_{2322} & \mathbf{C}_{2333} & \mathbf{C}_{2312} & \mathbf{C}_{2323} & \mathbf{C}_{2313} \\ \mathbf{C}_{1311} & \mathbf{C}_{1322} & \mathbf{C}_{1333} & \mathbf{C}_{1312} & \mathbf{C}_{1323} & \mathbf{C}_{1313} \end{bmatrix}.$$

B.1 B matrices

Due to the Voigt notation, the discretization of the strain tensor as well as of its virtual counterpart can be written in terms of the B matrices for the 3D case

$$\mathbf{B}_I = \begin{bmatrix} N_{I,1} & 0 & 0 \\ 0 & N_{I,2} & 0 \\ 0 & 0 & N_{I,3} \\ N_{I,2} & N_{I,1} & 0 \\ 0 & N_{I,3} & N_{I,2} \\ N_{I,3} & 0 & N_{I,1} \end{bmatrix}, \quad \mathbf{B}_{vI} = \begin{bmatrix} N_{I,1} \\ N_{I,2} \\ N_{I,3} \end{bmatrix} \quad (\text{B.1})$$

as well as for the 2D case

$$\mathbf{B}_I = \begin{bmatrix} N_{I,1} & 0 \\ 0 & N_{I,2} \\ N_{I,2} & N_{I,1} \end{bmatrix}, \quad \mathbf{B}_{nI} = \begin{bmatrix} N_I \hat{\mathbf{n}}_1 & 0 \\ 0 & N_I \hat{\mathbf{n}}_2 \\ N_I \hat{\mathbf{n}}_2 & N_I \hat{\mathbf{n}}_1 \end{bmatrix} \quad (\text{B.2})$$

where the latter ones are needed in chapter 9.

B.2 Elastic strain tensor

The linear elastic material tensor in Voigt notation is presented here in form of the Young's modulus E and the Poisson ratio ν

$$\mathbf{D}^e = \frac{E}{1+\nu} \begin{bmatrix} \frac{1-\nu}{1-2\nu} & \frac{\nu}{1-2\nu} & \frac{\nu}{1-2\nu} & 0 & 0 & 0 \\ \frac{\nu}{1-2\nu} & \frac{1-\nu}{1-2\nu} & \frac{\nu}{1-2\nu} & 0 & 0 & 0 \\ \frac{\nu}{1-2\nu} & \frac{\nu}{1-2\nu} & \frac{1-\nu}{1-2\nu} & 0 & 0 & 0 \\ 0 & 0 & 0 & \frac{1}{2} & 0 & 0 \\ 0 & 0 & 0 & 0 & \frac{1}{2} & 0 \\ 0 & 0 & 0 & 0 & 0 & \frac{1}{2} \end{bmatrix}, \quad (\text{B.3})$$

but it can also be linked to different elastic constants, like the Lamé parameters λ and μ or the bulk modulus K . The relationship between all constants is summarized in table B.1

	λ, μ	K, μ	μ, ν	E, ν	E, μ
λ	λ	$K - \frac{2}{3}\mu$	$\frac{2\mu\nu}{1-2\nu}$	$\frac{E\nu}{(1+\nu)(1-2\nu)}$	$\frac{\mu(E-2\mu)}{3\mu-E}$
μ	μ	μ	μ	$\frac{E}{2(1+\nu)}$	μ
K	$\lambda + \frac{2}{3}\mu$	K	$\frac{2\mu(1+\nu)}{3(1-2\nu)}$	$\frac{E}{3(1-2\nu)}$	$\frac{E\mu}{3(3\mu-E)}$
E	$\frac{\mu(3\lambda+2\mu)}{\lambda+\mu}$	$\frac{9K\mu}{3K+\mu}$	$2(1+\nu)\mu$	E	E
ν	$\frac{\lambda}{2(\lambda+\mu)}$	$\frac{3K-2\mu}{6K+2\mu}$	ν	ν	$\frac{E-2\mu}{2\mu}$

Table B.1: Relationship between different elastic material parameters

B.3 Invariants and its derivations

For a symmetric stress tensor its invariants can be specified as

$$\text{I}_\sigma = \sigma_{11} + \sigma_{22} + \sigma_{33}, \quad \text{II}_s = \frac{1}{2} (s_{11}^2 + s_{22}^2 + s_{33}^2) + s_{12}^2 + s_{23}^2 + s_{13}^2, \quad (\text{B.4})$$

$$\text{III}_s = s_{11}s_{22}s_{33} + 2s_{12}s_{23}s_{13} - s_{11}s_{23}^2 - s_{22}s_{13}^2 - s_{33}s_{12}^2$$

and hence the first derivative with respect to the stress can be written in vector form

$$\begin{aligned} \partial_\sigma \text{I}_\sigma &= [1 \ 1 \ 1 \ 0 \ 0 \ 0]^T, \\ \partial_\sigma \text{II}_s &= [s_{11} \ s_{22} \ s_{33} \ 2s_{12} \ 2s_{23} \ 2s_{13}]^T, \\ \partial_\sigma \text{III}_s &= \begin{bmatrix} \frac{2}{3}s_{22}s_{33} - \frac{1}{3}s_{11}s_{33} - \frac{1}{3}s_{11}s_{22} - \frac{2}{3}s_{23}^2 + \frac{1}{3}s_{13}^2 + \frac{1}{3}s_{12}^2 \\ \frac{2}{3}s_{11}s_{33} - \frac{1}{3}s_{22}s_{33} - \frac{1}{3}s_{11}s_{22} - \frac{2}{3}s_{13}^2 + \frac{1}{3}s_{23}^2 + \frac{1}{3}s_{12}^2 \\ \frac{2}{3}s_{11}s_{22} - \frac{1}{3}s_{11}s_{33} - \frac{1}{3}s_{22}s_{33} - \frac{2}{3}s_{12}^2 + \frac{1}{3}s_{23}^2 + \frac{1}{3}s_{13}^2 \\ 2s_{23}s_{13} - 2s_{33}s_{12} \\ 2s_{12}s_{13} - 2s_{11}s_{23} \\ 2s_{12}s_{23} - 2s_{22}s_{13} \end{bmatrix}. \end{aligned} \quad (\text{B.5})$$

The second derivative of the second invariant of the deviatoric stress tensor simplifies also to the matrix

$$\partial_{\sigma\sigma}^2 \Pi_s = \begin{bmatrix} 2/3 & -1/3 & -1/3 & 0 & 0 & 0 \\ -1/3 & 2/3 & -1/3 & 0 & 0 & 0 \\ -1/3 & -1/3 & 2/3 & 0 & 0 & 0 \\ 0 & 0 & 0 & 2 & 0 & 0 \\ 0 & 0 & 0 & 0 & 2 & 0 \\ 0 & 0 & 0 & 0 & 0 & 2 \end{bmatrix}. \quad (\text{B.6})$$

B.4 Shell transformation tensor

Also the transformation tensor of the solid shell concept simplifies in the case of a symmetric stress-strain relation to

$$\mathbf{T}^e = \begin{bmatrix} t_{33}t_{33} & t_{31}t_{33} & t_{32}t_{33} & t_{31}t_{31} & t_{32}t_{32} & t_{31}t_{32} \\ 2t_{13}t_{33} & t_{11}t_{33} + t_{13}t_{31} & t_{12}t_{33} + t_{13}t_{32} & 2t_{11}t_{31} & 2t_{12}t_{32} & t_{11}t_{32} + t_{12}t_{31} \\ 2t_{23}t_{33} & t_{21}t_{33} + t_{23}t_{31} & t_{22}t_{33} + t_{23}t_{32} & 2t_{21}t_{31} & 2t_{22}t_{32} & t_{21}t_{32} + t_{22}t_{31} \\ t_{13}t_{13} & t_{11}t_{13} & t_{12}t_{13} & t_{11}t_{11} & t_{12}t_{12} & t_{11}t_{12} \\ t_{23}t_{23} & t_{21}t_{23} & t_{22}t_{23} & t_{21}t_{21} & t_{22}t_{22} & t_{21}t_{22} \\ 2t_{13}t_{23} & t_{11}t_{23} + t_{13}t_{21} & t_{12}t_{23} + t_{13}t_{22} & 2t_{11}t_{21} & 2t_{12}t_{22} & t_{11}t_{22} + t_{12}t_{21} \end{bmatrix} \quad (\text{B.7})$$

where the components are given as

$$\begin{aligned} t_{11} &= \mathbf{e}_1 \cdot \mathbf{g}^1, & t_{12} &= \mathbf{e}_1 \cdot \mathbf{g}^2, & t_{13} &= \mathbf{e}_1 \cdot \mathbf{g}^3 \\ t_{21} &= \mathbf{e}_2 \cdot \mathbf{g}^1, & t_{22} &= \mathbf{e}_2 \cdot \mathbf{g}^2, & t_{23} &= \mathbf{e}_2 \cdot \mathbf{g}^3 \\ t_{31} &= \mathbf{e}_3 \cdot \mathbf{g}^1, & t_{32} &= \mathbf{e}_3 \cdot \mathbf{g}^2, & t_{33} &= \mathbf{e}_3 \cdot \mathbf{g}^3. \end{aligned} \quad (\text{B.8})$$

The transformation tensor in Voigt notation can also be found in Klinkel et al. [1999].

Appendix C

Contact vectors and storage arrays

In this section, all the vectors for the node to surface and all the matrices for the Mortar method which are not mentioned in the main part are listed. And also the additional storage arrays which have to be introduced in the case of the Mortar method are summarized briefly.

C.1 Node to surface vectors

In the case of the node to surface formulation, for the normal part three vectors are needed at each slave node s

$$\mathbf{N}_s = \begin{pmatrix} \bar{\mathbf{n}}^2 \\ -N_1 \bar{\mathbf{n}}^2 \\ -N_2 \bar{\mathbf{n}}^2 \\ -N_3 \bar{\mathbf{n}}^2 \\ -N_4 \bar{\mathbf{n}}^2 \end{pmatrix}, \mathbf{N}_\alpha = \begin{pmatrix} \mathbf{0} \\ -N_{1,\alpha} \bar{\mathbf{n}}^2 \\ -N_{2,\alpha} \bar{\mathbf{n}}^2 \\ -N_{3,\alpha} \bar{\mathbf{n}}^2 \\ -N_{4,\alpha} \bar{\mathbf{n}}^2 \end{pmatrix}, \mathbf{T}_\alpha = \begin{pmatrix} \bar{\mathbf{a}}_\alpha^2 \\ -N_1 \bar{\mathbf{a}}_\alpha^2 \\ -N_2 \bar{\mathbf{a}}_\alpha^2 \\ -N_3 \bar{\mathbf{a}}_\alpha^2 \\ -N_4 \bar{\mathbf{a}}_\alpha^2 \end{pmatrix} \quad (\text{C.1})$$

depending on the base vectors at the projection point on the master surface $\bar{\mathbf{n}}^2, \bar{\mathbf{a}}_\alpha^2$. Then the stiffness vector for the local coordinates

$$\mathbf{D}^\alpha = \bar{H}^{\alpha\beta} [\mathbf{T}_\beta - \bar{g}_n \mathbf{N}_\beta] \quad (\text{C.2})$$

and the vectors needed for the tangential part

$$\mathbf{N}_{\alpha\beta} = \begin{pmatrix} \mathbf{0} \\ -N_{1,\alpha\beta} \bar{\mathbf{n}}^2 \\ -N_{2,\alpha\beta} \bar{\mathbf{n}}^2 \\ -N_{3,\alpha\beta} \bar{\mathbf{n}}^2 \\ -N_{4,\alpha\beta} \bar{\mathbf{n}}^2 \end{pmatrix}, \mathbf{T}_{\alpha\beta} = \begin{pmatrix} \mathbf{0} \\ -N_{1,\beta} \bar{\mathbf{a}}_\alpha^2 \\ -N_{2,\beta} \bar{\mathbf{a}}_\alpha^2 \\ -N_{3,\beta} \bar{\mathbf{a}}_\alpha^2 \\ -N_{4,\beta} \bar{\mathbf{a}}_\alpha^2 \end{pmatrix} \quad (\text{C.3})$$

can be specified as well.

C.2 Mortar tensors

The linear Mortar B matrices and the derivatives with respect to the slave and the master local coordinates can be formulated in terms of the unity tensor of three-dimensional continuum $\mathbf{1}^3 \in \mathbb{R}^3$

$$\begin{aligned}
 \mathbf{B}_{lin} &= \begin{bmatrix} -N_1^1 \mathbf{1}^3 & -N_2^1 \mathbf{1}^3 & -N_3^1 \mathbf{1}^3 & -N_4^1 \mathbf{1}^3 & N_1^2 \mathbf{1}^3 & N_2^2 \mathbf{1}^3 & N_3^2 \mathbf{1}^3 & N_4^2 \mathbf{1}^3 \end{bmatrix} \in \mathbb{R}^{3 \times 24} \\
 \mathbf{B}_{lin,\alpha}^1 &= \begin{bmatrix} -N_{1,\alpha}^1 \mathbf{1}^3 & -N_{2,\alpha}^1 \mathbf{1}^3 & -N_{3,\alpha}^1 \mathbf{1}^3 & -N_{4,\alpha}^1 \mathbf{1}^3 & \mathbf{0}^3 & \mathbf{0}^3 & \mathbf{0}^3 & \mathbf{0}^3 \end{bmatrix} \in \mathbb{R}^{3 \times 24} \\
 \mathbf{B}_{lin,\alpha}^2 &= \begin{bmatrix} \mathbf{0}^3 & \mathbf{0}^3 & \mathbf{0}^3 & \mathbf{0}^3 & N_{1,\alpha}^2 \mathbf{1}^3 & N_{2,\alpha}^2 \mathbf{1}^3 & N_{3,\alpha}^2 \mathbf{1}^3 & N_{4,\alpha}^2 \mathbf{1}^3 \end{bmatrix} \in \mathbb{R}^{3 \times 24} \\
 \mathbf{B}_{lin,\alpha\beta}^1 &= \begin{bmatrix} -N_{1,\alpha\beta}^1 \mathbf{1}^3 & -N_{2,\alpha\beta}^1 \mathbf{1}^3 & -N_{3,\alpha\beta}^1 \mathbf{1}^3 & -N_{4,\alpha\beta}^1 \mathbf{1}^3 & \mathbf{0}^3 & \mathbf{0}^3 & \mathbf{0}^3 & \mathbf{0}^3 \end{bmatrix} \in \mathbb{R}^{3 \times 24} \\
 \mathbf{B}_{lin,\alpha\beta}^2 &= \begin{bmatrix} \mathbf{0}^3 & \mathbf{0}^3 & \mathbf{0}^3 & \mathbf{0}^3 & N_{1,\alpha\beta}^2 \mathbf{1}^3 & N_{2,\alpha\beta}^2 \mathbf{1}^3 & N_{3,\alpha\beta}^2 \mathbf{1}^3 & N_{4,\alpha\beta}^2 \mathbf{1}^3 \end{bmatrix} \in \mathbb{R}^{3 \times 24}.
 \end{aligned} \tag{C.4}$$

The projection tensor for the shape functions of the slave \mathbf{P}_N^1 and of the master \mathbf{P}_N^2 surface as well as the projection tensor for the shape functions of the Lagrange multiplier \mathbf{P}_N^l are also specified using the corresponding unity tensors. For the back projection of the integration points from the pallets to the elements the projection tensor \mathbf{P}_N^p is needed which is written by means of the shape functions of a triangle

$$\begin{aligned}
 \mathbf{P}_N^1 &= \begin{bmatrix} N_1^1 \mathbf{1}^3 & N_2^1 \mathbf{1}^3 & N_3^1 \mathbf{1}^3 & N_4^1 \mathbf{1}^3 & \mathbf{0}^3 & \mathbf{0}^3 & \mathbf{0}^3 & \mathbf{0}^3 \end{bmatrix} \in \mathbb{R}^{3 \times 24} \\
 \mathbf{P}_N^2 &= \begin{bmatrix} \mathbf{0}^3 & \mathbf{0}^3 & \mathbf{0}^3 & \mathbf{0}^3 & N_1^2 \mathbf{1}^3 & N_2^2 \mathbf{1}^3 & N_3^2 \mathbf{1}^3 & N_4^2 \mathbf{1}^3 \end{bmatrix} \in \mathbb{R}^{3 \times 24} \\
 \mathbf{P}_N^l &= \begin{bmatrix} N_1^1 \mathbf{1}^3 & N_2^1 \mathbf{1}^3 & N_3^1 \mathbf{1}^3 & N_4^1 \mathbf{1}^3 \end{bmatrix} \in \mathbb{R}^{3 \times 12} \\
 \mathbf{P}_N^{ln} &= \begin{bmatrix} N_1^1 & N_2^1 & N_3^1 & N_4^1 \end{bmatrix} \in \mathbb{R}^{4a} \\
 \mathbf{P}_N^{lt\alpha} &= \begin{bmatrix} N_1^1 \mathbf{1}^\alpha & N_2^1 \mathbf{1}^\alpha & N_3^1 \mathbf{1}^\alpha & N_4^1 \mathbf{1}^\alpha \end{bmatrix} \in \mathbb{R}^{2 \times 12} \\
 \mathbf{P}_N^c &= \begin{bmatrix} N_1^1 & N_2^1 & N_3^1 & N_4^1 \end{bmatrix} \in \mathbb{R}^4 \\
 \mathbf{P}_{N_B}^{l3d} &= \begin{bmatrix} N_1^1 \mathbf{1}^6 & N_2^1 \mathbf{1}^6 & N_3^1 \mathbf{1}^6 & N_4^1 \mathbf{1}^6 \end{bmatrix} \in \mathbb{R}^{6 \times 12} \\
 \mathbf{P}_N^p &= \begin{bmatrix} N_1 \mathbf{1}^3 & N_2 \mathbf{1}^3 & N_3 \mathbf{1}^3 \end{bmatrix} \in \mathbb{R}^{3 \times 9}.
 \end{aligned} \tag{C.5}$$

The cross products within the linearization process are defined by means of cross matrices

$$\boldsymbol{\Omega}(\mathbf{x}) = \begin{bmatrix} 0 & -x_3 & x_2 \\ x_3 & 0 & -x_1 \\ -x_2 & x_1 & 0 \end{bmatrix}. \tag{C.6}$$

which ease the implementation.

C.3 Mortar storage arrays

Extensions to the classical storage behavior in the finite element code FEAP are listed in table C.1 and the additional storage arrays are given in detail in C.2 where additionally,

Variable	Definition
node1	Number node/slave element
node2	Number node/master element
neps1	Number slave elements
neps2	Number master elements
tnsg	Total number segments
tnpa	Total number pallets/polygon points

Table C.1: Mortar common block definition

Name	Pointer number	Description	Length
intp	hr(up(44))	Polygon points per segment	tnpa
intt	mr(up(45))	Type of polygon point 1: ma. node, 2: sl. node 3: int. point	tnpa
inte	mr(up(46))	Number of polygon points/segment	neps1 x neps2
slsg	mr(up(47))	Number of segments/slave element	neps1
mast	mr(up(49))	Master element/segment	tnsg
intn	mr(up(50))	Node number of polygon point If int. point 2 sl. and 2 ma. nodes	4 x tnpa

Table C.2: Mortar storage arrays

all the neighboring elements and the base vectors of each slave node have to be stored.

Appendix D

Derivation of the Reynolds equation

In the last section, it will be shown that the derivation of the Reynolds equation applied to lubricated contact formulations is at the end also based on the shell kinematics together with an integration over the height. An alternative derivation of the Reynolds equation is presented in the following statements starting with the velocity written in terms of a Cosserat surface of order 2

$$\mathbf{v}(\xi^\alpha, \xi) = \bar{\mathbf{v}}(\xi^\alpha) + \frac{\xi}{h} \widehat{\mathbf{v}}(\xi^\alpha) + \frac{\xi^2}{h^2} \widetilde{\mathbf{v}}(\xi^\alpha). \quad (\text{D.1})$$

Afterwards, the continuity equation (2.16) is integrated over the height

$$\int_0^h (\dot{\rho} + \rho \operatorname{div} \mathbf{v}) d\xi = 0 \quad (\text{D.2})$$

yielding the desired Reynolds equation. The unknown velocity contributions $\bar{\mathbf{v}}$, $\widehat{\mathbf{v}}$ and $\widetilde{\mathbf{v}}$ have to be specified by means of the boundary conditions

$$\mathbf{v}(\xi^\alpha, 0) = \mathbf{v}_l \quad \mathbf{v}(\xi^\alpha, h) = \mathbf{v}_u \quad (\text{D.3})$$

and of the Navier stokes equation which has to be fulfilled for the fluid film

$$\frac{d\mathbf{v}}{dt} = -\operatorname{grad} p + \mu \operatorname{div} (\operatorname{grad} \mathbf{v} + \operatorname{grad}^T \mathbf{v}) - \frac{2}{3} \mu \operatorname{grad} \operatorname{div} \mathbf{v} \quad (\text{D.4})$$

where μ corresponds to the viscosity. Neglecting the indication of the intrinsic coordinate system, the symmetric gradient of the divergence and the divergence of the gradient can be displayed in component form as

$$\begin{aligned} \operatorname{div} \operatorname{grad}^s \mathbf{v} &= (v_{i,jk} + v_{j,ik}) g^{jk} \mathbf{g}^i \\ \operatorname{grad} \operatorname{div} \mathbf{v} &= v_{i,jk} g^{ij} \mathbf{g}^k. \end{aligned} \quad (\text{D.5})$$

Since the height is very small, the bending parts (the derivatives with respect to α) in (D.5) can be neglected which is also applied in the derivation of the localization kinematics (Leppin [1999]). Assuming that the pressure is constant over the height

$$\operatorname{grad} p = p_{,\alpha} \mathbf{g}^\alpha, \quad (\text{D.6})$$

the Navier Stokes equation in the direction of flow and in the normal direction simplifies to

$$(-p_{,\alpha} + \mu v_{\alpha,33}) \mathbf{g}^\alpha = 0, \quad \frac{4}{3} \mu v_{\alpha,33} \mathbf{n} = 0 \quad (\text{D.7})$$

where inertia forces are also neglected since their influence in the fluid film is very small (Hamrock et al. [2004]). Applying (D.1) in (D.7), a relation between the unknown velocity part $\tilde{\mathbf{v}}$ and the pressure can be obtained

$$\tilde{v}_\alpha = \frac{h^2}{2\mu} p_{,\alpha}, \quad \tilde{v}_3 = 0. \quad (\text{D.8})$$

Together with the boundary conditions (D.3), the velocity in the fluid film (D.1) can now be specified without any unknowns

$$\begin{aligned} v_\alpha &= \left(1 - \frac{\xi}{h}\right) v_\alpha^l + \frac{\xi}{h} v_\alpha^u + \frac{\xi^2 - \xi h}{2\mu} p_{,\alpha} \\ v_3 &= \left(1 - \frac{\xi}{h}\right) v_3^l + \frac{\xi}{h} v_3^u. \end{aligned} \quad (\text{D.9})$$

Finally, applying the integration rule for the divergence only at the flow direction part (see Chipot and Luskin [1987] equation 7)

$$\int_0^h \text{div } v_\alpha \, d\xi = \text{div} \int_0^h v_\alpha \, d\xi - v_\alpha \Big|_{\xi=0}^{\xi=h} \text{div } h, \quad (\text{D.10})$$

the Reynolds equation in the generic form is obtained by (D.2) and exploiting (D.9), (D.10)

$$\begin{aligned} \int_0^h (\dot{\rho} + \rho \text{div } v_\alpha + \rho \text{div } v_3) \, d\xi &= \left(h \dot{\rho} - \frac{\rho h^3}{12\mu} p_{,\alpha} + \rho h \frac{v_\alpha^u + v_\alpha^l}{2} \right)_{,\alpha} \\ &\quad - \rho (v_\alpha^u - v_\alpha^l) h_{,\alpha} + \rho (v_3^u - v_3^l). \end{aligned} \quad (\text{D.11})$$

Alternatively, the classical derivation of the Reynolds equation can be found for instance in Hamrock et al. [2004] where (D.10) is slightly simplified. Another derivation of the Reynolds equation is formulated in Cameron [1981] using instead of the integrated continuity equation (D.2) or (D.11) the continuity of flow.

Bibliography

- M. Abramovitz and I. Stegun. *Handbook of Mathematical functions. With Formulas, Graphs and Mathematical Tables*. Dover Publications, 1972.
- P. Alart and A. Curnier. A mixed formulation for frictional contact problems prone to Newton like solution methods. *Computer Methods in Applied Mechanics and Engineering*, 92:353–375, 1991.
- I. Anastasopoulos and G. Gazetas. Foundation-structure systems over a rupturing normal fault: Part II. Analysis of the Kocaeli case histories. *Bulletin Earthquake Engineering*, 5:277–301, 2007.
- D. Aubram. Differential Geometry Applied to Continuum Mechanics. Technical Report Heft 44, Fachgebiet Grundbau und Bodenmechanik - Degebo, Technische Universität Berlin, 2009.
- J. M. Ball. Convexity conditions and existence theorems in nonlinear elasticity. *Archive for Rational Mechanics and Analysis*, 63:337–403, 1977.
- E. Bauer. Calibration of the comprehensive hypoplastic model for granular materials. *Soils and Foundations*, 36:13–26, 1996.
- J. Bear. *Dynamics of Fluids in Porous Media*. Elsevier, New York, 1972.
- F.B. Belgacem, P. Hild, and P. Laborde. The mortar finite element method for contact problems. *Mathematical and Computational Modelling*, 28:263–271, 1998.
- A. Berg. *Beiträge zur geometrischen nichtlinearen Theorie und inkrementellen Finite-Element-Berechnung dünner elastischer Schalen*. PhD thesis, Universität Hannover, Germany, 1983.
- C. Bernardi, N. Debit, and Y. Maday. Coupling finite elements and spectral methods: First results. *Mathematics of Computation*, 54:21–39, 1990.
- C. Bernardi, Y. Maday, and A.T. Patera. A new nonconforming approach to domain decomposition: The mortar element method. In H. Brezia and J.L. Lions, editors, *Nonlinear Partial Differential Equations and their Applications*, pages 13–51. Pitman: London, Wiley: New York, 1992.

- P. Betsch and P. Steinmann. Conservation properties of a time FE method - part II: Time-stepping schemes for non-linear elastodynamics. *International Journal for Numerical Methods in Engineering*, 50:1931–1955, 2001.
- M. Bischoff. *Theorie und Numerik einer dreidimensionalen Schalenformulierung*. PhD thesis, Universität Stuttgart, Germany, 2000.
- R.L. Bishop and S.I. Goldberg. *Tensor Analysis on Manifolds*. Dover Publications, 1980.
- B. Boley and J. Weiner. *Theory of thermal stresses*. John Wiley, London, 1960.
- R.M. Bowen and C.C. Wang. *Introduction to Vectors and Tensors*, volume 1,2. Plenum Press, New York, 1976.
- D. Braess. *Finite Elements: Theory, fast solvers, and applications in solid mechanics*. Cambridge University Press, 3rd edition, 2007.
- A. Cameron. *Basic Lubrication Theory*. Ellis Horwood Limited, Chichester, 3rd edition, 1981.
- S. Casciati and R.I. Borja. Dynamic FE analysis of South Memnon Colossus including 3D soil-foundation-structure interaction. *Computers and Structures*, 82:1719–1736, 2004.
- E.S. Chan and I.S. Tuba. A finite element method for contact problems in solid bodies. *International Journal of Mechanical Sciences*, 13:615–639, 1971.
- M. Chipot and M. Luskin. The compressible Reynolds lubrication equation. In S. Antman, J.L. Ericksen, D. Kinderlehrer, and I. Müller, editors, *Metastability and incompletely posed problems*, pages 61–75. Springer Verlag, New York, 1987.
- P.W. Christensen, A. Klarbring, J.S. Pang, and N. Strömberg. Formulation and comparison of algorithms for frictional contact problems. *International Journal of Mechanical Sciences*, 42:145–173, 1998.
- J. Chung and G.M. Hulbert. A time integration algorithm for structural dynamics with improved numerical dissipation: The generalized- α method. *Journal of Applied Mechanics*, 60:371–375, 1993.
- P. G. Ciarlet. *Mathematical Elasticity: Three Dimensional Elasticity*. North-Holland, Amsterdam, New York, 1988.
- R. Courant. Variational methods for solutions of problems of equilibrium and vibrations. *Bulletin of the American Mathematical Society*, 49:1–61, 1943.
- M.A. Crisfield. *Non-linear Finite Element Analysis of Solids and Structures*, volume Volume 1: Essentials. John Wiley & Sons Ltd, Chichester, 1991.

- A. Curnier. A theory of friction. *International Journal of Solids and Structures*, 20: 637–647, 1984.
- A. Curnier, Q.C. He, and A. Klarbring. Continuum mechanics modelling of large deformation contact with friction. In M. Raous, M. Jean, and J.J Moreau, editors, *Contact Mechanics, Proceedings of the 2nd Contact Mechanics International Symposium 1994*, pages 145–158, London, 1995. Plenum Publishing.
- M. Cyrus and J. Beck. Generalized two- and three-dimensional clipping. *Computers & Graphics*, 3:23–28, 1978.
- M. de Berg, O. Cheong, M. van Krefeld, and M. Overmars. *Computational Geometry: Algorithms and Applications*. Springer Verlag, Berlin, Heidelberg, 3rd edition, 2010.
- R. de Boer. *Trends in Continuum Mechanics of Porous Media*. Springer-Verlag, Dordrecht, 2005.
- C. Agelet de Saracibar. A new frictional time integration algorithm for large slip multi-body frictional contact problems. *Computer Methods in Applied Mechanics and Engineering*, 142:303–334, 1997.
- E.A. de Souza Neto, D. Peric, and D.R.J. Owen. *Computational Methods for Plasticity - Theory and Applications*. John Wiley & Sons, Chicester, 2008.
- J.W. Demmel. *Applied Numerical Linear Algebra*. SIAM, Philadelphia, 1997.
- C. S. Desai and H.J. Siriwardane. *Constitutive Laws for Engineering Materials with Emphasis on Geologic Materials*. Prentice-Hall, Englewood Cliffs, 1984.
- C.S. Desai. Numerical design-analysis for piles in sands. *Journal of the Geotechnical Engineering Division*, GT6:613–635, 1974.
- G. Dhatt and G. Touzot. *The Finite Element Method Displayed*. John Wiley & Sons Ltd, Chicester, 1984.
- G. Duvaut and J.L. Lions. *Inequalities in Mechanics and Physics*. Springer-Verlag, Berlin, Heidelberg, 1976.
- R. Eberlein. *Finite-Element-Konzepte für Schalen mit großen elastischen und plastischen Verzerrungen*. PhD thesis, Technische Hochschule Darmstadt, Germany, 1997.
- U. Edlund. Surface adhesive joint description with coupled elastic-plastic damage behavior and numerical applications. *Computer Methods in Applied Mechanics and Engineering*, 115:253–276, 1994.
- W. Ehlers. A single-surface yield function for geomaterials. *Archive of Applied Mechanics*, 65:246–259, 1995.

- W. Ehlers. Foundations of multiphase and porous media. In W. Ehlers and J. Bluhm, editors, *Porous media: Theory, experiments and numerical applications*, pages 3–86. Springer-Verlag, Berlin, 2002.
- W. Ehlers and O. Avci. Stress-dependent hardening and failure surfaces of dry sand. *International Journal for Numerical and Analytical Methods in Geomechanics*, Published online:DOI:10.1002/nag.1121, 2012.
- W. Ehlers and B. Scholz. An inverse algorithm for the identification and the sensitivity analysis of the parameters governing micropolar elasto-plastic granular material. *Archive of Applied Mechanics*, 77:911–931, 2007.
- W. Ehlers, O. Avci, and B. Markert. Computation of slope movements initiated by rain-induced shear bands in small-scale tests and in situ. *Vadose Zone Journal*, 10: 512–525, 2011.
- G. Eipper. *Theorie und Numerik finiter elastischer Deformationen in fluidgesättigten porösen Festkörpern*. PhD thesis, Universität Stuttgart, Germany, 1998.
- N. El-Abbasi and K.-J. Bathe. Stability and patch test performance of contact discretizations and a new solution algorithm. *Computers & Structures*, 79:1473–1486, 2001.
- P. Ellsiepen. *Zeit- und ortsadaptive Verfahren angewandt auf Mehrphasenprobleme poröser Medien*. PhD thesis, Universität Stuttgart, Germany, 1999.
- A.C. Eringen and C.B. Kafadar. Polar field theories. In A. C. Eringen, editor, *Continuum Physics*, volume IV - Polar and nonlocal field theories, pages 1–74. Academic Press, New York, 1976.
- K.A. Fischer and P. Wriggers. Frictionless 2d contact formulations for finite deformations based on the Mortar method. *Computational Mechanics*, 36:226–244, 2005.
- K.A. Fischer and P. Wriggers. Mortar-based frictional contact formulation for higher order interpolations using the moving friction cone. *Computer Methods in Applied Mechanics and Engineering*, 195:5020–5036, 2006.
- K.A. Fischer, D. Sheng, and A.J. Abbo. Modeling of pile installation using contact mechanics and quadratic elements. *Computers and Geotechnics*, 34:449–461, 2007.
- A.C. Fischer-Cripps. *Introduction to Contact Mechanics*. Springer-Verlag, New York, 2nd edition, 2007.
- J.D. Foley, A. van Dam, S.K. Feiner, and J.F. Hughes. *Computer Graphics: Principles and Practice*. Addison-Wesley, Boston, San Francisco, 2nd edition, 1996.
- A. Francavilla and O.C. Zienkiewicz. A note on numerical computation of elastic contact problems. *International Journal for Numerical Methods in Engineering*, 9: 913–924, 1975.

- D. Franke, A. Düster, V. Nübel, and E. Rank. A comparison of the h-, p-, hp-, and rp-version of the FEM for the solution of the 2D Hertzian contact problem. *Computational Mechanics*, 45:513–522, 2010.
- T.P. Fries and T. Belytschko. The extended/generalized finite element method: An overview of the method and its applications. *International Journal for Numerical Methods in Engineering*, 84:253–304, 2010.
- A. Gerstenberger and W.A. Wall. An eXtended Finite Element Method/Lagrange multiplier based approach for fluid-structure interactions. *Computer Methods in Applied Mechanics and Engineering*, 197:1699–1714, 2008.
- A. Gerstenberger and W.A. Wall. An embedded Dirichlet formulation for 3D continua. *International Journal for Numerical Methods in Engineering*, 82:537–563, 2010.
- J. Ghaboussi, E.L. Wilson, and J. Isenberg. Finite element for rock joints and interfaces. *Journal of the Soil Mechanics and Foundations Division*, 10:833–848, 1973.
- A.E. Giannakopoulos. The return mapping method for the integration of friction constitutive relations. *Computers & Structures*, 32:157–167, 1989.
- G. Gudehus. Elastoplastische Stoffgleichungen für trockenen Sand. *Ingenieur-Archiv*, 42:151–169, 1973.
- E. Hairer and G. Wanner. *Solving Ordinary Differential Equations II: Stiff and Differential-Algebraic Problems*. Springer-Verlag, Berlin, Heidelberg, 2nd edition, 2002.
- E. Hairer, S.P. Nørsett, and G. Wanner. *Solving Ordinary Differential Equations I: Nonstiff Problems*. Springer-Verlag, Berlin, Heidelberg, 2nd edition, 2008.
- J. O. Hallquist. Nike2d: An implicit, finite-deformation, finite element code for analyzing the static and dynamic response of two dimensional solids. Technical report, UCRL-52678, University of California, Lawrence Livermore National Laboratory, 1979.
- B.J. Hamrock, S.R. Schmid, and B.O. Jacobson. *Fundamentals of Fluid Film Lubrication*. Marcel Dekker, New York, Basel, 2nd edition, 2004.
- A. Haraldsson. *Formulierung und Simulation der Kontaktvorgänge in der Baugrund-Tragwerk-Interaktion*. PhD thesis, Universität Hannover, Germany, 2003.
- A. Haraldsson and P. Wriggers. A strategy for numerical testing of frictional laws with application to contact between soil and concrete. *Computer Methods in Applied Mechanics and Engineering*, 190:963–977, 2000.
- P. Haupt. *Continuum Mechanics and Theory of Materials*. Springer-Verlag, Berlin, Heidelberg, Wien, 2nd edition, 2002.

- R. Hauptmann and K. Schweizerhof. A systematic development of 'solid shell' element formulations for linear and non-linear analysis employing only displacement degrees of freedom. *International Journal for Numerical Methods in Engineering*, 42:49–69, 1998.
- E. Hellinger. Die allgemeinen Ansätze der Mechanik der Kontinua. *Encyklopädie der Mathematischen Wissenschaften*, 4/4:601–694, 1914.
- I. Herle. *Hypoplastizität und Granulometrie einfacher Korngrüste*. PhD thesis, Universität Fridericiana in Karlsruhe, Germany, 1997.
- H. Hertz. Ueber die Berührung fester elastischer Körper. *Journal für die reine und angewandte Mathematik*, 92:156–171, 1881.
- A. Hettler and G. Gudehus. Influence of the foundation width on the bearing capacity factor. *Soils and Foundations*, 28:81–92, 1988.
- R. Hill. *The Mathematical Theory of Plasticity*. Clarendon Press, Oxford, 1950.
- G. A. Holzapfel. *Nonlinear Solid Mechanics. A Continuum Approach for Engineering*. John Wiley, Chichester, 2000.
- S. Hübner and B.I. Wohlmuth. A primal-dual active set strategy for nonlinear multi-body contact problems. *Computer Methods in Applied Mechanics and Engineering*, 194:3147–3166, 2005.
- S. Hübner, G. Stadler, and B.I. Wohlmuth. A primal-dual active set algorithm for three-dimensional contact problems with coulomb friction. *SIAM Journal on Scientific Computing*, 30:572–596, 2008.
- T.J.R. Hughes, R.L. Taylor, J.L. Sackman, A. Curnier, and W. Kanoknukulchai. A finite element method for a class of contact-impact problems. *Computer Methods in Applied Mechanics and Engineering*, 8:249–276, 1976.
- T.R.J. Hughes. *The Finite Element Method*. Prentice Hall, Englewood Cliffs, New Jersey, 1987.
- K. Hutter and A. F. van de Ven. *Field Matter Interactions in Thermoelastic Solids*. Springer-Verlag, Berlin, Heidelberg, Wien, 1978.
- R.P. Jensen, P.J. Bosscher, M.E. Plesha, and T.B. Edil. DEM simulation of granular media - structure interface: Effects of surface roughness and particle shape. *International Journal for Numerical and Analytical methods in Geomechanics*, 23:531–547, 1999.
- K.L. Johnson. *Contact Mechanics*. Cambridge University Press, 1985.
- N. Kikuchi and J.T. Oden. *Contact Problems in Elasticity: A Study of Variational Inequalities and Finite Element Methods*. SIAM, Philadelphia, 1988.

- T.Y. Kim, J. Dolbow, and T.A. Laursen. A mortar finite element method for frictional contact on arbitrary interfaces. *Computational Mechanics*, 39:223–235, 2007.
- S. Klinkel, F. Gruttmann, and W. Wagner. A continuum based three-dimensional shell element for laminated structures. *Computers & Structures*, 71:43–62, 1999.
- D. Kolymbas. *Introduction to Hypoplasticity*. A.A. Balkema, Rotterdam, Brookfield, 2000.
- A. Konyukhov and K. Schweizerhof. Covariant description for frictional contact problems. *Computational Mechanics*, 35:190–213, 2005.
- W. Kosinski. *Field Singularities and Wave Analysis in Continuum Mechanics*. Ellis Horwood, Chichester, 1986.
- A. Kovetz. *Electromagnetic Theory*. Oxford University Press, 2000.
- I.V. Kragelsky, M.N. Dobychin, and V.S. Kombalov. *Friction and Wear: Calculation Methods*. Pergamon Press, Oxford, 1982.
- A. Krawietz. *Materialtheorie*. Springer-Verlag, Berlin, Heidelberg, 1986.
- D. Kuhl and M.A. Crisfield. Energy-conserving and decaying algorithms in non-linear structural dynamics. *International Journal for Numerical Methods in Engineering*, 45:569–599, 1999.
- R. Larsson and K. Runesson. Plastic localization captured by discontinuous displacement approximation. In D.R.J. Owen, E. Onate, and E. Hinton, editors, *Computational Plasticity - fundamentals and applications*, pages 605–616. Pineridge Press, Swansea, 1992.
- T. A. Laursen. *Computational Contact and Impact Mechanics*. Springer-Verlag, Berlin, Heidelberg, 2006.
- T. A. Laursen and J. C. Simo. A continuum-based finite element formulation for the implicit solution of multibody, large deformation frictional contact problems. *International Journal for Numerical Methods in Engineering*, 36:3451–3485, 1993.
- J. Lemaitre and J.L. Chaboche. *Mechanics of solid materials*. Cambridge University Press, 1990.
- C. Leppin. *Ein diskontinuierliches Finite-Element-Modell für Lokalisierungsversagen in metallischen und granularen Materialien*. PhD thesis, Universität Hannover, Germany, 1999.
- S. Li and W.K. Liu. *Meshfree Particle Methods*. Springer-Verlag, Berlin, Heidelberg, New York, 2007.
- J. Lubliner. *Plasticity Theory*. Macmillan, London, 1990.

- D. G. Luenberger. *Linear and Nonlinear Programming*. Addison Wesley, Reading Mass., 2nd edition, 1984.
- S.H. Lutzenberger. *Ein differentiell-algebraisches Simulationsmodell zur Fahrzeug-Fahrweg Interaktion*. PhD thesis, Technische Universität München, Germany, 2002.
- D.K. Maharaj and S.R. Gandhi. Non-linear finite element analysis of piled raft foundations. *Proceedings of the Institution of Civil Engineers - Geotechnical Engineering*, 157:107–113, 2004.
- J. Marsden and T. J. R. Hughes. *Mathematical Foundations of Elasticity*. Prentice-Hall, Inc., Englewood Cliffs, 1983.
- C.M. Mate. *Tribology on the small scale: A bottom up approach to friction, lubrication and wear*. Oxford University Press, New York, 2008.
- R. Michalowski and Z. Mroz. Associated and non-associated sliding rules in contact friction problems. *Archieve of Mechanics*, 30:259–276, 1978.
- C. Miehe. *Zur numerischen Behandlung thermomechanischer Prozesse*. PhD thesis, Universität Hannover, Germany, 1988.
- C. Miehe. Kanonische Modelle multiplikativer Elasto-Plastizität. Thermodynamische Formulierung und numerische Implementation. Technical Report F 93/1, Forschungs- und Seminarbereiche aus dem Bereich der Mechanik der Universität Hannover, 1993.
- C. Miehe. Aspects of the formulation and finite element implementation of large strain isotropic elasticity. *International Journal for Numerical Methods in Engineering*, 37: 1981–2004, 1994.
- C. Miehe and J. Schröder. Post-critical discontinuous localization analysis of small-strain softening elasoplastic solids. *Archieve of Applied Mechanics*, 64:267–285, 1994.
- R.D. Mindlin. Second gradient of strain and surface-tension in linear elasticity. *International Journal of Solid and Structures*, 1:417–438, 1965.
- N. Moes, J. Dolbow, and T. Belytschko. A finite element method for crack growth without remeshing. *International Journal for Numerical Methods in Engineering*, 46:131–150, 1999.
- N. Moes, M. Cloirec, P. Cartraud, and J.F. Remacle. A computational approach to handle complex microstructure geometries. *Computer Methods in Applied Mechanics and Engineering*, 192:3163–3177, 2003.
- P.M. Naghdi. *The Theory of Shells and Plates*. Handbuch der Physik Bd. VIa/2. Springer-Verlag, Berlin, Heidelberg, 1972.
- G.C. Nayak and O.C. Zienkiewicz. Convenient form of stress invariants for plasticity. *Journal of Structural Division, Proceedings of the American Society of Civil Engineers*, 98:949–954, 1972.

- A. Niemunis, T. Wichtmann, and T. Triantafyllidis. A high-cycle accumulation model for sand. *Computer and Geotechnics*, 32:245–263, 2005.
- J.T. Oden. Exterior penalty methods for contact problems in elasticity. In W. Wunderlich, E. Stein, and K.J. Bathe, editors, *Nonlinear Finite Element Analysis in Struktural Mechanics*, pages 3–86. Springer-Verlag, Berlin, 1981.
- J.T. Oden and J.A.C. Martins. Models and computational methods for dynamic friction phenomena. *Computer Methods in Applied Mechanics and Engineering*, 52:527–634, 1985.
- R.W. Ogden. *Non-Linear Elastic Deformations*. Ellis Horwood and John Wiley, Chichester, 1984.
- P. Papadopoulos and R.L. Taylor. A mixed formulation for the finite element solution of contact problems. *Computer Methods in Applied Mechanics and Engineering*, 94:373–389, 1992.
- H. Parisch. A continuum-based shell theory for non-linear applications. *International Journal for Numerical Methods in Engineering*, 38:1855–1883, 1995.
- N. Patir. A numerical procedure for random generation of rough surfaces. *Wear*, 47:263–277, 1978.
- A. Perez-Foguet, A. Rodriguez-Ferran, and A. Huerta. Consistent tangnet matrices for substepping schemes. *Computer Methods in Applied Mechanics and Engineering*, 190:4627–4647, 2001.
- G. Pietrzak and A. Curnier. Large deformation frictional contact mechanics: continuum formulation and augmented lagrangian treatment. *Computer Methods in Applied Mechanics and Engineering*, 177:351–381, 1999.
- A. Popp, M.W. Gee, and W.A. Wall. A finite deformation mortar contact formulation using a primal-dual active set strategy. *International Journal for Numerical Methods in Engineering*, 79:1354–1391, 2009.
- A. Popp, M. Gitterle, M.W. Gee, and W.A. Wall. A dual mortar approach for 3D finite deformation contact with consistent linearization. *International Journal for Numerical Methods in Engineering*, 83:1428–1465, 2010a.
- A. Popp, M. Gitterle, M.W. Gee, and W.A. Wall. Finite deformation frictional mortar contact using a semi-smooth Newton method with consistent linearization. *International Journal for Numerical Methods in Engineering*, 84:543–571, 2010b.
- J.G. Potyondy. Skin friction between various soils and construction materials. *Géotechnique*, 11:339–353, 1961.
- M.A. Puso. A 3d mortar method for solid mechanics. *International Journal for Numerical Methods in Engineering*, 59:315–336, 2004.

- M.A. Puso and T.A. Laursen. A mortar segment-to-segment contact method for large deformation solid mechanics. *Computer Methods in Applied Mechanics and Engineering*, 193:601–629, 2004a.
- M.A. Puso and T.A. Laursen. A mortar segment-to-segment frictional contact method for large deformations. *Computer Methods in Applied Mechanics and Engineering*, 193:4891–4913, 2004b.
- D. Rebstock. *Verspannung und Entspannung von Sand entlang von Baukörpern*. PhD thesis, Universität Fridericiana in Karlsruhe, Germany, 2011.
- E. Reissner. On a variational theorem in elasticity. *Journal of Mathematics and Physics*, 29:90–95, 1950.
- O. Reul. *In-situ Messungen und numerische Studien zum Tragverhalten der kombinierten Pfahl-Plattengründungen*. PhD thesis, Technischen Hochschule Darmstadt, Germany, 2000.
- A. Rieger. *Adaptive Algorithmen für thermomechanisch gekoppelte Kontaktprobleme*. PhD thesis, Universität Hannover, Germany, 2002.
- J.D. Sanders, J. Dolbow, and T.A. Laursen. On methods for stabilizing constraints over enriched interfaces in elasticity. *International Journal for Numerical Methods in Engineering*, 78:1009–1036, 2009.
- S.A. Savidis, D. Aubram, and F. Rackwitz. Arbitrary Lagrangian-Eulerian finite element formulation for geotechnical construction processes. *Journal of Theoretical and Applied Mechanics*, 38:165–194, 2008.
- T. Schanz. Zur Modellierung des mechanischen Verhaltens von Reibungsmaterialien. Technical Report 45, Mitteilung Institut für Geotechnik Stuttgart, 1998.
- O. Schenk, K. Gärtner, W. Fichtner, and A. Stricker. Pardiso: a high-performance serial and parallel sparse linear solver in semiconductor device simulation. *Future Generation Computer Systems*, 18:69–78, 2001.
- O. Scherf. *Kontinuumsmechanische Modellierung nichtlinearer Kontaktprobleme und ihre numerische Analyse mit adaptiven Finite-Element-Methoden*. PhD thesis, Technische Hochschule Darmstadt, Germany, 1997.
- B. Scholz. *Application of a Micropolar Model to the Localization Phenomena in Granular Materials: General Model, Sensitivity Analysis and Parameter Optimization*. PhD thesis, Universität Stuttgart, Germany, 2007.
- H. Schoop. Oberflächenorientierte Schalentheorie endlicher Verschiebungen. *Ingenieur-Archiv*, 56:427–437, 1986.
- H.R. Schwarz. *Methode der finiten Elemente: Eine Einführung unter Berücksichtigung der Rechenpraxis*. Teubner, Stuttgart, 1991.

- K. Schweizerhof and E. Ramm. Displacement dependent pressure loads in nonlinear finite element analysis. *Computers & Structures*, 6:1099–1114, 1984.
- H. Schwetlick and H. Kretschmar. *Numerische Verfahren für Naturwissenschaftler und Ingenieure*. Fachbuchverlag Leipzig, 1991.
- R. Sedgewick. *Algorithmen*. Addison-Wesley, Bonn, München, 1992.
- D. Sheng, K.D. Eigenbrod, and P. Wriggers. Finite element analysis of pile installation using large-slip frictional contact. *Computers and Geotechnics*, 32:17–26, 2005.
- D. Sheng, P. Wriggers, and S.W. Sloan. Improved numerical algorithm for frictional contact in pile penetration analysis. *Computers and Geotechnics*, 33:341–354, 2006.
- D. Sheng, M. Nazem, and J.P. Carter. Some computational aspects for solving deep penetration problems in geomechanics. *Computational Mechanics*, 44:549–561, 2009.
- M. Silhavy. *The Mechanics and Thermodynamics of Continuous Media*. Springer-Verlag, Berlin, Heidelberg, Wien, 1997.
- J.C. Simo. *Numerical Analysis and Simulation of Plasticity*. Handbook of Numerical Analysis VI. Elsevier Science B.V., 1998.
- J.C. Simo and D.D. Fox. On a stress resultant geometrically exact shell model. Part I: Formulation and optimal parametrization. *Computer Methods in Applied Mechanics and Engineering*, 72:267–304, 1989.
- J.C. Simo and T.A. Laursen. An augmented Lagrangian treatment of contact problems involving friction. *Computers & Structures*, 42:97–116, 1992.
- J.C. Simo and K.S. Pister. Remarks on rate constitutive equations for finite deformation problems: computational implications. *Computer Methods in Applied Mechanics and Engineering*, 46:201–215, 1984.
- J.C. Simo and N. Tarnow. The discrete energy-momentum method. conserving algorithms for nonlinear elastodynamics. *Zeitschrift für angewandte Mathematik and Physik*, 7:513–525, 1991.
- J.C. Simo and R.L. Taylor. Consistent tangent operators for rate-independent elastoplasticity. *Computer Methods in Applied Mechanics and Engineering*, 48:101–118, 1985.
- J.C. Simo, P. Wriggers, and R.L. Taylor. A perturbed Lagrangian formulation for the finite element solution of contact problems. *Computer Methods in Applied Mechanics and Engineering*, 50:163–180, 1985.
- J.C. Simo, R.L. Taylor, and P. Wriggers. A note on finite-element implementation of pressure boundary loading. *Communications in Applied Numerical Methods*, 7: 513–525, 1991.

- S.W. Sloan. Substepping schemes for the numerical integration of elastoplastic stress-strain relations. *International Journal for Numerical Methods in Engineering*, 24: 893–911, 1987.
- A. J. M. Spencer. *Continuum Mechanics*. Longman, London, 1980.
- W. Sprenger, F. Gruttmann, and W. Wagner. Delamination growth analysis in laminated structures with continuum based 3D-shell elements and a viscoplastic softening model. *Computer Methods in Applied Mechanics and Engineering*, 185:123–139, 2000.
- G. Stadler. Semismooth Newton and augmented Lagrangian methods for a simplified friction problem. *SIAM Journal on Optimization*, 15:39–62, 2004.
- G. Strang and G.J. Fix. *An Analysis of the Finite Element Method*. Prentice-Hall, Englewood Cliffs, N.J., 1973.
- N. Strömberg, L. Johansson, and A. Klarbring. Derivation and analysis of a generalized standard model for contact, friction and wear. *International Journal of Solids and Structures*, 33:1817–1836, 1996.
- D. Tabor. Friction - the present state of our understanding. *Journal of Lubrication Technology*, 103:169–179, 1981.
- M. Taiebat and Y.F. Dafalias. Sanisand: Simple anisotropic sand plasticity model. *International Journal for Numerical and Analytical Methods in Geomechanics*, 32: 915–948, 2008.
- J. Teichmann and W. Wu. Fe-investigations of micro-polar boundary conditions along interface between soil and structure. *Granular Matter*, 12:399–410, 2010.
- I. Temizer. A mixed formulation of mortar-based frictionless contact. *Computer Methods in Applied Mechanics and Engineering*, 223-224:173–185, 2012.
- K. Terzaghi, R.B. Peck, and G. Mesri. *Soil Mechanics in Engineering Practice*. John Wiley & Sons, New York, 3rd edition, 1996.
- H.J. Tillemans and H.J. Herrmann. Simulating deformations of granular solids under shear. *Pysica*, 217:261–288, 1995.
- S.P. Timoshenko and J.N. Goodier. *Theory of Elasticity*. McGraw-Hill, New York, 3rd edition, 1970.
- T. Triantafyllidis. Neue Erkenntnisse aus Messungen an tiefen Baugruben am Postdamer Platz in Berlin. *Bautechnik*, 75:133–154, 1998.
- C. Truesdell. *Rational Thermodynamics*. Springer-Verlag, New York, 2rd edition, 1984.
- C. Truesdell and W. Noll. *The Non-Linear Field Theories of Mechanics*. Springer-Verlag, Berlin, Heidelberg, New York, 3rd edition, 2004.

- C. Truesdell and R. A. Toupin. *The classical field theories*. Handbuch der Physik Bd. III/1. Springer-Verlag, Berlin, Heidelberg, Wien, 1960.
- M. Tur, F.J. Fuenmayor, and P. Wriggers. A mortar-based frictional contact formulation for large deformations using Lagrange multipliers. *Computer Methods in Applied Mechanics and Engineering*, 198:2860–2873, 2009.
- M. Uesugi, H. Kishida, and Y. Uchikawa. Friction between dry sand and concrete under monotonic and repeated loading. *Soils and Foundations*, 30:115–128, 1990.
- P.A. von Wolffersdorff. A hypoplastic relation for granular materials with a predefined limit state surface. *Mechanics of Cohesive-Frictional Materials*, 1:251–271, 1996.
- W. Wagner. *Eine geometrisch nichtlineare Theorie schubelastischer Schalen mit Anwendung auf Finite-Element-Berechnungen von Durchschlag- und Kontaktproblemen*. PhD thesis, Universität Hannover, Germany, 1985.
- K. Washizu. *Variational Methods in Elasticity and Plasticity*. Pergamon Press, Oxford, 2nd edition, 1975.
- C. Weißenfels and P. Wriggers. Numerical modeling of electrical contacts. *Computational Mechanics*, 46:301–314, 2010.
- C. Wellmann and P. Wriggers. A two-scale model of granular materials. *Computer Methods in Applied Mechanics and Engineering*, 205:46–58, 2012.
- E.A. Wilson and B. Parson. Finite element analysis of elastic coact problems using differential displacement. *International Journal for Numerical Methods in Engineering*, 2:387–395, 1970.
- B.I. Wohlmuth. A mortar finite element method using dual spaces for the lagrange multiplier. *SIAM Journal on Numerical Analysis*, 38:989–1012, 2000.
- B.I. Wohlmuth. Variationally consistent discretization schemes and numerical algorithms for contact problems. *Acta Numerica*, 20:569–734, 2011.
- P. Wriggers. On consistent tangent matrices for frictional contact problems. In G. Pande and J. Middleton, editors, *Proceedings of NUMETA 87*, pages 145–158, Dordrecht, 1987. M. Nijhoff Publishers.
- P. Wriggers. *Nichtlineare Finite-Element-Methoden*. Springer-Verlag, Berlin, Heidelberg, New York, 2001.
- P. Wriggers. *Computational Contact Mechanics*. Springer-Verlag, Berlin, Heidelberg, 2nd edition, 2006.
- P. Wriggers and C. Miehe. On the treatment of contact constraints within coupled thermomechanical analysis. In D. Besdo and E. Stein, editors, *Finite Elastic Deformations, Proceedings of EUROMECH*, pages 333–347, Berlin, 1992. Springer-Verlag.

- P. Wriggers and C. Miehe. Contact constraints within coupled thermomechanical analysis - a finite element model. *Computer Methods in Applied Mechanics and Engineering*, 113:301–319, 1994.
- P. Wriggers and J. Reinelt. Multi-scale approach for frictional contact of elastomers on rough rigid surfaces. *Computer Methods in Applied Mechanics and Engineering*, 198:1996–2008, 2009.
- P. Wriggers, T. Vu Van, and E. Stein. Finite element formulation of large deformation impact-contact problems with friction. *Computers & Structures*, 37:319–331, 1990.
- Y. Yamada and K. Ishihara. Anisotropic deformation characteristics of sand under three dimensional stress conditions. *Soils and Foundations*, 19:79–94, 1979.
- B. Yang, T.A. Laursen, and X. Meng. Two dimensional mortar contact methods for large deformation frictional sliding. *International Journal for Numerical Methods in Engineering*, 62:1183–1225, 2005.
- Y. Basar and W.B. Krätzig. Theory of Shell Structures. Technical Report 18/258, Fortschritt-Bereichte VDI, 2000.
- M.M. Zaman, C.S. Desai, and E.C. Drumm. Interface model for dynamic soil-structure interaction. *Journal of the Geotechnical Engineering*, 110:1257–1273, 1984.
- G. Zavarise and R.L. Taylor. Point-to-segment contact geometry revisited. In *Proceedings of joint conference of the Italian group of Computational Mechanics and Ibero-Latin-American Association of Computational Methods in Engineering*, pages 884–891, 1996.
- M. Zhao, D. Liu, L. Zhang, and C. Jiang. 3d finite element analysis on pile-soil interaction passive pile group. *Journal of Central South University of Technology*, 15: 75–80, 2008.
- O.C. Zienkiewicz and R.L. Taylor. *The Finite Element Method*, volume Volume 1. McGraw Hill, London, 4rd edition, 1989.
- O.C. Zienkiewicz and R.L. Taylor. *The Finite Element Method*, volume Volume 2. McGraw Hill, London, 4rd edition, 1991.
- A. Zilian and T.P. Fries. A localized mixed-hybrid method for imposing interfacial constraints in the extended finite element method (xfem). *International Journal for Numerical Methods in Engineering*, 79:733–752, 2009.



Institut für
Kontinuumsmechanik

Contact methods integrating plasticity models with application to soil mechanics

Christian Weißenfels

Leibniz
Universität
Hannover

ISBN 978-3-941302-06-8

This work is focused on the development of novel concepts for a direct integration of three-dimensional plasticity models into a contact formulation which can be applied to different kinds of contact discretizations. These generic concepts are applied to the investigation of soil structure interactions where the new friction laws are implemented into the Mortar method.

Within the Mortar framework for the first time a pure Lagrange multiplier method and a new mixed version are presented and compared to standard Mortar formulations.

At the end a concept to integrate the contact formulations into the eXtended-Finite-Element-Method is presented which is based on the Hu Washizu principle and which needs to additional stabilization schemes.